



TECHNISCHE UNIVERSITÄT  
**ILMENAU**

Fakultät für Elektrotechnik und Informationstechnik  
der Technischen Universität Ilmenau

Dissertation  
zur Erlangung des akademischen Grades  
Doktor-Ingenieur (Dr.-Ing.)

# **Wideband MIMO Radio Channel Modeling**

by

**Dipl.-Ing. Milan Narandžić**

Anfertigung im: Fachgebiet Elektronische Messtechnik  
Institut für Informationstechnik

Vorgelegt am: 08.04.2014

Gutachter: Univ.-Prof. Dr.-Ing. habil. Reiner S. Thomä  
Univ.-Prof. Dr.-Ing. Giovanni Del Galdo  
o. Univ.-Prof. Dr.-Ing. Vladimir Milošević

Verteidigung am: 09.04.2015



*To my family*





---

# Acknowledgments

---

Due to specific requirements related to experimental characterization of the radio propagation channel, the results presented in this thesis do not come solely as a contribution of the author. Instead, tremendous effort is hidden behind the short description of the measurement campaigns that provide the necessary data input for the “knowledge extraction process”. Although many people were involved in measurement experiments from TU Ilmenau side, the key logistic was provided by Gerd Sommerkorn, Christian Schneider and Markus Landmann. Due to excessive costs and complex setups, the measurements were performed jointly with other institutions, and author would like to recognize the contributions of the University of Ulm, TU Karlsruhe, Fraunhofer Heinrich Hertz Institute, Berlin and Medav GmbH. The measurements in Ilmenau city center were partially supported by the research excellence cluster UMIC at RWTH Aachen, while the measurements in Dresden were performed in the framework of EASY-C project. The author would like to thank Volker Jungnickel (FhG-HHI, Berlin) and Carsten Jandura (Vodafone AG, i.e. Actix GmbH) for technical support in these measurements.

The reconstruction of the spatial propagation dimensions from sounding data was carefully guided by Markus Landmann and Martin Käske. Estimations were performed on TU Ilmenau computational cluster with well established RIMAX algorithm, developed at Electronic Measurement Research Lab.

The WINNER channel model was developed in the framework of the IST projects WINNER I (IST-2003-507581) and WINNER II (IST-4-027756), which are partly funded by the European Union. Further progress was continued within CELTIC WINNER+ project. During the second phase of the project TU Ilmenau had a fruitful cooperation with Elektrobit, University of Oulu and Nokia Research Center, all from Finland, and Communications Research Centre, Canada. This resulted in numerous joint publications, which are partially presented in this thesis. I would especially like to acknowledge the contributions of Aihua Hong, Christian Schneider, Martin Käske, Markus Landmann, Pekka Kyösti, Lassi Hentilä, Tommi Jamsä, Juha Meinilä and Annika Böttcher. The WINNER related MATLAB implementations were, from TU Ilmenau side, done jointly with Martin Käske, and “Verification of WINNER II Channel Model” was delegated to Carolin Fratzscher in the form of the student project.

My further research on this topic was supported by Deutsche Forschungsgemeinschaft (DFG) within ‘TakeOFDM’ framework, and therefore some material

have already been presented in the channel modeling chapter of the project report “TakeOFDM – Techniques, Algorithms, and Concepts for Future OFDM Systems” which is edited by Hermann Rohling.

As shown in the thesis, the presented modeling activities constantly interact with COST research community, therefore in the thesis I used the work originally contributed to COST2100 “temporary documents” and the final report “Pervasive Mobile and Ambient Wireless Communications”, edited by Roberto Verdone and Alberto Zanella. This somehow completes the cycle, since I originally started my research on this topic, and joined the research group at TU Ilmenau owing to COST framework.

I would also like to thank all reviewers for helping me to improve the content and the language of the thesis, especially to Wim Kotterman. At the end, I would like to thank Reiner Thomä for his endless patience during the preparation of the presented material.

---

# Abstract

---

Without smart usage of spatial propagation dimensions, the achievable spectral efficiency of a radio link stays limited by the logarithm of signal-to-noise ratio. Only after careful management of the interference caused by a spatially distributed access to the propagation media, the ultimate efficiency increases with the number of transmit and receive antenna pairs. Additional gains on the system level could be met by cooperation of spatially distributed transceivers. Therefore, the development and performance evaluation of multi-antenna systems call for models capable of reproducing the spatial channel features properly. In order to support system level simulations, the targeted model should offer low complexity as well. A construction of both realistic and simple spatial propagation model requires a deep insight into physical propagation phenomena and their simplified reproduction.

This thesis concentrates on the class of geometry-based stochastic channel models that offer a good trade-off between complexity and realism. The assumed double-directional model deals with physical ray propagation, which enables proper reproduction of the targeted spatial features. Furthermore, the flexible structure of the geometry-based stochastic channel model enables generic representation of different propagation scenarios, making the model suitable for simulation of heterogeneous networks.

The realism of the developed model can be provided by the immediate use of the experimental data that is collected during measurement experiments. The usage of a dedicated sounding equipment and calibrated measurement antennas enables the reconstruction of spatial properties of physical multipath components. However, due to inherent limitations of the measurement system and the high-resolution estimation procedure, it is not possible to reliably resolve parameters of all propagation paths. Thus, the resulting representation of the propagation channel does not account for the total transmitted energy, and the radio channel model has to be complemented with an antenna dependent (filtering-based) part.

Since the parameterization of the double-directional model does not require information on the positions of the scattering objects relative to the transmitting and receiving antennas, it is possible to design a model that does not explicitly position the scatterers during the synthesis. Development of such a model, which uses purely parametric domains to represent physical propagation started with the 3GPP Spatial Channel Model, and it advanced during the WINNER project. Since a realization of the channel cannot be related to “random” positioning of scatterers,

other driving parameters that govern the large-scale model evolution were introduced. These particular models use the control parameters such as “delay spread”, “angular spread”, “shadowing”, etc. to quantify the power distribution over different channel dimensions. Their statistical properties (statistical distributions and correlation functions) are characterized on the propagation scenario level, and represent the most important part of the model.

In order to cope with an increased number of dimensions in parametric space, the large scale parameters are characterized independently using marginal distributions and auto-correlations over distance. However, independent analysis of channel dimensions introduces dependence of estimated parameters from the particular processing sequence and available dynamic range. This prevents the comparison of parameters extracted under different processing setups. Therefore, the proposed parameterization of the WINNER model uses a well established computation sequence and processing methods to reduce uncertainty.

The representation of measurement in WINNER parametric space and its further abstraction as a multi-variate normal process enables the straightforward quantification of the similarity by relative entropy measure. This similarity metric can be exploited to minimize the required number of distinct reference scenario classes, which reduces the overall model complexity.

The simplified parameterization of the 3GPP Spatial Channel Model results in weak consistency of the spatio-temporal channel evolution. This comes as a direct consequence of the abstracted propagation environment, i.e., the lack of predefined scatterer setup. In the WINNER model, the intra-cell correlations are exploited to enforce similarity in the close positions of a mobile terminal. The intra-cell correlations are still not properly represented and reproduced by this model, which defines the necessary future work. The thesis proposes a model extension in which the interaction of large-scale parameters, describing the cooperative (down)links, is established through a limited dynamic range of the receiver.

The WINNER model is implemented in MATLAB/C and verified with respect to the reproduced stochastic properties. The validation of the underlying scenario concept is performed by measurements in different cities corresponding to the same class of macro-cell urban environments. This model is taken as the reference for evaluation of the IMT-Advanced radio interface technologies by the ITU-R recommendation M.2135.

---

# Zusammenfassung

---

Ohne die intelligente Ausnutzung der räumlichen Ausbreitungsdimensionen ist die erreichbare spektrale Effizienz einer Funkverbindung durch den Logarithmus des Signal-zu-Rausch-Verhältnis begrenzt. Nur durch ein kluges Management der Interferenzen, welche durch den räumlich verteilten Zugriff auf die Ausbreitungsmedien verursacht werden, steigt die Effizienz mit der Anzahl der Sende- und Empfangsantennenpaare. Zusätzliche Gewinne können auf System-Level-Ebene durch die Kooperation von räumlich verteilten Transceivern erreicht werden. Deshalb sind für die Entwicklung und Leistungsbewertung von Mehrantennensystemen Modelle notwendig, mit denen die Wiedergabe der räumlichen Kanaleigenschaften geeignet gelingt. Um die Anforderungen an eine System-Level-Simulation gerecht zu werden, sollten diese Modelle eine geringe Komplexität bieten. Die Entwicklung realistischer und einfacher räumlicher Ausbreitungsmodelle erfordert einen tiefen Einblick in physikalische Ausbreitungsphänomene und ihre vereinfachte Wiedergabe.

Diese Arbeit konzentriert sich auf die Klasse der stochastischen geometrie-basierten Kanalmodelle, die einen guten Kompromiss zwischen Komplexität und Realismus bieten. Das zweiseitig richtungsaufgelöste Modell befasst sich mit der physikalischen Wellenausbreitung, diese ermöglicht eine richtige Wiedergabe der gewünschten räumlichen Funktionen. Die flexible Struktur des geometrie-basierten stochastischen Kanalmodells ermöglicht eine generische Darstellung der unterschiedlichen Ausbreitungsszenarien, so dass dieses Modell für die Simulation von heterogenen Netzwerken geeignet ist.

Der Realismus des entwickelten Modells kann durch die Verwendung von Kanal-datensätzen aus sogenannte Channel Sounding Experimente erreicht werden. Der Einsatz von dedizierten Messgeräten und kalibrierten Messantennen ermöglicht die Rekonstruktion der räumlichen Eigenschaften der physischen Mehrwegekomponenten. Jedoch aufgrund der inhärenten Beschränkungen des Messsystems und der hochauflösenden Schätzverfahren ist es nicht möglich, die Parameter aller Ausbreitungspfade zuverlässig aufzulösen. Somit ist die resultierende Darstellung des Ausbreitungskanals nicht vollständig bzgl. der gesamten Sendeleistung und muss um einen antennenabhängigen Teil (filterbasierend und nicht richtungsabhängig) ergänzt werden.

Da die Parametrisierung des zweiseitig richtungsaufgelösten Modells keine Information über die Positionen der Streuobjekte relativ zu dem Sende- und Empfangsantennen erfordert, ist es möglich, ein Modell zu entwerfen, welches nicht

explizit die Position der Streuer während der Synthese bestimmt. Die Entwicklung eines solchen Modells, welches für die Beschreibung der physikalischen Wellenausbreitung nur die parametrische Dimensionen verwendet, begann mit dem 3GPP Spatial Channel Modell und es während der verschiedenen WINNER Projekte weiterentwickelt. Da eine Realisierung des Funkkanals nicht allein auf einer “zufälligen” Positionierung der Streuer beruhen kann, wurden weitere Kontrollparameter, die Large Scale Parameter, eingeführt. Die betrachteten Modelle nutzen diese Parameter wie “Delay Spread”, “Winkelstreuung”, “Shadowing”, etc. um die Leistungsverteilung in den verschiedenen Kanaldimensionen zu quantifizieren. Deren statistischen Eigenschaften (statistische Verteilungen und Korrelationsfunktionen) werden auf der Ebene der Ausbreitungsszenarien charakterisiert und stellen damit den wichtigsten Teil des Modells dar.

Um mit der erhöhten Anzahl von der parametrischen Dimensionen zurechtzukommen, werden die Large Scale Parameter unabhängig voneinander mittels Randverteilungen und abstandsabhängigen Autokorrelationsfunktionen beschrieben. Allerdings verursacht eine unabhängige Analyse der verschiedenen Kanaldimensionen eine Abhängigkeit der geschätzten Parameter von den Verarbeitungsmethoden und des verfügbaren Dynamikbereichs. Dies führt dazu, dass ein Vergleich der Parameter unter verschiedenen Analysesetups schwierig wird. Daher berücksichtigt die vorgeschlagene Parametrierung der WINNER-Modelle etablierte Berechnungsvorschriften und Analysemethoden um Unsicherheiten zu verringern.

Die Repräsentation der Messdaten/Kanaleigenschaften in WINNER spezifischen parametrischen Dimensionen und deren weitere Abstraktion als multivariaten normalverteilten Prozess ermöglicht eine einfache Quantifizierung der Szenarioähnlichkeit basierend auf einer relativen Entropiemetrik. Dieses Ähnlichkeitsmaß kann dann genutzt werden, um die erforderliche Anzahl von unterschiedlichen Klassen an Referenzszenario zu minimieren, welches die Komplexität des Gesamtmodells reduziert.

Die vereinfachte Parametrierung des 3GPP Spatial Channel Modell führt zu einer schwachen Konsistenz der räumlich-zeitlichen Kanalevolution. Die Ursache liegt in der abstrahierten Ausbreitungs Umgebung, also dem Fehlen von vordefinierten Streuobjekten. Im WINNER-Modell werden die Intra-Zell-Korrelationen ausgenutzt um Ähnlichkeiten von benachbarten Positionen mobiler Endgerät zu erzwingen. Die Intra-Zell-Korrelationen sind aber immer noch nicht angemessen vertreten und reproduziert durch dieses Modell. Hier sind weitere zukünftige Arbeiten notwendig. Diese Doktorarbeit schlägt eine Modellerweiterung für kooperative (Down)Links vor, hierbei wird die Interaktion der Large Scale Parameter durch eine Begrenzung des Dynamikbereichs der Empfänger eingeführt.

Das WINNER-Modell ist in MATLAB/C implementiert und bezüglich der wiederzugebenden stochastischen Eigenschaften verifiziert. Die Validierung des zugrunde gelegten Szenariokonzeptes wurde anhand von Messungen in verschiedenen Städten der gleiche Klasse (macro-cell urban) durchgeführt. Dieses Modell wird als Referenz für die Evaluierung der IMT-Advanced Radio Interface-Technologien der ITU-R Empfehlung M.2135 genommen.

---

# Contents

---

<b>Contents</b>	<b>xi</b>
<b>List of Figures</b>	<b>xv</b>
<b>List of Tables</b>	<b>xix</b>
<b>List of Acronyms</b>	<b>xxi</b>
<b>List of Symbols</b>	<b>xxvii</b>
<b>1 Introduction</b>	<b>1</b>
1.1 Overview and Contributions . . . . .	2
1.2 Notation and Terminology . . . . .	5
<b>2 Radio Communications</b>	<b>7</b>
2.1 Communication Process . . . . .	7
2.1.1 Signal Transmission through the 1-D LTI Channel . . . . .	8
2.1.2 Degradation Sources . . . . .	9
2.2 Spatial Dimension of Communication . . . . .	9
2.2.1 Antenna Radiation Pattern . . . . .	10
2.2.2 Reference Coordinate Systems . . . . .	11
2.2.3 Relations between Spatial and Temporal Channel Dimensions for Moving Terminal . . . . .	13
2.2.4 Channel Decomposition . . . . .	13
2.3 Physical Propagation Channel . . . . .	15
2.3.1 Propagation of Electromagnetic Waves . . . . .	15
2.3.2 Multipath Components . . . . .	19
2.4 Space-Time Radio Channel . . . . .	19
2.4.1 LSTV Nature of Radio Channel . . . . .	19
2.4.2 Channel Impulse Response (CIR) . . . . .	21
2.4.3 Spatio-Temporal Channel Representation by System Functions	24
2.4.4 MIMO Radio Channel . . . . .	28
2.5 Selectivity of Radio Channel . . . . .	29

2.5.1	Auto-Correlation Functions and Power Spectral Densities of Jointly WSS Process . . . . .	30
2.5.2	Relations between ACF Extent and Power Spreading within PSD . . . . .	31
2.5.3	Decomposition of ACF/PSD . . . . .	32
2.5.4	Channel Classification . . . . .	37
2.5.5	Fading of Total Received Power in Narrowband Channel . . . . .	38
<b>3</b>	<b>General Modeling Aspects</b>	<b>41</b>
3.1	Relations between Model Concept and Representation Domain: Constituting (Resolved) vs. Faded . . . . .	41
3.2	Filtering Approach . . . . .	43
3.2.1	Correlation Tensor-Based Model for Selective Multidimensional Channels . . . . .	43
3.2.2	Decomposition of Correlation Matrices . . . . .	44
3.3	Finite Sum-of-Rays Representation of CIR . . . . .	45
3.3.1	Representation of Band-Limited Channels . . . . .	46
3.3.2	Synthetic Fading Models . . . . .	48
3.4	Mixed Modeling Approach . . . . .	49
3.4.1	Classification of Multipath Components . . . . .	50
3.4.2	Rice Fading Model . . . . .	51
3.5	Geometry-based Stochastic Channel Modeling . . . . .	51
3.5.1	Concept of Local-area Approximation . . . . .	52
3.5.2	Classification of Radio Environments . . . . .	53
3.5.3	Clustering of MPCs . . . . .	54
3.6	Stochastic Driving of Multipath Model . . . . .	54
3.6.1	Usage of the Large-Scale Parameters for Channel Characterization . . . . .	55
3.7	WINNER Channel Model . . . . .	56
3.7.1	Structure of the WINNER Channel Model . . . . .	57
<b>4</b>	<b>Parameterization of WINNER Model</b>	<b>65</b>
4.1	Alternative Representations of Measurement Data . . . . .	65
4.1.1	Development and Parameterization of a Channel Model . . . . .	66
4.2	Reconstruction of Spatial Propagation Dimension . . . . .	67
4.2.1	High-Resolution Parameter Estimation with RIMAX Algorithm . . . . .	68
4.3	Estimation of the WIM Parameters . . . . .	72
4.3.1	Segmentation of Measurement Data . . . . .	75
4.3.2	WIM Analysis Items and Methods . . . . .	77
4.4	Influence of Extraction Procedures on WIM Large-Scale Parameters . . . . .	85
4.4.1	Ambiguity of Delay-domain Features . . . . .	86
4.4.2	Equivalence of Estimates Obtained by Different Procedures . . . . .	90
<b>5</b>	<b>Representation of Multiple Scenarios by a Generic Model</b>	<b>93</b>
5.1	WINNER Reference Propagation Scenarios . . . . .	94
5.2	WIM TLSPs Viewed as Correlated Multivariate Random Process . . . . .	97
5.2.1	Parameters of WINNER Channel Model Describing MVN Distributions . . . . .	98



5.2.2	Problem of Negative Definite Covariance Matrices . . . . .	102
5.2.3	Distances in WIM Scenarios . . . . .	103
5.3	Quantification of Distances Between WINNER Scenarios . . . . .	103
5.3.1	Mean KL Scenario Divergence . . . . .	105
5.3.2	Classification of Measurements . . . . .	108
5.4	Generation of WINNER Channel Coefficients . . . . .	110
5.4.1	General Parameters: . . . . .	111
5.4.2	Large-scale Parameters: . . . . .	111
5.4.3	Small-scale (Cluster and Ray) Parameters: . . . . .	111
5.4.4	Coefficient Generation: . . . . .	114
<b>6</b>	<b>System-level, Wideband, MIMO Radio Channel Models</b>	<b>119</b>
6.1	Model Optimization . . . . .	120
6.1.1	Simplification (Approximation) of the WINNER Model . . . . .	121
6.1.2	Estimation of Computational Complexity . . . . .	124
6.2	Usage of 3-D Antenna Arrays in Simulations . . . . .	129
6.2.1	Representations of 3D Antenna Arrays in WIM . . . . .	130
6.2.2	Representation of Radiation Pattern . . . . .	131
6.3	Space-Time Model Evolution . . . . .	134
6.3.1	Stationarity Assumptions . . . . .	135
6.3.2	Drop-based Simulations . . . . .	136
6.3.3	ST Evolution of WINNER Model . . . . .	138
6.4	Interlink Dependencies . . . . .	143
6.4.1	Channel Similarity Measures . . . . .	143
6.4.2	Impact of Common Scatterers on Interlink Correlation . . . . .	144
6.4.3	Correlations of LSPs Describing Different Links . . . . .	145
6.5	Comparison of WIM with Other State-of-Art System-level Models . . . . .	150
6.5.1	Common Modeling Concepts . . . . .	151
6.5.2	(Extended) Spatial Channel Model . . . . .	152
6.5.3	COST Models . . . . .	158
<b>7</b>	<b>Concluding Remarks</b>	<b>163</b>
<b>A</b>	<b>Experimental Characterization</b>	<b>169</b>
A.1	Multidimensional Channel Sounding . . . . .	169
A.1.1	RUSK Channel Sounder . . . . .	170
A.1.2	Measurement Antenna Arrays . . . . .	172
A.1.3	Measurement Dataset . . . . .	173
A.2	Representation of Measurements in WINNER Parametric Space . . . . .	177
A.2.1	Indoor Hotspot Measurements - WINNER B3 Scenario . . . . .	177
A.2.2	Moving network measurements – WINNER D2 Scenario . . . . .	187
A.2.3	Urban Macro-cell Measurements – WINNER C2 Scenario . . . . .	193
<b>B</b>	<b>Implementation and Verification of WINNER Channel Model</b>	<b>205</b>
B.1	MATLAB Implementation of WINNER Channel Model . . . . .	205
B.1.1	Model Input Parameters . . . . .	206
B.1.2	Construction of Antenna Array Model in Pre-processing Phase . . . . .	208
B.1.3	Description of Network Layout . . . . .	209

- B.1.4 Channel Matrix Generation . . . . . 209
- B.1.5 Comparison of Phase I and Phase II Implementations . . . . . 212
- B.2 Reproduction of Targeted Statistics . . . . . 212
  - B.2.1 Verification Strategy . . . . . 213
  - B.2.2 Statistics of Generated Large-Scale Parameters . . . . . 214
  - B.2.3 Distributions of Generated Low-Level Parameters . . . . . 216
  - B.2.4 Reconstructing LSP Distributions from Model Output . . . . . 222
- C Random Variables and Stochastic Processes . . . . . 227**
  - C.1 Statistical Moments . . . . . 227
    - C.1.1 Correlation and Covariance Functions . . . . . 227
  - C.2 Wide Sense Stationarity . . . . . 228
  - C.3 Ergodicity . . . . . 228
  - C.4 Probability Density Functions – Overview . . . . . 231
    - C.4.1 The Circularly Wrapped Gaussian Distribution . . . . . 231
- Bibliography . . . . . 233**

---

# List of Figures

---

2.1	Communicating terminals. . . . .	10
2.2	Coordinate system definitions: GCS, ACS and ECS. . . . .	11
2.3	Effects of 3-D antenna rotation. . . . .	13
2.4	Decomposition of communication channel. . . . .	14
2.5	Multipath effects handled by ray-tracer: reflection, diffraction and scattering. . . . .	18
2.6	Multipath propagation. . . . .	20
2.7	Structural parameters. . . . .	22
2.8	Relations between aperture and wavevector. . . . .	26
2.9	Transformation cube. . . . .	27
2.10	Faded vs. resolved domains . . . . .	30
2.11	Relations between ACF and PSD functions. . . . .	33
2.12	Power Delay Profile . . . . .	34
2.13	Classification of fading channels . . . . .	37
2.14	Power budget and error performance of fading channel. . . . .	40
3.1	The modeling strategies: sum-of-rays versus filtering. . . . .	42
3.2	Bandlimited representation of propagation channel. . . . .	47
3.3	Generation of empirical, scenario-based multipath channel model. . . . .	56
3.4	The single realization of the modeled MIMO channel. . . . .	57
3.5	Probability distributions of arriving angles, obtained from RIMAX high resolution data analysis. . . . .	59
3.6	LSP are characterized and synthesized in transformed domain. . . . .	60
3.7	Delay spread PDFs in transformed domain. . . . .	61
3.8	Distribution of excess delays, obtained from RIMAX high resolution data analysis. . . . .	62
3.9	An introduction of the delay dispersion to the two strongest WIM2 clusters. . . . .	63
4.1	Domains used for characterization of wideband SISO radio channel. . . . .	67
4.2	Different domains used for parameterization of WINNER model. . . . .	74
4.3	Structure of the CIR tensor that is obtained from the measurements. . . . .	74
4.4	Usage of ST blocks for processing of the measurement data. . . . .	75

4.5	Grouping of analysis items. . . . .	77
4.6	Item computation sequence. . . . .	78
4.7	Examples of WIM analysis items. . . . .	81
4.8	Distribution of WIM LSPs. . . . .	83
4.9	Impact of the PDP averaging over consecutive snapshots before calculating DS. . . . .	87
4.10	Influence of PDP noise thresholding onto DS values. . . . .	88
4.11	Influence of PDP noise thresholding onto DS statistics. . . . .	88
4.12	Dependence of calculated DS in [ns] from dynamic range and Tx-Rx distance. . . . .	89
4.13	Impact of data filtering and noise estimation to resulting DS CDF. . . . .	89
4.14	Impact of the measurement setup/equipment. . . . .	91
4.15	Comparison of DS statistics obtained by different extraction procedures. . . . .	91
5.1	Genesis and representation of WINNER reference propagation scenarios. . . . .	97
5.2	Comparison of joint (DS,SF) PDFs for B3 and C2 WINNER scenarios, for LoS and NLoS propagation. . . . .	104
5.3	Comparison of joint WINNER C2 2-D PDFs with the LSP realizations from Ilmenau (black pluses) and Dresden (white dots), for NLoS propagation. . . . .	109
5.4	WINNER model of single radio link. . . . .	110
5.5	Generation procedure of WINNER channel coefficients. . . . .	110
6.1	Process of model optimization: relations between validation, simplification and refinement. . . . .	120
6.2	In WIM system-level approach, the spatial simulation area is divided into channel segments (drops). . . . .	121
6.3	Simplification/approximation of the WINNER model. . . . .	122
6.4	Preprocessing complexity comparison of geom. and corr. approach for different number of Tx/Rx antennas. . . . .	130
6.5	EADF compression capabilities. . . . .	132
6.6	Number of simulated drops that compensates complexity of 3-D antenna radiation pattern rotation, parameterized with number of MPCs. . . . .	134
6.7	Variations of BER and ergodic capacity between different drops. . . . .	138
6.8	Model evolution: smooth transition between channel segments along mobile route is attained by power ramp-up and ramp-down of clusters. . . . .	140
6.9	Correlation of radio links with common station. . . . .	141
6.10	Distance dependent correlation coefficients used in WINNER channel model. . . . .	142
6.11	System layout defined by positions of communication terminals. . . . .	145
6.12	a) Perceived power spreading, b) DS PDF as a function of effective dynamic range. . . . .	147
6.13	a) PDF of relative shadowing, b) dependence of power spread log-normal PDF parameters from effective dynamic range. . . . .	149
6.14	Relation between 3GPP SCM, WINNER and COST modeling activities. . . . .	151
6.15	Comparison of correlation function between SCM, SCME, and WIM. . . . .	157
6.16	MIMO antenna configuration for capacity calculation. . . . .	157

6.17	Comparison of outage capacity between SCM, SCME, and WINNER. . . . .	158
6.18	COST 273 model scenarios. . . . .	161
A.1	MIMO sounder switching time frame. . . . .	171
A.2	Block diagram of the RUSK channel sounder from Medav. . . . .	172
A.3	Sounding signals and estimated CIR. . . . .	175
A.4	Interior of Humboldt building, TU Ilmenau campus. . . . .	178
A.5	Interior of the hall for rapid prototyping and testing, Newton building, TU Ilmenau campus. . . . .	178
A.6	Measurements routes in Newton building. . . . .	179
A.7	Transmission loss under LoS propagation condition. . . . .	180
A.8	Shadow Fading distribution under LoS propagation condition for B3 scenario. . . . .	180
A.9	CDF of Ricean K factor for B3 LoS scenario. . . . .	181
A.10	Scenario B3 LoS: Ricean K factor as a function of distance. . . . .	182
A.11	Cross-Polarization Ratio (XPR) for B3 LoS scenario. . . . .	182
A.12	B3 LoS – RMS delay spread. . . . .	183
A.13	RMS azimuth spreads for the B3 scenario under LoS propagation con- dition. . . . .	184
A.14	RMS AoA elevation spreads (@MS) for the B3 LoS (industrial) scenario. . . . .	185
A.15	Distance dependence of the LSP autocorrelation function in B3 LoS scenario. . . . .	186
A.16	Moving network (D2) reference scenario. . . . .	187
A.17	Car-to-bridge measurements. . . . .	188
A.18	Sketch of the fast train measurements. . . . .	189
A.19	Fast train measurement @ 5.2 GHz: (a) transmission loss, and (b) shadow fading. . . . .	190
A.20	Car-to-bridge measurement: (a) transmission loss, and (b) shadow fading. . . . .	190
A.21	CDF of Ricean K-factor for car-to-bridge measurement. . . . .	191
A.22	Probability functions of RMS delay spread for D2a LoS scenario. . . . .	191
A.23	RMS angular spreads at BS for the car-2-bridge measurement, under LoS propagation condition. . . . .	192
A.24	Ilmenau macro-cell measurement setup. . . . .	195
A.25	Sketch of the Dresden scenario: a) Mobile tracks and base station posi- tions, b) Placement of antennas in measurement environment. . . . .	196
A.26	Spatial (2-D) positions of calculated LSPs in the Dresden scenario. . . . .	197
A.27	Transmission loss for LoS and NLoS classes of Dresden measurement. . . . .	198
A.28	Histograms and normal fit of $V \rightarrow H$ cross-polarization ratios (XPRs). . . . .	200
A.29	Fitting of empirical DS and ASA CDFs. . . . .	200
A.30	Empirical CDFs for angular spreads in Ilmenau measurement. . . . .	201
A.31	Distance dependence of correlation coefficients. . . . .	203
B.1	Development time-line of WINNER model. . . . .	206
B.2	High-level description of the WIM computation. . . . .	207
B.3	Construction of antenna array. . . . .	209
B.4	Examples of the network layout visualization. . . . .	210
B.5	Simplified structure of the WIM. . . . .	212

B.6	Validation and verification procedures. . . . .	213
B.7	Flow chart of the functions for verification and their targeting points in WIM. . . . .	215
B.8	Verification of LSP marginal distributions for A1 LoS scenario. . . . .	217
B.9	Comparison of the implemented and the recalculated cross-correlation coefficients. . . . .	217
B.10	Graphical representation of the LSP values selected for LLP verification. . . . .	218
B.11	A1 LoS delay distribution: a) without LoS peak, and b) with LoS peak. . . . .	220
B.12	Power related distributions in A1 LoS scenario. . . . .	220
B.13	PDFs related to generation of departure angles. . . . .	221
B.14	The effect of the wrapping of normally distributed angles to interval $[-180^\circ, 180^\circ)$ . . . . .	222
B.15	Distribution of regenerated azimuth spreads at arrival (ASA) from model output. . . . .	223
B.16	Regenerated delay spread values from LLP. . . . .	223
B.17	LSP distributions regenerated from LLPs with Phase II implementation. . . . .	224
B.18	Angular spreads regenerated with Phase II implementation, without angle wrapping. . . . .	225
B.19	Regenerated angle spreads with WIM Phase I implementation. . . . .	225
C.1	Wrapping of the Gaussian distribution as implemented in WIM. . . . .	231
C.2	Von-Mises distributions for $\mu = 0$ and varying $\kappa$ . . . . .	232

---

# List of Tables

---

2.1	Maxwell's equations. . . . .	15
2.2	Relations between representation domains are established via Fourier transform. . . . .	24
3.1	Large-scale parameters of WINNER model. . . . .	59
5.1	WINNER Reference Propagation Scenarios. . . . .	95
5.2	WIM LSP marginal PDF parameters. . . . .	99
5.3	WIM LSP correlation coefficients. . . . .	100
5.4	Approximation of empirical corr. matrix $\rho$ with positive definite matrix $\hat{\rho}$ is performed by APM. . . . .	101
5.5	Mean KL Divergence between WINNER scenarios and Ilmenau and Dresden measurements. . . . .	106
5.6	Closest (scenario, propagation) pairs according to mean KL divergence. . . . .	107
5.7	Average distance between WINNER scenario groups: A, B, C, D. . . . .	107
5.8	Average distance between WINNER LoS and NLoS propagation conditions. . . . .	108
5.9	Scaling factor applied in inverse Gaussian mapping is related to total number of clusters. . . . .	112
5.10	Ray offset angles within a cluster, given for 1° RMS angle spread. . . . .	113
5.11	Sub-cluster information for intra cluster delay spread clusters. . . . .	115
5.12	Parameters of WIM generic model. . . . .	117
6.1	Equivalent computational complexity of mathematical functions and operations. . . . .	124
6.2	Complexity of WINNER coefficient generation for ULA geometries under NLoS. . . . .	125
6.3	Computational complexity of geometry-based and correlation-based methods. . . . .	128
6.4	Complexity comparison for different usage of array in simulations. . . . .	133
6.5	Dependence of power spread distributions from effective dynamic range. . . . .	149
6.6	Feature comparison of SCM, SCME, WIM1 and WIM2. . . . .	155
6.7	Numerical comparison of SCM, SCME, WIM1 and WIM2. . . . .	156

A.1	Key features of the Medav RUSK TUI-FAU channel sounder. . . . .	173
A.2	Overview of TU-Ilmenau measurement antenna arrays. . . . .	174
A.3	K-factor [dB] in B3 scenario for VV polarization. . . . .	181
A.4	CDF levels of the cross-polarization ratio for B3 LoS propagation. . . . .	181
A.5	RMS delay spread [ns] for B3 LoS scenario and VV polarization. . . . .	183
A.6	RMS azimuth spread [deg] for the B3 scenario under LoS condition for VV polarization. . . . .	184
A.7	RMS AoA elevation spreads (@MS) for the B3 (industrial) scenario and VV polarization. . . . .	185
A.8	CDF levels of RMS delay spread under LoS propagation for D2a scenario. . . . .	192
A.9	Percentiles of the RMS azimuth spread for D2a scenario. . . . .	192
A.10	Channel sounder settings. . . . .	193
A.11	Antenna arrays. . . . .	194
A.12	Transmission loss parameters for urban macro-cell. . . . .	199
A.13	LSP decorrelation distances for urban macro-cell. . . . .	203
B.1	MATLAB output parameters. . . . .	211
C.1	The relevant probability density functions. . . . .	229



---

# List of Acronyms

---

<b>AA</b>	Antenna Array
<b>ACF</b>	Auto-Correlation Function
<b>ACS</b>	Array Coordinate System
<b>AGC</b>	Automatic Gain Control
<b>AoA</b>	Azimuth of Arrival
<b>AoD</b>	Azimuth of Departure
<b>AP</b>	Access Point
<b>APM</b>	Alternate Projections Method
<b>AS</b>	Angular Spread
<b>ASA</b>	Azimuth Spread on Arrival
<b>ASD</b>	Azimuth Spread on Departure
<b>BER</b>	Bit Error Rate
<b>BS</b>	Base Station
<b>B3G</b>	Beyond 3G
<b>CAS</b>	intra-cluster angular spread
<b>CC</b>	Cluster Centroid
<b>CDF</b>	Cumulative Distribution Function
<b>CDL</b>	Clustered Delay Line
<b>CDS</b>	intra-cluster delay spread
<b>CEM</b>	Computational Electromagnetics

<b>CIR</b>	Channel Impulse Response
<b>CM</b>	Correlation Matrix
<b>COST</b>	European Cooperation in Science and Technology
<b>CRLB</b>	Cramér-Rao lower bound
<b>CS</b>	Coordinate System
<b>CSI</b>	Channel State Information
<b>DL</b>	Down-Link
<b>DMC</b>	Dense Multipath Component
<b>DoA</b>	Direction of Arrival
<b>DoD</b>	Direction of Departure
<b>DR</b>	Dynamic Range
<b>DS</b>	Delay Spread
<b>EADF</b>	Effective Aperture Distribution Function
<b>ECS</b>	Element Coordinate System
<b>EM</b>	Electromagnetic
<b>EMW</b>	Electromagnetic Wave
<b>ESA</b>	Elevation Spread on Arrival
<b>ESD</b>	Elevation Spread on Departure
<b>ESPRIT</b>	Estimation Of Signal Parameters Via Rotational Invariance Techniques
<b>FCF</b>	Frequency Correlation Function
<b>FDD</b>	Frequency-Division Duplex
<b>FFT</b>	Fast Fourier Transform
<b>FT</b>	Fourier Transform
<b>GCS</b>	Global Coordinate System
<b>GPS</b>	Global Positioning System
<b>GSCM</b>	Geometry-based Stochastic Channel Model
<b>HOSVD</b>	Higher-Order Singular Value Decomposition
<b>HRPE</b>	high-resolution parameter estimation

<b>i.i.d.</b>	independent identically distributed
<b>IMT</b>	International Mobile Telecommunications
<b>IO</b>	Interacting Object
<b>IR</b>	Impulse Response
<b>ISI</b>	Inter-Symbol Interference
<b>ISIS</b>	Initialization and Search Improved SAGE
<b>ITU</b>	International Telecommunication Union
<b>KPI</b>	Key Performance Indicator
<b>LA</b>	Local Area
<b>LLP</b>	low-level parameter
<b>LoS</b>	line-of-sight
<b>LPF</b>	Low-Pass Filter
<b>LSP</b>	Large-Scale Parameter
<b>LSR</b>	Local Stationarity Region
<b>LTE</b>	3GPP-Long Term Evolution
<b>LSTV</b>	Linear Space-Time Variant
<b>LTI</b>	Linear Time Invariant
<b>LTV</b>	Linear Time Variant
<b>MA</b>	Metropolitan Area
<b>MATLAB</b>	Matrix Laboratory - Mathworks, Inc.
<b>MED</b>	Maximum Excess Delay
<b>MIMO</b>	Multiple-Input Multiple-Output
<b>ML</b>	Maximum Likelihood
<b>MPC</b>	Multi-Path Component
<b>MRS</b>	Moving Relay Station
<b>MS</b>	Mobile Station
<b>MT</b>	Mobile Terminal
<b>MVN</b>	Multi-Variate Normal
<b>NLoS</b>	Non Line-of-Sight

<b>OFDM</b>	Orthogonal Frequency Division Multiplexing
<b>OLoS</b>	Obstructed Line-of-Sight
<b>PAS</b>	Power Angular Spectrum
<b>PDF</b>	Probability Density Function
<b>PDP</b>	Power-Delay Profile
<b>PSD</b>	Power Spectral Density
<b>QoS</b>	Quality-of-service
<b>RIMAX</b>	iterative gradient-based ML parameter estimation algorithm
<b>RMS</b>	Root-Mean-Square
<b>RO</b>	Real Operation
<b>RP</b>	Radiation Pattern
<b>RPS</b>	Reference Propagation Scenario
<b>RV</b>	Random Variable
<b>Rx</b>	Receiver
<b>SAGE</b>	Space-Alternating Generalized Expectation-maximization
<b>SC</b>	Specular Component
<b>SCF</b>	Spatial Correlation Function
<b>SCM</b>	Spatial Channel Model
<b>SCME</b>	Spatial Channel Model Extended
<b>SF</b>	Shadow Fading
<b>SIMO</b>	Single-Input Multiple-Output
<b>SISO</b>	Single-Input Single-Output
<b>SLAC</b>	Stochastic Local-Area Channel
<b>SM</b>	Spatial Multiplexing
<b>SNR</b>	Signal-to-Noise-Ratio
<b>SoS</b>	Sum-of-Sinusoids
<b>SRR</b>	Signal-to-Remainder-Ratio
<b>SS</b>	Snapshot Set
<b>SSS</b>	Strict-Sense Stationary

<b>ST</b>	Space-Time
<b>std.</b>	standard deviation
<b>SVD</b>	Singular Value Decomposition
<b>TCF</b>	Time Correlation Function
<b>TDD</b>	Time Division Duplex
<b>TDL</b>	Tapped Delay Line
<b>TL</b>	Transmission Loss
<b>TLSP</b>	Transformed Large-Scale Parameter
<b>T<sub>x</sub></b>	Transmitter
<b>UCA</b>	Uniform Circular Array
<b>UE</b>	User Equipment
<b>UHF</b>	Ultra High Frequency
<b>UL</b>	Up-Link
<b>ULA</b>	Uniform Linear Arrays
<b>US</b>	Uncorrelated Scattering
<b>UWB</b>	Ultra-Wideband
<b>VSFT</b>	Vector Spherical Fourier Transform
<b>WA</b>	Wide Area
<b>WINNER</b>	Wireless World Initiative New Radio
<b>WIM</b>	WINNER Channel Model
<b>WIM1</b>	WINNER Channel Model Phase I
<b>WIM2</b>	WINNER Channel Model Phase II
<b>WGN</b>	White Gaussian Noise
<b>XPD</b>	Cross-Polar Discrimination
<b>WSS</b>	Wide-Sense Stationary
<b>WSSUS</b>	Wide-Sense Stationary Uncorrelated Scattering
<b>XPR</b>	Cross-Polarization Ratio
<b>XPD</b>	Cross-Polarization Discrimination
<b>ZDSC</b>	Zero Delay Spread Cluster

<b>1-D</b>	One-Dimensional
<b>2-D</b>	Two-Dimensional
<b>3-D</b>	Three-Dimensional
<b>3DAA</b>	3-D Antenna Array
<b>3G</b>	Third Generation
<b>3GPP</b>	3rd Generation Partnership Project
<b>4-D</b>	Four-Dimensional

---

# List of Symbols

---

Symbol	Description	Reference page
$\mathbf{S}$	Spatial characteristics	9
$\vec{r}$	Position	11
$\vec{\Theta}$	Orientation	11
$\vec{\Omega}$	Direction	10
$\varphi$	Azimuth angle	12
$\theta$	Co-elevation angle	12
$t$	Time	8
$f$	Frequency	8
$\vec{v}$	Velocity	13
$Q$	Space-time realization of radio-link	21
$\lambda$	Wavelength	52
$\vec{k}$	Wavevector	25
$\nu$	Doppler shift	19
$\tau$	Delay	21
$\alpha$	2x2 polarimetric gain matrix	22
$\mathbf{h}$	Channel impulse response	23
$\underline{H}$	Channel transfer function	20
$\mathcal{H}$	Channel tensor	43
$R$	Auto-Correlation	30
$\rho$	Correlation Coefficient	60
$S$	Power Spectral Density	31
$P$	Power	82
$L$	Transmission Loss	82
$\sigma$	Standard Deviation/RMS Spread	31
$B_c$	Coherence Bandwidth	34
$t_C$	Coherence Time	36
$d_C$	Coherence Distance	35
$\vec{E}$	Electric field	15
$\vec{D}$	Displacement field	15
$\vec{H}$	Magnetizing field	15
$\vec{B}$	Magnetic field	15
$\vec{J}$	Current density	15
$\rho$	Charge density	15

---

Symbol	Description	Reference page
$\underline{e}$	Electromotive force	19
$\varepsilon$	Permittivity	16
$\mu$	Permeability	16
$\nabla$	Hamiltonian	15
*	Convolution	20
$(\cdot)^T$	Transpose	12
$(\cdot)^H$	Hermitian (conjugate) transpose	44
$\odot$	Schur (element-by-element) product	45
$\otimes$	Kronecker product	44
$\circ$	Tensor outer product	44
$J_0(\cdot)$	zero-order Bessel function of the first kind	35



# Chapter 1

---

## Introduction

---

The properties of the propagation channel will strongly influence:

- development of the new transmission and processing algorithms,
- optimization of a mobile communication system.

Characterization of the radio-channel propagation has always been an important part of the radio-system design: “Accurate and efficient computer-based channel modeling is important to validate and/or compare different digital schemes under realistic channel conditions and to optimize digital modem design” [1]. By looking back in history it can be noted that development of a channel model was following system enhancement and different aspects of the very same radio channel were becoming relevant. Therefore, even in its motivation the radio channel modeling was not independent from system aspects. It is important to realize that the underlying system concept defines a set of features that should be properly reproduced by the model. This restricts the model complexity that is the main issue of the modeling task. To clarify, a radio-channel itself is not influenced by the deployed system, but rather by the level in which we try (or are able) to characterize it.

According to the above reasoning it happens that the development of the new systems requires reconsideration of existing channel models, and usually – development of the new ones. E.g., in the Orthogonal Frequency Division Multiplexing (OFDM) signaling concept, the wide-band radio-communication channel is effectively utilized as a collection of narrow-band channels. Basic system parameters like the number of subcarriers and symbol duration are selected to mitigate the key channel impairments: Inter-Symbol Interference (ISI) induced by frequency selectivity and loss of subcarrier orthogonality due to time selectivity [2]. Therefore, a proper channel model is required both for system design and for performance evaluation. Additionally, when the Channel State Information (CSI) is available during the system operation, transmission characteristics, such as the signal constellation or the allocated power, could be adaptively adjusted at the transmitter per subcarrier in order to maximize total throughput.

Further improvements of the spectral efficiency could be obtained by simultaneous transmission and/or reception from/by multiple antenna elements. In addition to time and frequency, this concept known as Multiple-Input Multiple-Output (MIMO) exploits the spatial propagation dimension or, more specifically, multiplicity of energy propagation paths. The MIMO systems combine existing spatial concepts such as: beamforming and (receive) diversity, with new transmission strategy called Spatial Multiplexing (SM). This significantly improves the system flexibility and throughput since the appropriate transmission mode can be selected according to the observed propagation channel. Furthermore, the spatial dimension can be combined with the time dimension (Space-Time coding), or used instead to achieve equivalent coding gains.

Since the achievable spectral efficiency is tightly related to the signal correlation across the antenna array [3], the proper representation of correlation levels becomes essential for the analysis of MIMO systems. In order to obtain an antenna-independent representation of the channel that implicitly comprises correlation properties, *geometry-based* models are generally used. With geometry-based approach different antennas in array will observe different correlation levels, depending on the directional distribution of transmit/receive energy.

The optimization of radio transmission can be focused on the single radio link or the entire system consisting of many, possibly interacting, links. In order to reach optimal complexity of the model, usually different modeling strategies are employed for channel representation in link-level and system-level contexts.

This thesis focuses on the development and optimization of geometry based models for system-level simulations. The targeted future systems will use the large transmission bandwidths (up to 100 MHz) and antenna arrays on both ends to exploit the spatial propagation dimension. The developed empirical model is limited to the transmission bandwidth of the used channel sounding equipment. Therefore, wideband spatial models analyzed in the framework of this thesis are not suitable for Ultra-Wideband (UWB) systems: due to extremely large bandwidth of the UWB system, the perception of the multipath propagation will change.

## 1.1 Overview and Contributions

The thesis is organized into 7 chapters and 3 appendices.

- The second chapter introduces the concept of a double-directional propagation channel, and the relevant dimensions for its characterization. Different methods providing the most realistic insight into physical propagation phenomena: Computational Electromagnetics (CEM) and diffraction theories applicable for ray-tracing are briefly discussed. The radio channel is introduced as a concatenation of a random propagation channel and a deterministic antenna, and the Bello's notation for the signal transmission through such a channel is presented. Consequently, the autocorrelations and power spreading are given as dual means for characterization of the radio-channel selectivity.
- General modeling aspects are discussed in the third chapter. The sum-of-ray approach and the filtering-based method are compared with respect to

the used representation domain and overall modeling strategy. Possibility to combine both methods within a hybrid model is reconsidered. The basic concepts behind geometry-based stochastic modeling are given. Two strategies for stochastic model driving are identified. They handle the interacting objects in different manners and result in models with different complexities. The **WINNER** channel model, being the state-of-the-art representative for wideband **MIMO** (simplified) system-level modeling, is presented.

- The fourth chapter is dedicated to parameterization of the **WINNER** channel model. Since the originally acquired **MIMO** channel samples have limited applicability in geometry-based channel modeling, alternative representation, with reconstructed spatial dimension, has to be acquired. The high-resolution **RIMAX** algorithm is employed for the estimation of the hybrid model parameters. Due to limited number of channel observations, only limited number of specular multi-path components can be reliably parameterized. Additional limitations in spatial reconstruction stem from limitations of the measurement system. The thesis discusses effects of the limited precision of the antenna array model on the estimated multipath profile and the resulting model's structure.

The transparent procedure for parameterization of the **WINNER** channel model that uses both structured parameters and channel tensors is defined. All features being independent from spatial reconstruction (delays, powers) are estimated from the channel tensor in the time-delay domain. The cluster-based analysis and estimation of angular parameters are accomplished from resolved MPC parameters. Evaluation of the impact of the parameterization procedure on the obtained model parameters is performed.

- The notion of scenario and its formulation in **WINNER** are discussed in the fifth chapter. It was demonstrated that objective classification of **WINNER** scenarios, based on quantified similarities of the **WINNER** parametric space, would result in different taxonomy. Using the proposed similarity metric, the **WINNER** C2 urban macro-cell parameters are validated with new measurements taken in different cities. Description of each scenario is condensed in channel model parameters. In this chapter the synthesis of the WIM space-time realizations from scenario parameters is presented.
- The aspects of the system-level modeling are discussed in the sixth chapter. Due to increased number of interdependent links, the optimization of the model complexity becomes crucial. The complexity of the **WINNER** model is approximated and compared with filtering-based approach that uses explicit correlation between antennas. While both models are evolved according to the targeted Large-Scale Parameter (**LSP**) distributions, the **WINNER** model keeps lower complexity. However, further approximation steps of **WINNER**, that reduce the model accuracy, could result in simpler models (e.g., cluster-delay line). The optimal description of the antenna arrays for the simulation purposes is also analyzed. The concepts like local-stationarity and virtual placement of clusters in parametric domains are introduced to reduce model

complexity. However, they affect the consistency of the model space-time evolution and interlink dependencies. It was, therefore, necessary to introduce correlations between LSPs and gradual cluster replacement to fix inconsistencies. The comparison of the WINNER model with 3GPP SCM and COST 273/2100 generic, wideband, MIMO system-level models is carried out.

- The concluding remarks are given in the seventh chapter.
- The process of experimental channel characterization is elaborated in the first appendix. The concept of channel sounding and necessary components of the measurement system are discussed. The WINNER LSPs estimated from different measurements and propagation environments are given in this chapter. Evaluation of environment stationarity between consecutive measurements performed by single (Tx,Rx) sounding pair is presented.
- The top overview of the MATLAB implementation of the Wireless World Initiative New Radio (WINNER) channel model is given in the second appendix. The model output and intermediate results are verified with respect to the targeted probability density functions.
- The third appendix contains the elements of the probability theory and stochastic processes being relevant for the thesis: statistical moments, wide sense stationarity, ergodicity etc.

The main contributions of this thesis are related to the development, parameterization, implementation, verification and validation of the WINNER channel model.

- The transparent parameterization procedure of the WINNER channel model is introduced in Sec. 4.3\* and implemented in MATLAB. The developed tools are exploited for postprocessing of measured channel tensors and estimated structural parameters, for many measurements and propagation environments. Some of the obtained large-scale WINNER parameters are presented in Sec. A.2.
- The influence of extraction procedures to the estimated WINNER parameters is analyzed in Sec. 4.4. The observed interdependencies between effective dynamic range and spread distributions are exploited to introduce a consistent model for cooperative downlink in Sec. 6.4.3.
- Starting from the abstraction of the WINNER model in the form of multivariate normal process (Sec. 5.2), similarity metric based on mean Kullback-Leibler divergence is proposed. This metric enables simple comparison of measurements in the WINNER parametric space. It is consequently exploited in Sec. 5.3 to evaluate the WINNER scenario definitions and validate existing parameters for WINNER C2 urban macro-cell scenario.

---

\*The thesis presents only estimation of large-scale parameters. The complete procedure is described in [4] and [5].

- The correlation coefficients describing the cross-correlations of large-scale WINNER Channel Model (WIM) parameters are fixed for numerous scenarios to form a positive definite correlation matrix. It is shown that a precision of two decimal digits is required to ensure positive definiteness.
- The consistency of the WINNER model is improved in Phase 2 by relating the cluster angles and delays over the associated powers, Sec. 5.4 and Sec. B.1.5. The smooth model evolution along the given route, among neighboring drops and during transitions between scenarios, is enabled by gradual cluster replacement, Sec. 6.3.3.
- In Sec. 6.5, the WINNER model is compared with other relevant system-level models: 3GPP SCM and COST 273/2100.
- The implementation of the WINNER model in Phase II is extended to support Three-Dimensional (3-D) antenna arrays, and to properly handle their rotation. Additionally, Effective Aperture Distribution Function (EADF) representation of the radiation pattern is supported for model validation with realistic representation of measurement antenna. The optimal representation of the antenna arrays for simulation purposes is given in Sec. 6.2.
- The procedure for verification of the WINNER model implementation is proposed in Sec. B.2. The presented results show that implemented model reproduces targeted statistic with some minor deviations.

The majority of the presented findings are already published in the form of white, conference or journal papers, project reports or book chapters. The omitted aspects, still being relevant for the presented work are appropriately referenced. Therefore, the thesis as a whole offers a systematic overview of the state-of-the-art system-level channel modeling. The relevance of the WINNER model is pronounced by the fact that ITU-R recommendation M.2135 takes it as a reference model for evaluation of IMT-Advanced radio interface technologies.

## 1.2 Notation and Terminology

This thesis always assumes a *radio channel context* in a discussion about propagation, modeling, and validation, unless specified differently. The assumed context enables usage of more concise descriptions.

Due to historical reasons, different notation is used to differentiate between communication terminals (formerly radio-stations): terms Base Station (BS), Access Point (AP), Mobile Station (MS), User Equipment (UE) are combining a role of terminal in a radio network and its mobility.

Vectors are labeled with arrow  $\vec{x}$ , and matrices are shown in bold letters  $\mathbf{X}$ . Throughout the thesis the baseband representation,  $\underline{x}$ , for signal  $x(t)$  is used, Sec. 2.1.1.

Parenthesis () are used to designate function argument, while the usage of curly brackets {} assumes application of an operator, e.g., probability, expectation, Fourier transform, etc. The parameter sets whose members are scalars, vectors and

matrices (equivalent to **MATLAB** cells) are represented by ordered  $n$ -tuples. They are designated by bold letters and their elements are listed in parentheses  $\mathbf{X} = (\dots)$ .

In order to avoid confusion of the transpose symbol  $(\cdot)^T$  with transmitter label, the latter is identified in subscripts and superscripts with  $Tx$ . Analogously, the receiver is labeled by  $Rx$ .

In cases where both acronyms and abbreviations could be used, the acronyms are chosen to improve readability. E.g., *probability density function* and *cumulative distribution function* are denoted as PDF/CDF rather than pdf/cdf.

### Abbreviations

e.g.,	exempli gratia (for example),
etc.	et cetera (and so forth),
i.e.,	id est (that is),
w.r.t.	with respect to,
vs.	versus.

## Chapter 2

---

# Radio Communications

---

Leakage of Electromagnetic (EM) energy into surrounding area (radiation) accompanies all electrical circuits where electrons are accelerated/decelerated or conductors have discontinuities [6]. By choosing appropriate structures, named *antennas*, the significant part of produced electrical energy can be transformed into free EM waves traveling through the space with speed of light. Starting from the end of 19<sup>th</sup> century this phenomena is employed to establish different forms of wireless communication. The physical environment between two antennas can serve as communication medium used for transmission of information between associated terminals. Since antenna efficiently radiates EM energy only on wavelengths that are comparable to its size, the emitted signal has to be modified by appropriate modulation process. In this process parameters of carrier wave (having appropriate wavelength) are modified according to digital or analog information signal that should be transmitted. As a result of modulation the complete frequency spectrum is placed to the frequency range where efficient radiation occurs.

The first section of the chapter introduce baseband notation for the transmission of a signal through the communication channel. Section 2 considers the decomposition of the channel according to the temporal and spatial dependencies. The tools for the characterization of the physical propagation channel are discussed in 3<sup>rd</sup> section. The section 4 describes the differences between radio and propagation channel. It also discusses antenna (de)embedding and equivalent representations of a channel in different Fourier domains. The selectivity of radio channel is analyzed in the last section, based on properties of auto-correlation functions and power spectral densities. The relative classification of channels w.r.t. used data transmission rate is given, and distinction between large-scale and small-scale fading effects is established.

### 2.1 Communication Process

The information is typically represented by appropriate set of symbols in the form of the message. In current communication systems message was represented in

the form of One-Dimensional (1-D) signals, showing variations over the time domain. In order to represent interaction of transmitted signal with channel certain mathematical notation is necessary.

### 2.1.1 Signal Transmission through the 1-D LTI Channel

Transmission of signals through the *Linear Time Invariant* (LTI) system can be described in time domain by the convolution of transmitted signal with *Channel Impulse Response* (CIR)-  $h(t)$ , or in frequency domain by multiplication of transmitted signal spectra with channel *transfer function*,  $H(f)$ .

#### Baseband (Analytic) Signal Representation

In this thesis baseband representation of linearly modulated (passband) signals will be used, which omits the dependence of a passband signal from its carrier frequency, and therefore simplifies notation. Any passband signal  $s(t)$  can be represented by its complex envelope  $\underline{s}(t)$ :

$$\underline{s}(t) = (s(t) \cdot e^{-j2\pi f_c t}) * h_{LPF}(t), \quad (2.1)$$

where  $f_c$  represents carrier frequency, and  $h_{LPF}(t)$  is the impulse response of an ideal *Low-Pass Filter* (LPF). Within the complex baseband representation all relevant information about modulated passband signal is contained. The complex envelope representation can be easily recognized, even without special notation, due to appearance of complex exponential terms.

The original passband signal can be reconstructed by transformation:

$$s(t) = \mathcal{R} \{ \underline{s}(t) \cdot e^{-j2\pi f_c t} \}, \quad (2.2)$$

where  $\mathcal{R} \{ \cdot \}$  denotes real part of a complex number. Physically realizable modulated (passband) signals are real-valued, what is reflected in mapping (2.2) since any complex baseband signal will produce real modulated signal.

#### Baseband CIR Representation

The same formalism can be applied to obtain baseband equivalent of the passband CIR,  $h(t)$ . However, the obtained complex representation has twice more power than its passband counterpart. Therefore normalization with factor  $\frac{1}{2}$  is necessary to avoid input-output power mismatch:

$$\underline{y}(t) = \underline{x}(t) * \frac{1}{2} \underline{h}(t). \quad (2.3)$$

The relevant transmitter and receiver stages as pulse shaping filter, matched filter, equalizer, channel estimator, etc. could be equivalently represented in baseband domain using the complex number notation.



### 2.1.2 Degradation Sources

**Noise** The primary source of performance degradation is thermal noise generated in the receiver. The thermal noise usually has a flat power spectral density over the signal band and a zero-mean Gaussian Probability Density Function (PDF).

**Interference** For radio links of cell-based mobile communication systems external interference received by the antenna is more significant than thermal noise. Such channels are referred to as interference-limited (in contrast to noise-limited), and their performance is expressed with signal-to-interference (+noise) ratio.

**Fading** Significant change of the received power over time, frequency or space. Channel exhibiting fading are referred as selective.

Classification of the channel with respect to exhibited fading will be further analyzed in Sec. 2.5.4.

## 2.2 Spatial Dimension of Communication

The spatial dimension exist in all types of communications (cable length, attenuation per [m], propagation delays, etc.) since the fundamental assumption of telecommunications was that information should be transmitted between spatially displaced terminals. Even if only temporal dimension of process is analyzed it is always conditioned by terminal deployment with respect to environment  $\mathbf{S}_{Tx/Rx}$ :

$$y(t|\mathbf{S}_{Rx}) = \int_{-\infty}^{\infty} h(\tau|\mathbf{S}_{Tx}, \mathbf{S}_{Rx})x(t - \tau |\mathbf{S}_{Tx})d\tau.$$

For stationary terminals we can relax notation and drop dependencies from Tx/Rx spatial characteristics. However the spatial dimension becomes more pronounced in radio-communications, due to specifics of communication medium and potentially moving terminals.

In classical communication systems 1-1 and 1-M (broadcasting) configuration were analyzed, i.e. generated context from single source was transmitted to the single or multiple sinks. In this context wireless communications are enabling “continuous” service for moving terminals. For the purpose of transmission of message over radio medium (ST-coding, beamforming, distributed antenna systems), spatial dimension in representation may be added, however this is not of interest for the targeted sink. Namely, currently used sinks does not require or use spatial notion of a message. This is not changed in spatially-aware services, where only selection of sources is related to spatial position of sink. The sink typically use message at non-distributed spatial position (after fully assembling it - meaning that time dimension is also removed). From the perspective of communication service provider a M-M configuration problem has to be solved, where (due to terminal mobility) sinks/sources have assigned spatial position. Furthermore, an antenna introduces additional spatial dependence due to directional filtering of emitted/received energy, which is described by its radiation pattern.

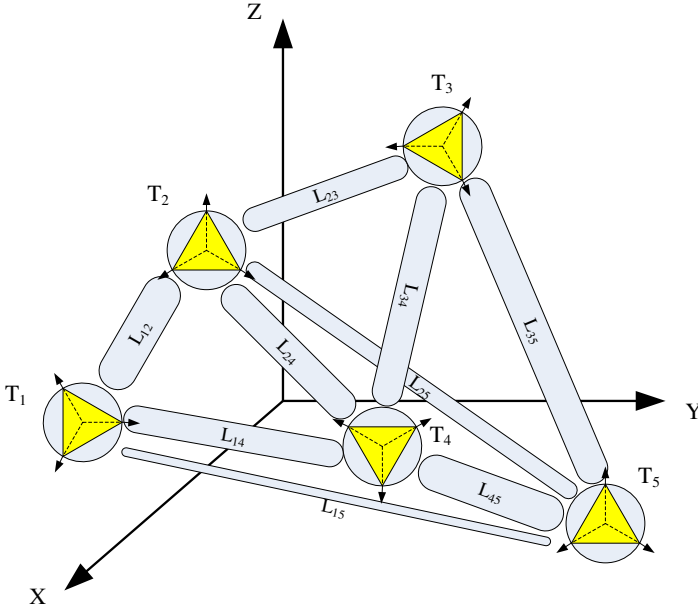


Figure 2.1: Communicating terminals.

### 2.2.1 Antenna Radiation Pattern

Communicating Tx and Rx antennas are, usually, sufficiently separated to avoid their coupling and to describe directional characteristics of terminals with their radiation patterns  $\vec{F}_i(\vec{\Omega})$ ,  $i \in \{Tx, Rx\}$ . These assumptions enable characterization of propagation radio-channel by many different techniques additionally to CEM (Sec. 2.3.1), since the directional distribution of electrical field in Fraunhofer region surrounding Tx antenna becomes deterministic property of antenna that is described by its *radiation pattern*.

The radiation pattern  $\vec{F}(\vec{\Omega})$  is function of direction  $\vec{\Omega} \equiv (\theta, \phi)$ , but does not depend on distance from transmitting antenna. Therefore, with the concept of radiation pattern antenna can be described as deterministic system block. The electrical field in Fraunhofer region will be also proportional to temporal variations of the transmitted signal  $\underline{s}(t)$ , or equivalently the spectral content of E-field would correspond to the short time Fourier transform of complex baseband signal,  $\underline{S}(f) = \mathcal{F}\{\underline{s}(t)\}$ :

$$\vec{E}_{Tx}(d, f, \vec{\Omega}) \approx \alpha(d, f) \cdot \underline{S}(f) \cdot \vec{F}_{Tx}(f, \vec{\Omega}). \quad (2.4)$$

In the free space the strength of E-field,  $\alpha$ , decays inversely with distance from antenna,  $d$ . Due to antenna directional selectivity  $\vec{F}(\vec{\Omega})$ , its placement has to

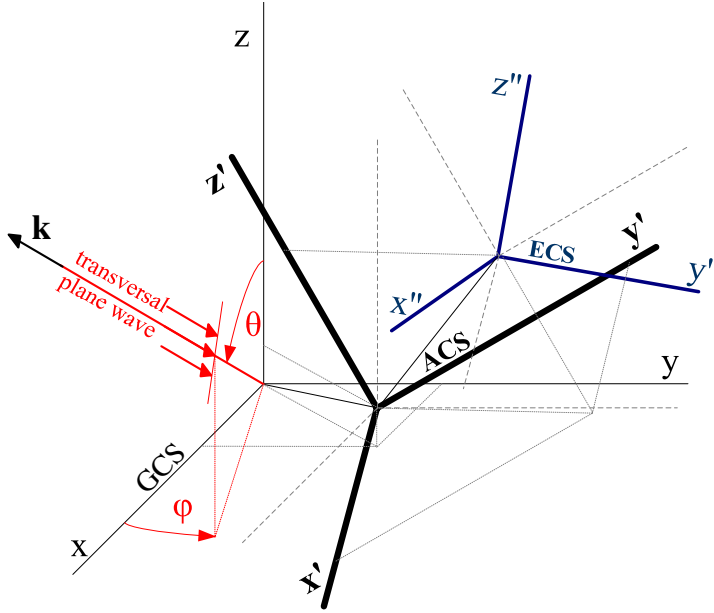


Figure 2.2: Coordinate system definitions: GCS, ACS and ECS.

described with 3-D position and orientation parameters,

$$\mathbf{S}_i = (\vec{r}_i, \vec{\Theta}_i). \quad (2.5)$$

For the multi-antenna terminal the spatial characteristics of the individual antennas define array geometry. The orientation parameters of the single antenna implicitly determine its radiation pattern  $\vec{F}(\vec{\Omega})$  w.r.t. propagation environment (Sec. 2.2.2).

### 2.2.2 Reference Coordinate Systems

Additionally to a spatial position and orientation of the mobile terminal, for radio channel it is necessary to describe radiation pattern of antenna and geometry of antenna array. The usage of the single coordinate system to handle all dependences would be ineffective. Therefore multiple nested coordinate systems are employed as shown in Fig. 2.2.

The antenna array is modeled as a collection of single elements. Each antenna element has its own *Element Coordinate System* (ECS) that can be placed and oriented anywhere with respect to the *Array Coordinate System* (ACS). Similarly, to allow arbitrary array positioning, a third reference system, called *Global Coordinate System* (GCS) is used.

In order to completely define a position of one Coordinate System (CS) inside another, it is necessary to describe orientation and translation, both in 3-D space. The orientation of the embedded CS is defined by three rotation angles that define the rotation about the respective axis of the containing CS, assuming that origins of CSs are aligned.

### Preferred Coordinate Systems

For plane wave assumption spherical coordinate system may be preferable to describe direction of impinging wave in ACS/ECS. In spherical coordinate system, the directional filtering and polarization mismatch could be jointly expressed in the form:

$$\vec{F}(\vec{\Omega}, f) = [F_\theta(\vec{\Omega}, f), F_\varphi(\vec{\Omega}, f)]^T. \quad (2.6)$$

where  $F_\theta$  and  $F_\varphi$  represent projections of radiation vector onto unit vectors of spherical CS.

The term co-elevation is used to designate complementary angle from elevation. Since elevation is well defined w.r.t. azimuthal plane, this convention leaves no doubt in contrast to alternatives inclination, normal angle. The proposed term is compatible with “co-latitude”, and shorter from other alternatives: zenith angle or polar angle.

When using the coordinate system to describe position on Earth, term *azimuth* defines *clockwise* rotation w.r.t. to the North direction. This is exactly opposite to the angle  $\varphi$  in spherical Specular Component (SC) that is measured from  $x$ -axis of Cartesian CS in the positive mathematical direction (counter clockwise). The usage of the same term would introduce the confusion about reference direction. Therefore, we assume that  $y$ -axis of Cartesian GCS, being placed on Earth surface, always indicates the North. As a consequence angle  $\varphi$  becomes complementary to azimuth angle, and results in *co-azimuth* naming convention. Thus, the spherical coordinates  $(r, \theta, \varphi)$  are referred as radial distance, co-elevation and co-azimuth.

### Relations between Antenna Rotation and Polarization Vector

Transmission polarization vector is related to rotation of transmit Array Coordinate System (ACS). Receive polarization vector is dependent on transmission polarization vector, and environment properties, i.e. propagation mechanism. Since environment interaction may not be invariant to rotation of transmit polarization vector, channel model has to account for this dependence.

Fig. 2.3a illustrates the effect of Element Coordinate System (ECS) rotation to antenna element polarization vectors: the rotated ECS (black sphere) is rotated for certain angle around the  $x$ - and  $z$ -axis in respect to the original ECS (gray sphere). Since polarization plane is defined by Direction of Departure (DoD)/Direction of Arrival (DoA) it stays unchanged after ECS rotation, however projections to  $\vec{i}_\theta$  and  $\vec{i}_\varphi$  polarization vectors are changed. This would mean that perception of polarization direction is not the same after the rotation of CS i.e., that  $\theta$  and  $\varphi$  components of E-field defined inside Global Coordinate System (GCS), does not align with antenna geometry after ECS rotation. To resolve this, it is necessary to calculate projections of GCS  $\theta$  and  $\varphi$  components to the new  $\theta$  and  $\varphi$  polarization directions defined by an antenna-dependant CS, as shown in Fig. 2.3b.

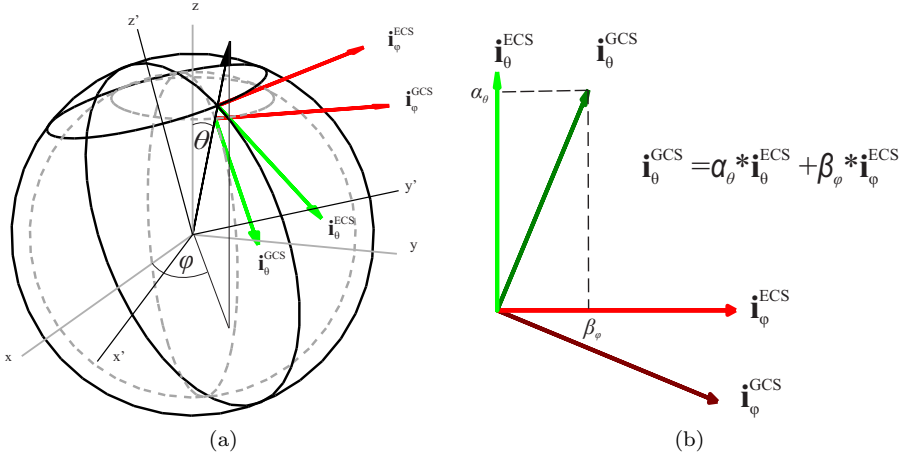


Figure 2.3: Effects of 3-D antenna rotation: a) changes in  $\theta$  and  $\varphi$  polarization directions, and b) calculation of the new polarization vectors (Käske [7]).

### 2.2.3 Relations between Spatial and Temporal Channel Dimensions for Moving Terminal

For the moving terminal spatial position and temporal dimensions are related in the following manner:

$$\vec{r}(t) = \vec{r}_0 + \int_{t_0}^t \vec{v}(t) dt, \quad (2.7)$$

where  $\vec{v}(t)$  designates time dependent velocity vector. Assumptions regarding the evolution of  $\vec{v}(t)$  in space-time determine the *mobility pattern*, that can be employed to position terminal in simulation. Typically, a rotation of the terminal is not considered and constant velocity is assumed.

Spatial changes will be observed in temporal domain, and reconstruction of spatial dependence would require exact knowledge of terminal movement and changes that have occurred in environment. Since environment changes are often not under control or tractable, reconstruction of spatial dimension from e.g. measurement data can not be performed perfectly, even if exact trajectories of the mobile terminal are available. This opens two additional topics, namely: environment representation and gathering of spatial information during channel measurements that are addressed in Appendix A, which is dedicated to experimental channel characterization. Further aspects of space-time model evolution will be discussed in Sec. 6.3.

### 2.2.4 Channel Decomposition

Using the system theory we can perform the following decomposition of the communication channel [8]:

1. *Transmission channel* enables transmission of 1-D (temporal) signals representing data streams. It performs necessary transformation of the input signal(s) into  $N$  separate temporal signals  $x_i(t), i = 1, \dots, N$  that will be fed

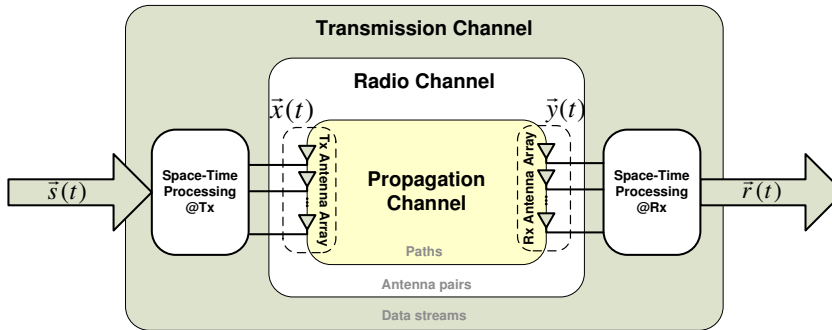


Figure 2.4: Decomposition of communication channel (after Steinbauer [8]).

to  $N$  different antenna elements. This process is designated as space-time processing since an association of the signal  $x_i(t)$  with  $i^{\text{th}}$  antenna array element creates the spatial dimension of signal. The ST processing is the most suitable way to improve the communication performance: adjustment of the format of transmitted signals provides matching to the spatial characteristics of the radio/propagation subchannels.

2. *Radio channel* enables transmission of (multiple) temporal signals through the physical environment without the dedicated transmission media. Instead, information is carried through the space by electromagnetic waves. The formation of radio channel requires the transformation of electrical energy into EMW, which is performed by *antenna*. Antenna can also be seen as deterministic system block that establishes the relation between the spatial and temporal dimension. The cooperative insertion of time signals into chosen points in space (defined by antenna elements position) can impact the distribution of EM energy in the space (beamforming) or improve the overall performance (throughput, power or spectral efficiency). The performance of radio channel is related to the position and orientation antenna, as well as antenna radiation characteristics. When multiple antenna elements are used their relative positioning also becomes relevant. Although, antennas could be repositioned in space, this is rarely used to improve the channel performance adaptively during communication. Equivalently, on the receiver side antennas perform projection of spatial dependencies into temporal domain, where further post-processing takes place.
3. *Propagation channel* describes physical environment in which EMW propagate. It shows dependence from both temporal and spatial dimensions. The effects of physical propagation environment will be further analyzed in Sec. 2.3.

Table 2.1: Maxwell's equations.

Name	Differential form	Integral form
Gauss's law	$\nabla \cdot \vec{D} = \rho$	$\oint_V \vec{D} \cdot d\vec{A} = \int_V \rho \cdot dV$
Gauss's law for magnetism	$\nabla \cdot \vec{B} = 0$	$\oint_V \vec{B} \cdot d\vec{A} = 0$
Faraday's law of induction	$\nabla \times \vec{E} = -\frac{\partial \vec{B}}{\partial t}$	$\oint_C \vec{E} \cdot d\vec{l} = -\int_S \frac{\partial \vec{B}}{\partial t} \cdot d\vec{A}$
Ampere's circuital law	$\nabla \times \vec{H} = \vec{J} + \frac{\partial \vec{D}}{\partial t}$	$\oint_C \vec{H} \cdot d\vec{l} = I + \int_S \frac{\partial \vec{D}}{\partial t} \cdot d\vec{A}$

## 2.3 Physical Propagation Channel

“For most practical channels, where signal propagation takes place in the atmosphere and near the ground, the free space propagation model is inadequate to describe the channel and predict system performance.” [9]

Electromagnetic Wave (EMW) leaving the Transmitter (Tx) antenna will interact with physical objects in the propagation environment causing different electromagnetic effects such as scattering, refraction, reflection, or diffraction (shadowing).

**Reflection** occurs when a propagating electromagnetic wave impinges on a smooth surface with very large dimensions compared to the wavelength of EMW.

**Shadowing** appears when the radio path between the transmitter and receiver is obstructed by a dense body. In general shadowing considerably effects level of the received signal.

- If dimensions of the body obstructing a line-of-sight path are greater than wavelength, a phenomenon called *diffraction* causes secondary waves behind the obstructing body.

**Scattering** occurs when a radio wave impinges on either a large rough surface or any surface whose dimensions are on the order of wavelength or less, causing the reflected energy to spread out (scattered) in all directions. In an urban environment, typical signal obstructions that yield scattering are lampposts, street signs, and foliage.

Those objects in the immediate radio propagation environment of transmitter and receiver, that have non-negligible influence to the considered propagation of the electromagnetic waves are referred as *Interacting Objects* (IO) [10].

### 2.3.1 Propagation of Electromagnetic Waves

The propagation of EMW through the space-time is nicely described by Maxwell theory. The energy contained in the traveling wave is repeatedly exchanged between electrical and magnetic fields. The complete process of EMW generation is initiated with appropriate distribution of electrical charges and an alternate current over the antenna. The following changes in electrical  $\vec{E}$  and magnetic  $\vec{H}$  fields could be described by only four differential equations, Tab. 2.1 [11]:

For a linear, isotropic and homogeneous medium without elementary sources it is possible to describe space-time propagation of electrical and magnetic field by the separate second order differential equations:

$$\nabla^2 \vec{E} - \mu\epsilon \frac{\partial^2 \vec{E}}{\partial t^2} = 0, \quad \nabla^2 \vec{H} - \mu\epsilon \frac{\partial^2 \vec{H}}{\partial t^2} = 0. \quad (2.8)$$

These equations are known as *wave equations*, and they are indicating that both fields are traveling through the space with the velocity

$$v = \frac{1}{\sqrt{\mu\epsilon}}. \quad (2.9)$$

For the free space the velocity of EM wave propagation will be equal to the speed of the light,  $c \approx 3 \cdot 10^8$  m/s.

Solving Maxwell's equations requires accurate description of boundary conditions, therefore propagation environment is represented as deterministic distribution of materials with given electrical and magnetic properties around the EM radiation source. All interactions with objects in propagation environment (as diffraction, reflection and scattering) are therefore implicitly contained in final solutions. This would be advantage with respect to some other approaches as ray-tracing for complex environments of limited extent. It appears that solving Maxwell's equations in general case have high computational complexity and requires application of well established, computationally efficient techniques. All these techniques, that model interaction of electromagnetic fields with physical objects using numerical approximations of Maxwell's equations, are known as **CEM**.

**Source Decoupling** Since traveling **EMWs** interact with other charges and currents, closely spaced antennas would become coupled meaning that they can not be treated as independent sources. However, the coupling of **EM** sources would decrease with their respective distance what enables their independent analysis for linear media. Since lower layers of atmosphere and large number of interacting objects belong to this class, propagation of **EMW** can be decomposed to analysis of separate uncoupled sources, and the total field distribution is reconstructed by superposition principle.

**TEM Approximation** At large distances from antenna the radial wavefront of **EMWs** can be approximated with planar, where intensity within plane is nearly constant. For large antenna separations above assumptions lead to simplified model of uniform, transversal waves with planar wavefront.

## Computational Electromagnetics - CEM

Since Maxwell equations, in general, can not be solved analytically it is necessary to employ some numeric methods, which require discretization of the spatial and temporal/frequency dimensions.

For that purpose integral or differential equation solvers could be applied, where analysis can be performed in either time or frequency domain.



The choice of particular method is somehow application specific. Since transient effects are more accurately represented in time domain, Finite-Difference-Time-Domain (FDTD) method would be appropriate choice in that case. Usage of wideband source in FDTD method resolves the EM field distribution over the large frequency range in single simulation run. The Finite-Element-Method (FEM), which uses discretization in the frequency domain, is suitable for curved geometrical objects and low frequencies.

These numerical methods approximate integrals with finite sums and derivatives with finite differences, what leads, after some additional manipulation, to linear system of equations, i.e. “system” matrix [12]. The methods based on discretization of differential equations (DEs) are referred as finite-difference, finite-area (or volume), or finite-element procedures. A numerical model based on an IE is also called a *boundary element* methods.

Usage of differential methods requires discretization of the entire space what results in large computational requirements. With integral methods it is possible to select only important segments of the space where physical laws will be enforced. This leads to significant differences between DE and IE methods: DE method produces sparse matrices, simply handles all material types, provides straightforward code generation and easy parallel computing. On the other hand IE solutions are more accurate and efficient: contrary to DE, IE methods enforce radiation condition and does not suffer from spurious solutions.

The usage of numerical methods requires proper selection of spatial and time/frequency resolution, i.e., time/frequency steps. The proper space-time sampling grid would depend on the particular method, however there is a practical rule to adopt spatial step that is smaller than one-tenth of the smallest wavelength of interest. [13] The size of the spatial grid would determine the precision in which object shapes (e.g. wall details) could be represented. However the grid itself have to support the solution for the highest frequencies (the smallest wavelengths) relevant for the investigated radio-channel. With the predefined resolution of the spatial grid it is clear that complexity of the Maxwell equation’s solving will be proportional with volume of the targeted space. Therefore computational or time resources could be easily exceeded for larger radio environments (outdoor propagation, or interior or large buildings). Since finite-difference methods update EM fields according to the values in neighboring cells, the procedure iterates until steady-state solution is reached.

### Deterministic Channel Assembling

The numeric CEM methods are often inefficient for areas being larger than several wavelengths. Substantially lower complexity and computing time are achievable with geometric-optical models [14], [15], [16]. These models are based on iterated approaches, which use the border behavior of electromagnetic fields for high frequencies [17]. The use of these procedures substantially simplifies the description of the wave propagation. This allows to compute electrically very large problems very efficiently and exactly.

When an appropriate description of the EM environment is available (in the form of databases defining geometry and material properties), the propagation of

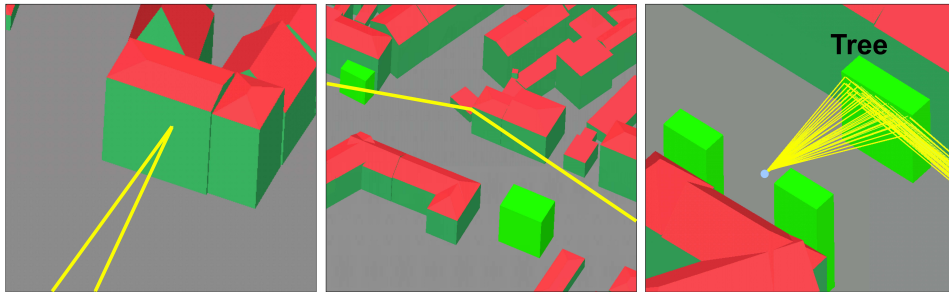


Figure 2.5: Multipath effects handled by ray-tracer: reflection (left), diffraction (middle) and scattering (right), (Reichardt et al. [19]).

the EMW could be predicted by use of the Geometrical or Uniform Theory of Diffraction (GTD/UTD). Then, the channel within given spatial volume can be represented by deterministic assembling of EMW. This approach requires an environment model and a wave propagation model. The environment model describes position, geometry, material composition and surface properties of the wave propagation relevant objects and obstacles (e.g. trees, houses, vehicles, walls, etc.). Interaction of EMW with object in propagation environment depends on the geometrical and electromagnetic properties (permittivity, conductivity, surface irregularities, etc.).

**Relevant GTD/UTD Aspects** The modern geometrical optics (GO) is an important representative of these iterated procedures, and it forms the basis for the uniform geometrical theory of diffraction (UTD). The validity of the GO does not alone depend on the frequency. A further condition is, that the scattering objects contained in the propagation vicinity are large in relation to the wavelength. Additionally the surface texture is not allowed to change over a wavelength. Further the material properties of the propagation medium must be constant within the range of a wavelength [17]. Usually these conditions are met for frequencies above 1 GHz.

**3D Ray-Tracing Engines** The ray-optics are based on the assumption that the wavelength is small compared to the dimensions of the modeled objects in the simulation scenario. If this is the case, the multi-path components corresponding to different types of propagation phenomena (e.g. reflection, diffraction, scattering) can be considered. This is illustrated in Fig. 2.5 for 3-D ray-tracer developed at the Institut für Hochfrequenztechnik und Elektronik, [18]. Each multi-path is represented by a ray, which may consecutively experience several different propagation phenomena. The modified Fresnel reflection coefficients that account for slightly rough surfaces are used to model the reflections. Diffractions are described by the Uniform Theory of Diffraction (UTD) and the corresponding coefficients for wedge diffraction. To describe scattering, e.g. from trees, the surface of scattering objects is subdivided into small squared tiles. Depending on the energy, which is incident on the surface of the objects, each tile gives rise to a Lambertian scattering source.

The accuracy of deterministic channel models was investigated in many publications: [14], [20], [21], [22]. The results of the applied ray tracing algorithms have been verified by measurements in different scenarios and have shown to reach a very high accuracy [23].

Due to its flexibility and accuracy geometric-optical models applied for the site-specific prediction of the full-polarimetric field strength and/or receiving power in the regarded propagation area. These engines enable the complete description of the propagation channel. However, the realistic evaluation of a communication system performance require the multiple realizations of the propagation environment. Due to the complexity of geometric-optical models, a substantial computing and time expenditures must be taken into account. The main advantage of deterministic channel assembling is that spatially-colored multi-user interference, one of the most limiting factors for the achievable performance in multi-user MIMO-systems, is inherently considered [24].

### 2.3.2 Multipath Components

Due to occurrence of reflections, diffraction and scattering, the energy between transmitter and receiver is transmitted over the multiple propagation paths. **EMW** coming to the receiver from different directions  $\vec{\Omega}_i^{Rx}$  travel across different geometrical paths and have different delays  $\tau_i$  w.r.t. some referent moment on Tx side. For single propagation component its delay  $\tau_i$ , direction of departure  $\vec{\Omega}_i^{Tx}$  and arrival  $\vec{\Omega}_i^{Rx}$  are related, and possibly changing in time. Therefore, E-field arriving to Rx antenna from direction  $\vec{\Omega}_i^{Rx}$  corresponds to the signal emitted  $\tau_i$  seconds earlier in departure direction  $\vec{\Omega}_i^{Tx}$ ,

$$\vec{E}_{Rx}(\vec{\Omega}_i^{Rx}, f, t) = \underline{S}(f) \cdot e^{-j2\pi(f\tau_i + \nu_i t)} \cdot \alpha_i^T \cdot \vec{F}_{Tx}(\vec{\Omega}_i^{Tx}, f). \quad (2.10)$$

The change of amplitude and phase of i-th MPC, as well as its depolarization, due to interaction with physical objects is represented by complex matrix  $\alpha_i$ . The change of the perceived frequency due to relative movement of terminal with respect to environment is taken into account by Doppler frequency shift,  $\nu_i$ .

The multiple interactions for the particular **EMW** will combine together, and produce an overall attenuation of the amplitude accompanied by a phase rotation which is accounted for by a complex gain coefficients [25]. The propagation over multiple paths can cause fluctuations in the received signal's amplitude and phase that is referred to as *multipath fading*.\*

## 2.4 Space-Time Radio Channel

### 2.4.1 LSTV Nature of Radio Channel

The linearity of the radio channel comes from the linearity of the propagation media and from superposition of induced voltages in antenna:

$$\underline{e}(f, t) = \frac{\lambda}{\pi} \cdot \sum_i \vec{E}_{Rx}^T(\vec{\Omega}_i^{Rx}, f, t) \cdot \vec{F}_{Rx}(\vec{\Omega}_i^{Rx}, f), \quad (2.11)$$

---

\* Alternatively, the signal variations or fading can be caused by changes in transmission medium or shadowing itself.

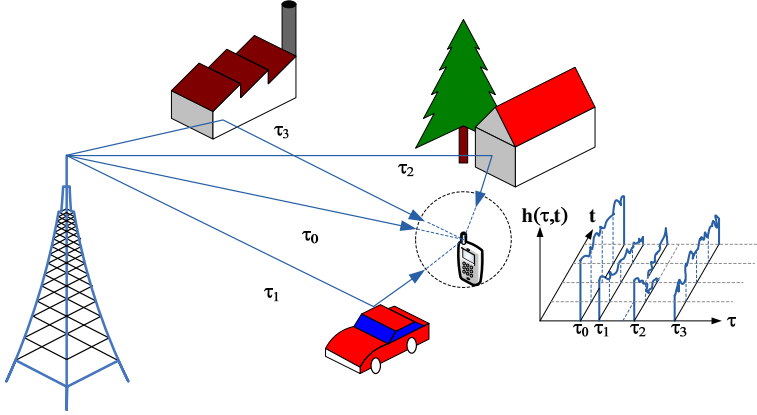


Figure 2.6: Multipath propagation.

where  $\vec{E}_{Rx}(\vec{\Omega}_i, f, t)$  represents electric field vector impinging on Receiver (Rx) antenna with complex radiation pattern  $\vec{F}_{Rx}(\vec{\Omega}_i^{Rx}, f)$  from direction  $\vec{\Omega}_i^{Rx}$ .

By substitution of (2.10) into (2.11) the spectrum of induced voltage becomes:

$$\begin{aligned} \underline{e}(f, t) &= \underline{s}(f) \cdot \frac{\lambda}{\pi} \sum_i e^{-j2\pi(f\tau_i + \nu_i t)} \cdot \vec{F}_{Tx}^T(\vec{\Omega}_i^{Tx}, f) \cdot \alpha_i \cdot \vec{F}_{Rx}(\vec{\Omega}_i^{Rx}, f) \\ &= \underline{s}(f) \cdot \frac{1}{2} \underline{H}(f, t) \end{aligned} \quad (2.12)$$

The linear relation between the spectra at channel input and output, allows the channel representation by time-variant transfer function  $H(f, t)$  and application of corresponding Linear Time Variant (LTV) system theory. Since realization of  $H(f, t, \mathbf{S}_{Tx}, \mathbf{S}_{Rx})$  depends on position and orientation of terminals  $\mathbf{S}_{Tx}$  and  $\mathbf{S}_{Rx}$  complete transfer function changes in space-time and we have *Linear Space-Time Variant* (LSTV) system.

The frequency dependence of antenna radiation pattern becomes relevant only for **UWB** communications and for smaller transmission bandwidths can be neglected. Therefore the induced voltage at Rx antenna can be represented as convolution over time-delay domain:

$$\begin{aligned} \underline{e}(t) &= \sum_i \underline{s}(t - \tau_i) \cdot \frac{\lambda}{\pi} \cdot \delta(\tau - \tau_i) \cdot e^{-j2\pi\nu_i t} \cdot \vec{F}_{Tx}^T(\vec{\Omega}_i^{Tx}) \cdot \alpha_i \cdot \vec{F}_{Rx}(\vec{\Omega}_i^{Rx}) \\ &= \sum_i \underline{s}(t - \tau_i) \cdot \frac{1}{2} \underline{h}(\tau_i, t) \\ &= \underline{s}(t) * \frac{1}{2} \underline{h}(t). \end{aligned} \quad (2.13)$$

### 2.4.2 Channel Impulse Response (CIR)

Duration of propagation is typically measured from transmitting instant  $t_0$ , while antenna array coordinating system is used to characterize directions of departure/arriving waves. The position of the antenna coordinating systems in “global” common coordinating system is fully defined with  $\mathbf{S}_i = (\vec{r}_i, \vec{\Theta}_i)$ ,  $i \in \{Tx, Rx\}$ .

#### Time-Delay Dimension

According to this assumptions, the impulse response of *propagation* channel can be determined as response to full spatial excitation with Dirac time-impulse in the form:

$$\underline{\mathbf{h}}(t, t_0, \vec{\Omega}_T, \vec{\Omega}_R) = \Gamma \left\{ \delta(t - t_0, \forall \vec{\Omega}_T) \right\}. \quad (2.14)$$

Typically, difference between observation and emission time is named propagation delay:  $\tau = t - t_0$ , and it represents the new dimension in analysis of wideband channels:

$$\underline{\mathbf{h}}(t_0 + \tau, t_0, \vec{\Omega}_T, \vec{\Omega}_R) = \Gamma \left\{ \delta(t - t_0, \forall \vec{\Omega}_T) \right\}. \quad (2.15)$$

Expression (2.15) can be interpreted as joint (Tx,Rx) directional selectivity of environment, showing also short-term memory in the form of different propagation paths/delays.

#### Space-Time Dependency

In order to simplify notation we can define *space-time realization* of radio-link, having two communicating terminals:

$$\mathbf{Q} \equiv (t_0, \mathbf{S}_{Tx}(t_0), \mathbf{S}_{Rx}(t_0 + \tau)). \quad (2.16)$$

Therefore, the space-time realization depends on 2 temporal dimensions  $t_0, \tau$  and 6 spatial dimensions defining position and orientation of Tx and Rx terminals in moments of transmission and reception,  $\mathbf{S}_{Tx}(t_0), \mathbf{S}_{Rx}(t_0 + \tau)$ . Note that time-delay,  $\tau$ , and position of Rx terminal  $\mathbf{S}_{Rx}$  are not independent dimensions.

Any changes in terminal spatial characteristics  $\mathbf{Q}$  or in environment (Interacting Object (IO) movement or change in propagation medium) will influence changes of delay-directional structure characterizing propagation channel:

$$\begin{aligned} \underline{\mathbf{h}}(\tau(\mathbf{Q}), \nu(\mathbf{Q}), \vec{\Omega}_{Tx}(\mathbf{Q}), \vec{\Omega}_{Rx}(\mathbf{Q})) &= \underline{\mathbf{h}}(\tau, \nu, \vec{\Omega}_{Tx}, \vec{\Omega}_{Rx} | \mathbf{Q}) \\ &= \underline{\mathbf{h}}(\tau, \nu, \vec{\Omega}_{Tx}, \vec{\Omega}_{Rx} | (t_0, \mathbf{S}_{Tx}(t_0), \mathbf{S}_{Rx}(t_0 + \tau))). \end{aligned} \quad (2.17)$$

#### Structural Parameters

Under the assumption that single EMW can be described with discrete values of propagation delay, departure and arriving angles we arrive to ray-based representation of Channel Impulse Response (CIR):

$$\begin{aligned} \underline{\mathbf{h}}(\tau, \nu, \vec{\Omega}^{Tx}, \vec{\Omega}^{Rx} | \mathbf{Q}) &= \sum_i \alpha_i \cdot \delta(\tau - \tau_i(\mathbf{Q}_i)) \cdot \delta(\nu - \nu_i(\mathbf{Q}_i)) \cdot \\ &\cdot \delta(\vec{\Omega}^{Tx} - \vec{\Omega}_i^{Tx}(\mathbf{Q}_i)) \cdot \delta(\vec{\Omega}^{Rx} - \vec{\Omega}_i^{Rx}(\mathbf{Q}_i)). \end{aligned} \quad (2.18)$$

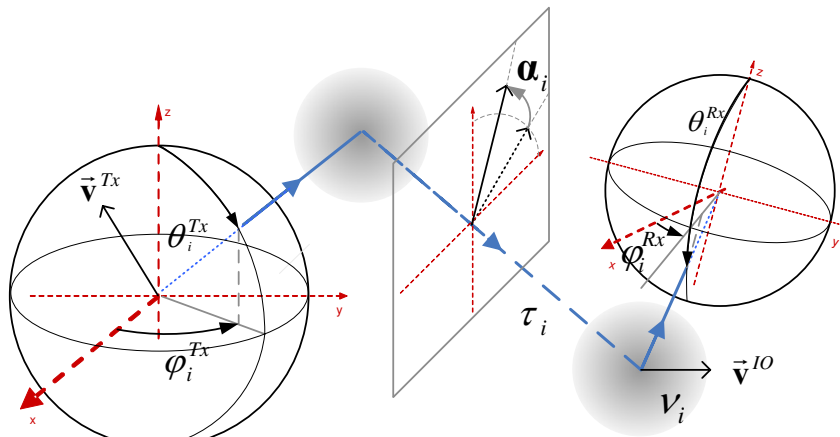


Figure 2.7: Structural parameters.

Note that certain assumption about exciting polarization vector (that relates to  $\mathbf{T}_x$  orientation and  $\mathbf{T}_x$  antenna radiation pattern) is necessary when determining CIR. When characterization (2.15) is repeated for two orthogonal  $(\varphi, \theta)$  polarizations at  $\mathbf{T}_x$  and  $\mathbf{R}_x$  full spatial characterization in the sense of  $\mathbf{S}^{T_x}$  and  $\mathbf{S}^{R_x}$  is obtained. This is represented with 2x2 matrix notation whose rows (first subscript) are related to  $\mathbf{T}_x$  and columns (second subscript) to  $\mathbf{R}_x$ :

$$\alpha = \begin{bmatrix} \alpha_{\theta\theta} & \alpha_{\theta\varphi} \\ \alpha_{\varphi\theta} & \alpha_{\varphi\varphi} \end{bmatrix}. \quad (2.19)$$

The common GCS, Sec. 2.2.2, that encompass all terminals is necessary to characterize environment interaction with polarization dimension [7].

Each of multipath components have its evolution in time, that can be described by associated Doppler frequency shift,  $\nu$ . This enables representation of CIR using only resolvable (“constructive”) domains, where each multipath component is described by the following parameters: delay, Doppler shift, depolarization matrix with complex gains, direction of departure and direction of arrival,

$$\mathbf{p}_i = (\tau_i, \nu_i, \alpha_i, \vec{\Omega}_i^{T_x}, \vec{\Omega}_i^{R_x}). \quad (2.20)$$

The (2.18) accounts for departure and arrival directions of multipath components and offers *double-directional* channel representation [26]. Double-directional concept uses antenna-centric view of environment: positions and orientations of transmitting  $\mathbf{S}_{T_x} = (\vec{r}_{T_x}, \vec{\Theta}_{T_x})$  and receiving  $\mathbf{S}_{R_x} = (\vec{r}_{R_x}, \vec{\Theta}_{R_x})$  terminal are taken as a reference. In the respective coordinating systems energy that is transmitted through environment can be characterized with arrival time and direction.

### Antenna (de)Embedding

Starting from expression (2.13) for induced electromotive force it can be seen that interaction of directionally dependent propagation channel with antenna radiation

patterns does not depend on transmitted signal. It is therefore possible to introduce impulse response of the wideband *radio* channel in the form:

$$\begin{aligned} \underline{h}(\tau|t, \mathbf{S}_{Tx}, \mathbf{S}_{Rx}) &= \underline{h}(\tau|\mathbf{Q}) \\ &= \sum_i \vec{F}_{Rx}(\vec{\Omega}_i^{Rx}|\mathbf{S}_{Rx}) \underline{\mathbf{h}}(\tau, \vec{\Omega}^{Tx}, \vec{\Omega}^{Rx}|\mathbf{Q}) \vec{F}_{Tx}(\vec{\Omega}_i^{Tx}|\mathbf{S}_{Tx}). \end{aligned} \quad (2.21)$$

We have seen that both radio and physical propagation channel show dependencies from space-time radio-link realization  $\mathbf{Q}$ . However, the impulse response of radio channel,  $\underline{h}(\tau|\mathbf{Q})$ , includes the response of the antenna radiation pattern and therefore does not show explicit dependence on departure and arriving directions of the multipath components. Additionally, impulse response of radio channel is complex scalar, while CIR of physical propagation channel can take form of 2x2 matrix with complex elements that describes depolarization due to environment.

The (2.21) shows that all multipath components arriving from different directions but having the same delay  $\tau_i$  are contributing to  $h(\tau_i, t)$ . This projection of directional content to the antenna radiation pattern can be expressed in the form of convolution of propagation channel impulse response with radiation patterns:

$$\begin{aligned} \underline{h}(\tau|\mathbf{Q}) &= \int_0^{4\pi} \int_0^{4\pi} \vec{F}_{Rx}(\vec{\Omega}^{Rx}|\mathbf{S}_{Rx}) \cdot \underline{\mathbf{h}}(\tau, \vec{\Omega}^{Tx}, \vec{\Omega}^{Rx}|\mathbf{Q}) \cdot \vec{F}_{Tx}(\vec{\Omega}^{Tx}|\mathbf{S}_{Tx}) d\vec{\Omega}^{Rx} d\vec{\Omega}^{Tx} \\ &= \vec{F}_{Rx}(\vec{\Omega}^{Rx}|\mathbf{S}_{Rx}) * \underline{\mathbf{h}}(\tau, \vec{\Omega}^{Tx}, \vec{\Omega}^{Rx}|\mathbf{Q}) * \vec{F}_{Tx}(\vec{\Omega}^{Tx}|\mathbf{S}_{Tx}). \end{aligned} \quad (2.22)$$

This process of marginalizing response of propagation channel and antenna directivity will be also referred as *antenna embedding*. The opposite process where antenna influence should be removed in order to characterize pure propagation channel is called *antenna de-embedding*.

The MIMO concept is expected to significantly increase transfer rates and the reliability or power efficiency. However the realistic performance of MIMO systems can be properly investigated only if antenna inter-correlation is properly represented. For a given antenna arrays the average correlations-levels could be explicitly expressed. This thesis, however, concentrate on antenna independent geometry-based models where correlations are implicitly contained in the multi-path realizations. The characterization of every multi-path component requires multiple parameters (delay, directions of departure and arrival, polarization-dependent weights, and Doppler shift). Resolving the multipath components allows antenna de-embedding and independent characterization of propagation channel.

Only if all energy is resolved in Tx and Rx directional domains it is possible to characterize propagation channel independently from deterministic radiation patterns of Tx and Rx antennas. This will impose certain limitation in reconstruction of propagation channel from channel sounding data, i.e., from multiple spatially offset realizations of radio channel (Sec. 4.2).

### Transmission through a Radio Channel

Recapitulating above discussion we can identify the following dimension of radio channel:

Table 2.2: Relations between representation domains are established via Fourier transform.

Resolved domain	Faded domain	Transform	Inverse transform
Doppler shift, $\nu$	time, $t$	$\int_{-\infty}^{\infty} (\cdot) \exp(j2\pi\nu t) d\nu$	$\int_{-\infty}^{\infty} (\cdot) \exp(-j2\pi\nu t) dt$
delay, $\tau$	frequency, $f$	$\int_{-\infty}^{\infty} (\cdot) \exp(-j2\pi f\tau) d\tau$	$\int_{-\infty}^{\infty} (\cdot) \exp(j2\pi f\tau) df$
wavevector, $\vec{k}$	position, $\vec{r}$	$\frac{1}{(2\pi)^3} \int_{-\infty}^{\infty} (\cdot) \exp(j\vec{k}^T \vec{r}) d\vec{k}$	$\int_{-\infty}^{\infty} (\cdot) \exp(-j\vec{k}^T \vec{r}) d\vec{r}$

- time,  $t$ ,
- propagation delay,  $\tau$  (coming from wideband property),
- position and orientation of terminals at Tx and Rx:  $\mathbf{S}_{Tx}(t)$  and  $\mathbf{S}_{Rx}(t + \tau)$ .

For a Linear Space-Time Variant (**LSTV**) channel, the Single-Input Single-Output (**SISO**) received signal can be determined via time-delay convolution:

$$\underline{y}(t|\mathbf{S}_{Rx}) = \frac{1}{2} \int_{-\infty}^{\infty} \underline{x}(t - \tau|\mathbf{S}_{Tx}) \underline{h}(\tau|t, \mathbf{S}_{Tx}, \mathbf{S}_{Rx}) d\tau, \quad (2.23)$$

or via filtering in frequency domain

$$\underline{y}(t|\mathbf{S}_{Rx}) = \frac{1}{2} \int_{-\infty}^{\infty} \underline{X}(f|\mathbf{S}_{Tx}) \cdot \underline{h}(f|t, \mathbf{S}_{Tx}, \mathbf{S}_{Rx}) \cdot e^{-j2\pi ft} df.$$

### 2.4.3 Spatio-Temporal Channel Representation by System Functions

It was showed [27] that radio-channel can be equivalently represented in other domains, being Fourier transformations of the original domains. Relations between them are given in Tab. 2.2 [28]

Doppler spectrum can be calculated by short-time Fourier transform of temporal dimension. If channel response would be constant in time, the Doppler spectrum would consist of single spectral line at  $\nu = 0$ . Therefore, the spreading in Doppler domain is proportional to the extent of temporal variations.

Original wideband domains from [27] could be extended with spatial dimensions i.e. *apertures*.

The transformation of 3-D spatial channel to the wavevector domain is calculated as triple integral [28]:

$$\underline{\mathbf{h}}(k_x, k_y, k_z) = \int_{-\infty}^{\infty} \int_{-\infty}^{\infty} \int_{-\infty}^{\infty} \underline{\mathbf{h}}(x, y, z) e^{-j(k_x x + k_y y + k_z z)} dx dy dz, \quad (2.24)$$

which is equivalent to 3-D Fourier transformation. By using vector representations

$$\vec{k} = k_x \vec{i}_x + k_y \vec{i}_y + k_z \vec{i}_z, \quad \vec{r} = x \vec{i}_x + y \vec{i}_y + z \vec{i}_z,$$

and notation

$$\int_{-\infty}^{\infty} d\vec{r} = \int_{-\infty}^{\infty} \int_{-\infty}^{\infty} \int_{-\infty}^{\infty} dx dy dz, \quad \int_{-\infty}^{\infty} d\vec{k} = \int_{-\infty}^{\infty} \int_{-\infty}^{\infty} \int_{-\infty}^{\infty} dk_x dk_y dk_z,$$



the condensed forms are obtained:

$$\underline{\mathbf{h}}(\vec{k}) = \int_{-\infty}^{\infty} (\underline{\mathbf{h}}(\vec{r})) \exp(-j\vec{k}^T \vec{r}) d\vec{r}, \quad (2.25)$$

$$\underline{\mathbf{h}}(\vec{r}) = \frac{1}{(2\pi)^3} \int_{-\infty}^{\infty} (\underline{\mathbf{h}}(\vec{k})) \exp(j\vec{k}^T \vec{r}) d\vec{k}. \quad (2.26)$$

The wavevector  $\vec{k}$  correspond to “spatial angular frequency”, i.e., number of wavelength repetitions per unit space (1 m) measured along direction  $\vec{\Omega}$  and multiplied by factor  $2\pi$ .

$$\begin{aligned} \vec{k} &= \frac{2\pi}{\lambda} \vec{\Omega} \\ &= \frac{2\pi}{\lambda} [\sin(\theta) \cos(\varphi) \vec{i}_x + \sin(\theta) \sin(\varphi) \vec{i}_y + \cos(\theta) \vec{i}_z]. \end{aligned} \quad (2.27)$$

The vector  $\vec{\Omega} = \vec{i}_\theta \times \vec{i}_\varphi$  points in direction of radial component of spherical coordinate system, and it is determined by co-elevation  $\theta$  and azimuth  $\varphi$  angles as shown on Fig. 2.8.

For stationary distribution of channel realizations in 3-D space (2.25) finds the spectral content for all directions  $\vec{\Omega}$  in spherical coordinate system. The kernel used for Fourier transform of aperture,  $e^{-j\vec{k}^T \vec{r}}$ , describes the phase change that would experience the plain EMW arriving to the position  $\vec{r}$  from direction  $\vec{\Omega}$ , before it reaches the center of the coordinate system. From directions that are different than considered, a phase difference of planar waves is taken into account. Since product  $\vec{k}^T \vec{r}$  will be the same in all directions perpendicular to the  $\vec{k}$  (equiphase surface of planar wave), the transformation (2.25) sums all function values from the orthogonal planes and then performs 1-D Fourier transformation. The Fourier transformation of 3-D space (aperture) is based on inner product of vectors  $\vec{k}^T \vec{r}$  and therefore can be determined as sequence of independent 1-D transformations.

By exploiting the relation (2.27) is possible to establish correspondence between directional radiation pattern  $\underline{h}(\vec{\Omega})$  and 3-D channel impulse response that would be limited to the single sphere of radius  $k_0 = \frac{2\pi}{\lambda}$ :

$$\underline{\mathbf{h}}(\vec{k}) = \frac{\delta(|\vec{k}| - k_0)}{k_0^2} \cdot \underline{\mathbf{h}}(\vec{\Omega}). \quad (2.28)$$

The normalization by the sphere radius  $k_0$  comes from the relation of the elementary solid angle  $d\Omega$  and the elementary area on the sphere:  $dA = k_0^2 d\Omega$ . For this special case Fourier transform of directional domain becomes:

$$\begin{aligned} \underline{\mathbf{h}}(\vec{r}) &= \frac{1}{(2\pi)^3} \int_{\mathcal{R}^3} \underline{\mathbf{h}}(\vec{k}) \cdot e^{j\vec{k}^T \vec{r}} d\vec{k} \\ &= \frac{1}{(2\pi)} \int_{\mathcal{R}} \int_{\mathcal{A}} \frac{\delta(|\vec{k}| - k_0)}{k_0^2} \cdot \underline{\mathbf{h}}(\vec{\Omega}) \cdot e^{j\vec{k}_0^T \vec{r}} \cdot dA \cdot d(|\vec{k}|) \\ &= \int_{\vec{\Omega}} \underline{\mathbf{h}}(\vec{\Omega}) \cdot e^{j\vec{k}_0 \vec{\Omega}^T \vec{r}} \cdot d\vec{\Omega}. \end{aligned} \quad (2.29)$$

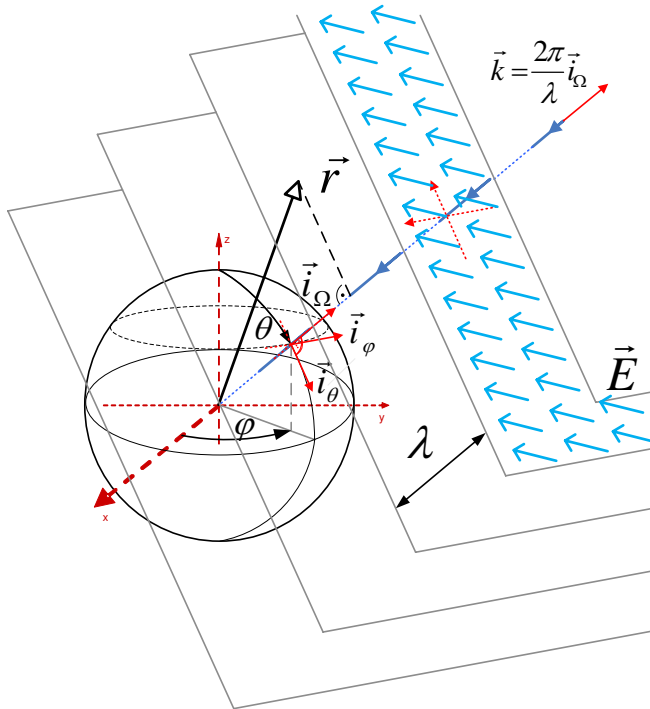


Figure 2.8: Relations between aperture and wavevector.

This transformation relates 3-D spatial channel realizations and directional distribution of traveling plane waves: the “aperture domain” is obtained as Fourier transform of directional channel properties.

The *Effective Aperture Distribution Function* (EADF) represent example of this transformation in 2-D space that is defined by co-elevation and azimuth angles,  $\vec{\Omega} \equiv (\theta, \varphi)$

Equation (2.29) has similar form as (2.21), however directional and polarization properties of antenna are not included - only a phase shift corresponding to spatial displacement is considered. This means that EMW interact in the free space and define propagation channel, since antenna is absent. The radio channels observed with measurement arrays always include effect of the radiation pattern. If antenna radiation pattern could be removed from gathered spatial samples (including its polarization properties), the inverse transform of (2.29) could be used to reconstruct spatial propagation dimension. In this case reconstruction would be based on the limited number of the spatial samples, since available samples does not cover complete  $R^3$  space.

The effect of depolarization is not properly accounted by (2.29). In order to sum vector fields it would be necessary to independently sum their orthogonal

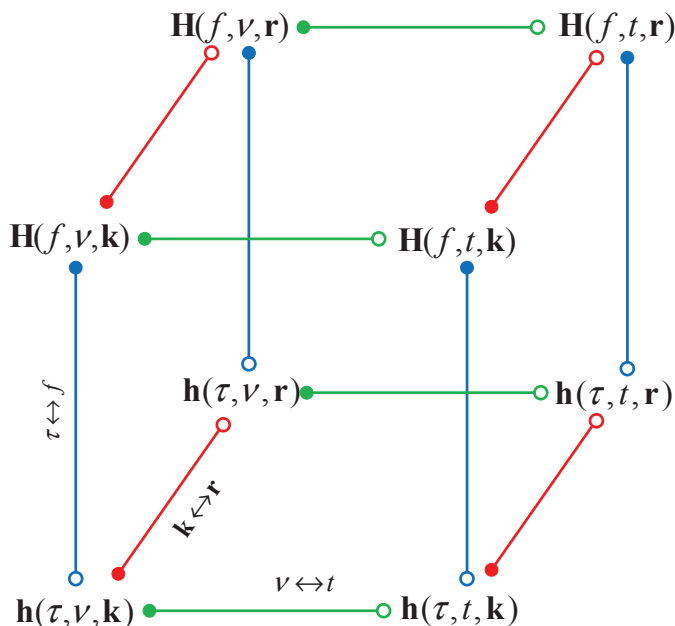


Figure 2.9: Transformation cube (after Del Galdo [29]).

components which additionally complicates the transformation. Anyway, notation  $\underline{\mathbf{h}}$  is kept in order to emphasize that *propagation* channel is being analyzed.

The existing relations are usually visualized in the form of transformation cube (Figure 2.9), but only for single side of radio-link (Tx or Rx) and without considering polarization. Otherwise, multidimensional hyper-cube will be necessary.

If apertures on both **Tx** and **Rx** side are represented with departure/arrival directions the double directional description of the channel is obtained:

$$\underline{\mathbf{h}}(\tau, \nu, \vec{\Omega}_{Tx}, \vec{\Omega}_{Rx}) = \int_{\mathcal{R}^3} \int_{\mathcal{R}^3} \int_{\mathcal{R}} \left( \int_{\mathcal{R}} \underline{\mathbf{H}}(f, t, \vec{r}_{Tx}, \vec{r}_{Rx}) \cdot e^{j2\pi f \tau} df \right) \cdot e^{-j2\pi \nu t} dt \cdot e^{-j \frac{2\pi}{\lambda} \vec{\Omega}_{Tx}^T \vec{r}_{Tx}} \frac{d\vec{r}_{Tx}}{\lambda^3} \cdot e^{-j \frac{2\pi}{\lambda} \vec{\Omega}_{Rx}^T \vec{r}_{Rx}} \frac{d\vec{r}_{Rx}}{\lambda^3}. \quad (2.30)$$

### Classification of Domains

Multipath propagation causes the signal to spread in delay, Doppler shift, and directions (DoD, DoA). In these domains it is possible to resolve the contribution of multipath components, and they are referred to as *resolvable* domains. As the consequence of spreading in one domain, channel becomes selective in corresponding FT domain (Tab. 2.2). Therefore propagation channel varies as a function of time, frequency, and space. These domains are called *faded* domains. For example, the channel representation in the equation (2.30) is transformed from purely faded domains into purely resolvable domains.

### 2.4.4 MIMO Radio Channel

Under plane wave assumption, a phase shift corresponding to spatial displacement of element inside Antenna Array (AA) becomes independent from distance to the source or the nearest IO. This can be exploited to extend the representation of antenna radiation pattern (2.6) toward its specific position within the antenna array.

#### Antenna Array Model

The antenna array is modeled as a collection of elements being voluntarily placed and oriented with respect to the ACS and additionally characterized with corresponding radiation patterns. The full 3-D Antenna Array (3DAA) model includes following effects:

1. spatial displacement: translation of antenna elements (i.e., ECS) in respect to phase center of array (ACS origin) is resulting in element (and Multi-Path Component (MPC) direction) dependent phase shift,
2. directional filtering: antenna element radiation patterns will introduce direction-specific gain for incoming waves,
3. polarization mismatch: non-ideal radiation characteristics will cause direction dependent rotation of polarization vector, i.e. directional dependent Cross-Polarization Discrimination (XPD). This effect is handled by two radiation patterns that are determined for orthogonal polarizations.
4. frequency dependence of polarization patterns.

The plane wave assumption enables a separate analysis of effects of antenna translation (spatial displacement) and rotation (directional filtering and polarization mismatch). As a consequence, the usage of the Four-Dimensional (4-D) homogeneous coordinates [30], enabling a simultaneous description of both translation and multiplication through a single matrix multiplication, is unnecessary.

Directional filtering and polarization mismatch are handled by the representation of radiation pattern  $[F_\theta(\theta, \varphi), F_\varphi(\theta, \varphi)]^T$  for two orthogonal polarizations as in (2.6).

**Spatial Displacement** ACS is introduced in Sec. 2.2.2 to describe joint movement of elements constituting AA. The placement of individual antenna elements is described jointly by position and orientation parameters (2.5), of which only position influences the MPC propagation distance. The displacement of the ECS origin and corresponding  $k^{th}$  antenna element inside the ACS can be expressed w.r.t. origin of ACS by:

$$\vec{d}_k^{ACS} = x_k \vec{i}_x^{ACS} + y_k \vec{i}_y^{ACS} + z_k \vec{i}_z^{ACS}, k = 1, \dots, K.$$

If DoD/DoA of MPC are given in ACS by  $(\theta_A, \varphi_A)$  i.e.,

$$\vec{\Omega}_{ACS} = \left[ \sin(\theta_A) \left( \cos(\varphi_A) \vec{i}_x^{ACS} + \sin(\varphi_A) \vec{i}_y^{ACS} \right) + \cos(\theta_A) \vec{i}_z^{ACS} \right]^T,$$

the corresponding phase offset at  $k^{th}$  antenna element in respect to ACS origin is

$$\Delta\phi_k^{ACS} = \frac{2\pi}{\lambda} \vec{\Omega}_{ACS}^T \vec{d}_k^{ACS}.$$

The phase offsets have to be calculated for each MPC for all antenna elements, since the angles  $\theta_A$  and  $\varphi_A$  are different for different MPCs.

**Complex Polarimetric Radiation Pattern** The influence of spatial displacements is included through exponential term  $e^{(-j\Delta\phi_k^{ACS})}$ . For complete description of radiation properties of single antenna element, this information has to be supplemented with rotation and the intrinsic radiation pattern:

$$\vec{F}_k(\vec{\Omega})^{ACS} = \vec{\Theta}\{\vec{F}_k(\vec{\Omega})^{ECS}\} e^{-j\frac{2\pi}{\lambda} \vec{\Omega}_{ACS}^T \vec{d}_k^{ACS}}. \quad (2.31)$$

The intrinsic radiation pattern of antenna element is usually expressed in ECS that is aligned with antenna geometry, and  $\vec{\Theta}\{\cdot\}$  designates rotation of ECS within ACS. The given *complex* radiation pattern covers all spatial degrees of freedom: transversal movement and antenna rotation, as well as any array geometry for the MIMO case.

### MISO Received Signal

For M transmitting antenna arrays consisting of S antenna elements, a received signal on  $u^{th}$  antenna element can be represented as:

$$\begin{aligned} \underline{y}_u(t|\mathbf{S}_{\{m,s\}}, \mathbf{S}_u) &= \frac{1}{2} \sum_{m=1}^M \sum_{s=1}^S \int_{-\infty}^{\infty} \int_0^{4\pi} \int_0^{4\pi} \vec{F}_u^T(\vec{\Omega}_{Rx}|\mathbf{S}_u) \underline{\mathbf{h}}(\tau, t, \vec{\Omega}_T, \vec{\Omega}_R|\mathbf{S}_{m,s}, \mathbf{S}_u) \cdot \\ &\cdot \vec{F}_{m,s}(\vec{\Omega}_{Tx}|\mathbf{S}_{m,s}) \underline{x}_{m,s}(t - \tau|\mathbf{S}_{m,s}) d\vec{\Omega}_{Tx} d\vec{\Omega}_{Rx} d\tau \end{aligned} \quad (2.32)$$

When multiple input sources belong to the same array, they share the same rotation in global CS,  $\vec{\Theta}$  and therefore could be represented with position offset from reference point in array (typically – from phase center):  $\vec{d}_{m,s} = \vec{d}_m + \vec{d}_s$ .

## 2.5 Selectivity of Radio Channel

Multipath propagation causes the spread of signal in Doppler shift, delay, and angle. As consequence a channel becomes selective in time, frequency, or space. The channel is considered to be selective if it varies as a function of either time, frequency or space. The selectivity within faded domains can be described by the extent of the corresponding Auto-Correlation Functions (ACFs), The *coherence* quantifies the speed of variations in the form of time, frequency or space interval (range) without significant changes. The faded and resolved domains form Fourier transformation pairs, as indicated on Fig. 2.10 and Fig. 2.11. Interpretation of the spreading in resolved domains becomes intuitive when discrete multipath components are used to describe physical propagation process.

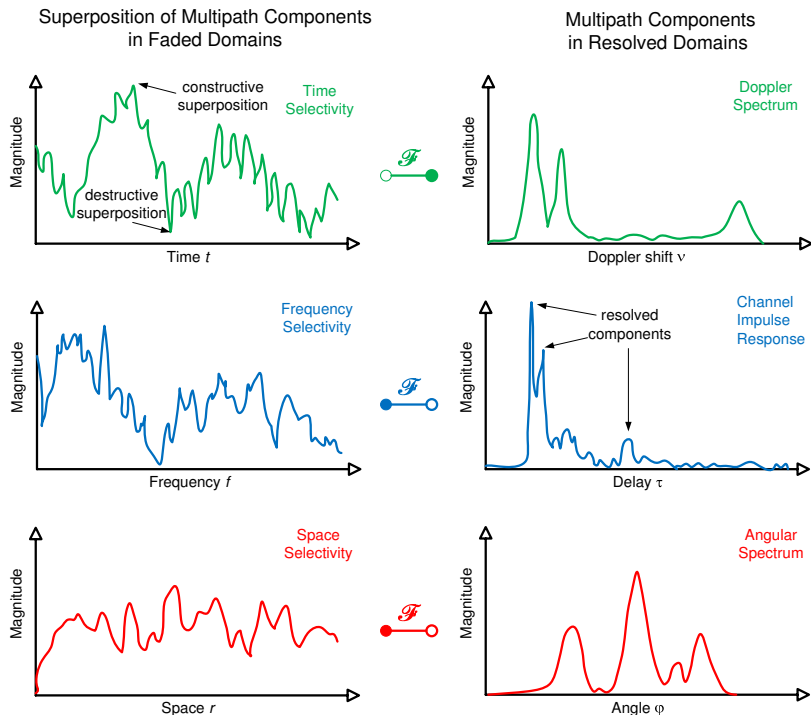


Figure 2.10: Faded vs. resolved domains (after Kattenbach [31]).

## 2.5.1 Auto-Correlation Functions and Power Spectral Densities of Jointly WSS Process

The system functions describing a radio channel are multidimensional in general case. The calculation of a correlation function increases number of variables for every with every considered dimension. Therefore, the correlation function accounting for all dimension doubles the number of independent dimension w.r.t. a system function.

$$R_{\underline{h}}(f_1, f_2, t_1, t_2, \vec{r}_1, \vec{r}_2) = E\left\{\underline{h}(f_1, t_1, \vec{r}_1) \cdot \underline{h}^*(f_2, t_2, \vec{r}_2)\right\} \quad (2.33)$$

In order to make correlation analysis tractable, a special class of Wide-Sense Stationary Uncorrelated Scattering (**WSSUS**) processes is typically analyzed.

### Jointly WSS (US) Process

The **WSSUS** terminology is introduced by Bello in [27], where only time and delay dependencies are considered. *Uncorrelated Scattering* was indicating that signal components arriving with different delays are uncorrelated. (An independent fading behavior for different components of band-limited channel is possibly caused by the irregularity of the scattering structures [32].)

When the spatial propagation dimension is analyzed, it would be more appropriate to address them as *jointly Wide-Sense Stationary (WSS)* in faded (selective) domains: (time, frequency, position), or *jointly uncorrelated* across resolved (spectral) domains: (Doppler, delay, wavevector). **WSS** property (Sec. C.2) reduces dimensionality of correlation function to half.

$$\begin{aligned} R_{\underline{h}}(\tau_1, \tau_2, \nu_1, \nu_2, \vec{k}_1, \vec{k}_2) &= E\{\underline{h}(\tau_1, \nu_1, \vec{k}_1) \cdot \underline{h}^*(\tau_2, \nu_2, \vec{k}_2)\} \\ &= 2\pi S_{\underline{h}}(\tau_1, \nu_1, \vec{k}_1) \delta(\tau_1 - \tau_2) \delta(\nu_1 - \nu_2) \delta(\vec{k}_1 - \vec{k}_2) \end{aligned} \quad (2.34)$$

Additionally, under **WSS** assumption favorable relations could be established between Auto-Correlation Function and *Power Spectral Density (PSD)*, as stated by Wiener-Khintchine Theorem (Sec. C.2):

$$R_{\underline{h}}(\Delta f, \Delta t, \Delta \vec{r}) = \mathcal{F}\{S_{\underline{h}}(\tau, \nu, \vec{k})\} \quad (2.35)$$

#### Validity of WSS Assumption

For short time intervals it is possible to assume that the physical scattering process generating the stochastic behavior changes only little, causing a **WSS** behavior of the short-term fading. This enables approximation of observed stochastic process with jointly **WSS** process within ranges of a few tens of wavelengths [32]. For the long-term variations (over large spatial extent) a nonstationarity of the random process that describes a radio channel is expected.

### 2.5.2 Relations between ACF Extent and Power Spreading within PSD

One of the basic properties of Fourier transformation is that inversely relates extent of signal between related transformation domains: if signal becomes narrower in one domain, its Fourier transform becomes wider in the transformed domain. “Therefore, the RMS width of a power spectrum can provide insight into the coherence of a channel: as the power spectrum widens in the transform domain, its autocorrelation becomes narrower and coherence decreases”. [28]

**Channel coherence** corresponds to extent of time, frequency or space where predefined level of **ACF** is kept.

**RMS Power Spread** describes dispersion of power over single resolved channel dimension  $x$ : Doppler, delay or wavevector (direction). Root-Mean-Square (**RMS**) power spreading can be determined from corresponding 1-D power spectrum densities. The generic expression for **RMS** spreading over dimension  $x$  is:

$$\sigma_x = \sqrt{x^2 - \bar{x}^2}. \quad (2.36)$$

The  $n^{th}$  non-central moment of  $x$

$$\overline{x^n} = \int_{-\infty}^{\infty} x^n \cdot p(x) dx \quad (2.37)$$

is estimated from normalized PSD:

$$p(x) = \frac{S(x)}{\int_{-\infty}^{\infty} S(x)dx}. \quad (2.38)$$

According to established duality RMS spread of PSD and corresponding coherence in ACF will be inversely related.

### 2.5.3 Decomposition of ACF/PSD

If channel does not exhibit changes over some dimensions they may be dropped from analysis. E.g., for fixed single-antenna receiver, channel has no spatial dependency and therefore joint time-frequency autocorrelation  $R_{\underline{h}}(\Delta f, \Delta t)$  or its **PSD** - *scattering function*,  $S_{\underline{h}}(\tau, \nu)$ , are sufficient for its characterization. Further, to represent transmission of narrowband signal toward fixed single-antenna receiver, it suffices to use time autocorrelation or Doppler power spectrum.

$$R_{\underline{h}}(\Delta t) = R_{\underline{h}}(\Delta f, \Delta t)|_{\Delta f=0} \quad (2.39)$$

$$S_{\underline{h}}(\nu) = \int_{-\infty}^{\infty} S_{\underline{h}}(\tau, \nu)d\tau \quad (2.40)$$

The nice symmetry between of jointly **WSS** process is kept during its decomposition, thus  $R_{\underline{h}}(\Delta t) = \mathcal{F}^{-1}\{S_{\underline{h}}(\nu)\}$  as illustrated in Fig. 2.11.<sup>†</sup> The analysis and characterization of multidimensional channel could be simplified if performed in **ACF/PSD** domains with reduced dimensionality. In the following we analyze the most important parameters of **1-D** ACF/PSD functions.

#### Power-Delay Profile

The Power-Delay Profile (**PDP**) shows how the average received power vary as a function of time delay,  $\tau$ . It is obtained by accumulating powers of  $S(\nu, \tau, \Omega_{Tx}, \Omega_{Rx})$  over all other resolved domains except delay.

$$S_{\underline{h}}(\tau|LSR) = \int \int \int S_{\underline{h}}(\nu, \tau, \Omega_{Tx}, \Omega_{Rx}|LSR)d\nu d\Omega_{Tx} d\Omega_{Rx} \quad (2.41)$$

The obtained function is related to *Local Stationarity Region* (**LSR**) where the multipath structure stays approximately unchanged. In stationary environments where interacting objects do not move this region is assumed to have extent of 20 to 40 wavelengths. Otherwise, it will be dependent on positions and velocities of the interacting objects. The extent of Local Stationarity Region (**LSR**) will be further analyzed in Sec. 4.3.1.

For an ideal system (zero maximum excess delay), the function  $S(\tau)$  would consist of an single impulse with weight equal to the total average received signal power. However, the typical propagation channel introduce a time spreading and have **CIR** that is different from Dirac delta function. The same applies to channels

<sup>†</sup>Fourier dependencies between single dimensional **ACFs** and Power Spectral Densities (**PSDs**) are given in Tab. 2.2.



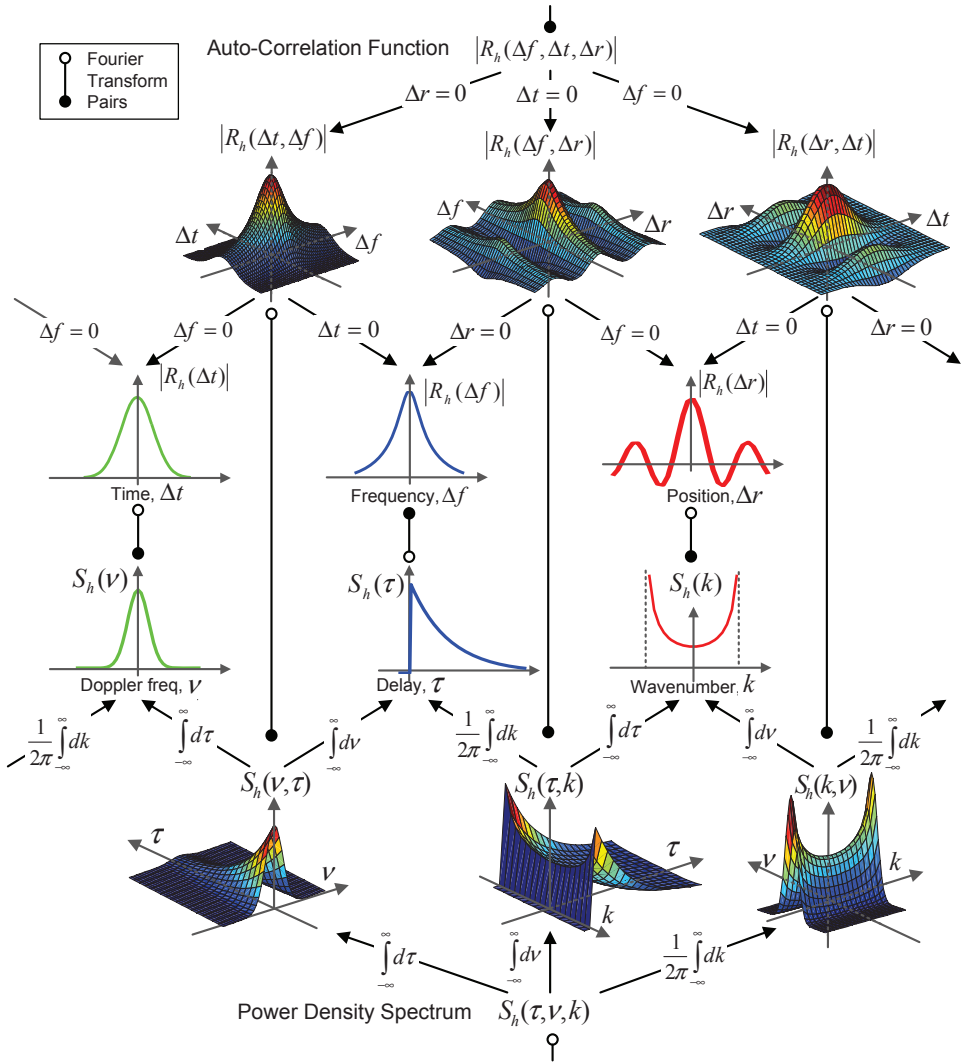


Figure 2.11: Relations between ACF and PSD functions (after Durgin [28]).

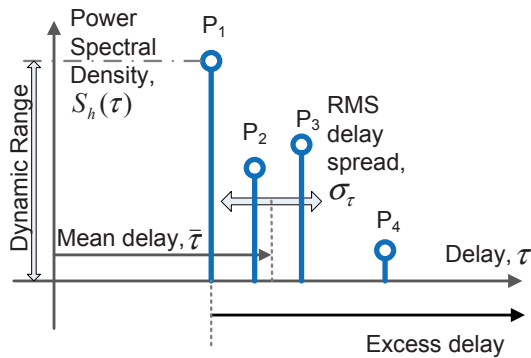


Figure 2.12: Power Delay Profile

exhibiting multipath propagation, where arrival time between the first and the last received component differ.

An extent of PDP depends on adopted magnitude range for relevant multipath components. Typically, the components weaker for 20 or 40 dB than the strongest component are considered as irrelevant due to limited dynamic range of receiver.

**Excess Delay** represents the additional propagation delay with respect to the first signal arrival at the receiver.

**Maximum Excess Delay (MED)** corresponds to the time between the first and last received component.

**Delay Spread** is determined according to (2.36) as the square root of the second central moment (standard deviation) of  $S(\tau)$ .

## Frequency Correlation Function

**Frequency Correlation Function (FCF)** shows the correlation between received signals that are spaced in frequency for  $\Delta f$ .

**Coherence Bandwidth**,  $B_c$ , represents a frequency range over which a signal's spectral components are similarly affected (gain and phase shift) by the channel. Similarity of channel's complex transfer function results in significant levels of auto-correlation function. The coherence bandwidth is typically determined as frequency range in which normalized **ACF** exceeds predefined level, e.g., 0.5.

For **WSS** channel **Frequency Correlation Function (FCF)** is inverse Fourier transform of **PDP**. It is, therefore, possible to establish approximate relation of coherence bandwidth and delay spread. If coherence bandwidth is defined as the frequency interval over which the correlation of channel's complex frequency transfer function is least 0.5, the coherence bandwidth is:

$$B_c \approx \frac{1}{5\sigma_\tau} \quad (2.42)$$

### Power Angular (Wavevector) Spectrum

Arriving direction of MPCs that propagate in Two-Dimensional (2-D) plain containing receiver can be described with single, azimuth angle. In 1-D angular power spectrum, the power of every multipath component is associated with its azimuth angle.

Under assumption of dense scattering environment, MPCs from all arriving angles have approximately equal power, i.e., power is uniformly distributed over all angles.

$$S_{\underline{h}}(\varphi) = \frac{P_{tot}}{2\pi} \quad (2.43)$$

The corresponding 1-D wavenumber power spectrum will be [28] [33]:

$$\begin{aligned} S_{\underline{h}}(k) &= 2\pi \int_0^{2\pi} S_{\underline{h}}(\varphi) \delta(k - k_0 \cos(\varphi - \varphi_R)) d\varphi \\ &= \frac{2P_{tot}}{\sqrt{k_0^2 - k^2}}, \end{aligned} \quad (2.44)$$

where  $\varphi_R$  represents direction of receiver movement.

**Angular Spread** expresses spreading of the power around a mean departure/arrival angle. Due to angular wrapping to domain  $[-\pi, \pi)$ , angular spread is defined as minimal value for all possible angular offsets of the original spectra [34].

### Spatial Correlation Function

In the case of dense scattering channel, the normalized Spatial Correlation Function (SCF) is [33]:

$$\frac{R_{\underline{h}}(\Delta r)}{P_{tot}} = J_0(k_0 \Delta r) \quad (2.45)$$

where  $J_0(\cdot)$  is the zero-order Bessel function of the first kind,  $k_0 = \frac{2\pi}{\lambda}$  and  $\Delta r$  is mobile terminal displacement. The channel impulse responses become statistically uncorrelated for a spatial displacement of  $\Delta r = 0.38\lambda$  since the first zero of  $J_0(x)$  occurs for  $x = 2.4048$  [35].

**Coherence Distance**,  $d_C$ , provides the measure of the maximum spatial separation over which the signal amplitudes have strong correlation. Within the *coherence distance* the channel appears to be static. The coherence distance is inversely proportional to angular spread.

### Doppler Power Spectrum

Doppler power spectrum describes the spectral spreading of a transmitted sinusoid (impulse in frequency) in the Doppler shift domain. In a typical multipath environment, components arriving from different directions produce different Doppler shifts. This effect on the received signal is seen as a Doppler spreading or spectral broadening of the transmitted signal frequency, rather than a shift.

For the case of the dense scattering channel in which mobile moves with constant velocity and therefore  $\nu = \frac{|\vec{v}|}{2\pi}k$  and  $\nu_m = \frac{|\vec{v}|}{2\pi}k_0$ , the Doppler power spectrum is equivalent to wavenumber power spectrum (2.45):

$$S_{\underline{h}}(\nu) = \frac{2P_{tot}}{\sqrt{\nu_m^2 - \nu^2}}, \quad (2.46)$$

The dense scattering model is not suitable for all environments: e.g., for the indoor propagation assumption of a flat Doppler spectrum is more appropriate [9].

**Doppler Spread** describes extent of the power spreading in Doppler frequency shift domain. For dense scattering channel Doppler spread,  $\sigma_\nu = \frac{\nu_m}{\sqrt{2}}$ , is proportional to maximum Doppler shift  $\nu_m$

Doppler power spectrum  $S_{\underline{h}}(\nu)$  is the Fourier of transform time correlation function  $R_{\underline{h}}(\Delta t)$ .

### Time Correlation Function

The time correlation function  $R_{\underline{h}}(\Delta t)$  describes the rapidity of the channel fading. This is the autocorrelation function of the channel responses to a single sinusoid (narrowband signal with  $\Delta f = 0$ ) taken at time instances  $t_1$  and  $t_2$  with spacing  $\Delta t = t_2 - t_1$ .

For an ideal time-invariant channel the CIR would be highly correlated for all values of  $\Delta t$  and  $R_{\underline{h}}(\Delta t)$  would be a constant function. In the case of dense scattering channel, the normalized Time Correlation Function (TCF) is

$$\frac{R_{\underline{h}}(\Delta t)}{P_{tot}} = J_0(2\pi\nu_m\Delta t) \quad (2.47)$$

where  $J_0(\cdot)$  is the zero-order Bessel function of the first kind, and  $\nu_m = \frac{|\vec{v}|}{\lambda}$  is maximal Doppler frequency shift for terminal moving with velocity  $\vec{v}$ .

**Coherence Time** ,  $t_C$ , is a measure of the expected time duration over which the channel's response is essentially invariant. Thus, the coherence time is equivalent to a time window over which the received signals have strong correlation.

At high frequencies the temporal incoherence is usually caused by motion of either the transmitter or the dominant scatterers. [28] For a constant velocity of motion and dense scattering channel, a coherence time is proportional to the coherence distance of (2.45). For WSS channel TCF is inverse Fourier transform of Doppler power spectrum, and coherence time is inversely proportional to the Doppler spread.

It is empirically shown in [36], that fine details and structure of the Doppler spectrum do not significantly affect temporal channel coherence. This approximation is valid for a small values of  $\Delta t$ , i.e. until significant correlation exist.

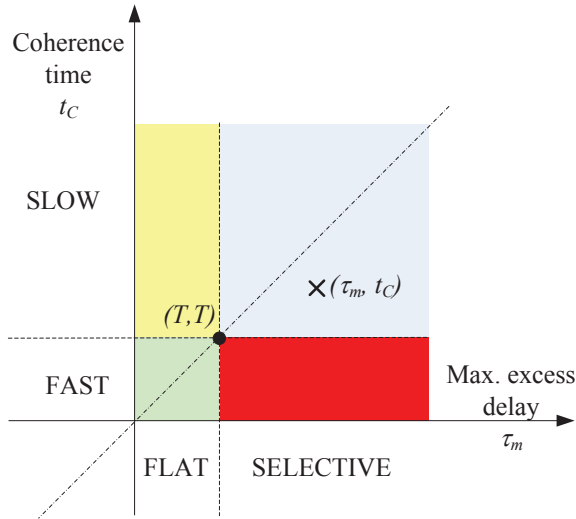


Figure 2.13: Classification of fading in wideband channel based on relation between symbol period  $T$  and channel parameters  $(t_c, \tau_m)$ . For different transmission rates (movement along diagonal line) the same physical channel can be perceived in a different manner.

## 2.5.4 Channel Classification

The absolute channel properties are quantified in previous sections by stochastic measures. However, the channel is used to transmit the data being structured in symbols and code words having certain duration in temporal domain. The impact of the channel to the transmitted data is related to the ratio of data signaling and channel parameters. Therefore, it is useful to introduce relative channel classification, that qualitatively describes channel effects to data transmission.

### Frequency Selective Channel

If Maximum Excess Delay (**MED**) becomes longer than symbol period then channel exhibits *frequency selective* fading. The extended spreading in delay domain reduces the coherence bandwidth in frequency domain. The coherence bandwidth of frequency selective channels is narrower than frequency bandwidth of signal, causing unequal (selective) modification of different spectral components. Otherwise, if a coherence bandwidth exceeds the bandwidth of transmitted signal, a channel fading is frequency *flat* or non-selective.

### Fast/Slow Channel

If channel show variation of **CIR** over time, the *coherence time* approximate interval without considerable changes. If this interval is shorter than symbol period, we have the *fast* fading channel, otherwise it is *slow* fading channel. Equivalently, for fast fading channels the width of Doppler spectrum exceeds the signal bandwidth.

From Fig. 2.13 it can be noted that choice of transmission rate, in general, selects among three of four channel fading manifestations. Possible combinations

are dependent of ratio between max. excess delay and coherence time: if  $\tau_m > t_C$  fading can not be *slow* and *flat*, and in opposite case it can not be *selective* and *fast*.

#### Underspread/Overspread Channel

Channels with  $\tau_m \gg t_C$  are classified as *overspread* (dominantly selective) channels. On an overspread channel, the total average energy in a received signal is divided among a large number of independently fading components. In the opposite case when  $\tau_m \ll t_C$  channel is *underspread* (dominantly slow).

#### Ergodic Channel

Sometimes fast and frequency non-selective (flat) channels are referred to as *ergodic*. [25] The reason for such categorization lies in the fact that, during transmission, a long enough code word experiences essentially all states of the channel, and hence it “averages out” the channel randomness. For such channels is therefore possible to determine average capacity. Otherwise, for *non-ergodic* channels statistic in the form of outage capacity has to be used.

### 2.5.5 Fading of Total Received Power in Narrowband Channel

The main issue with radio channel is its spatio-temporal variability. Starting from 1-D (narrowband) channel where only time-delay dimension was relevant, the classification of channel variations to small-scale and large-scale effects was introduced.

*Large-scale fading* represents the average signal power attenuation due to motion over large areas. This phenomenon is caused by changed impact of dominant objects in propagation environment (hills, forests, billboards, clumps of buildings, etc.) or propagation media (refractivity gradient, precipitation, etc.) that “shadow” a receiver in different manners.

*Small-scale fading* refers to the dramatic changes in signal amplitude and phase that can be experienced as a result of small changes (as small as a half-wavelength) in the spatial separation between a receiver and transmitter. A channel experiences *small-scale fading* when terminal traverses the distance greater then coherence distance, or elapsed time exceeds time coherence. The small-scale fading occurs in narrowband systems since the unresolvable multipath components add up destructively resulting in a substantial power loss.

This classification is exploited to simplify analysis and characterization of the radio channel by two independent random processes. The total fading effect to the narrowband received signal is therefore partitioned in two multiplicative random components that represent small and large-scale fading. When powers are expressed in [dB], due to properties of logarithm, multiplicative components become additive. Therefore spatio-temporal distribution of total received power is governed by 3 terms: single component that reflects average deterministic power attenuation, and two random components describing large- and small-scale fading.

**Mean Transmission Loss** is a function of distance, frequency, antenna heights, and propagation environment. In simple transmission models the average

received power  $\bar{P}_R$  (without impact of fading) decays exponentially with distance,  $d$ . Therefore,

$$\bar{L} = \frac{P_{Tx}}{\bar{P}_{Rx}} \sim d^n \quad (2.48)$$

In [dB] domain a transmission loss increases linearly with  $\log_{10}(d)$ , and its slope is determined by exponent  $n$ :

$$\bar{L}(d)[dB] = P_{Tx}[dBm] - \bar{P}_{Rx}[dBm] = \bar{L}(d_0) + 10n \log_{10}\left(\frac{d}{d_0}\right) \quad (2.49)$$

The reference distance  $d_0$  is taken in the far field of the antenna, and is typically 1 km for large cells, 100 m for microcells, and 1 m for indoor channels [9].  $\bar{L}(d)$  is the average transmission loss (over a multitude of different sites) for a given value of  $d$ . It is usually obtained by linear regression of  $L(d)$  versus  $d$  on a log-log scale which yields a straight line with a slope equal to  $10n$  dB/decade. The power loss exponent  $n$  equals 2 in free space, and increases when obstructions are present. However, in the presence of wave guided phenomenon (like urban streets),  $n$  can become lower than 2, due to coherent signal summation. Since the environment of different sites may be quite different for similar transmitter-receiver separations it is necessary to allow variations around the mean attenuation.

**Large-scale Fading**,  $X_\sigma$ , describes the deviation from the mean transmission loss. Therefore, the typical realization of a transmission loss  $L(d)$  equals

$$L(d) = \bar{L}(d) + X_\sigma. \quad (2.50)$$

For any value of  $d$ , the realizations of transmission loss  $L(d)$  in decibels, appear as normally distributed around  $\bar{L}(d)$ . Therefore additional term  $X_\sigma$  is represented with zero-mean Gaussian variable. Typically, a standard deviation of  $X_\sigma$  is in the range 6-10 dB.

**Small-scale Fading** describes rapid changes of signal envelope over space or time.

Variations of envelope are often described by Rayleigh process in order to account for near-worst fading statistic. The severity of small-scale fading is quantified with of *level-crossing rate* and *average fade duration*. [28]

### Power Budget and Performance of Radio Link

A narrowband SISO radio communication link is designed to account for all power attenuation causes: mean transmission loss, large- and small-scale fading [37]. These effects jointly determine the level of received power, and the chosen receiver design (i.e. its sensitivity) will correspondingly determine communication distance range and outage time of radio link.

In order to reduce channel outage (loss of service), radio-design includes so called fade margins. A fade margin is the difference, usually in dB, between the average received power and the minimum power level for reliable communications (receiver sensitivity) [28]. These margins could be independently determined for

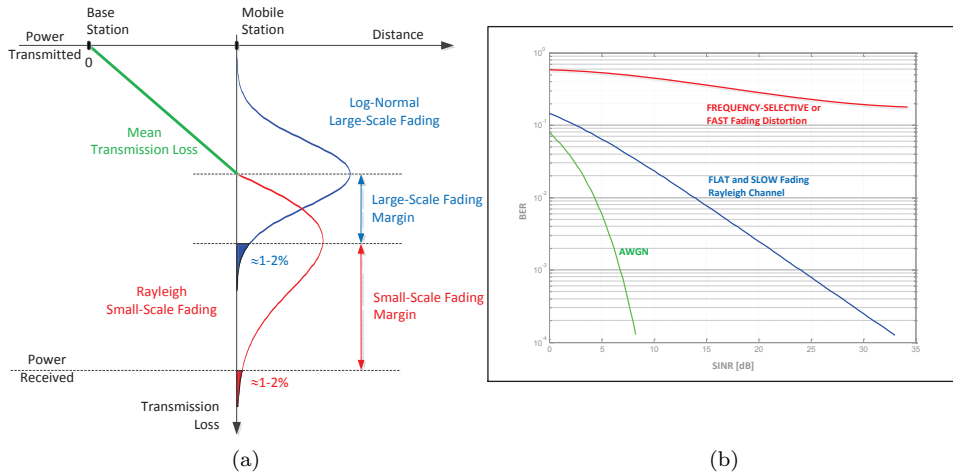


Figure 2.14: Fading channel: (a) Power Budget, (b) Error performance (after Sklar [37]).

large- and small-scale fading according to targeted percentage of outage, as indicated on Fig. 2.14.

If the **SISO** narrowband channel experiences the small-scale fading the system performance could be significantly impacted. The level of impairment will depend on relative fading manifestation. The flat and slow fading results in power loss: the targeted error rate requires larger Signal-to-Noise-Ratio (**SNR**). The frequency selective or fast fading can introduce *error floor* when further increase of **SNR** does not decrease error rate. In such cases, the performance can be improved only by advanced transmission techniques that will mitigate or reduce the fading induced distortion.

With increase of system bandwidth (i.e. reduction of symbol duration) the individual multi-path components become resolvable and their interference causes less severe fading of received power. The wideband systems, although exhibited to selective fading, rarely show significant power fading since different portions of spectra are not affected in the same manner. In this context coherence bandwidth determines the level of frequency diversity. In similar manner a spatial diversity will determine a performance of multi-antenna systems: the lower coherence distance results in reduced correlation of received signals in neighboring antennas. In this way, the realistic representation of channel conditions becomes crucial for system design and performance analysis.



## Chapter 3

---

# General Modeling Aspects

---

In order to maximize transmission efficiency, wireless communication systems are forced to exploit the spatial and temporal dimensions of the radio-channel to the full. The design and performance analysis of such system requires the channel model to reflect all relevant propagation aspects, which imposes serious constraints on the minimal complexity of the model. Since the chosen representation domain has the most important impact to the model structure and the resulting complexity, this chapter analyzes and compares different possible alternatives.

The relations between model concept and representation domain are discussed in the first section. The filtering approach for reproduction of observed correlation properties is elaborated in the second section. The section 3 considers assembling of sinusoids to represent the CIR. The reasoning behind hybrid models that combine the noise filtering and Sum-of-Sinusoids (SoS) is given in 4<sup>th</sup> section. For system design and performance evaluation, site-independent modeling with lower complexity is preferred. For this purpose, stochastic characterization of different radio-environment classes could be combined with geometry based propagation aspects. This results in the class of *geometry-based stochastic* channel models that are described in Sec. 3.5. In order to properly reproduce space-time channel evolution, this class of models uses either positioning of interacting objects in simulated environment or virtual positioning of MPCs in parametric domain. These approaches are shortly compared in 6<sup>th</sup> section. A development of empirical model that uses stochastic characterization of *Large-Scale-Parameters* (LSPs) is explained in Sec. 3.6.1. The last section presents the most important features of the WINNER channel model, which is representative of a geometry-based stochastic model governed by large-scale parameter statistic.

### 3.1 Relations between Model Concept and Representation Domain: Constituting (Resolved) vs. Faded

Although the final goal is quite clear: the model should reproduce the channel behavior, it is necessary to determine the appropriate domains for representation

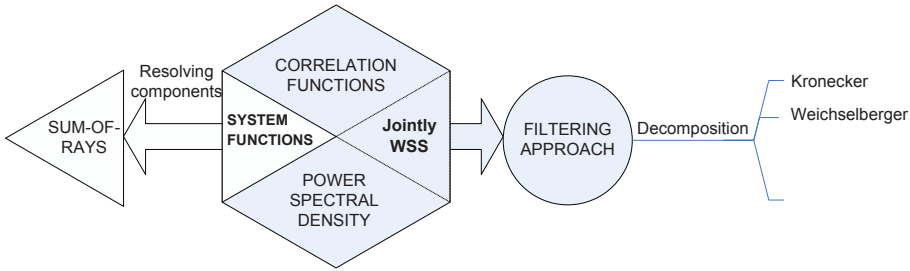


Figure 3.1: The modeling strategies: sum-of-rays versus filtering.

of the stochastic features and consequent channel synthesis. In Sec. 2.5 available representation domains are classified into selective (fading) domains and constitutive (resolved) domains. In the latter each multi-path component is identified with joint set of physical propagation parameters, that describe transmission of energy between transmitter and receiver. In faded domains, unresolved components are superimposed, producing fluctuations (fading). If we synthesize the channel as sum of MPCs (sometimes referred to as *rays* or *sinusoids*) we have to resolve their individual spatio-temporal properties and distribution of total power, and fit targeted statistic using deterministic constituents, i.e., MPCs. Alternative would be reproduction of observed fading statistic without use of identified constituting elements. The statistical properties could be extracted directly from faded domains in the form of probability density and correlation functions.

With increased resolvability (i.e. increased measurement/system bandwidth) the statistical approach has to be reconsidered since the number of interfering (unresolved) MPCs is reducing, which changes a statistic of fading. An example could be the IEEE 802.15.3a UWB channel [38] where several interfering (unresolved) components does not follow common (Rayleigh/Rice) fading distributions. In extreme cases, when all MPCs are resolved, there is no fading and the model parameters can not be related to its statistics. Even in that case, the channel is properly represented with MPCs constituents.

In cases where fading appears due to superposition of many MPCs, the faded domains  $(t, f, \vec{r}^{(u)}, \vec{r}^{(s)})$  are more appropriate for statistical modeling, since analytical probability distributions could be exploited to reduce model complexity. This avoids introduction of numerous MPCs only to reach “random” appearance of system functions. From the perspective of the stochastic modeling, radio-channel is the random process, whose properties could be captured from observed realizations. Since only few control parameters are necessary to describe standard distribution functions, complexity of this modeling approach is rather low.

However, the pure stochastic modeling shows limited flexibility in representing spatial channel dimensions that are important for MIMO transmission. From above arguments, the selection of a appropriate modeling method is dependent on the relative channel properties with respect to the considered transmission system (Sec. 2.5.4). In the following sections so called “filtering approach” and sum-of-rays method will be compared, Fig. 3.1. The first approach uses faded domains while second is based on resolved domains.

## 3.2 Filtering Approach

In narrowband **SISO** systems, discussed in Sec. 2.5.5, the (Rayleigh) **PDF** is used to describe the small-scale fading of signal envelope. This produces a channel model with parameters defining the probability distribution. However, for realistic representation it is necessary to account for correlation between consecutive realizations in space-time. This smoothing of independently generated realizations can be performed with appropriate filtering. If we assume jointly **WSS** process where **PSD** and **ACF** form Fourier transformation pair, design of filter targeting particular **ACF** can be also based on corresponding **PSD**.

If the targeted time selective behavior is quantified by correlation function  $R(\Delta t)$ , then corresponding Doppler spectrum is given as the Fourier transform:  $S(\nu) = \mathcal{F}\{R(\Delta t)\}$ . Rayleigh fading can be simulated by filtering complex White-Gaussian-Noise (**WGN**) with filter that is determined as the square root of the tap Power Spectral Density (**PSD**):

$$T_n(z = e^{j2\pi\nu T}) = \sqrt{S_n(\nu)}. \quad (3.1)$$

### 3.2.1 Correlation Tensor-Based Model for Selective Multidimensional Channels

The filtering approach has a significant complexity when many channel dimensions are relevant, and are represented jointly in the form of a channel tensor. The frequency selective **MIMO** channel observed in  $k^{\text{th}}$  time segment of width  $T_w$  and having  $M_{Tx}/M_{Rx}$  transmitting/receiving antennas, and  $N_f$  frequency bins can be represented by the channel tensor

$$\mathcal{H}_k \in \mathbb{C}^{M_{Tx} \times M_{Rx} \times N_f \times T_w}. \quad (3.2)$$

Assuming that the channel is block-wise stationary in time, it is possible to estimate a correlation tensor within each block consisting of  $T_w$  snapshots by averaging over time:

$$\hat{\mathcal{R}}_k = \frac{1}{T_w} \sum_{n=1}^{T_w} (\mathcal{H}_k)_{i_4=n} \circ (\mathcal{H}_k)_{i_4=n}^H \in \mathbb{C}^{M_{Tx} \times M_{Rx} \times N_f \times M_{Tx} \times M_{Rx} \times N_f}. \quad (3.3)$$

Here,  $i_4 = n$  indicates that indexing is performed with respect to  $4^{\text{th}}$  dimension of channel tensor, and  $\circ$  represents tensor outer product. The similar models of sixth-order wideband correlation tensor were proposed in [39] and [40]. The random channel  $\mathcal{H}_k$  having the same spatio-frequency correlation as observed channel can be synthesized by filtering a complex White Gaussian Noise (**WGN**) by square root of tensor  $\hat{\mathcal{R}}_k$ . Although, the required filter can be found by Higher-Order Singular Value Decomposition (**HOSVD**) of  $\hat{\mathcal{R}}_k$ , the process can be simplified by unfolding of the channel tensor prior to computation of the correlation matrix [39]:

$$\hat{\mathbf{R}}_k = \frac{1}{T_w} \sum_{n=1}^{T_w} \text{vec}(\mathcal{H}_k) \cdot \text{vec}(\mathcal{H}_k)^H \in \mathbb{C}^{M_{Tx} \cdot M_{Rx} \cdot N_f \times M_{Tx} \cdot M_{Rx} \cdot N_f} \quad (3.4)$$

In this case the square-root of matrix can be determined by eigenvalue decomposition

$$\hat{\mathbf{R}}_k^{\frac{1}{2}} = \mathbf{U}_k \cdot \mathbf{\Lambda}_k^{\frac{1}{2}}, \quad (3.5)$$

where  $\mathbf{U}_k$  is unitary and  $\mathbf{\Lambda}_k$  is diagonal matrix. The unfolded realization of synthesized channel is obtained as:

$$\text{vec}(\tilde{\mathcal{H}}_k) = \hat{\mathbf{R}}_k^{\frac{1}{2}} \text{vec}(\mathbf{G}), \quad (3.6)$$

where  $\mathbf{G}$  is independent identically distributed (i.i.d.) random matrix, whose elements are taken from circularly symmetric zero-mean complex Gaussian, with unit variance -  $\mathcal{CN}(0, 1)$ .

It could be recognized that empirical observation of channel with  $N_t$  snapshots provides  $K = \lfloor N_t/T_w \rfloor$  realizations of correlation tensor/matrix. The number of parameters in this model and therefore its complexity are proportional to the number of Tx and Rx antennas, frequency bins and independent temporal realizations  $k = 1, \dots, K$ .

### 3.2.2 Decomposition of Correlation Matrices

Often, the model complexity is reduced by ignoring correlation between different domains of the channel. This means that correlations between spatial, temporal and frequency domains are disregarded, and analyzed characterizations are performed independently for each dimension.

The Weichselberger model [41] introduces *vector decomposition* of MIMO channel  $\mathbf{H} \in \mathbb{C}^{M_{Tx} \times M_{Rx}}$  with so called *structural vector modes*. These modes can be determined from the full correlation matrix or from the one-sided (transmitting or receiving) correlation matrices. In the first case, the structural modes correspond to the singular vectors obtained by Singular Value Decomposition (SVD) of asymmetric correlation matrix

$$\mathbf{R}_H = E\{\mathbf{H}^* \otimes \mathbf{H}\} \in \mathbb{C}^{M_{Tx}^2 \times M_{Rx}^2}, \quad (3.7)$$

where  $\otimes$  denotes Kronecker product.

Alternatively, the necessary vector modes of Weichselberger's model can be estimated from eigenvalue decompositions of one-sided correlation matrices:

$$\mathbf{R}_{Tx} = E\{\mathbf{H}^H \cdot \mathbf{H}\} = \sum_{m=1}^{M_{Tx}} \lambda_{Tx,m} \cdot \vec{v}_m \cdot \vec{v}_m^H = \mathbf{V} \mathbf{\Lambda}_{Tx} \mathbf{V}^H \in \mathbb{C}^{M_{Tx} \times M_{Tx}}, \quad (3.8)$$

and

$$\mathbf{R}_{Rx} = E\{\mathbf{H} \cdot \mathbf{H}^H\} = \sum_{n=1}^{M_{Rx}} \lambda_{Rx,n} \cdot \vec{w}_n \cdot \vec{w}_n^H = \mathbf{W} \mathbf{\Lambda}_{Rx} \mathbf{W}^H \in \mathbb{C}^{M_{Rx} \times M_{Rx}}. \quad (3.9)$$

In this case the expansion with structured vector modes have a form

$$\mathbf{R}_H = \sum_{n=1}^{M_{Rx}} \sum_{m=1}^{M_{Tx}} \omega_{n,m} \cdot (\vec{v}_m \otimes \vec{w}_n) \cdot (\vec{v}_m \otimes \vec{w}_n)^H \in \mathbb{C}^{M_{Tx} \cdot M_{Rx} \times M_{Tx} \cdot M_{Rx}}, \quad (3.10)$$

and coefficients  $\omega_{n,m}$  are determined from projections

$$\omega_{n,m} = (\vec{v}_m \otimes \vec{w}_n)^H \cdot \mathbf{R}_H \cdot (\vec{v}_m \otimes \vec{w}_n). \quad (3.11)$$

From projection coefficients and vectors, the MIMO channel matrix can be synthesized by

$$\tilde{\mathbf{H}} = \sum_{n=1}^{M_{Rx}} \sum_{m=1}^{M_{Tx}} g_{n,m} \sqrt{\omega_{n,m}} \vec{w}_n \vec{v}_m^T = \mathbf{W}(\sqrt{\mathbf{\Omega}} \odot \mathbf{G})\mathbf{V}^T. \quad (3.12)$$

The matrices  $\mathbf{W} = [\vec{w}_1, \vec{w}_2 \dots \vec{w}_{M_{Rx}}]$  and  $\mathbf{V} = [\vec{v}_1, \vec{v}_2 \dots \vec{v}_{M_{Tx}}]$  are formed by stacking the Rx and Tx eigenvectors respectively. The operator  $\odot$  designates element-by-element (Schur) product. The entries of  $\mathbf{\Omega} = \omega_{n,m}$ , represent a coupling between Tx and Rx structured vector modes, while matrix  $\mathbf{G}$  contains normally distributed random variables  $g_{n,m}$ .

### Decoupling of Transmitting and Receiving Side of MIMO Link

The Kronecker model [42] ignores the coupling between transmitting and receiving antennas which is appropriate only for separable joint angular spectra [43]. The correlation matrix is expressed as Kronecker product of transmitting and receiving correlation matrices, (3.8) and (3.9):

$$\mathbf{R}_H = \frac{1}{\text{tr}\{\mathbf{R}_{Rx}\}} \mathbf{R}_{Tx} \otimes \mathbf{R}_{Rx} \in \mathbb{C}^{M_{Tx} \cdot M_{Rx} \times M_{Tx} \cdot M_{Rx}}. \quad (3.13)$$

As a consequence of this approximation is a poor reproduction of the channel capacity: it can be underestimated or overestimated, depending on the underlying structure of the reference channel [44]. According to the Kronecker model, a channel is synthesized by filtering the normally distributed random process  $\mathbf{G}$  in the following way:

$$\tilde{\mathbf{H}} = \frac{1}{\text{tr}\{\mathbf{R}_{Rx}\}} \mathbf{R}_{Rx}^{1/2} \cdot \mathbf{G} \cdot (\mathbf{R}_{Tx}^{1/2})^T = \mathbf{W} \left( \frac{1}{\text{tr}\{\mathbf{R}_{Rx}\}} \sqrt{\mathbf{\Lambda}_{Rx}} \mathbf{G} \sqrt{\mathbf{\Lambda}_{Tx}} \right) \mathbf{V}^T. \quad (3.14)$$

By comparing (3.12) and (3.14) one observes that the ‘‘coupling matrix’’ of the Kronecker channel is separable:

$$\sqrt{\mathbf{\Omega}_K} = \frac{1}{\text{tr}\{\mathbf{R}_{Rx}\}} \begin{bmatrix} \sqrt{\lambda_{Rx,1}} \\ \sqrt{\lambda_{Rx,2}} \\ \vdots \\ \sqrt{\lambda_{Rx,M_{Rx}}} \end{bmatrix} \begin{bmatrix} \sqrt{\lambda_{Tx,1}} & \sqrt{\lambda_{Tx,2}} & \dots & \sqrt{\lambda_{Tx,M_{Tx}}} \end{bmatrix} \quad (3.15)$$

### 3.3 Finite Sum-of-Rays Representation of CIR

Although instantaneous realizations of the channel may seem random, the underlying physical process can be described by deterministic means, which are addressed

in Sec. 2.4.2 as *structural parameters*\*. According to (2.18) the propagation channel can be approximated with finite sum of discrete MPCs which are positioned in delay, Doppler shift, and departure/arrival directions by means of delta functions. Since resolved and fading domains represent Fourier transformations pairs, delta-impulses from resolved domains correspond to complex exponentials in faded domains.

$$\begin{aligned}
\mathbf{H}(f, t, \vec{r}_{Tx}, \vec{r}_{Rx} | \mathbf{Q}) &= \mathcal{F} \{ \mathbf{h}(\tau, \nu, \vec{\Omega}^{Tx}, \vec{\Omega}^{Rx} | \mathbf{Q}) \} \\
&= \mathcal{F} \left\{ \sum_i \alpha_i \cdot \delta(\tau - \tau_i) \cdot \delta(\nu - \nu_i) \cdot \delta(\vec{\Omega}^{Tx} - \vec{\Omega}_i^{Tx}) \cdot \delta(\vec{\Omega}^{Rx} - \vec{\Omega}_i^{Rx}) \right\} \\
&= \sum_i \alpha_i \cdot \exp \left\{ -j[2\pi f \tau_i + 2\pi t \nu_i + k \vec{\Omega}_i^{Tx} \vec{r}_{Tx} + k \vec{\Omega}_i^{Rx} \vec{r}_{Rx}] \right\}.
\end{aligned} \tag{3.16}$$

Therefore, the obtained representation is also referred to as “sum-of-rays” (or sinusoids). Equivalently, this can be regarded as a multipath model with discrete components. Throughout this thesis it is considered that terms ray/sinusoid and single Multi-Path Component (MPC) are equivalent, and that they are characterized by the following parameters:

- polarimetric 2x2 matrix of complex gains  $\alpha$  - (2.19), describing jointly strength of the transmitted ray, carrier phase and rotation of polarization vector,  $\alpha_{i,j} = a_{i,j} e^{\phi_{i,j}}$ , where  $i$  and  $j$  denote the rows and columns of the matrix,
- propagation delay  $\tau$ , expressing the time elapsed between transmission and reception,
- direction of departure  $\vec{\Omega}_{Tx}$  is given with respect to Tx antenna ACS, defined by  $(\vec{r}_{Tx}, \vec{\Theta}_{Tx})$ ,
- direction of arrival  $\vec{\Omega}_{Rx}$  is given with respect to Rx antenna array CS, defined by  $(\vec{r}_{Rx}, \vec{\Theta}_{Rx})$ , and
- Doppler shift  $\nu$ .

### 3.3.1 Representation of Band-Limited Channels

From (2.22) it is clear that Rx antenna performs weighted summation of rays arriving at the same time instant (i.e. at reference propagation delay). In general there will be a continuum of delays, however due to limited system bandwidth there is a certain inertia that is proportional to the extent of CIR. This limits the speed of system response to individual MPCs, and due to superposition of their individual responses the fading occurs. This manifestation enables reduction of deterministic model with large number of MPCs into model with limited number

---

\*Since structural parameters describe physical propagation process, they implicitly define the structural vector modes of Weichselberger’s model. However, this pursuit is not further developed in the thesis.

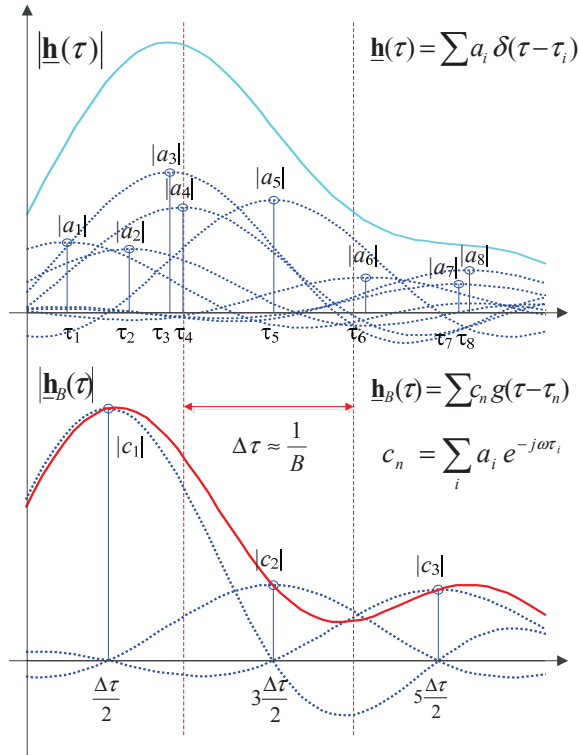


Figure 3.2: Bandlimited representation of propagation channel (after Vaughan [46]).

of equally-spaced delay taps, whose coefficients appear as random variables. The non-faded components of bandwidth unlimited model are called the *specular components* [9]. Due to limited bandwidth we are not able to resolve parameters of specular components from measurements. Instead several specular components has to be characterized jointly in the form of the *fading group*. Increased resolution results in lower number of specular components in the fading group.<sup>†</sup>

### Tapped Delay Model

The finite system bandwidth  $B$  limits the required resolution for the impulse response representation due to the smearing of  $\delta$ -pulses over a width  $\Delta\tau \approx \frac{1}{B}$  [32]. Depending on  $B$ , different smoothing of the impulse response  $g(\tau)$  applies, as illustrated in Fig. 3.2.

The efficient Tapped Delay Line (TDL) model of wideband communication system that includes Tx/Rx filters is proposed in [1]. This model uses a tap spacing equal to the inverse of the symbol rate.<sup>‡</sup> The time-variant tap coefficients are

<sup>†</sup>It is shown in [45] that the average area size of multipath component visibility (representing unfaded contribution) increases with the signal bandwidth.

<sup>‡</sup>It is demonstrated in [47] that samples at output of the Rx filter taken once per-symbol provide a set of sufficient statistic.

determined by projecting total CIR to the representation basis:

$$c_n(t) = \int_{-\infty}^{\infty} h(t, \tau) \cdot g(\tau - nT) d\tau \quad (3.17)$$

The basis functions are created by shifting Tx/Rx filter Impulse Response (IR)  $g(\tau)$  for integer multiple of symbol period.

After accounting for bandwidth limited resolvability, non-spatial wideband channel can be represented in the form:

$$\underline{h}_B(t, \tau) = \sum_{n=1}^N c_n(t) \cdot g(\tau - \tau_n) \quad (3.18)$$

where  $g(\tau)$  is impulse response of bandlimited filter, and  $c_n(t)$  represents sum of non-resolved components being in vicinity of  $\tau_n$ .  $c_n(t)$  is usually referred as gain of  $n^{\text{th}}$  tap.

**Total number of taps** The relevant number of taps is related to per-tap SNR. For maximum observable excess delay  $\tau_m$  the number of taps can be estimated as  $\lfloor B\tau_m \rfloor$ , with  $B$  denoting the signal bandwidth.

In the extreme case, a TDL consisting of single tap represents the frequency flat (narrowband) model. When the bandwidth of a transmitted signal increases to the extent of showing frequency-dependence, the model is extended with additional number of narrowband contributions that are distributed over delay dimension.

**Statistical properties of taps** Since tap gains  $c_n(t)$  experience frequency flat fading, they could be characterized by the envelope distribution and correlation function as described in Sec. 3.2. Although empirical data suggest that fading tap coefficients are Nakagami- $m$  distributed (Tab. C.1), for practical purposes the assumption of Rice or Rayleigh fading, as special cases of Nakagami- $m$  fading, is sufficient [32]. If direct line-of-sight (LoS) ray exist it usually have dedicated tap with nonfading amplitude but possibly changing phase [1].

Segmentation over delay domain is performed according to delay resolution which is inversely proportional to system bandwidth. As the consequence of disregarding channel delay resolution (i.e. channel bandwidth) and depending on equivalent system response, the tap coefficients  $c_n(t)$  may become correlated.

The TDL representation is suited for delay regions with densely spaced rays (including the continuous delay CIR), while the straightforward implementation, using the exact delay profile, is favorable when the real CIR consists of several rays with uncorrelated coefficients.

### 3.3.2 Synthetic Fading Models

The targeted “random” behavior of the channel can be reproduced by the SoS model. The modeling goal is to emulate targeted fading distribution and correlations functions, possibly with minimum number of components. When spatial



dependences (including polarizations) are omitted from (3.16) the SoS narrowband model reduces to:

$$\underline{\mathbf{h}}(t) = \sum_i a_i \cdot \exp(-j[2\pi t\nu_i - \phi_i]) \quad (3.19)$$

The free model parameters: gains, (Doppler) frequencies and phases of sinusoid functions could be generated randomly or computed by fitting the relevant statistical properties, typically PDFs and ACF [48]. It is also possible to combine these strategies and to calculate some sinusoid parameters, while randomly generating others. By considering different combinations of random and pre-calculated parameters it is possible to define  $2^3$  different classes of simulators that have different stationarity and ergodicity properties. It is shown in [49] that simulators having fixed gains and frequencies, and random phases are stationary and ergodic.

#### Deterministic SoS Approach

Deterministic approach tends to produce simple model (by minimizing number of sinusoids) that is statistically matching to (hypothetic, ideal) reference according to predefined criteria. The major issues are, therefore, selection/construction of reference model and selection of relevant criteria.

The reference model can be theoretic, not necessary related to reality. Typically, simple analytic models (Rayleigh, Rice, etc.) are selected for this purpose.

Many different methods are proposed for parameter calculation, having their specificities and disadvantages: slow-convergence, non-ergodicity, small period etc. According to [49], the  $L_p$ -Norm method [50] is the most suitable for deterministic SoS parameterization.

#### Jakes' Model

Jakes' model [51] is the classical example of an efficient SoS fading simulator. Its efficiency comes from the careful model structuring: the complexity of the straightforward realization with  $N$  low-frequency Doppler shift oscillators is reduced to  $M = \frac{1}{2}(\frac{N}{2} - 1)$ . The savings are attained by selection of symmetric arriving angles relative to the direction of movement and perpendicular direction. It was shown in [52] that this reduction leads to the generation of a non-stationary signal.

### 3.4 Mixed Modeling Approach

The optimal modeling approach can be found as combination of the noise filtering and sum-of-rays models. In order to perform a segmentation of the model to the noise filtering and SoS parts, it is necessary to identify which MPCs should be removed and replaced by the noise filtering. Effect of MPCs, having significant power and being well separated from other components in resolved domains, could be easily identified. Impact of such MPCs could be classified as dominantly deterministic. In cases where it is not possible to identify all present MPC but only results of their superposition are observable, the effect of such MPC is dominantly stochastic. The MPC belonging to the latter category are suitable candidates for replacement with filtering approach.

### 3.4.1 Classification of Multipath Components

According to the contained power and possibility of identification MPCs can be classified as [28]:

- *Specular* component corresponds to the single homogeneous plane wave: direct line-of-sight wave or strong reflection/diffraction. The single component does not introduce spread in resolved (delay, wavenumber) domains and therefore coherence in faded domains is infinite. Within local stationarity region the specular component is not subjected to fading.
- *Non-specular* component is collection of homogeneous plane waves that is represented by sum of differently phased specular waves. This component is similar to fading group, being introduced in Sec. 3.3.1 for representation of band-limited channels.
- *Diffuse* component can be defined as non-specular component where all constituent specular components carry power that is negligible compared to the total power of diffuse component. Therefore,

$$[\max_i \{A_i\}]^2 \ll \sum_i A_i^2 \quad (3.20)$$

where  $A_i = \|\alpha_i\|_F$  is magnitude of  $i^{th}$  MPC.

Diffuse non-specular components are observable in majority of propagation environments due to existence of numerous objects that re-scatter received energy. After numerous interactions, or after transversing long distances, the significantly attenuated components arrive from many directions in space. Although they individually have negligible power, due to their large quantity their joint contribution to the received power can be significant.

In a local area, the hybrid model expresses the channel as the sum of a finite number of specular waves and a single non-specular (possibly diffuse) component:

$$\begin{aligned} \underline{\mathbf{H}}(f, t, \vec{r}_{Tx}, \vec{r}_{Rx}) &= \sum_i \alpha_i \cdot \exp\left(-j[2\pi f\tau_i + 2\pi t\nu_i + k\vec{\Omega}_i^{Tx} \vec{r}_{Tx} + k\vec{\Omega}_i^{Rx} \vec{r}_{Rx}]\right) \\ &+ \underline{\mathbf{H}}_{\text{diff}}(f, t, \vec{r}_{Tx}, \vec{r}_{Rx}) \end{aligned} \quad (3.21)$$

The complexity of a channel representation can be reduced if minimum necessary number of specular components is used. For known amplitudes  $\{A_i\}$  the simple procedure is proposed in [28] that initially classifies all components as diffuse. The strongest components are then iteratively removed (one-by-one) until condition (3.20) is satisfied for all components being classified as diffuse.

In experimental channel characterization the assumption about known amplitudes is not satisfied, therefore another way for selection of the model order (i.e. number of significant specular components) was necessary. This will be further discussed within context of dedicated algorithms for estimation of specular MPC parameters in Sec. 4.2.

### 3.4.2 Rice Fading Model

The Rayleigh PDF can be extended to Rice distribution by addition of single dominant (typically line-of-sight) component. Therefore the Rice fading model represents an example of mixed modeling approach. The ratio of powers between the single dominant component and remaining (diffuse) components defines the K-factor of Rice distribution. This concept can be further extended by considering combinations of different number of specular components and inclusion/omission of diffuse part [28].

## 3.5 Geometry-based Stochastic Channel Modeling

When designing a wireless transmission system, it is necessary to evaluate its performance over a sufficient number of channel realizations. These could be generated by deterministic propagation models described in the Sec. 2.3, however, their high computational complexity prohibits the intensive link or system level simulations required during system design.

Thus, procedures with a lower computational complexity that could emulate a different radio-propagation environments are preferred. These requirements have led to the *Geometry-based Stochastic Channel Models* (GSCMs) where generated multipath components are not directly related to any particular (or very detailed) radio-environment. Instead, the channel realizations are determined as realizations of a multidimensional random process that characterises all aspect of physical plane-wave propagation.

The models of GSCM class combine stochastic and deterministic elements in order to offer good trade-off between complexity and performance (realism). These models deal with physical ray propagation, and therefore implicitly or explicitly include the geometry of the propagation environment.

The form of (3.16) supports the claim in [28] that the received baseband signal can be represented as superposition of “homogeneous” and “inhomogeneous” plane waves, i.e., complex sinusoids. Each of these sinusoids have real-valued amplitude, phase and polarization as indicated in Fig. 2.7. The phase of the sinusoid will change in time and frequency according to positions of transmitter, receiver and movement of Interacting Objects (IOs):

- $\phi_{i,j}$  - accumulated phase change between  $i$  and  $j$  polarizations due to antenna and scatterer interaction,
- $2\pi f\tau_i$  - phase change due to total distance traveled,
- $2\pi t\nu_i$  - phase change due to movement of IO,
- $\frac{2\pi}{\lambda}\vec{\Omega}_i \cdot \vec{r}$  - phase change due to motion of the transmitter or receiver.

The interaction with scatterers in the propagation environment produce multipath waves with different time delays and wavevectors. This results in both spatial and frequency selectivity. Temporal selectivity is caused by the motion of scatterers, that will result in the change of structural parameters  $\mathbf{p}_i$  in (2.20). This is included

into (3.16) through the conditioning on the spatio-temporal realization of the radio link,  $\mathbf{Q}$ , that determines the particular realization of structural parameters.

In general terminal/IO velocity (change of spatial position) is the cause of evolution of all ray parameters. However, it is often assumed that their movement in short observation period cause only change in carrier phase, therefore representing small-scale effects [5]. This concept corresponds to Local Stationarity Regions (LSRs) [8], i.e., “drops” where ray gains, propagation delays, DoD/DoA, are kept constant while only carrier phase evolves. The phase changes are, under given assumptions, related to terminal movement and resulting Doppler shifts.

### 3.5.1 Concept of Local-area Approximation

Based on concept of a local stationarity area it is possible to construct geometry-based stochastic channel model in which all structural parameters that describe the multipath profile are kept constant within “local-area”. In this model the parameters  $\mathbf{p}_i = (\tau_i, \nu_i, \boldsymbol{\alpha}_i, \vec{\Omega}_i^{Tx}, \vec{\Omega}_i^{Rx})$  of all MPCs, are constants and determined by the propagation that characterizes the local area. When terminal traverses the extent of “local-area” it enters the new local-area with new (again constant) structural parameters. The phases of MPCs, for all entries of polarimetric matrix contain random terms  $\{\phi_i\}$ .

According to the term “local-area” the class of *Stochastic Local-Area Channel (SLAC)* models is introduced in [28]. If compared with (3.16), these models are single-directional and do not consider MPC polarizations, but could be easily extended to equivalent form. The random phases in the Stochastic Local-Area Channel (SLAC) model are uniformly distributed over the interval  $[0, 2\pi)$ . The dependences between phase realizations (arbitrary, uncorrelated, or independent) will determine the level of model stationarity. The model with uncorrelated phases  $E\{\exp(j[\phi_k - \phi_n])\} = 0, k \neq n$  will be Wide-Sense Stationary (WSS), and independently distributed phases result in *Strict-Sense Stationary (SSS)* process [28]. The SLAC models are assuming frequency-space decoupling that is discussed in the following section.

### Frequency-Space Dependence

The geometry-based model uses finite sum of homogeneous plane waves to represent the frequency and space selectivity of the propagation channel. The frequency bandwidth and extent of space (i.e., LSR) in which the structural parameters does not change significantly are very important features of the Geometry-based Stochastic Channel Model (GSCM). Since frequency and spatial domains jointly impact amplitudes and phases of constituting MPCs it is necessary to consider joint limitation of frequency-space range in which approximation is valid. For known signal bandwidth this results in the measure of space where approximation is valid, i.e. with extent of the local area.

If a wavelength is expressed as function of carrier frequency and baseband signal frequency:  $\lambda = \frac{c}{f_c + \Delta f}$  than the phase term

$$\frac{2\pi}{\lambda} \vec{\Omega}_i \vec{r} = \frac{2\pi f_c}{c} \vec{\Omega}_i \vec{r} + \frac{2\pi \Delta f}{c} \vec{\Omega}_i \vec{r} \quad (3.22)$$

of (3.16) can be divided into purely spatial term (that does not depend on  $\Delta f$ ) and cross product term. If the cross product term causes the phase change lower than  $\frac{2\pi\Delta f}{c}\vec{\Omega}_i\vec{r} < \frac{\pi}{2}$  it can be neglected [28], and the structural parameters need not be updated. The resulting channel model uses summation of *band-limited* homogeneous plane waves that have uncorrelated scattering between frequency and space.

The maximum extent of local area over frequency and space i.e.  $\Delta f_{max} = \frac{B}{2}$  and  $\max(\vec{\Omega}_i\vec{r}) = \frac{L_A}{2}$  gives bandwidth-distance relation

$$L_A < \frac{c}{B}, \quad (3.23)$$

where  $c$  designates the speed of light. Thus, the spatial range where multipath profile representation can be considered constant reduces for the higher signal bandwidth. The extent of  $L_A$  is related to the signal bandwidth only for channels that exhibit joint space-frequency selectivity: cross term vanishes for narrowband channel or stationary receiver.

### 3.5.2 Classification of Radio Environments

The basic classification of radio environments can be performed by considering general deployment assumptions (e.g. above or below the rooftop), and general characteristics of the environment itself (indoor, outdoor, etc.). Positions of terminal in respect to environment are also relevant since they change the interaction pattern and determine the coverage range.

The radio environments could be additionally classified according the density of a significant scatterers, and corresponding regularity of MPC distribution. [32]. Existence of large number of buildings in town centers increases possibility of multiple interactions causing the large number of strong MPCs. On the other hand, a shadowing from buildings can also strongly attenuate all contributions. This results in quite irregular distribution of observed MPCs in delay-directional domains. In open areas, with lower density of strong scatterers the direct path occurs with higher probability due to less shadowing, and multipath profile changes less abruptly. In hilly and mountainous areas, the strong components with longer delays could appear due to reflection from the mountain/hill slopes.

In this way the multitude of possible configurations can be reduced into relatively small number of classes. Although this classification is very coarse, with high level of abstraction, it allows radio-network planners to deal with a quite a low number of a typical cases, that are usually referred to as *propagation scenarios*. This approach allows *scenario-based* modeling approach in which the *generic* channel model is used to represent the multiple scenarios.

**Scenario based modeling** assumes that observed stochastic properties are “stable” when complete environment is characterized jointly. This means that all collected data is used together for extraction stochastic parameters. This is typical approach for the state of the art channels models that are analyzed in this theses. Alternative would be to divide the environments into sub-classes and perform their separate characterization. E.g. the results of Cross-Polarization Ratio (XPR) analysis in

[53] indicate different behavior for corners and streets in the same measurement environment (city).

### 3.5.3 Clustering of MPCs

The concept of *cluster* is introduced to reflect observed energy grouping in directional and delay domains. Among many clusters definitions this formulation seems the most complete: “the wave components behaving similarly, in terms of angular and delay evolution as function of receiver location, were considered to belong to the same cluster” [54]. Therefore, in the context of this thesis cluster represents collection of MPCs having similar structural parameters, that also evolve in ST in the similar manner. Therefore, a cluster is not necessarily related to the single interacting object, but to group(s) of co-located objects.

The goal of clustering is not just multi-dimensional classification of MPCs to the finite number of groups, but representation of a phenomena observed in physical propagation. Influence of physical clustering in directional domains becomes relevant for beamforming, while clustering in in the delay domain influences the design of receivers or equalizers [55].

The clustering of MPCs, luckily, additionally simplifies construction of the channel model [56], [57].

The LoS component, accompanied with reflections in the vicinity of transmitter and receiver could be identified as LoS cluster. When present, the LoS cluster is dominant and significantly impacts the channel and its statistic.

## 3.6 Stochastic Driving of Multipath Model

The stochastic generation of multipath can be done in several different forms. We would distinguish two classes according to the use of the scattering (or interacting) objects during the physical model synthesis. One possibility is to place all *interacting objects* that contribute to multipath propagation in a 2-D/3-D coordinate system. An alternative would be to fully remove scatterers from the model synthesis. In this case multipath components are no longer related to particular scatterers, but are generated in the *parametric domain* instead. The term “parametric” relates to the parameters of multipath components as given by (2.20).

### Positioning of Interacting Objects in Real Space

The scatterers are placed in certain geographic area around transmitter and/or receiver. According to chosen 2-D area it is possible to distinguish a elliptical, models with one or two rings, disk models, etc. [58] If 3-D distribution is modeled then solid figures are used as in the double-cylindrical model [59]. These models typically categorize the MPCs according to number of interactions: none (LoS (direct) component), single, double, multiple. Apart from the area/volume containing IOs, the scatterer density should be properly determined in order to appropriately represent the targeted statistic features. E.g. the time correlation will be implicitly determined by the spatial distribution of scatterers, i.e. Doppler spectrum will be determined by arriving directions.

The interacting objects could be abstracted as multipath clusters like in the COST 273 model [60]. By assigning *visibility regions* [61] to these clusters, a simplified ray-tracing engine is obtained. The randomness in this approach is attained by random selection of visibility regions and the intra-cluster structure.

#### Virtual Positioning of MPCs in Parametric Domain

In general, distribution of scatterers to fit statistical properties of multipath profile is not the simplest approach to stochastic driving of **GSCM**. If double-directional concept is used, than the propagation environment can be described from perspective of transmitting and receiving antenna. The interactions with scatterers, are in this approach replaced by virtual positioning of **MPCs** in parametric domain. As consequence, these models deal with the virtual clusters for which relations between departure/arrival directions and delay are not established by principles of geometrical optics, but randomly.

Typical representatives are the Spatial Channel Model (**SCM**) [62], the channel model developed in the **WINNER** project [5], and the reference model for evaluation of International Mobile Telecommunications (**IMT**)-Advanced radio interface technologies [63]. The stochastic equivalence with the realistic radio propagation environment is a crucial assumption behind Geometry-based Stochastic Channel Model (**GSCM**). Within the **3GPP SCM** and **WINNER** models, the global properties of the underlying stochastic process are expressed by Large-Scale Parameters (**LSPs**), describing the distribution of the transmitted power over different dimensions of the channel.

### 3.6.1 Usage of the Large-Scale Parameters for Channel Characterization

The consequence of the environment abstraction introduced by parametric domain synthesis is that the evolution of a space-time model can not be implicitly given by relative distances of scattering objects. Instead, the channel dynamic is represented by correlated realisations (over space-time) of so called *Large-Scale-Parameters* (**LSPs**). The term **LSPs** is used to denote a group of channel parameters that typically experience notable change only over distances exceeding several wavelengths. In these models, individual multi-path components are described jointly by clustering them and then describing the global position of clusters in the multidimensional space with aid of **LSPs**.

(Dis)appearance or reallocation of significant clusters/**MPCs** will effect the marginal (e.g. delay and directional) spread parameters and thus they could be exploited for abstraction of large-scale channel behavior. The main role of the **LSPs** is, therefore, to describe the joint distribution of the **MPC** power over different domains (direction, polarization, delay, Doppler, etc.) and additionally to describe space-time channel evolution. These parameters are capturing gradual changes in the structure (angles, delays, powers . . .) of multipath (opposite to small-scale signal fading due to interference between multipath components). The set of relevant **LSPs** established within the **SCM/WINNER** models is listed in Tab. 3.1<sup>§</sup>.

<sup>§</sup>Doppler shift is not explicitly parameterized, but for a given velocity vector it will be implicitly determined by the directions of departure and arrival.

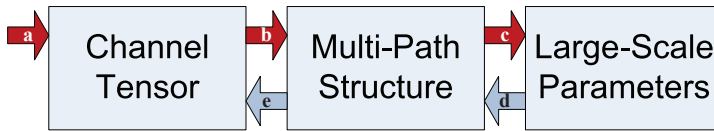


Figure 3.3: Generation of empirical, scenario-based multipath channel model [64]:

- a** *Multidimensional channel sounding;*
- b** *High-resolution estimation of joint MPC parameters;*
- c** *Statistic characterisation of LSPs and their space-time dependencies;*
- d** *Guided random positioning of MPC in parameter space, according to random realization of multivariate LSP process;*
- e** *Determination of antenna array response to given multi-path structure.*

The Large-Scale Parameter statistics is obtained from **MIMO** channel measurements and appropriate post processing procedures. Using the concept of correlated random **LSPs** it is easy to reproduce stochastic properties being observed during channel sounding and therefore this enables the straightforward scenario-based representation. By performing the measurement experiment with particular antenna deployment defining the scenario, it is possible to develop an empirical multipath model. This process is illustrated in Fig. 3.3.

Empirically obtained probability density functions of **LSPs** are approximated with simple analytical distributions. The relevance of obtained model will depend on gathered **LSP** realizations: in order to claim that the model represents the whole urban scenario, it is necessary to perform extensive measurements in multiple corresponding environments. If so, it is expected that model predictions will be accurate for other environments too.

Within the modeling context **LSPs** govern evolution of the synthesized channel, however their significance is not limited to that purpose only. Since **LSPs** show strong correlation with system performance indicators (e.g. Bit Error Rate (**BER**)) they could be employed for system performance evaluation or adaptation of transmission parameters on radio-link [65].

### 3.7 WINNER Channel Model

The WINNER Channel Model (**WIM**) is a generic model, whose scenario-specific parameters are determined from extensive wideband **MIMO** radio-channel measurement campaigns and results found in the open literature. The **WINNER** wideband **MIMO** radio channel model ([66], [67], [68], [5]) has been developed in the course of the **IST-WINNER**<sup>¶</sup> project [69] as a part of a system-level test-platform. The model was developed in order to provide a reliable tool for estimation of system performance, covering frequencies in the range from 2-6 GHz and bandwidths up to

<sup>¶</sup>The Wireless World Initiative New Radio (**WINNER**) project [69] was conducted in three phases (I, II, +) from 2004 until 2010, with the aim to define a single ubiquitous radio access system concept, scalable and adaptable to different short range and wide area scenarios.



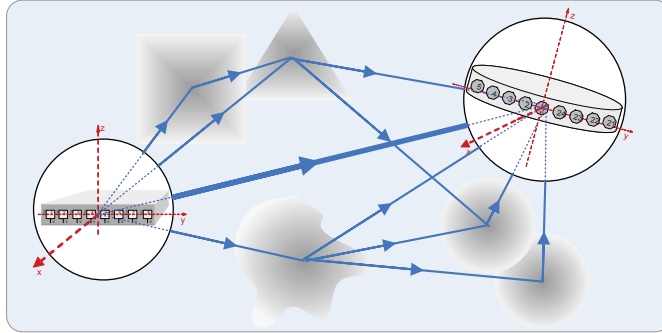


Figure 3.4: The single realization of the modeled MIMO channel.

100 MHz in different types of propagation environments. The WINNER Channel Model (**WIM**) was developed starting from the Spatial Channel Model (**SCM**) [34]. At first, a backward compatible extension toward higher bandwidths was provided (Spatial Channel Model Extended (**SCME**), [66]), but later, compatibility was abandoned and the model was improved in many aspects (**WIM1**) [70].

The **WIM** offers a complete channel model description in a sense of large-scale as well as small-scale effects in **MIMO** radio-channel for Beyond 3G (**B3G**) system designs. **WIM** is a generic model, whose scenario-specific parameters are determined from **MIMO** radio channel-sounding [5]. The **WINNER** generic model can describe an infinite number of propagation environment realizations for single or multiple radio links, for all the defined scenarios, and for arbitrary antenna configurations, with one mathematical framework by using different parameter sets.

### 3.7.1 Structure of the WINNER Channel Model

In **WINNER** channel model large-scale as well as small-scale effects of **MIMO** radio-channel (with  $S$  transmitting and  $U$  receiving antennas) are reflected in channel matrix:

$$\mathbf{h}_{U \times S}(t, \tau) = \begin{bmatrix} \underline{h}_{1,1}(t, \tau) & \cdots & \underline{h}_{1,S}(t, \tau) \\ \vdots & \ddots & \vdots \\ \underline{h}_{U,1}(t, \tau) & \cdots & \underline{h}_{U,S}(t, \tau) \end{bmatrix}, \quad (3.24)$$

where  $\underline{h}_{u,s}(t, \tau)$  represents time-dependant channel impulse response between  $s^{th}$  transmitting and  $u^{th}$  receiving antenna.

**WIM** is a double-directional [26] geometry-based stochastic channel model, in which a time-variable channel impulse response is constructed as a finite sum of Multi-Path Components (**MPCs**) which are conveniently grouped into clusters.

#### Geometry Aspects

The constituting **MPCs** are characterized by departure (from **Tx**) and arriving (to **Rx**) directions, propagation delay and power. Channel realizations between

transmitter antenna element  $s$  and receiver antenna element  $u$  are generated by summing contributions of  $N$  clusters, each having  $M$  rays:

$$\begin{aligned} \underline{h}(t; \tau) = & \sum_{n=1}^N \sum_{m=1}^M \vec{F}_s^T(\vec{\Omega}_{n,m}^{Rx}) \cdot \boldsymbol{\alpha}_{n,m} \cdot \vec{F}_u(\vec{\Omega}_{n,m}^{Tx}) \cdot \\ & \cdot \exp j2\pi\nu_{n,m}t \cdot \delta(\tau - \tau_{n,m}) \end{aligned} \quad (3.25)$$

The superposition (3.25) of specular paths, with different propagation delays  $\tau_{n,m}$ , results in the correlation between antenna elements and temporal fading with a geometry dependent Doppler spectrum.

In **WIM** necessary MPC (low-level) parameters are calculated from probability distributions. This applies to all model parameters, except transmitting and receiving antenna gains which are deterministic and related to the chosen antenna arrays. Although **WINNER** uses double-directional propagation modeling approach that should be completely antenna independent, a generation of channel outputs requires antenna embedding [7]. The complex, polarimetric response of an element in the antenna array is given by (2.31). During the **WINNER** Phase II the suitable polarimetric representation for 3-D antenna arrays is provided [71] and distributions of elevation angles are provided for indoor scenarios [68], [5].

An influence of the environment to the orthogonal wave polarizations is described by Cross-Polarization Ratios (**XPRs**). Random **XPR** realizations,  $\kappa$ , are used for the construction of 2x2 matrix  $\boldsymbol{\alpha}_{n,m}$ . Additionally, elements of this matrix incorporate complex MPC gains: all MPCs in cluster have the same power and random (independent) uniformly distributed phases  $\Phi$ .

$$\boldsymbol{\alpha}_{n,m} = \sqrt{\frac{P'_n}{M}} \begin{bmatrix} e^{j\Phi_{n,m}^{vv}} & \sqrt{\kappa_{n,m}} e^{j\Phi_{n,m}^{hv}} \\ \sqrt{\kappa_{n,m}} e^{j\Phi_{n,m}^{vh}} & e^{j\Phi_{n,m}^{hh}} \end{bmatrix} \quad (3.26)$$

Term  $e^{j2\pi\nu_{n,m}t}$  in (3.25) describes changes of ray phases that are consequence of terminal movement, and it is used to simulate small-fading effects.

An evolution of MPC parameters cannot be based on the ray-tracing since *positions of scattering clusters are unknown*. Instead, their positions are stochastic as are their evolutions.

### Stochastic Aspects (Randomness and Correlations)

The positions of MPC clusters in multidimensional space are determined by Large-Scale Parameter (**LSP**) realizations. **LSPs** are controlling the distribution of the power (spreading) over the individual dimensions of the channel, as indicated in Tab. 3.1. In **WIM** **LSPs** are reflecting physical propagation measures, being commonly used to characterize power related distributions in wideband/narrowband radio-channels. **WINNER** model uses up to 8 **LSPs**: distributions of departure and arrival angles are dependent upon *Azimuth and Elevation Spreads on Departure (ASD/ESD)* and *Arrival(ASA/ESA)*, distribution of delays is controlled by *Delay Spread (DS)*, *Shadow Fading (SF)* standard deviation is used to describe deviation from average transmission loss, *Ricean K-factor* is expressing the ratio of powers

Table 3.1: Large-scale parameters of WINNER model.

LSP Name	Acronym	Power distribution:
Shadow Fading	SF	around mean transmission loss
Delay Spread	DS	over delay domain
angular Spread	ASD/ASA ESD/ESA	over angular domain: - at Departure and Arrival - over Azimuth and Elevation
narrowband K-factor	K	betw. LoS and NLoS clusters
CROSS Polar. Ratio	XPR	betw. co- and cross-polar MPCs

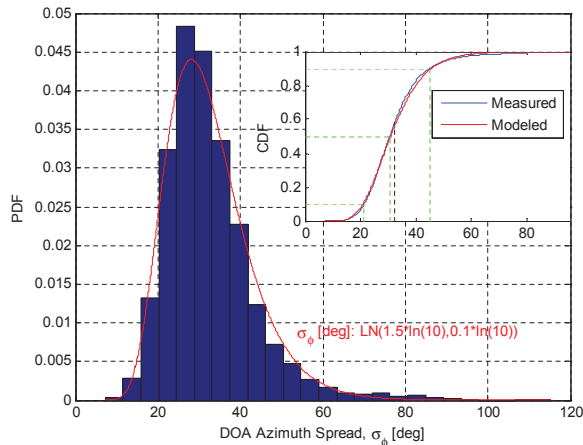


Figure 3.5: Probability distributions of arriving angles, obtained from RIMAX high resolution data analysis.

between line-of-sight (LoS) and remaining paths, and XPRs are used to quantify interaction between orthogonal polarizations.

Within the modeling context LSPs are exploited to govern the evolution of the synthesized channel. Experimental distributions of LSPs are determined from measurement data, and suitable analytical models are introduced. In this way whole channel model is finally parameterized with few parameters of LSP distributions. In WINNER modeling, most often, log-normal model distribution is used, as shown in Fig. 3.5 for distribution of arrival angles.

The generic WINNER model is a stochastic model with two levels of randomness. At first, large-scale parameters (LSPs) like shadow fading, delay and angular spreads are drawn randomly from tabulated distribution functions. Next, small-scale parameters describing rays (plain waves) like delays, powers and directions of arrival and departure are drawn randomly according to tabulated distribution functions and random LSPs. At this stage, the geometric setup is fixed and the only free variables are the random initial phases of the scatterers. By (randomly) picking different initial phases, an infinite number of different realizations of the model can be generated (Fig. 3.4).

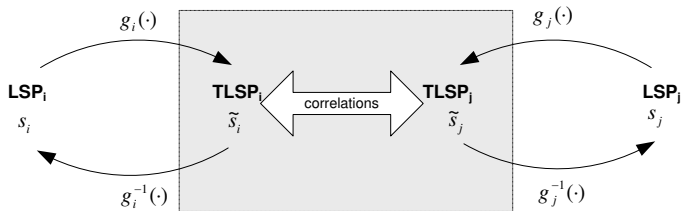


Figure 3.6: LSP are characterized and synthesized in transformed domain.

The entire process of WIM channel synthesis can be done in three hierarchy levels [72]:

### 1. Large-Scale Parameters

On top level, Large-Scale Parameter (LSP) listed in Tab. 3.1 are drawn randomly from tabulated log-normal PDFs. With the exception of XPR, all other LSPs are generated as *correlated* random variables.

Since spatial, temporal, frequency, and power domains of MIMO channel are not independent, it is necessary to quantify observed interdependence. For that purpose the cross-correlation coefficient between different LSPs is used. A similar approach was proposed in Spatial Channel Model (SCM) [62] to correlate parameters of the single link (link-level correlations). Additionally to SCM, WIM extends considered correlations to multiple links with the common Base Station (BS), Fig. 6.9. The relations of link-level and distance-based intra-cell correlations of WIM LSPs are illustrated in Fig. 6.10 and analyzed in Sec. 6.3.3.

In WINNER channel model, both auto-correlations and cross-correlations of LSPs are reproduced by correlating realizations of independent Gaussian random processes in so-called “transformed domain”.

**Transformed LSP Domain** The WINNER model investigates LSP distributions and their correlations in transformed domain [5] where normal distributions for all transformed LSPs are assumed. For log-normally distributed LSPs (delay and angular spreads) the mapping  $\tilde{s} = g(s) = \log_{10}(s)$  is applied (Fig. 3.6). The remaining LSPs (SF, XPR, K-factor) have Gaussian distributions when expressed in [dB]. The WINNER tables specify marginal (per-dimension) TLSP distributions with mean and variance parameters  $(\mu_i, \sigma_i)_{i=1, \dots, k}$  and matrix of correlation coefficients  $\boldsymbol{\rho} = [\rho_{i,j}]_{i=1, \dots, k; j=1, \dots, k}$ . The entries of this matrix express pair-wise correlations of the LSPs  $x_i$  and  $x_j$  in the form of the correlation coefficient:

$$\rho_{i,j} = \frac{\text{Cov}[x_i, x_j]}{\sqrt{\text{Cov}[x_i, x_i] \text{Cov}[x_j, x_j]}} = \frac{\sigma_{i,j}^2}{\sigma_i \sigma_j} \quad (3.27)$$

where  $\sigma_{i,j} = \text{Cov}[x_i, x_j] = \text{E}[(x_i - \text{E}[x_i])(x_j - \text{E}[x_j])]$ . Fig. 3.7 shows marginal distributions of delay spread in transformed domain for all WIM reference scenarios having Non Line-of-Sight (NLoS) propagation and additionally includes the maximum likelihood estimate of normal distributions for Ilmenau and Dresden measurements, which will be discussed in the following sections.

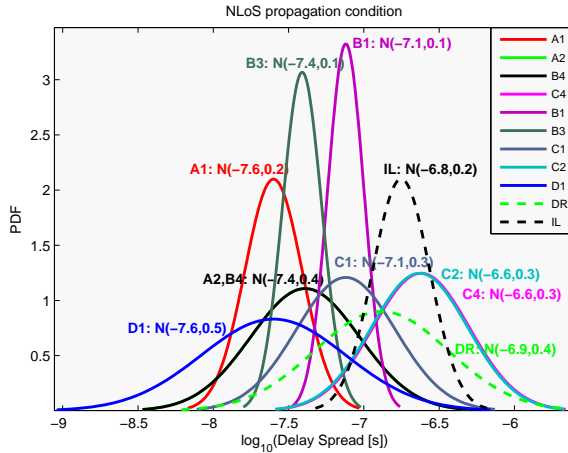


Figure 3.7: Delay spread PDFs in transformed domain.

## 2. MPC Cluster Centroids

On the second level, cluster centroid parameters are determined. Since radio-channel is non-stationary, probability distributions of cluster parameters are also time dependent. In WINNER channel modeling these distributions are approximated with probability distributions (exponential or normal) that are fully parameterized by the first and second statistical central moments. Example, showing fitting of experimentally determined PDF of MPC propagation delays and corresponding exponential model is given in Fig. 3.8. In this way, the probability distributions would be time-varying if their control parameters are changing. Parameters that are controlling probability distributions of Cluster Centroid (CC) parameters are belonging to the LSP group: Delay Spread (DS) controls decay for exponentially distributed CC delays, while Angular Spread (AS) controls dispersion of CC DoD/DoA having wrapped Gaussian distribution (Sec. C.4.1).

For the sake of the simplicity, the cluster characterization is simplified in SCM/WIM. Therefore, only cluster centroid (CC) parameters are drawn randomly from tabulated marginal distributions and all clusters share the same (scenario dependent) intra-cluster angular spread (CAS). Additionally, irrespective from WIM scenario, intra-cluster delay spread (CDS) can be either 0 or 3.9 ns.

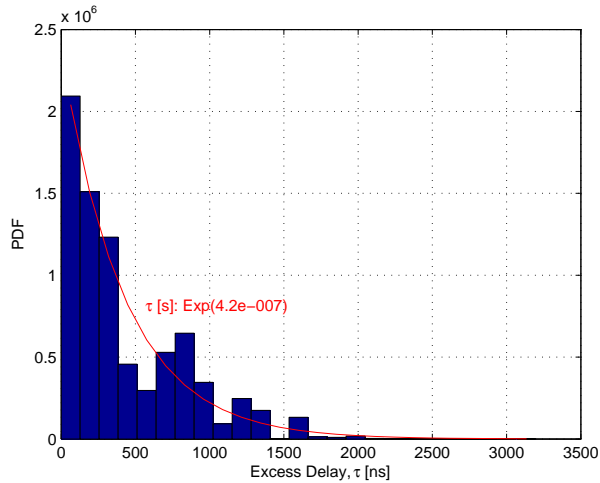


Figure 3.8: Distribution of excess delays, obtained from *RIMAX* high resolution data analysis.

### Frequency Correlation Function and Intra-Cluster Delay Spread

The clusters identified from measurements are, in general, dispersed in angular and delay domains. In order to simplify model and to establish straightforward relation to Tapped Delay Line (TDL) model, *SCM/WIM1* have introduced Zero Delay Spread Clusters (ZDSCs). Since WINNER Channel Model is targeting much broader frequency bandwidths, the total number of identified ZDSC clusters (and paths) in *WIM1* was larger than for *SCM*.

Dispersion in delay domain was firstly introduced in *SCME* [66] to account for higher bandwidths and to reproduce the proper level of the frequency correlation. In [70] it is shown that *SCME* with intra-cluster delay spread shows similar frequency correlation as *WIM1* based on ZDSC, however the total number of paths was considerably lower in the *SCME* case. Since disregarding of CDS increases frequency correlation, ZDSC concept is not fully suitable for wideband models. As a compromise two strongest clusters are spread in WINNER Channel Model Phase II (*WIM2*), by using the constant CAS of 3.9 ns. The original *SCM/WIM1* angular-only distributed paths of a single cluster are re-grouped to three fixed delay offsets (Fig. 3.9), thus the cluster subdivision in delay domain does not increase total number of paths.

### 3. Multi-Path Components

In order to further simplify cluster characterization *SCM/WIM* does not deal with random placement of MPCs in “delay-directional” domain. Instead, on the 3<sup>rd</sup> level, the same, simple internal structure of the cluster is used and MPC parameters are calculated in deterministic manner. This structure assumes fixed number of MPCs with equal power. Angular separations between MPCs account for assumed Laplacian Power Angular Spectrum (PAS) and given CAS. This *WIM* functionality is realized by scaling predefined angular

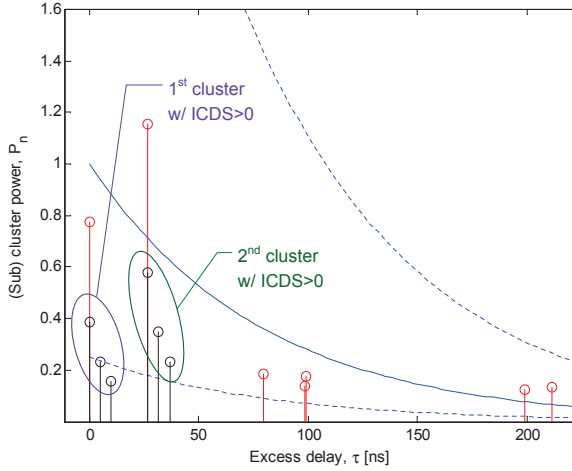


Figure 3.9: An introduction of the delay dispersion to the two strongest WIM2 clusters: the fixed delay offsets in respect to an excess delay of the original cluster are 0, 5 and 10 ns, and normalized powers of sub-clusters are 10/20, 6/20 and 4/20.

“one-degree” offsets with targeted CAS. This is achievable since “one-degree” offsets are symmetric around mean cluster direction, and MPCs have the same power. In ZDSCs all MPCs share the same propagation delay corresponding to cluster centroid. Clusters with 3.9 ns delay spread are constructed by the fixed delay offsets of 0, 5 and 10 ns in respect to a reference CC delay. The normalized powers of formed sub-clusters are 10/20, 6/20 and 4/20, which means that delay offset of 0 ns is assign to 10 from 20 available MPCs, 5 ns offset to 6 MPCs and 10 ns offset is given to 4 MPCs in cluster (Fig. 3.9).

The random initial phases,  $\Phi$  in (3.26), are taken from uniform distribution.

MPC’s Doppler shift is related to the mobility pattern, i.e. velocity of Mobile Terminal (MT).

With introduced approximations in WIM structure, the LSPs become the most important for the particular scenario characterization. We would therefore ignore the lower hierarchy levels when computing a scenario divergence in the Sec. 5.3.





## Chapter 4

---

# Parameterization of WINNER Model

---

The usability of different channel representations for model development is discussed in the first section. From channel tensors being collected during multidimensional channel sounding, a joint space-time-frequency representation that offers the most detailed insight into propagation mechanisms is obtained. The process of propagation channel reconstruction from multiple observations of radio channel is based on high-resolution parameter estimation algorithms, which are presented in the second section. The third section describes the processing sequence for estimation of large-scale parameters of **WINNER** channel model. The last, fourth, section demonstrates that usage of incomplete measures (not covering all data dimensions) for processing of multidimensional sounding data causes ambiguity of estimated parameter values.

### 4.1 Alternative Representations of Measurement Data

The measurements are performed in order to observe behavior of propagation channel, and eventually to apply gained knowledge to the design of communication system. Typically, link and system level simulations are used in the development and evaluation of new algorithms and transmission strategies, before implementation trials are done. These simulations can use the measurement data in direct form (*measurement replay*) or some altered representations.

In measurement replay, the obtained channel realizations over specific tracks and pre-determined measurement antennas, are exploited for system performance testing. However, the abstraction of a single measurement is preferred representation of gained knowledge since communication system design should be universal and not specific to the environment investigated within single measurement experiment. Otherwise, the measurement replay simulations should use numerous experiments conducted in different propagations environments. This assumes huge amounts of data, hard even to store and very impractical to use in system design process.

Therefore, the goal of altered forms of measurement data is to reduce the complexity of channel representation. These modified forms should preserve acquired realism of measured radio-channel, and thus benefit to the system design process [65].

The process of finding appropriate trade-off between the channel representation complexity and its realism is known as *channel modeling*.

Reliable channel models are essential for network planning and link design. For the design of Next Generation Wireless Networks specified in **WINNER** or 3rd Generation Partnership Project (3GPP) LTE-Advanced dedicated channel models are defined: **SCM** [62], **SCME** [66] and **WINNER** channel model [69], [70]. Using the measured and processed impulse responses a statistical analysis of small and large-scale parameters can be carried out. This leads to a more generalized representation of the measured channel data without neglecting the real scenario.

#### 4.1.1 Development and Parameterization of a Channel Model

The multidimensional channel transfer function can be equivalently expressed using the system functions [27] in either *faded domains* ( $\vec{r}$ -space,  $t$ -time,  $f$ -frequency) or *resolved domains* ( $\vec{\Omega}$ -directions,  $\nu$ -Doppler shift,  $\tau$ -delay) [31].

According to the dependence of data from the particular measurement we can distinguish representations that are dependent and independent from measurement antenna arrays. This distinction becomes very important for analysis of **MIMO** transmission where spatial correlations (specific to the used antenna arrays) are crucial for obtained link/system performance. The applied methods for channel analysis differ between these model groups since the underlying data representation is different. The measured transfer functions are related to spatial sampling predetermined by measurement antenna array properties (geometry, polarizations, etc.). Therefore the number of used antennas determines the representation in spatial domain, as a collection of time-varying, wideband **SISO** channels. When the representation of propagation channel is given by structural parameters that independently describe multipath components, the number of relevant parameters is basically determined by propagation environment.

#### Non-Directional Representation - Radio Channel

According to introduced terminology for channel decomposition (Sec. 2.2), joint description of the space-time propagation channel and antenna is referred to as *radio channel*. Since an antenna projects a spatial response into time-delay dimension according to (2.21), the channel tensor  $H(t, f, s, u, p)$  obtained by measurements covers all relevant dimensions for separate analysis of temporal (time-varying wideband) and MIMO properties of radio channel.

In general, channel characterization can be performed in one of Fourier-related domains from Fig. 4.1, which correspond to Bello's system functions from Sec. 2.4.3. The selection of the particular domain for parameter estimation is related to target channel representation. E.g., for estimation of delay spread instead of  $H(t, f)$  its 1-D FT pair,  $h(t, \tau)$ , should be used. Some other parameters (e.g. transmission loss) could be equivalently determined from different domains.

The joint two-dimensional scattering function (Doppler spectrum versus delay power spectrum) gives partially resolved representation of the channel where the "resolution" is determined by both measurement time, antenna array aperture size, and system bandwidth. The scattering function enables limited channel characterization directly from measured data.

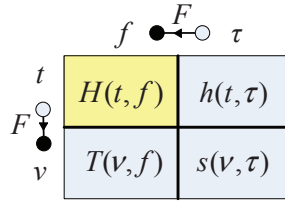


Figure 4.1: Domains used for characterization of wideband SISO radio channel [2].

This can be viewed as a natural way of processing since only time projections of multidimensional data are collected during measurements. However, this represents analysis in subspace of available data, since spatial and polarization dimension are not included. Alternative representation can be obtained in the cases when it is possible to resolve missing dimensions from available time-domain projections. This goal is achievable if time-projections on spatially displaced antennas are not completely correlated. Using different spatial signature, the spatial dimension of propagation can be identified.

### Joint Space-Time-Frequency Channel Representation - Propagation Channel

Possibility to remove dependence of measured antennas (antenna de-embedding, Sec. 2.4.2) is related to the reconstruction of the missing directional and polarization dimensions of the channel. For that purpose DoD, DoA, and polarimetric gains  $\alpha$  should be estimated/resolved for each multipath component,  $i$ , providing the channel representation by means of structural parameters:

$$\underline{H}(\vec{r}_{Rx}, \vec{r}_{Tx}, f, t) = \sum_i \vec{F}_{Rx}^T(\vec{\Omega}_i^{Rx}) \alpha_i \vec{F}_{Tx}(\vec{\Omega}_i^{Tx}) e^{j2\pi(\tau_i f + \nu_i t)}. \quad (4.1)$$

Interaction of MPCs with antenna arrays is described by the complex, polarimetric antenna radiation patterns  $\vec{F}(\vec{\Omega})$  in (2.31). Due to inability to represent the PAS, in the general case, as a product of marginal spectra on departure and arrival, a joint characterisation of DoD and DoA is to be used - as suggested by the *double-directional* modeling concept [8], [55]. The complex 2-by-2 matrix  $\alpha \in \mathcal{C}^{2 \times 2}$  is used to jointly describe magnitude, phase, and cross-polarization effects for single MPC.

The estimated *structural parameters* provide an antenna independent set of specular multi-path parameters that describe realizations of propagation channel. This additional feature significantly extend the usability of measurement experiment, since it allows characterization of propagation channel independently from applied measurement antennas.

The reconstructed MPC propagation parameters improve the fundamental understanding of the mobile multipath channel, and facilitate development of the Geometry-based Stochastic Channel Model (GSCM).

## 4.2 Reconstruction of Spatial Propagation Dimension

Although the synthesis of the geometry-based model is quite straightforward to perform, this is not the case with measurement data analysis that is used for pa-

parameterization or model verification.

The necessary structural parameters, normally for a large number of MPCs, could be estimated from appropriate multidimensional channel sounding data. In order to be able to resolve directions of departure and arrival for transmitted waves, a radio channel is observed using multiple Tx and Rx antenna pairs [73]. These data is gathered during wide-band measurement experiments with specially designed antenna arrays and real-time channel sounding devices [74], [75], [10], [60]. By performing measurements with specific antenna arrays, the high-resolution path parameter estimation can be applied.

The most important feature of *high-resolution parameter estimation* (HRPE) is related to feasible *resolvability* of ray parameters in the measurement data. The resolution of estimated structural parameters is impacted by finite measurement bandwidth, the limited aperture and number of antennas in the measurement array, and the geometry of the array. The implementation of measurement array determines the distribution and number of spatial samples. HRPE algorithms are further evaluated according to *reliability* of the estimated ray parameters, and proper determination of the *relevant number* of rays. Above problems stem from the limits of the experimental-based characterization that are inherent to measurement procedures and actual equipment.

The estimation procedure of MPC parameters from channel sounding data requires the use of so called *high-resolution algorithms*, like e.g. Maximum Likelihood Estimation [76], ESPRIT (Estimation of Signal Parameters via Rotational Invariance Techniques) [77], [78], SAGE (Space-Alternating Generalized Expectation-maximization) [79], or RIMAX [80], [81], [82]. Due to the computational complexity of these algorithms, high-resolution analysis is one of the most time-consuming phases in the modeling work.

#### 4.2.1 High-Resolution Parameter Estimation with RIMAX Algorithm

For reconstruction of spatial and polarization dimensions from TU Ilmenau measurements, the gradient based maximum likelihood parameter estimation algorithm RIMAX is employed [81], [83]. Additionally to the parameter-per-parameter optimization applied in SAGE, the RIMAX uses simultaneous gradient based optimization over complete parameter set. This property enables reaching of the global minimum of a cost-function and improves results of reconstruction. When RIMAX is employed to perform high-resolution parameter estimation, separate characterization of numerous specular MPCs will be obtained. For each specular multipath components the parameters  $\mathbf{p}_i$  defined in (2.20) are estimated.

RIMAX uses a data model that describes every temporal observation of a wide-band MIMO channel (snapshot) as the superposition of SCs and Dense Multipath Components (DMCs).

$$\underline{\mathbf{H}}(u, s, f|t_0) = \mathbf{s}(\boldsymbol{\theta}_{sc}|t_0) + \mathbf{d}(\boldsymbol{\theta}_{dmc}|t_0) \in \mathbb{C}^{M_{Rx} \times M_{Tx} \times M_f}. \quad (4.2)$$

The  $L$ -tuple  $\boldsymbol{\theta}_{sc} = \{\mathbf{p}_i\}_{i=1, \dots, L}$  represents collection of MPC (structural) parameters that jointly describe multipath profile. The contribution of  $L$  specular components to  $\mathbf{s}(\boldsymbol{\theta}_{sc})$  at single frequency  $f$ , for MIMO sub-channel  $(u, s)$  defined by positions of Tx and Rx antennas  $(\vec{r}_{Rx}, \vec{r}_{Tx})$  can be calculated using the equation (4.1).

When **MPCs** parameters are jointly describing all available dimensions of measured data there is no ambiguity stemming from the subspace description (as long as the full description of measurement antennas is available). However, from limited number of observations it is possible to reliably estimate only limited number of parameters and **MPCs**. For each extracted parameter **RIMAX** provides reliability measure based on the Fischer information matrix [81].

### Dense-Multipath-Components

**RIMAX** algorithm increases reliability of estimated parameters by introducing concept of *Dense Multipath Component* (**DMC**): only limited number of specular components is resolved as such, while the rest of the observed energy is jointly characterized as **DMCs**. The presence of **DMCs** can be explained by diffuse scattering or otherwise unresolvable specular paths. However, the physical meaning of **DMCs** are not the crucial in this context – the introduced **DMC** model reduces the complexity of the channel representation and improves robustness of the Maximum Likelihood (**ML**) parameter estimator. Additionally to accounting for the unresolved paths, the **DMCs** absorbs influence of different modeling errors: shaped wave fronts, limited accuracy of the antenna calibration, etc. [82].

Dense multipath components are represented as correlated realizations of the stochastic process having zero-mean circularly symmetric complex Gaussian distribution:

$$\mathbf{d}(\theta_{dmc}) \sim \mathcal{N}_c(\mathbf{0}, \mathbf{R}(\theta_{dmc})) \in \mathbb{C}^{M \times 1}. \quad (4.3)$$

For finite measurement bandwidth, it is assumed that Power-Delay Profile of **DMC** show exponential decay over the time-delay:

$$S(\tau) = E\{|\underline{h}(\tau)|^2\} = \begin{cases} 0 & \tau < \tau_d \\ \frac{\alpha_1}{2} & \tau = \tau_d \\ \alpha_1 \cdot e^{B_d(\tau_d - \tau)} & \tau > \tau_d \end{cases}. \quad (4.4)$$

Therefore, the triplet  $\theta_{dmc} = (\tau_d, \alpha_1, B_d)$  describes the position, magnitude and decay of **DMC** model. The corresponding frequency correlation function in frequency domain, under Uncorrelated Scattering (**US**) assumption, can be determined as Fourier transform of (4.4):

$$R(\Delta f) = \frac{\alpha_1}{B_d + j2\pi\Delta f} \cdot e^{-j2\pi\Delta f\tau_d}. \quad (4.5)$$

The decay parameter  $B_d$  is proportional to coherence bandwidth of **FCF**. The frequency correlation matrix will contain the samples of **FCF** taken on multiples of  $\Delta f_0$ , where  $\Delta f_0$  designates regular offset between measured frequencies  $f_{i+1} = f_i + \Delta f_0, i = 0, \dots, M_f - 1$ .

$$\mathbf{R}_f(\theta_{dmc}) = \begin{bmatrix} R(0) & R(-\Delta f_0) & \dots & R(-(M_f-1)\Delta f_0) \\ R(\Delta f_0) & R(0) & \dots & \vdots \\ \vdots & \vdots & \ddots & R(-\Delta f_0) \\ R((M_f-1)\Delta f_0) & \dots & R(\Delta f_0) & R(0) \end{bmatrix} \quad (4.6)$$

The realizations of **DMC** process are reproduced by correlating the samples of multi-dimensional Gaussian noise, as discussed in Sec. 3.2 for filtering approach. The **RIMAX** does not consider the complete correlation matrix but it characterizes **DMC** independently over different dimensions of the channel. Therefore, the full correlation matrix of size  $M \times M$ ,  $M = M_{Tx} \cdot M_{Rx} \cdot M_f \cdot M_t$  is approximated with Kronecker model:

$$\mathbf{R}(\boldsymbol{\theta}_{dmc}) = \mathbf{R}_R(\boldsymbol{\theta}_{dmc}) \otimes \mathbf{R}_T(\boldsymbol{\theta}_{dmc}) \otimes \mathbf{R}_f(\boldsymbol{\theta}_{dmc}) \otimes \mathbf{R}_t(\boldsymbol{\theta}_{dmc}), \quad (4.7)$$

where  $\otimes$  designates Kronecker product, and  $\mathbf{R}_x(\boldsymbol{\theta}_{dmc})$ ,  $x \in \{Rx, Tx, f, t\}$ , are correlation matrices for individual channel dimensions: **Rx** antennas, **Tx** antennas, frequency and time.

The independence of channel dimensions (channel separability) used in Kronecker model is unlikely to hold for the whole wideband **MIMO** channel due to existence of the strong specular components in the channel. However, once the strong components are removed, it could be more suited for representation of **DMC** statistics.

The relevance of **DMC** part for data modeling will depend on the channel power contained in dominant (specular) MPCs. The *Signal-to-Remainder-Ratio* (**SRR**) defined as the ratio between the power of the estimated specular paths and the remaining signal (**DMC**) power is proposed in [82] to quantify **RIMAX** estimation quality. In the case of fast-train measurements (Sec. A.2.2), it is possible to model about 95% of total received power with specular components only. From that reason **DMCs** do not significantly influence global channel parameters. In some cases, however, only half of received power can be represented with specular components, and then **DMCs** become a very important part of data model.

With introduced **DMC** concept, the observed radio channel can be considered as a realization of the process:

$$\mathbf{H}(u, s, f|t_i) \sim \mathcal{N}_c(\mathbf{s}(\boldsymbol{\theta}_{sc}|t_i), \mathbf{R}(\boldsymbol{\theta}_{dmc}|t_i)) \in \mathbb{C}^{M \times 1}. \quad (4.8)$$

Therefore the single realization of a wideband **MIMO** radio-channel (snapshot) is represented with the parameters:

$$\boldsymbol{\theta}(t_i) = \begin{bmatrix} \boldsymbol{\theta}_{sc}(t_i) \\ \boldsymbol{\theta}_{dmc}(t_i) \end{bmatrix}, \quad (4.9)$$

and estimation of parameters  $\boldsymbol{\theta}(t_i)$  is based on the finding the best match of the reconstructed observation of  $\mathbf{H}(u, s, f|t_i)$ .

### Variance of Estimated Parameters

The accuracy of structural parameter estimates  $\hat{\boldsymbol{\theta}}_{sc} \in \mathbb{R}^{L \times 1}$  is expressed with the associated covariance matrix:

$$\mathbf{C}_{\hat{\boldsymbol{\theta}}_{sc}} = E\{(\hat{\boldsymbol{\theta}}_{sc} - \boldsymbol{\theta}_{sc})(\hat{\boldsymbol{\theta}}_{sc} - \boldsymbol{\theta}_{sc})^T\} \in \mathbb{R}^{L \times L}. \quad (4.10)$$

For unbiased estimator, satisfying  $E\{\hat{\boldsymbol{\theta}} - \boldsymbol{\theta}\} = 0$ , the *Cramér-Rao lower bound* (**CRLB**) defines the obtainable minimum for the estimation covariance matrix,  $\mathbf{C}_{\hat{\boldsymbol{\theta}}_{sc}} \geq \mathbf{CRLB}_{\hat{\boldsymbol{\theta}}_{sc}}$ . It is shown in [84] and [81] that the **RIMAX** maximum likelihood estimator reaches the Cramér-Rao lower bound, assuming the radio channel sounder and antenna arrays are properly calibrated.

### Model Order Selection

The number of specular components that could be reliably parameterized defines a model order. A proper selection of the model order is crucial for reaching the optimum between the accuracy and complexity. The Cramér-Rao lower bound provides an effective measure to decide whether a propagation path should be described as specular MPC or associated to DMC group. If the relative variance of the propagation path magnitude  $|\alpha|$  is small enough [81]:

$$\frac{CRLB_{|\alpha|}}{|\alpha|^2} < \varepsilon_{|\alpha|}^2 < 1, \quad (4.11)$$

then propagation path is represented as specular component. Otherwise, it is considered as a part of the stochastic process describing DMC. The proposed approach limits the model complexity and improves robustness of the high-resolution channel parameter estimator. However, it does not completely suppress the appearance of the “ghost” paths.

### Subdivision of Parameter Estimation Problem into Deterministic and Stochastic Parts

RIMAX algorithm assumes that structural parameters  $\theta_{sc}$  are asymptotically uncoupled with parameters  $\theta_{dmc}$  that characterize DMC. Thus, both Fisher information matrix  $\mathbf{F}(\theta)$  and Cramér-Rao lower bound have form of block diagonal matrices:

$$CRLB_{\hat{\theta}} = \mathbf{F}^{-1}(\theta) = \begin{bmatrix} CRLB_{\hat{\theta}_{sc}} & \mathbf{0} \\ \mathbf{0} & CRLB_{\hat{\theta}_{dmc}} \end{bmatrix}, \quad (4.12)$$

where  $\theta$  is formed by the concatenation of structural and DMC parameters, (4.9). The block diagonal structure is exploited for splitting of ML estimation problem into deterministic and stochastic parts. Parameters of deterministic part describe SoS model, while stochastic part corresponds to DMC parameters (diffuse/dense component) that are represented by filtering approach. However, deterministic and stochastic parts of the RIMAX mixed model are not completely independent since significant correlation exists between certain specular and DMC parameters [85].

### Impact of Limited AA Model Precision on High-Resolution Parameter Estimation

Some limitations on the performance of the parameter estimation algorithms are imposed by the random phenomena contained in the channel-sounding data and are typically characterized by the Cramér-Rao lower bound. There are, however, additional limitations stemming from the achievable accuracy of the model of the measurement system that is used for the estimation purposes. More specifically, inaccuracies of the antenna array model reduce dynamic range of the measurement data that can be reliably characterized [82].

Due to the inherent spatial characteristics of antennas, their separation from the propagation channel can not be performed prior to HRPE. Therefore, the HRPE procedure has to rely on a model of the AA that is used throughout the measurements. Required AA model is created through the calibration procedure.

The accuracy of the obtained AA model may be impaired by multiple causes (e.g., phase noise, disregarded frequency dependence of radiation pattern, or by

unavoidable parasitic reflections present in the anechoic chamber during antenna calibration) and therefore an impact on channel parameter estimation is to be expected. **AA** calibration, being conducted in an anechoic chamber, typically assumes the existence of a single direct path between the reference antenna and the antenna under test and disregards possible parasitic reflections. However, this may not fully correspond to reality: for frequencies between 4 GHz and 6 GHz, the reflection coefficients of the chamber walls are between -10 dB and -40 dB, depending on the angle of the incoming wave and the height of the cones of the absorbing material [86]. The achievable model accuracy will also depend on the properties of the anechoic chamber, positioning system, and analyzed antenna arrays; however, average values in the range from 25 dB to 30 dB can be expected [82].

### Impact of AA Model Distortion

The impact of **AA** model distortion is evaluated in [82] and [87] for a simulated single-path excitation. Estimation of the fixed number of specular components,  $K = 10$ , is repeated for different arrival directions corresponding to the full co-elevation range  $[-180^\circ, 180^\circ]$ . It was found that the estimation quality depends on the direction of the incoming wave, and can be expressed by the number of artifacts (ghost **SCs**), their relative powers, and the deviation of their estimated directional parameters from the true arrival direction.

The consequence of distortion is that each **SC** will tend to spread in parameter space, producing clusters of the estimated **SC** parameters. This important effect may lead to the false conclusion that clustering of **SC** parameters observed in measurements is a characteristic of the radio propagation. Instead, clustering may come solely from the usage of inaccurate **AA** models in parameter estimation algorithms.

An antenna independent channel characterization can be performed under the assumption that it is possible to characterize all received energy with specular components only and that an ideal model for the measurement system (including antenna arrays) can be constructed. Unfortunately, inaccuracies incorporated into the **AA** model during antenna calibration will increase the number of artifacts in the overall channel representation. For **ML** parameter estimation algorithms without a proper model order control, the distorted radiation patterns will increase computational time due to the estimation of physically meaningless components. The resulting power distribution and angular spreads could lead to a wrong interpretation of the channel characteristics w.r.t., e.g., clustering properties. These effects are similar to those caused by an incomplete **AA** model (meaning non-polarimetric or not **3-D** or both) [88], [89].

## 4.3 Estimation of the WIM Parameters

The systematic approach to channel parameter extraction, with corresponding methods and formulas is developed in **WINNER** project [4], [5]. The given procedures enable simple and transparent generation of channel model parameters. The structure of **WINNER** channel model [5] requires characterization on the several levels: i) global, ii) cluster, and iii) ray-level, however this thesis focuses on the global model behavior that is governed by large-scale parameters.



The particularities of the **3GPP SCM** [62] and **WINNER** model [5] is the simplified characterization of the power dispersion over delay and angular dimension only by appropriate spreads. The total received power is expressed by the empirical transmission-loss model, and deviations from the regression are given by shadow fading (**SF**). The remaining LSPs describe existence of line-of-sight component (narrowband K-factor), and cross polarization ratio (**XPR**).

The Large-Scale Parameters (**LSPs**) in **WINNER** model are characterized stochastically and described by appropriate log-normal Probability Density Functions (**PDFs**). Instead of joint **PDFs**, **3GPP SCM** and **WINNER** characterize marginal distributions. Cross-correlation coefficients between **LSPs** (excluding **XPR**) are introduced to reflect interdependence observed in measurements. These models also embed the simple exponential model for intra-site correlations: when displacement of **MT** exceeds decorrelation distance **LSP** correlation drops below  $\frac{1}{e}$ .

The measurement data can take two alternative representations being discussed in Sec. 4.1: a 5-dimensional tensor\*  $h(t, \tau, s, u, p)$  shown in Fig. 4.3 with dimensions:  $t$  – time (snapshot number),  $\tau$  – delay,  $s$  – Tx antenna,  $u$  – Rx antenna, and  $p$  – polarization pair, or **RIMAX** parameters  $\theta(t)$  from (4.9), being estimated on snapshot bases  $t$ . In the letter representation, dimensions  $(\tau, s, u, p)$  are replaced by multitude of **MPC** parameters  $(\tau, \vec{\Omega}^{Tx}, \vec{\Omega}^{Rx}, \alpha)_i$ .

Even with different modifications of **EM** algorithms **HRPE** is complex and time consuming. Thus, the spatial dimensions are not necessarily reconstructed before parameters describing wideband nature of channel are calculated, and analysis is performed using delay/frequency and time/Doppler domains. The relevant **LSPs** and their distributions for the state-of-the-art channel models like **WINNER** and **COST** are estimated from multiple representation domains [5] [90] [71]. Fig. 4.2 illustrates usage of different representation domains for parameterization of **WIM**. While parameters as **DS**, Transmission Loss (**TL**), **SF** and the K-factor are typically derived from power delay profile, parameters as the Azimuth of Arrival (**AoA**) and Azimuth of Departure (**AoD**) are only accessible via sophisticated and time consuming **HRPE** algorithms, e.g., **RIMAX** [83] [88]. This separation possibly leads to a decorrelation between the **LSPs** from different domains as discussed in Sec. 4.4.2.

In order to get comparable results from the measurements performed with different equipments/setup, the common *signal processing assumptions* should be fulfilled:

1. Processing bandwidth is 100MHz, otherwise measurement data has to be equalized by interpolation/decimation.
2. Only data whose dynamic range exceeds predefined threshold of 20dB should be used. If the used dynamic range is artificially kept constant, then parameters such delay spread become independent from thresholding level (Sec. 4.4.1), however the systematic error is introduced and biased estimate is obtained.

---

\*The RUSK channel sounder provides 4-dimensional channel transfer tensor  $\mathcal{H}(t, f, s^*, u^*)$  that is transformed into channel impulse response tensor  $h(t, \tau, s, u, p)$  by Fast Fourier Transform (**FFT**) over frequency domain  $F : f \rightarrow \tau$  and **MIMO** sub-channel mapping  $(s^*, u^*) \rightarrow (s, u, p)$ .

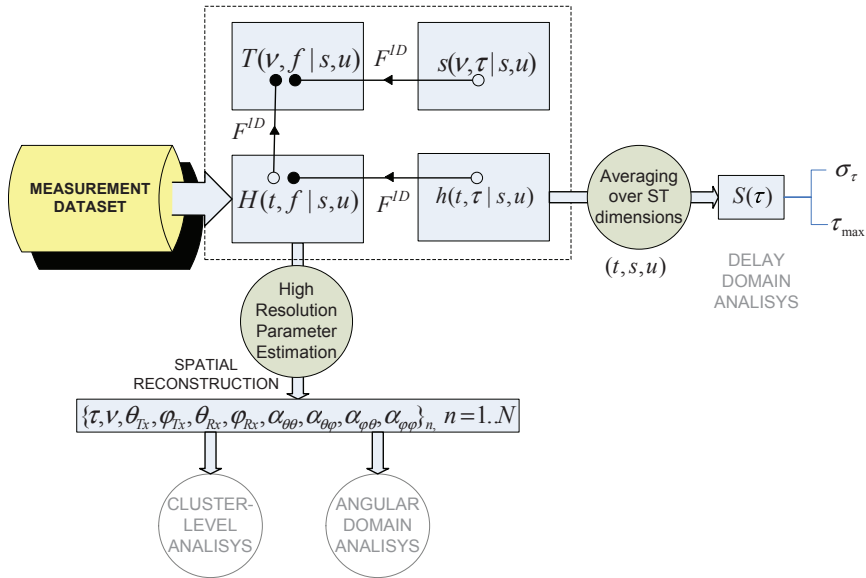


Figure 4.2: Different domains used for parameterization of WINNER model.

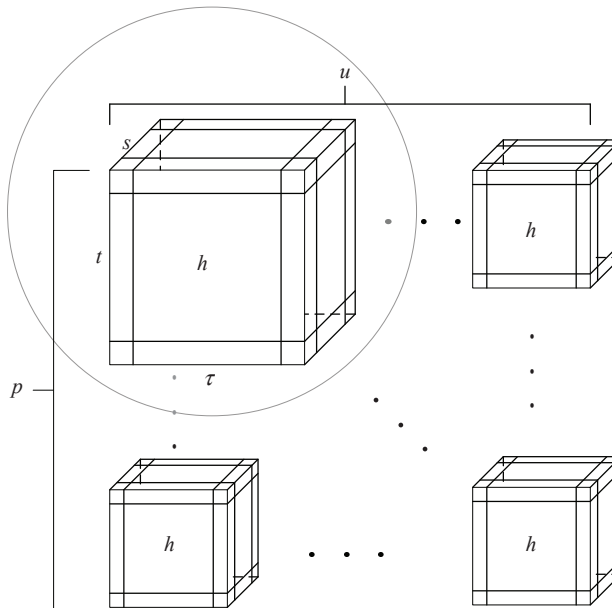


Figure 4.3: Structure of the CIR tensor that is obtained from the measurements.

3. Space-time averaging window has to be equivalent with the stationary region of the channel. Stationary region is often related to a distance range in which the channel realizations “look similar” for a system with given bandwidth of 100 MHz. Averaging distance taken in WINNER Phase I of approx. 1 meter ensures that cluster do not move significantly in the delay domain.

### 4.3.1 Segmentation of Measurement Data

For estimation of WIM parameters the following space-time processing units are introduced:

1. *Snapshot* - The collection, having one CIR,  $h(\tau)$ , for every  $(s, u, p)$  - triplet, is referred to as MIMO channel *snapshot* and is used as a basic processing unit. Following this terminology we can state that measurements are consisting of large number of snapshots (Fig. 4.4a).

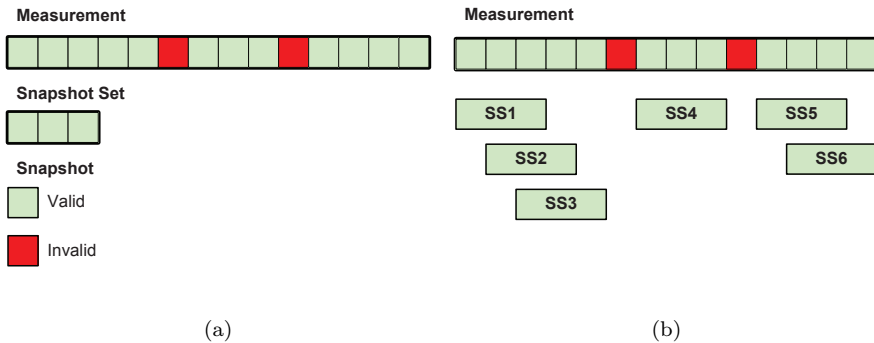


Figure 4.4: a) Space-time processing blocks; b) Processing of the measurement data based on “snapshot sets”.

The snapshots having acceptable quality are regarded as the valid ones and used in the analysis. The dynamic range (the highest peak-to-noise level) of the valid snapshots exceeds 20 dB for at least one  $(Tx, Rx, Pol)$  sub-channel.

Prior further WIM processing, the snapshots are classified into disjoint LoS/NLoS groups according to the existence of the line-of-sight condition.

2. *Snapshot Set* - When the parameter estimation is related to the channel stationarity region, a number of successive valid snapshots is of interest. Thus, *snapshot set* (SS) containing predefined number of the valid consecutive snapshots<sup>†</sup> is used as a higher-level processing unit. The extent of SS overlapping, Fig. 4.4b, is related to the processing strategy.

<sup>†</sup>In some cases (e.g., for time demanding MPC parameter estimation), the condition requiring all valid snapshots to be consecutive in time dimension may be too strict. In that case, the processing could be based on usage of all available SSs, which is equivalent to the usage of subintervals (exceeding predefined length) over time dimension.

### Extent of Stationarity Region(s)

The concept of **LSR** enables the differentiation of the large and small-scale effects. Since underlying physical process (and corresponding structural parameters) is unchanged, then only small-scale effects are exhibited within **LSR**. Therefore, **LSR** corresponds to the limited area where a wide-sense stationarity can be assumed [91]. The multi-path parameters significantly change between neighboring **LSRs**, which is considered as large-scale variation.

In cases when channel features exhibit stationarity over space-time realizations, the parameter extraction requires a prior segmentation of the available data according to the stationary regions. If the extent of the stationarity regions is to be estimated, a processing of the measurement data is divided into two phases. In the 1<sup>st</sup> phase, the borders of stationarity regions are determined (number of consecutive snapshots that constitute **SS**), whereas in 2<sup>nd</sup> phase the actual parameter computing is performed on **SS** bases, as shown in Fig. 4.4b. Another approach takes minimum **SS** that supports reliable parameter estimation. The extracted features from smaller **SS** will show space-time correlation, and enable adequate estimation of the **LSR** extent in post-processing phase. The computational burden comes from an increased (non-optimal) number of **SS** for which parameters are extracted.

### Separation of Large and Small-scale Effects Based on Feature Variability

**(Generalized) Lee Method** is proposed to determine optimal space-time region for the calculation of the statistical moments of the received signal strength. The quality of the separation of large and small scale effects, in this method, depends on properly calculated local mean values. While original method [92] makes assumptions about probability distributions of the analyzed signals, its generalization [93] does not. This method evaluates different sizes of Space-Time (**ST**) interval, and the size showing the lowest variance of the estimated mean values of signal is taken as the appropriate one.

In Lee's methods the small-scale deviations of signal straight around local mean are considered. This approach is typically applied for a narrowband channel characterization, where it appears sufficient to characterize large and small signal level variations using appropriate **PDFs** (Sec. 2.5.5). When considering wideband **MIMO** channels, other parameters, besides signal power, are to be analyzed as well. E.g., the authors of [94] point out that the correlation between eigenvectors of different **MIMO** links can be high under similar *dominant propagation mechanisms* (DPM)<sup>‡</sup>. The identification of the DPM similarity regions leads to a segmentation of the **ST** domain and by that reveals the large-scale evolution of the radio channel.

### Suppression of Small-scale Effects in MIMO Sounding Data

In **SISO** channel, the small-scale variations are typically suppressed by a space-time averaging over several consecutive **PDP** realizations. In **MIMO** case averaging

---

<sup>‡</sup>The concept of dominant propagation mechanisms is often applied in channel characterization: [94], [95], [96]. The relevance of existing propagation mechanisms (and related **MPCs**/clusters) is evaluated according to the level of received power.

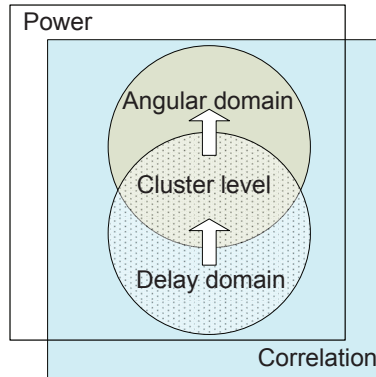


Figure 4.5: Grouping of analysis items.

can be also performed over the antenna array aperture, i.e., by combining the spatial samples from different antenna elements. When powers of the signals from different antennas are combined in non-coherent manner in order to emulate “isotropic” reception, the small-scale effects are already partially suppressed. Requirements for further ST averaging are therefore relaxed, or they even become excessive for large number of  $T_x$  and  $R_x$  antenna elements, as illustrated in Sec. 4.4.1.

### 4.3.2 WIM Analysis Items and Methods

The WIM analysis items will be classified according to domain that are calculated from (Delay, Angular, Cluster - joint processing of both domains), or to the property that they describe (Power, Correlation). This gives 5 groups (processing domains) being shown in Fig. 4.5. This thesis enlightens only particular items and methods, mainly related to LSP features, while detailed instructions are given in [4], [5].

#### Computation Sequence

Since the radio channel measurements are the basis for the research of the wireless propagation phenomena, it is important to consider the whole procedure from measurements to channel models.

The computation sequence in Fig. 4.6 defines order in which items (represented by the squared block) are calculated and indicates applied computation procedures (represented by the small circles). The figure contains intermediate items as ‘TimeVariantPowerDelayProfile (PerPolarization)’, ‘MPCParameters’, ‘Clusters’, etc., being required to calculate targeted analysis items.

The processing sequence is independently applied to different polarization dimensions. This enables comparison of the features for different polarizations or calculation of their ratios (such as XPR).

The autocorrelations and cross-correlations of the estimated items are typically calculated at the end, after an item processing is over.

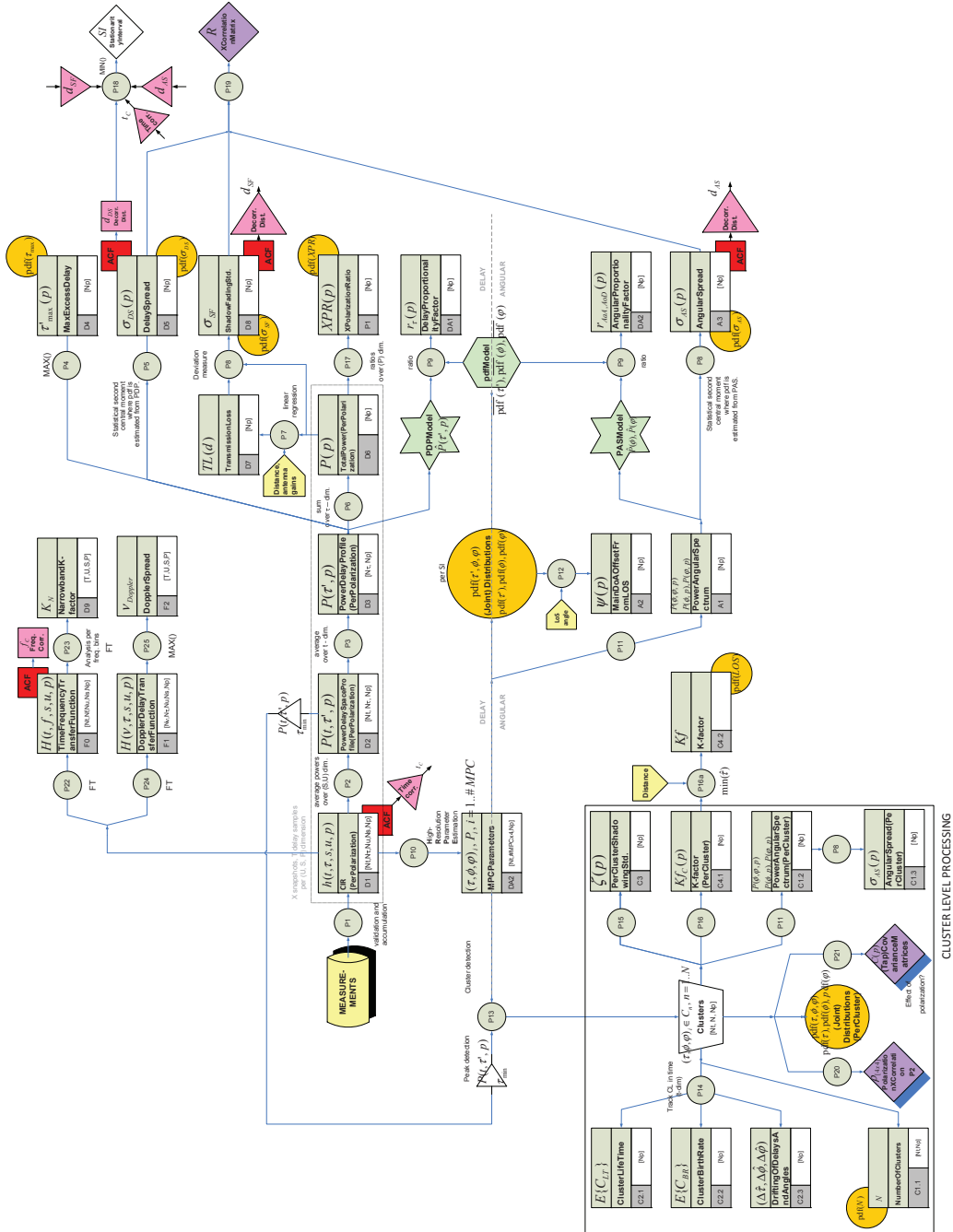


Figure 4.6: Item computation sequence.

### Common (Statistical) Processing Methods

Statistical procedures that are repeatedly used for computation of different items are identified as common processing methods: estimation of distribution (histogram), calculation of Auto-Correlation Function (ACF), and cross-correlation and covariance matrices.

For the estimation of the statistical properties it is important to identify the relevant subsets of data. E.g., since distribution of MPC delays and angles has to be calculated for each stationarity region (of the corresponding snapshot set), the input data has to be collected from each snapshot belonging to that SS. The autocorrelation functions for LSPs are typically calculated at measurement level. That would mean that delay, angular spread and shadow fading standard deviation (std.) data is collected for a whole scenario (one value is calculated per SS), and correlation coefficient is calculated.

### Delay-Domain Analysis

Channel Impulse Response (Per Polarisation)  $h(\tau'|p, t_0, s, u)$  is a realization of  $h(\tau')$  in time instant  $t_0$ , for given positions of Tx and Rx antennas ( $s, u$ ), and their polarization properties  $p$ . The estimation of the noise level in CIR enables partial suppression of the noise by thresholding and evaluation of the dynamic range, which describes snapshot quality. All CIR values below the estimated noise level (that is increased by a safety margin) are disregarded in the further delay-domain analysis.

**Noise Level Estimation** Noise level is estimated within a single snapshot for the subset  $G_k$  of spatial channels that share the same Automatic Gain Control (AGC) setting. Since measurement equipment have the same setup, the impact of thermal and quantization noise is similar in all considered samples.

$$\vec{h} = \text{vec}\{h(t_0, \forall \tau', (s, u, p) \in G_k)\}, \quad (4.13)$$

All samples are sorted in the ascending order, according to their instant power:

$$P^* = \text{sort}\{Re\{\vec{h}\}^2; Im\{\vec{h}\}^2\}. \quad (4.14)$$

When the average power over the lowest  $N$  samples, scaled by a predefined margin  $m$ , for the first time exceeds the instant power of the  $N$ -th sample, we assume that  $N$ -th sample is not generated by noise only.

$$\hat{N}_{t_0, G_k} = \min_N \left\{ \frac{m}{N} \sum_{n=1}^N P_i^* \geq P_N^* \right\}. \quad (4.15)$$

The variance of the complex noise (having the same power in real and imaginary samples) equals:

$$\sigma_N^2(t_0, G) = 2 \cdot P_{\hat{N}_{t_0, G_k} - 1}^*. \quad (4.16)$$

**Power Delay Profile (Per Polarization)** shows the distribution of received power over different delays. The **PDP** has been obtained from the measurement by averaging instantaneous **PDPs**  $S^*(t, \tau|p, s, u)$ , from all spatial sub-channels  $(s, u)$  within a local stationary region. For each snapshot the instant powers are calculated as the squared magnitude of the **CIR**:

$$S^*(t, \tau|p, s, u) = |h(t, \tau|p, s, u)|^2. \quad (4.17)$$

Afterward, the instantaneous power spectra is averaged over **Tx** and **Rx** antennas belonging to the same **AGC** group,  $(s, u) \in G_k$ .

$$S^*(t, \tau'|p, G_k) = \frac{1}{\#G_k} \sum_{(s,u) \in G_k} S^*(t, \tau'|p, s, u). \quad (4.18)$$

In the cases when directional antennas (e.g., patches) are applied to construct the measurement array, or neighboring antennas are shadowed due to array construction (e.g., Uniform Circular Array – **UCA**), each pair of antennas  $(s, u)$  observes **PDP** that is limited in departure and arrival directions. Only after spatial averaging (4.18), the appropriate representation of **PDP** is obtained.

**Thresholding** Due to the influence of the receiver thermal noise, the averaged **PDP** for single polarization (4.18) exhibits floor over the whole observed delay range. Removal of the noise artifacts is based on estimated noise power,  $\sigma_N^2$  from (4.16), and thresholding of **PDP**:

$$S(\tau'|p, t_n, G_k) = \begin{cases} S^*(\tau|p, t_n, G_k) & S^*(\tau|p, t_n, G_k) \geq \sigma_N^2(t_n, G_k) \cdot m \\ 0 & otherwise \end{cases}, \quad (4.19)$$

where  $m$  represents predefined margin. As a consequence, all further calculations based on  $S(\tau|p)$  become dependent upon procedure used for  $\sigma_N^2$  estimation and chosen value for margin  $m$ . The impact of the estimation procedure onto delay-domain parameters is further discussed in Sec. 4.4

If none of the resulting averaged **PDP** does not fulfill the dynamic range requirement, i.e., 20 dB from the peak to the noise floor, that snapshot is eliminated from the further analysis. In Fig. 4.7a an example **PDP** with the estimated threshold is illustrated.

**Space-Time Averaging and Delay Normalization** After thresholding, averaging over **AGC** sets and snapshots within **SS** is performed:

$$S(\tau'|p) = \frac{1}{n_t n_G} \sum_{n=1}^{n_t} \sum_{k=1}^{n_G} S(\tau'|p, t_n, G_k). \quad (4.20)$$

Additional shift of delay axis  $\tau' \rightarrow \tau$  could be applied to move the beginning (the first delay with non-zero power) of (4.20) into coordinate origin. The normalized axis obtained in this way is known as excess delay.

$$S(\tau|p) = S(\tau' - \tau'_{min}|p). \quad (4.21)$$



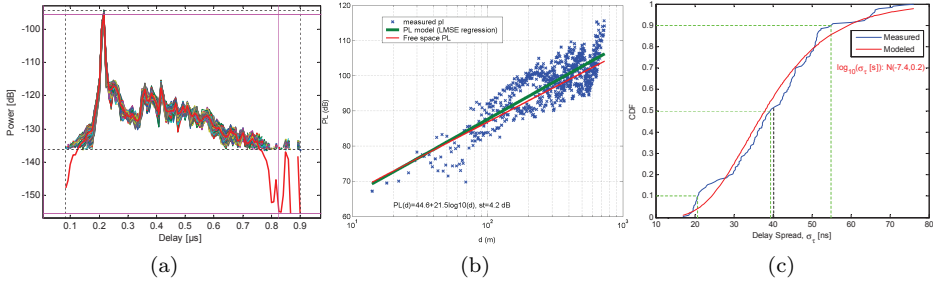


Figure 4.7: WIM analysis items: a) PDP example from the fast train measurements, b) Transmission loss for rural scenario, c) Delay spread for high speed networks. [97]

In delay domain, Maximum Excess Delay (**MED**) and delay spread are calculated from **PDP** to quantify the dispersion of power over excess delay. In **WINNER** model, **PDP** can be also used to determine the cluster power according to cluster delay.

**Delay spread (DS)** is used to characterize dispersiveness of wideband **SISO** channels. **DS** is determined as standard deviation:

$$\sigma_{\tau}(p) = \sqrt{\overline{\tau^2} - \bar{\tau}^2}, \quad (4.22)$$

where  $m^{th}$  moment:

$$\overline{\tau^m(p)} = \frac{\sum_k (\tau_k)^m S(\tau_k|p)}{\sum_k S(\tau_k|p)}, \quad (4.23)$$

is calculated from thresholded Power-Delay Profile (**PDP**) -  $S(\tau|p)$ . When **DS** is extracted from the channel impulse response data, the available dynamic range in measurement data will influence the obtained parameter values (Sec. 4.4.1). Thus, the results of different measurement campaigns in literature are not always comparable. To resolve this ambiguity, **WIM** parameterization limits the dynamic range of **PDP** to 20 dB below the dominant peak and skips snapshots that do not provide required dynamic.

$$S(\tau_i|p) = \begin{cases} S(\tau_i|p) & S(\tau_i|p) \geq \max\{S(\tau_i|p)\}/100 \\ 0 & \text{otherwise} \end{cases}. \quad (4.24)$$

Fig. 4.7c shows a Cumulative Distribution Function (**CDF**) of delay spread from a fast train measurement, Sec. A.2.2. The above mentioned 20 dB noise thresholding has been utilized for **DS** computation.

**Cross-polarization ratios (XPR)** is defined as a power ratio between the co- and cross-polarized components of the received signal. To get the **XPR** the total powers for each polarization are calculated by accumulating the power of **PDP** over the delay-dimension:

$$P(p) = \frac{1}{n_{\tau}} \sum_{k=1}^{n_{\tau}} S(\tau_k|p). \quad (4.25)$$

If horizontally (H) and vertically (V) polarized antennas are used on both transmitting and receiving side, 4 different (Tx,Rx) polarization combinations can be made, so that  $p \in \{VV, VH, HV, HH\}$ . Depending on reference transmit polarization, it is possible to define vertical-to-horizontal and horizontal-to-vertical XPRs:

$$XPR_V = \frac{P_{VV}}{P_{VH}}, \quad (4.26)$$

$$XPR_H = \frac{P_{HH}}{P_{HV}}. \quad (4.27)$$

These quantities could be conveniently represented by matrix if we introduce convention that rows/columns correspond to transmitter/receiver polarization and the vertical precedes the horizontal polarization:

$$XPR = \begin{bmatrix} 1 & \frac{P_{VV}}{P_{VH}} \\ \frac{P_{HH}}{P_{HV}} & 1 \end{bmatrix}. \quad (4.28)$$

**Transmission loss** is normally presented in decibels as a function of distance. Therefore, the corresponding Tx-Rx distance ( $d$ ) has to be associated with the received power levels in order to estimate the transmission loss:

$$\bar{L}(d) = P_{Tx} + \sum_i G_i - \sum_i A_i - \bar{P}(d). \quad (4.29)$$

Additional input parameters are also required: transmitter power ( $P_{Tx}$ ), total antenna gain ( $\sum_i G_i$ ) and total cable attenuation ( $\sum_i A_i$ ). All co-polar realizations of  $P(d)$  collected during measurement are exploited to parameterize the model:

$$\bar{L}(d) = A \cdot \log_{10}(d) + B. \quad (4.30)$$

The coefficients ( $A, B$ ), defining the linear dependence of transmission loss from logarithmic distance, are determined by linear regression<sup>§</sup>:

$$\begin{bmatrix} L(d_1) \\ \vdots \\ L(d_n) \end{bmatrix} = \begin{bmatrix} 1 & \log_{10}(d_1) \\ \vdots & \vdots \\ 1 & \log_{10}(d_n) \end{bmatrix} \begin{bmatrix} B \\ A \end{bmatrix}. \quad (4.31)$$

The **WINNER** model uses explicit transmission loss formulas that are independent from other parameters. As an example, the path loss results for a rural scenario are given in Fig. 4.7b, with a curve fitting of the data and the free space loss as a reference.

---

<sup>§</sup>The **MATLAB** function `regress()` can be exploited to calculate transmission loss coefficients.

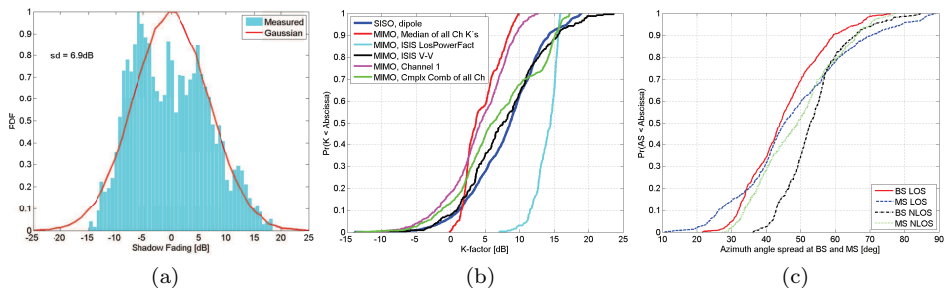


Figure 4.8: Distribution of WIM LSPs: a) shadow fading standard deviation for indoor-to-outdoor scenario, b) Rician K-factor: comparison of MIMO methods, c) azimuth angle spread for indoor scenario (Hentilä [97]).

**Shadow fading (SF)** expresses deviation of the measured data from expected (and modeled) transmission loss. The SF [dB] on Tx-Rx distance  $d_n, n = 1, \dots, N$ , represents difference between measured transmission losses  $L(d_n)$  and the loss  $\bar{L}(d_n)$  predicted by the model (4.30):

$$SF_n = L(d_n) - \bar{L}(d_n). \quad (4.32)$$

The SF is modeled as random variable with a zero mean Gaussian distribution. The standard deviation of the shadow fading is estimated as:

$$\sigma_{SF} = \sqrt{\frac{1}{N-1} \sum_{n=1}^N (SF_n)^2}. \quad (4.33)$$

Fig. 4.8a presents the PDF of the shadow fading for indoor-to-outdoor scenario.

**Narrowband Ricean K-factor** represents the ratio of powers between the dominant (LoS or NLoS) component and all other multi-path components. The narrowband CIR is emulated from wideband measurement by complex sum over delay-domain:

$$h_{NB}(t, s, u, p) = \sum_i h(t, \tau_i, s, u, p). \quad (4.34)$$

Only co-polar Tx/Rx polarization pairs,  $p \in \{VV, HH\}$ , are used and estimation is performed per subset  $G_j$  of MIMO channels that share the same AGC settings. This provides that the total narrowband powers are comparable within the selected subset of directional antennas. The K-factor is calculated using the Greenstein's moment's method [98] for each subset  $G_j$  and stationarity region  $T_i$ . The method of moments is based upon statistics of instant powers:

$$\mathbf{P}_{i,j} = \mathbf{P}(T_i, G_j) = \{\text{vec}\{\underline{h}_{NB}(t \in T_i, (s, u, p) \in G_j)\}^2\} = \{P_1, P_2, \dots, P_N\}. \quad (4.35)$$

The mean value and the variance of instant power are:

$$E\{\mathbf{P}_{i,j}\} = \frac{1}{N} \sum_{n=1}^N P_n, \quad (4.36)$$

$$Var\{\mathbf{P}_{i,j}\} = \frac{1}{N-1} \sum_{n=1}^N (P_n - E\{\mathbf{P}_{i,j}\})^2. \quad (4.37)$$

The K-factor in subset stationarity region  $T_i$  and  $G_j$  is:

$$K(T_i, G_j) = \frac{1}{\frac{E\{\mathbf{P}_{i,j}\}}{\sqrt{(E\{\mathbf{P}_{i,j}\})^2 - Var\{\mathbf{P}_{i,j}\}}} - 1}. \quad (4.38)$$

When directional antennas are used, a dominant component may contribute only to the particular subset. By selecting the maximum K-factor over subsets  $G_j$ , we tend to use only those antennas that sense the dominant component:

$$K(T_i) = \max_j \{K(T_i, G_j)\} \quad (4.39)$$

If distance information is available for all stationary regions  $T_i$ , dependence of K-factor over distance can be modeled, as shown in appendix on Fig. A.10. In WIM synthesis, randomly generated K-factor determines the power redistribution between LoS component and sum of all other components.

### Angular-Domain Analysis

Power Angular Spectrum (PAS) shows distribution of power over departure (D) and arrival (A) angles (directions) in both azimuth (A) or elevation (E),  $\phi \in \{AoD, EoD, AoA, EoA\}$ . After the structural parameters of MPCs have been determined by HRPE, the PAS is easily reconstructed for each snapshot in the form:

$$S(t_k, \phi) = \sum_i \|\alpha(t_k, \phi_i)\|_F^2, \quad (4.40)$$

where

$$\alpha = \begin{bmatrix} \alpha_{\varphi\varphi} & \alpha_{\varphi\theta} \\ \alpha_{\theta\varphi} & \alpha_{\theta\theta} \end{bmatrix}$$

defines polarimetric transmission coefficients, and  $\|\cdot\|_F$  is Frobenious norm. The resulting PASs are averaged over all snapshots in the stationary region:

$$S(\phi) = \frac{1}{n_t} \sum_{k=1}^{n_t} S(t_k, \phi). \quad (4.41)$$

Note that polarimetric properties of MPCs are expressed in polarization planes that are determined by directions of departure and arrival. Therefore, they can not be directly associated with reference V/H polarizations (variable  $p$  in delay-domain). Instead, the radiation characteristics of Tx and Rx antennas have to be defined first.

Angular Spread (AS) describes dispersion over the angular domain. Due to wrapping of angles,  $W : \phi \in (-\infty, \infty) \rightarrow [-\pi, \pi)$ , the angular offset can influence the calculated value of AS. In order to avoid ambiguity the 3GPP SCM specification [62] chooses the minimum AS value over all possible angular offsets. During this procedure, the effect of PAS angular shifts,  $\phi' = (\phi + \Delta)_W$ , is evaluated after wrapping to the range  $[-\pi, \pi)$ . The calculated  $m^{\text{th}}$  moment, and corresponding angular spread are therefore dependent on  $\Delta$ :

$$\overline{(\phi'(\Delta))^m} = \frac{\sum_k (\phi'_k)^m P(\phi'_k)}{\sum_k P(\phi'_k)}, \quad (4.42)$$

and

$$\sigma_{\phi'}(\Delta) = \sqrt{\overline{(\phi'(\Delta))^2} - \overline{\phi'(\Delta)}^2}. \quad (4.43)$$

The minimum value of AS over all circular shifts is chosen as SCM/WIM parameter:

$$\sigma_\phi = \min_{\Delta} \{\sigma_{\phi'}(\Delta)\}. \quad (4.44)$$

In WIM angle spreads are controlling wrapped Gaussian PAS of cluster centroids. Fig. 4.8c presents the CDF of angle spread for the indoor scenario.

### Correlation of LSPs

It is possible to distinguish two classes of LSP correlations in WIM: link-level cross-correlations and distance-based auto-correlations. Relevance of these correlations for WIM will be further analyzed in Sec. 6.3.3.

Link-level Cross-correlations are represented with correlation coefficient (3.27).

Distance-based Auto-correlations A correlation coefficient between two LSP realizations  $(X, X)_d$  being separated by distance  $d$  is calculated as:

$$\rho_X(d) = \frac{Cov\{(X, X)_d\}}{Cov\{X, X\}}, \quad (4.45)$$

where  $Cov\{X, Y\}$  designates covariance between random variables  $X$  and  $Y$ . At de-correlation distance  $d_{corr}$  correlation coefficient becomes lower than  $1/e$ .

## 4.4 Influence of Extraction Procedures on WIM Large-Scale Parameters

The properties of radio-channels were quantified through appropriate measures to enable comparison between different realizations, or to get suitable model representation. In past such measures are established for wideband SISO channels as well as for narrowband MIMO channels. The characterization of the multidimensional channel sounding data that depends upon time/Doppler shift, delay/frequency, spatial displacement and polarization of antennas inside Tx/Rx array, becomes more complicated as the number of relevant channel dimensions increases.

### Incomplete (Subspace-based) Measures

It would be desirable to process tera-bytes of channel sounding data in unique manner and undoubtedly get the definitive parameter values. Unfortunately, this is often not the case for multidimensional data, not only because measured signals are corrupted with noise, but also because incomplete measures (defined over subset of the available dimensions) introduce non-uniqueness of data processing sequence. The available and commonly used incomplete measures are usually characterizing data in respect to one dimension only. Due to lack of joint (complete) measures, radio-channels, being both wideband and MIMO, are still characterized separately with wideband and MIMO measures. Since usage of remaining dimensions is not predefined by the measure, a processing can be conducted in different ways. As a consequence, obtained parameters could not be compared without the complete knowledge about employed processing sequences. This section illustrates non-uniqueness of the incomplete (subspace-defined) measures in the context of WINNER wideband MIMO channel model parameterization. It is based on previously published results [71] and [99].

If calculated channel measures show dependence upon extraction procedure, the same numerical values could correspond to channels with different properties. Therefore, a fair comparison of the system features should always rely on the same procedures for channel characterization, meaning that the model parameterization procedure should not introduce any uncertainties. Therefore, the previous Sec. 4.3 defines processing sequence for the estimation of WIM parameters that are dependent (and calculated) only on a subset of multidimensional space.

## 4.4.1 Ambiguity of Delay-domain Features

### Influence of Stationarity Region Extent onto Probability Distribution

**Delay Spread** Since the mathematical formulation of Delay Spread (DS) [100] considers only a single delay-dimension of data set, there is an ambiguity when applying this measure to the whole data set.

The effect of averaging PDPs over different number of consecutive snapshots, prior DS computation, is shown in Fig. 4.9. Per-snapshot DS values are obtained according to (4.18) by averaging over 40 VV polarized (Tx,Rx) channels between ULA8 and Cube5 arrays, for single track of Ilmenau measurement (Sec. A.2.3). During measurement experiment approximately 7 snapshots (corresponding to different spatial samples) have been taken over the single wavelength distance,  $\lambda = 11.89$  cm. According to [100], appropriate averaging distance to suppress of small-scale effects in UHF range and SISO configuration is approximately  $40 \lambda$ , i.e. 4.7 m in the considered case.

Note that longer averaging of PDP results in the underestimated DS, if compared with per-snapshot estimates (i.e., mean curve over ST becomes lower for longer averaging, or the CDF curve shifts to the left). One possible interpretation is that the multipath structure changes within averaging window. This makes averaging over several tenths of wavelength too long. Following these findings, PDPs for the particular measurement are averaged over  $10\lambda$  before calculating parameters related to the time-delay domain (DS, Total Power, XPR). These findings match

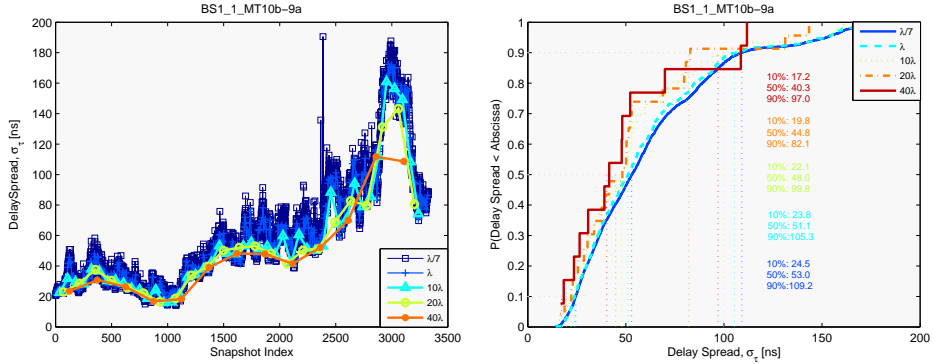


Figure 4.9: Impact of the *PDP* averaging over consecutive snapshots before calculating *DS*.

with *WIM1* bandwidth motivated limitation (related to noticeable delay shift) of 1m.

**K-factor** Direct impact of the selected stationary region (i.e., number of snapshots in *SS*) is also observed during *K*-factor estimation. By increasing the number of averaged snapshots in *SS*, we can increase obtained *K* values. The manipulation with *MIMO* subchannels will also impact the probability distribution of *K*-factor.

### Influence of Noise Thresholding on *DS* Statistics

Fig. 4.10b shows the impact of different noise level margins on two *PDP* realizations, having different dynamic range due to different *Tx-Rx* separation. The impact of *PDP* thresholding (4.19) on *DS* is evaluated for different values of noise margin  $M[\text{dB}] = 10 \cdot \log_{10}(m)$  and illustrated in Fig. 4.10 for car-to-bridge measurement, Sec. A.2.2.

The amount of *DS* variations along the measurement track will be inversely proportional to the applied thresholding margin, Fig. 4.10a. If *DS* results for  $M = 3$  dB are not seriously impacted by noise, than significant information is lost for an increased thresholding margin. The loss of dynamic range, when *Tx-Rx* distance exceeds 120 m, further pronounces this effect. This will impact other statistical features of *DS* like distance-based autocorrelation function, Fig. 4.11a.

The *ACF* curve for the  $M = 3$  dB is close to the other two up to a distance of 120m, but from this point this curve shows completely different behavior. The uncertainty remains: is the first curve corrupted by the noise samples, or the existing similarity is lost during the reduction dynamic range used for *DS* calculation.

Impact of noise thresholding to *DS* probability distribution is demonstrated in Fig. 4.11b. When lower margin is used for *PDP* thresholding, *DS* measure is increasing (cdf curves are shifted to the right) because larger portion of wideband power is taken into account. Since it is not possible to differentiate between contributions of “real *PDP*” and noise, it is not clear which of above curves offers the best estimate.

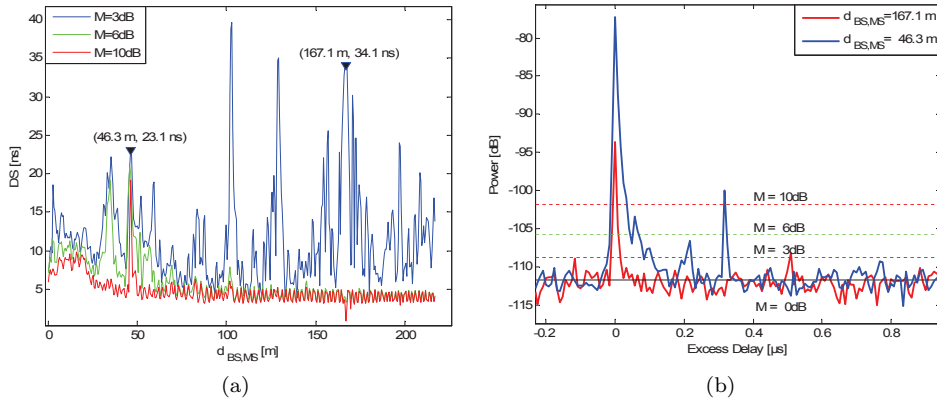


Figure 4.10: Influence of PDP noise thresholding onto DS values: a) DS along measurement route, b) impact of noise level margins on PDPs at different Tx-Rx separations [99].

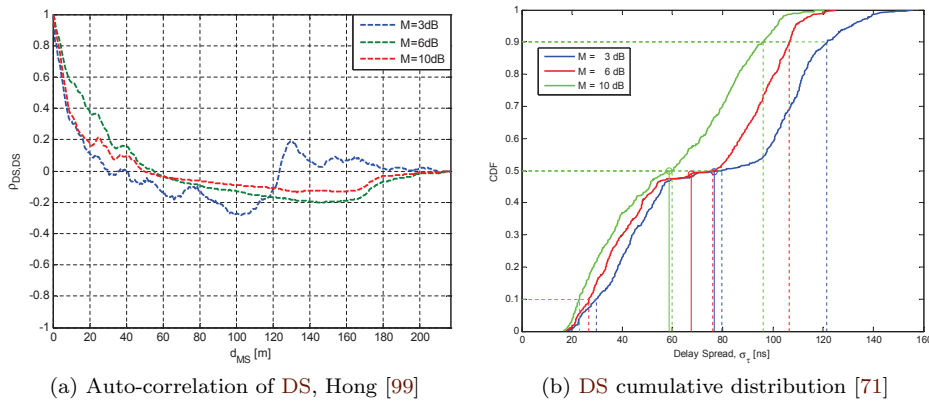


Figure 4.11: Influence of PDP noise thresholding onto DS statistics.

From the viewpoint of dynamic range in PDP:

$$DR \text{ [dB]} = 10 \cdot \log_{10} \left( \frac{\max \{S(\tau)\}}{P_N \cdot m} \right), \quad (4.46)$$

an increase of cutting level  $P_N \cdot m$  or decrease of maximal PDP level with distance would influence  $S(\tau)$  in the similar way. If the dynamic range is too small (due to large distances or noisy receiver), obtained parameter estimate (DS or MED) becomes biased since significant part of PDP is discarded. This reduces confidence in DS realizations from lower right corner of Fig. 4.12. This can be avoided only if some kind of data filtering (selection) is applied and parameters are estimated in subsets of available data. Data filtering increases reliability of estimated parameters and thus influences experimental distribution of the evaluated parameters, as shown in Fig. 4.13a. For subspace analysis in the delay domain, it was shown that the



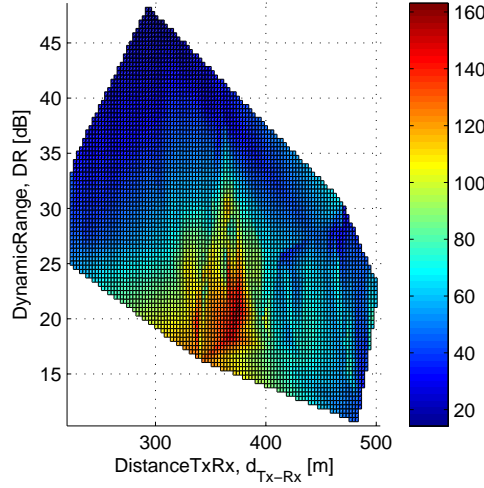


Figure 4.12: Dependence of calculated  $DS$  in [ns] from dynamic range and  $Tx-Rx$  distance.

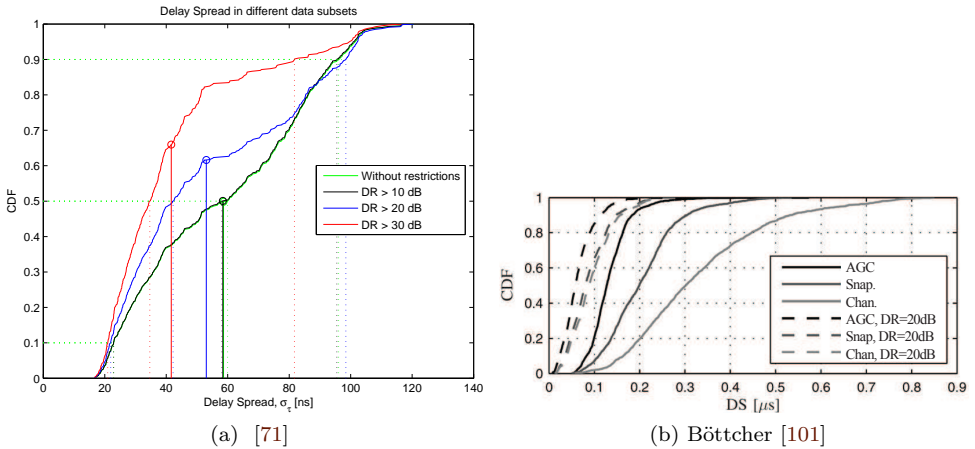


Figure 4.13: Impact of data filtering and noise estimation to resulting  $DS$  CDF: a) different data subsets for noise margin  $M = 10$  dB, b) different noise estimation approaches, with and without  $DR$  fixing to 20 dB.

estimated channel parameters could be also dependent on control parameters of the processing sequence. The influence of noise cutting level to **WIM** parameters calculated in delay domain is mitigated by using fixed observation range of 20 dB. This decision represents part of agreed procedure for **WINNER** model parameter estimation that should resolve ambiguity of both incomplete measures and control parameters of processing sequence. The effect of fixing **PDP** dynamic range to 20 dB is given in Fig. 4.13b: after the reduction of **DR** by thresholding the **DS CDF** curves shift to left side. This figure also analyzes the impact of the used data subset for noise level estimation: i) within groups of the spatial  $(s, u, p)$  subchannels having the same **AGC** settings, as described in Sec. 4.3.2, ii) for all **CIRs** in snapshot, and iii) for each **CIR** individually. The individual estimation of noise gives the largest **DS** values: due to reduced number of available samples a reliability is reduced, and possible underestimation of noise level increases **DS** values. The effect is similar if samples of data exhibited to different noise levels are mixed and the obtained noise-level estimate used to threshold all realizations (the second approach): the noise in some **PDP** realizations will exceed the threshold more frequently and cause increase of **DS** values.

Although examples are given for **DS** only, equivalent influence can be found in all parameters that could be calculated in the delay domain: **MED**, total received power, transmission loss, shadowing fading, etc.

### Impact of the Sounder's Per-Channel AGC onto XPR

In order to acquire better observation of the channel, RUSK HyEff sounder uses dynamic **AGC**, meaning that each measured **MIMO** subchannel, defined as combination of the one Tx and one Rx antenna element, has an independent gain control. This feature requires proper interpretation during the channel characterization: in Fig. 4.14a it is showed that cross-polar losses are partially compensated and therefore the observed dynamic ranges are similar for co-polarized (VV and HH) and cross-polarized combinations of Tx and Rx antenna elements. As a consequence, reported **XPR** values will be slightly reduced.

### Impact of the Terminal Height and Radiation Patterns to Received Power Level

By looking into the total received power per subgroups of the Rx antenna elements (Fig. 4.14b), it is possible to observe variations of the received power w.r.t. the antenna height above ground. A difference in RF attenuation between multiplexers has only limited impact to the observed power difference between the **MIMO** cube on top of the array and the remaining two rings of the array.

The significant dependence of the transmission loss from the array radiation pattern can be found for certain array geometries.

## 4.4.2 Equivalence of Estimates Obtained by Different Procedures

The delay-domain parameters could be also estimated after **HRPE**, from structural (**MPCs**) parameters. The **MPC** parameters are typically covering all available dimensions of the measured data and there is no ambiguity coming from subspace description. The problem in this case is that only limited number of **MPCs** could

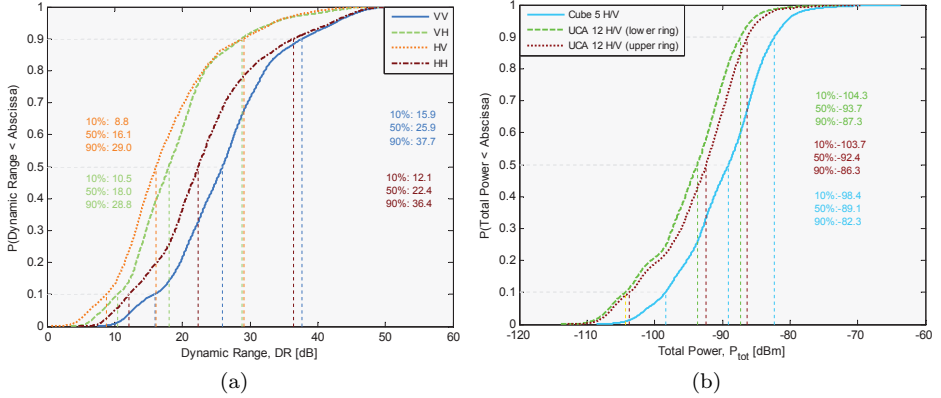


Figure 4.14: Impact of the measurement setup/equipment: a) CDF of per-snapshot dynamic ranges, for different combinations of  $T_x$  and  $R_x$  antenna element polarizations, b) distribution of the absolute received power for receiver elements being at different heights.

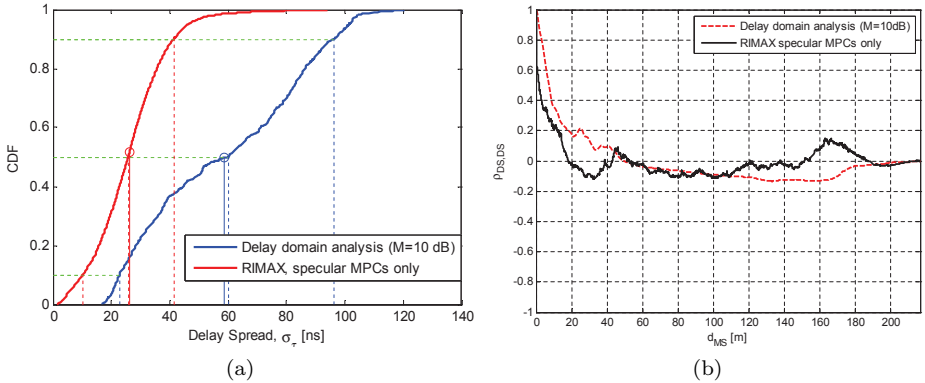


Figure 4.15: Comparison of DS statistics obtained by different extraction procedures: a) Cumulative Distribution Function (CDF), b) Auto-Correlation Function (ACF).

be reliably estimated. Therefore estimated MPC, that provide joint multidimensional representation, do not describe complete propagation process. This problem is mitigated in RIMAX by introduction of a mixed model in which the remainder (DMC) is represented only in the delay domain. However, this makes the structural parameter domain less preferable for calculation of the delay-related features.

From Fig. 4.15a, it can be seen that obtained DS measures with and without spatial reconstruction may differ considerably. In the delay domain analysis (without spatial reconstruction), given RIMAX DS measure would correspond to the low observation ranges. This however can not be true since 95% of total (signal+noise) power is contained in the presented RIMAX results. One possible reason for observed difference is spatial filtering of antenna field patterns: in RIMAX results antenna is de-embedded while delay domain data is fully dependent on measurement

antenna. (De-embedding can not be done if estimation is performed in delay domain only since directions of departure/arrival can not be resolved). Different delays are in general related to different departure/arrival angles. Since antennas are introducing spatially selective gain to MPCs, the PDP will experience re-distribution of total power between components and final measure will be distorted. If final goal is to characterize propagation channel independently from the measurement antenna, it can be achieved only with algorithms for complete reconstruction of the measured space. However, difference observed in Fig. 4.15a can be also the consequence of assumed SoS data model: DS calculated from the specular RIMAX components does not contain contribution of the DMCs, since the latter that can not be resolved in the angular domain. This means that distribution of the specular components over delay does not necessarily reflect the power distribution of complete continuous PDP.

Fig. 4.15b presents the auto-correlation of DS with and without spatial reconstruction from the car-to-bridge measurements. Up to  $d_{ms} = 45$  m the auto-correlation of DS calculated from specular RIMAX results is lower than that from delay domain analysis and a parallel shifting of the curves could be observed. This shifting is probably caused by omitting DMC part from analysis. Since a similarity of the transmission environment defines the auto-correlation behavior of DS [102], [103], [99], it is reasonable to conclude that DMC part of RIMAX hybrid model significantly contributes to the correlation measure and should not be omitted.

### Impact of Computation Procedure to K-factor Statistics

In [97], the K-factor empirical CDFs are determined in several ways and compared with reference SISO data being generated by dipole antennas. It is found that the vertical component of the ISIS algorithm best reflects the reference data, Fig. 4.8b.

The results presented in this section demonstrate that estimated parameters could not be taken as granted, without complete insight into extraction procedure. Accordingly, the channel model parameters are uniquely related to the measurement data set only for completely defined processing sequence. From the above arguments it follows that complete insight into measurement setup and processing sequence, being used for channel model parameterization, is necessary if we are willing to compare the channel model parameters.

## Chapter 5

---

# Representation of Multiple Scenarios by a Generic Model

---

The flexible structure of **GSCMs** enables the representation of different propagation environments by simple adjustment of model parameters, which is referred to as *generic* property. The generic models introduce abstract classes called *scenarios* that act as stochastic equivalents for many similar radio environments. As discussed in [55] these scenarios are not necessarily distinguished by the quantification of parametric space, but they represent a convenient terminology to designate typical deployment and propagation conditions. The morphology-based classification of radio environment does not imply that model control parameters could not have identical realization in different classes [8]. Historically, it was COST 207 [104] that started classifying environments based on the type of dispersion (delay spread and delay window) and involving some intuitive consideration of the (rather limited) parameter space was involved. But these types of differences have (almost) never been sought later on when defining new scenarios, especially following deployment schemes.

Nowadays we can distinguish between two major classes of generic models: COST 259/273/2100 ([10], [60] and [105] resp.) and 3GPP **SCM** [34]/**WINNER** [5], [63]. These generic models have been made by joint effort of many institutions, otherwise provision of parameters for different scenarios would be unattainable. Despite different model structures, significant overlap of propagation scenario definitions exists between **SCM/WINNER** and **COST** models as shown in Sec. 6.5 and [72]. In listed channel models, the scenarios are developed/parameterized to represent the the complete radio environment classes.

The need for generic models follows from the ever growing concept of heterogeneous networks, requiring simultaneous representation of multiple-scenarios or transitions between scenarios. For this purpose scenarios of generic models provide a uniform modeling approach and decrease the perceived complexity of handling different environments.

With respect to the number of scenarios, design and performance evaluation of communication systems will cost less time and effort with smaller numbers of scenarios. Since every environment is specific, the classification of propagation environments into the different (reference) scenarios is not a simple task: how many classes suffice and how much divergence within a class should be tolerated? Obviously, a meaningful answer can be provided only if we have a metric to quantify the similarity between propagation environments. Providing such a metric is the main goal of this chapter.

In absence of a scenario distance metric, reference scenarios are typically formed as a combination of system deployment schemes, mobility assumptions and narrative description of environments, as illustrated in the Sec. 5.1 for the **WINNER** reference propagation scenarios. For the purpose of comparison, the **WINNER** scenarios are in Sec. 5.2 approximated by Multi-Variate Normal (**MVN**) distributions of Large-Scale Parameters. By disregarding transmission loss and decorrelation distance, the distance measure is removed from scenario definitions. The mean Kullback-Liebler divergence is proposed in Sec. 5.3 for comparison of **MVN** scenario and measurement equivalents. For those scenarios/measurements where **WIM** correlation coefficients form a negative definite symmetric matrix, the alternating projection method is used to determine the closest correlation matrix. The resulting set of correlation coefficients is used for quantification of scenario/measurement divergence.

The Sec. 5.4 describes necessary steps for the synthesis of **WINNER** channel model.

## 5.1 WINNER Reference Propagation Scenarios

The **WINNER** system is designed to support ubiquitous coverage using different system-deployment schemes for Wide Area (**WA**), Metropolitan Area (**MA**) and Local Area (**LA**). Each deployment scheme was described by as few Reference Propagation Scenarios (**RPSs**) as possible. The outcome is that the **WINNER** scenarios cover some typical cases, without intent to encounter all possible propagation environments. The introduced **RPSs** abstract the effects of the radio-propagation to the overall system design.

The **WINNER** reference propagation scenarios [5] are determined by the aspects that have immediate impact on the radio-signal propagation:

- coverage type (e.g. ubiquitous, localized),
- propagation environment (e.g. indoor, outdoor),
  - LoS/NLoS condition,
  - limited distance range,
- terminal positions and heights with respect to environment,
- mobility model (terminal speed),
- carrier frequency range/bandwidth.

Table 5.1: WINNER Reference Propagation Scenarios.

Scenario	Definition	LoS/NLoS	Mob. [km/h]	AP ht [m]	UE ht [m]	Distance range [m]	Coverage
A1 (In building)	Indoor small office/residential	LoS/ NLoS	0 - 5	1 - 2.5	1 - 2.5	3 - 100	LA
A2	Indoor-to-outdoor	LoS/NLoS	0 - 5	2 - 5 + floor height	1 - 2	3 - 1000	LA
B1 (Hotspot)	Typical urban micro-cell	LoS/NLoS	0 - 70	Below RT (3 - 20),	1 - 2	10 - 5000	LA, MA
B2	Bad urban micro-cell	LoS/NLoS	0 - 70	Below RT	1 - 2	10 - 5000	MA
B3 (Hotspot)	Large indoor hall	LoS	0 - 5	2 - 6	1 - 2	5 - 100	LA
B4	Outdoor-to-indoor	LoS/NLoS	0 - 5	Below RT	1 - 2	3 - 1000	MA
B5a (Hotspot, Metropol.)	LoS stat. feeder, rooftop to rooftop	LoS	0	Above RT.	Above RT.	30 - 8000	MA
B5b/C5b (Hotspot, Metropol.)	LoS stat. feeder, street-level to street-level	LoS	0	3 - 5	3 - 5	20 - 400	MA
B5c (Hotspot, Metropol.)	LoS stat. feeder, below-rooftop to street-level	LoS	0	Below RT, e.g. 10	3 - 5	20 - 1000	MA
B5d (Hotspot, Metropol.)	NLoS stat. feeder, above rooftop to street-level	NLoS	0	Above RT, e.g. 32	3 - 5	35 - 3000	MA
B5f	Feeder link BS $\rightarrow$ FRS. Approximately RT to RT level	LoS/OLoS/NLoS	0	RT e.g. 25	RT e.g. 15	30 - 1500	WA,
C1 (Metropol.)	Suburban	LoS/NLoS	0 - 120	Above RT, 10 - 40	1 - 2	30 - 5000	MA, WA
C2 (Metropol.)	Typical urban macro-cell	NLoS	0 - 120	Above RT, e.g. 32	1 - 2	10 - 5000	MA, WA
C3	Bad Urban macro-cell	LoS/NLoS	0 - 70	Above RT	1 - 2	50 - 5000	-
C4	Outdoor to indoor.	LoS/NLoS	0 - 5	Above RT	1 - 2 + floor height	50 - 5000	MA
D1 (Rural)	Rural macro-cell	LoS/ NLoS	0 - 200	Above RT, e.g. 45	1 - 2	35 - 10000	WA
D2a	Moving networks: BS - MRS, rural	LoS	0 - 350	20 - 50	2.5 - 5	30 - 3000	WA
D2b	Moving networks:MRS - MS, rural	LoS/ OLoS/ NLoS	0 - 5	>2.5	1 - 2	3 - 100	WA

**WINNER** Reference Propagation Scenarios (RPSs) are based on “typical” environments, meaning that physical parameters of environment such as average rooftop height, width of roads, distance between buildings, road orientation with respect to direct path, size of rooms, number of floors between **BS** and **MT**, are not explicitly used. Some of them are implicitly included into **WINNER** scenario definitions, in order to reflect the actual parameters used during experimental characterization.

Starting from the premise that stochastic properties of a radio environment could be abstracted by scenarios, a generic **MIMO** channel model is developed within the **WINNER** project. Thus, all **WINNER** Reference Propagation Scenarios (RPSs) are represented by generic **WIM** channel model. The process of empirical channel characterization and scenario-specific parameterization of the *WINNER Channel Model* (**WIM**) is illustrated in Fig. 5.1. Due to different propagation mechanisms under **LoS** and **NLoS** conditions, these conditions are distinguished and separately characterized in all applicable physical environments.

The characterization of the reference propagation scenarios and the parametrization of the generic model are based on channel sounding results. In **IST-WINNER** projects wideband **MIMO** measurements were carried out in 2 and 5 GHz frequency ranges. In order to collect relevant data, a large number of measurement campaigns has been carried out during the project. Most of them were done using Medav’s **RUSK** [73] and Elektrobit’s **Propsound** [106] channel sounders. However, the realization of large-scale campaigns and the subsequent processing of the results are both complex and time consuming. As a consequence, the **WINNER** “scenario” is formed on basis of measurement results that are gathered by different institutions and are individually projected on the parameter set of **WINNER** model. Papers [107], [71], [108], [109] present a few of the **WINNER** measurement campaigns and some results extracted from the data. These measurements were conducted in radio environments providing the best possible match with defined reference scenarios. For that purpose, the position and movement of communication terminals were chosen according to the typical usage pattern. The “typical usage” is related to the environments that are found in European and North-American countries. At the end of Phase II, **WIM** was parameterized for 12 different scenarios, being listed in Tab. 5.1: A1–Indoor (small office/residential), A2–Indoor-to-outdoor, B1–Typical urban micro-cell, B2–Bad urban micro-cell, B3–Indoor hotspot, B4–Outdoor-to-indoor, B5–Stationary feeder links, C1– Suburban, C2–Typical urban macro-cell, C3–Bad urban macro-cell, D1–Rural macro-cell, and D2–Moving networks. For detailed descriptions of the scenarios refer to [110] and [111]. The measurement environments used to parametrize B3 and D2a **WINNER** scenarios, and to validate C2 scenario, are shown in Sec. A.2. For these measurements equivalent representation in **WINNER** parametric space is provided. The complete overview of **WINNER** measurements can be found in [112]. The full set of **WIM** RPS parameters can be found in Sec. 4.3 and 4.4 of the **WINNER** deliverable D1.1.2 [5], while selection is contained in Tables 5.2, 5.3 and 5.12.



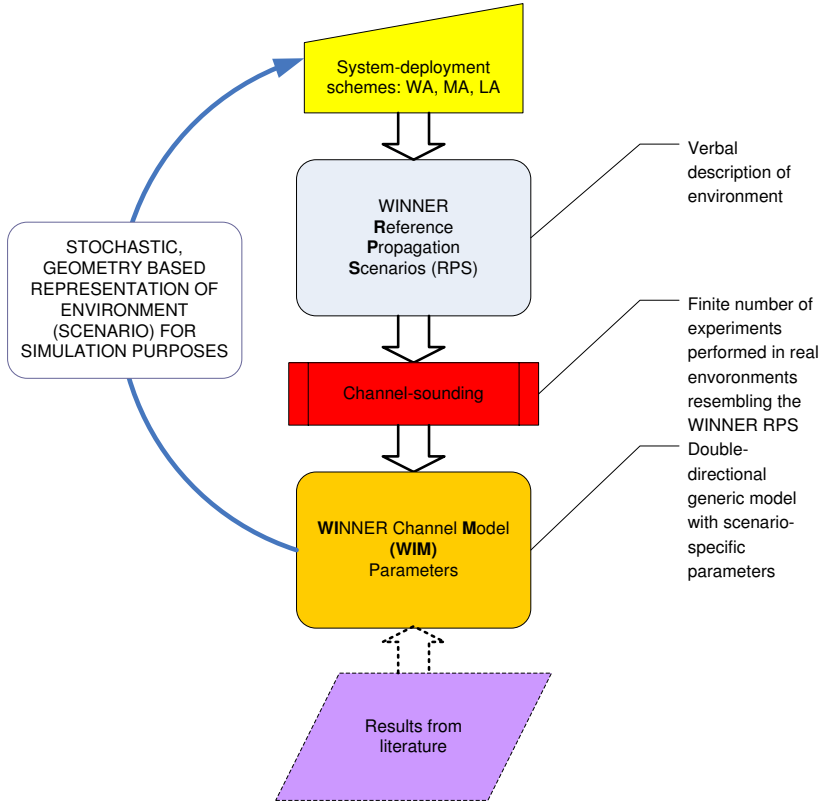


Figure 5.1: Genesis and representation of WINNER reference propagation scenarios. [72]

## 5.2 WIM TLSPs Viewed as Correlated Multivariate Random Process

The **WINNER** model requires random data to drive it, and correlations between the different dimensions make this model realistic. General methods for generation of Random Variables (**RVs**) with targeted probability distribution and second-order statistics (auto-correlation over time) have been suggested in [113], [114]. These methods reproduce statistical behavior of a random process w.r.t. its realization over time, by using a transformation of the Gaussian autoregressive process. In order to avoid complex matching of correlations between original and transformed domain, the **LSPs** are first mapped into new variables (*Transformed LSPs*) having Gaussian distributions and the subsequent analysis of **LSP** inter-dependence is performed in transformed domain [62], [5]. For **LSP**  $P_i$  with **CDF**  $F_i$ , the necessary mapping\* could be determined in the form of  $P_i = F_i^{-1}(\Phi(Q_i))$ , where  $Q_i$  designates the transformed **LSP** with normal **CDF**  $\Phi$ . Using a linear transformation

$$\mathbf{Q} = \mathbf{C}\boldsymbol{\xi} + \mathbf{b} \quad (5.1)$$

\*The solution of an inverse problem, [115].

of the standard multivariate normal process  $\boldsymbol{\xi}$  with distribution  $\mathcal{N}_{\boldsymbol{\xi}}(\mathbf{0}_{M \times 1}, \mathbf{I}_{M \times M})$ , a process  $\mathbf{Q} = [Q_1, Q_2, \dots, Q_M]^T$  with the targeted covariance matrix  $\mathbf{C}\mathbf{C}^T$  and mean  $\mathbf{b}$  could be easily reproduced.

### Multivariate Normal Distribution of TLSPs

The multivariate normal probability density function of a  $k$ -dimensional random vector  $\mathbf{x} = [x_1, x_2, \dots, x_k]^T \sim \mathcal{N}(\boldsymbol{\mu}, \boldsymbol{\Sigma})$  can be expressed as [116]

$$f(\mathbf{x}) = \frac{1}{(2\pi)^{k/2} |\boldsymbol{\Sigma}|^{1/2}} \exp\left(-\frac{1}{2}(\mathbf{x} - \boldsymbol{\mu})^T \boldsymbol{\Sigma}^{-1}(\mathbf{x} - \boldsymbol{\mu})\right), \quad (5.2)$$

where

$$\boldsymbol{\mu} = \mathbb{E}[\mathbf{x}] \in \mathbb{R}^k \quad (5.3)$$

is  $k$ -dimensional mean vector, and  $k \times k$  covariance matrix is

$$\boldsymbol{\Sigma} = \text{Cov}[\mathbf{x}, \mathbf{x}] = \mathbb{E}[(\mathbf{x} - \mathbb{E}[\mathbf{x}])(\mathbf{x} - \mathbb{E}[\mathbf{x}])^T] \in \mathbb{R}^{k \times k}. \quad (5.4)$$

Although the structuring of the **WIM TLSP** distribution parameters is slightly different, they basically represent maximum-likelihood estimates of a multivariate normal (**MVN**) distribution parameters (5.3) and (5.4)<sup>†</sup>. It is therefore possible to reconstruct the full covariance matrix of **MVN** distribution by the following scaling:

$$\boldsymbol{\Sigma} = \boldsymbol{\Sigma}_0^{\frac{1}{2}} \boldsymbol{\rho} \boldsymbol{\Sigma}_0^{\frac{1}{2}}, \quad (5.5)$$

where

$$\boldsymbol{\Sigma}_0 = \text{diag}(\sigma_1^2, \sigma_2^2, \dots, \sigma_k^2) \quad (5.6)$$

represents the diagonal covariance matrix of the uncorrelated **LSPs**. The entries of matrix  $\boldsymbol{\rho}$ , denoted  $\rho_{i,j}$ , correspond to covariance coefficients between **TLSPs**  $i$  and  $j$ . Accordingly, every **WINNER** scenario can be abstracted with (up to) 8 dimensional normally distributed random process where relevant dimensions describe different **LSPs** listed in Tab. 3.1. In the given case, the **MVN** process offers a straightforward approximation of **WINNER** scenario since the majority of them have identical cluster structure.

#### 5.2.1 Parameters of WINNER Channel Model Describing MVN Distributions

In order to ensure the traceability of the presented results, the relevant subset of **WINNER** parameters is given in Tables 5.2 and 5.3. These tables also include the **MVN** distribution parameters estimated from Ilmenau (IL) and Dresden (DR) measurements, Sec. A.2.3. Additionally, Tab. 5.3 contains the modified correlation coefficients  $\hat{\rho}$  that form positive definite correlation matrices. They will be used for scenario representation instead of original coefficients, for quantification of the scenario divergence in Sec. 5.3.

---

<sup>†</sup>The random variables showing very specific dependence are not jointly normally distributed even if their marginal distributions are normal. Since only dependence between continuous **WIM LSPs** is expressed by the correlation coefficient (3.27), we assume without explicit proof that the vector of **LSPs** will have jointly normal distribution.





Table 5.4: Approximation of empirical corr. matrix  $\rho$  with positive definite matrix  $\hat{\rho}$  is performed by APM: Frobenius distance (FD) between  $\rho$  and  $\hat{\rho}$ , the required number of decimal places (DP) in  $\hat{\rho}$  and maximal correction of original correlation coefficients  $\max\{|\Delta\rho_{i,j}|\}$  will be functions of the substituting eigenvalue  $\epsilon$ .

		10 <sup>-1</sup>			10 <sup>-2</sup>			10 <sup>-3</sup>			10 <sup>-6</sup>		
Scenario	Propagation	$\ \cdot\ _F$	DP	$\max( \Delta\rho )$	$\ \cdot\ _F$	DP	$\max( \Delta\rho )$	$\ \cdot\ _F$	DP	$\max( \Delta\rho )$	$\ \cdot\ _F$	DP	$\max( \Delta\rho )$
A1	LoS	0.245	1	0.1	0.123	2	0.04	0.108	2	0.03	0.108	2	0.03
B4	NLoS	0.316	1	0.1	0.241	2	0.1	0.227	3	0.091	0.226	4	0.091
B1	LoS	0.374	1	0.1	0.269	2	0.09	0.257	3	0.085	0.255	3	0.085
B1	NLoS	0.2	1	0.1	0.066	2	0.02	0.056	3	0.019	0.055	3	0.019
C1	LoS	0.346	1	0.1	0.203	2	0.07	0.191	3	0.065	0.19	4	0.064
C1	OLoS	0.346	1	0.1	0.203	2	0.07	0.191	3	0.065	0.19	4	0.064
C1	NLoS	0.245	1	0.1	0.245	1	0.1	0.245	1	0.1	0.245	1	0.1
C2	LoS	0.374	1	0.1	0.193	2	0.06	0.174	3	0.058	0.173	6	0.058
C2	OLoS	0.374	1	0.1	0.193	2	0.06	0.174	3	0.058	0.173	6	0.058
C2	NLoS	0.548	1	0.2	0.338	2	0.13	0.333	3	0.129	0.332	5	0.129
DR	LoS	0.168	1	0.048	0.168	1	0.048	0.168	1	0.048	0.168	1	0.048
DR	NLoS	0.116	1	0.046	0.116	1	0.046	0.116	1	0.046	0.116	1	0.046
IL	LoS	0.133	1	0.043	0.133	1	0.043	0.133	1	0.043	0.133	1	0.043
IL	NLoS	0.144	1	0.047	0.144	1	0.047	0.144	1	0.047	0.144	1	0.047

### 5.2.2 Problem of Negative Definite Covariance Matrices

In some cases the matrix of **WIM** correlation coefficients ( $\boldsymbol{\rho}$ ) is not positive semi-definite, i.e.  $\boldsymbol{\rho} < 0$ . The problem manifests itself only for scenarios with resolved elevation angles (Tab. 5.4) where the dimensionality of the MVN distribution is increased from 6 (**LoS**) / 5 (**NLoS**) to 7/6 or 8/7. The problem is, however, not related to the number of dimensions or elevation parameters themselves since simple removal of elevation dimension(s) does not resolve it. This means that correlation coefficients between **WINNER LSPs** analyzed jointly do not form a proper *Correlation Matrix* (**CM**) – even without elevations.

It is observed that the number of decimal places used for representation of Correlation Matrix (**CM**) elements cannot be arbitrarily reduced since resulting matrix may become negative definite. Since individual coefficients in **WINNER** parameter tables are expressed using only one decimal place, it is possible that this lack of precision causes negative definite **CM** for scenarios with an increased number of dimensions.

In order to enable the comparison of problematic scenarios their correlation coefficients have to be slightly modified to form positive definite **CM**. The “real” correlation matrix is computed using Alternate Projections Method (**APM**) [117] [118]. For a given symmetric matrix  $\boldsymbol{\rho} \in \mathbb{R}^{k \times k}$  this method finds the nearest correlation matrix  $\hat{\boldsymbol{\rho}}$  that is (semi) definite and has a unity main diagonal. The solution is found in the intersection of the following sets of symmetric matrices  $S = \{Y = Y^T \in \mathbb{R}^{k \times k} | Y \geq 0\}$  and  $U = \{Y = Y^T \in \mathbb{R}^{k \times k} | y_{ii} = 1, i = 1, \dots, k\}$ . The iterative procedure in  $n$ -th step applies updated Dykstra’s correction  $\Delta S_{n-1}$ , and subsequently projects intermediate result to both matrix sets, using projections  $P_S$  and  $P_U$ :

$$\begin{aligned}
 &\Delta \mathbf{S}_0 = 0, \mathbf{Y}_0 = \boldsymbol{\rho}, n = 0 \\
 &do \\
 &\quad n = n + 1 \\
 &\quad \mathbf{R}_n = \mathbf{Y}_{n-1} - \Delta \mathbf{S}_{n-1} \\
 &\quad \mathbf{X}_n = P_S\{\mathbf{R}_n\} \\
 &\quad \Delta \mathbf{S}_n = \mathbf{X}_n - \mathbf{R}_n \\
 &\quad \mathbf{Y}_n = P_U\{\mathbf{X}_n\} \\
 &while \|\mathbf{Y}_n - \mathbf{Y}_{n-1}\|_F < tol
 \end{aligned} \tag{5.7}$$

The projection  $P_S$  replaces all negative eigenvalues of the matrix with a small positive constant  $\epsilon$  and  $P_U$  forces ones along the main diagonal. The procedure stops when Frobenius distance  $\|\cdot\|_F$  between  $\mathbf{Y}_n$  projections from two consecutive iterations drops below a predefined tolerance  $tol$ . Note, however that the small tolerance parameter does not insure that Frobenius Distance (FD) from the original matrix is equally small.

The positive definite approximation  $\hat{\boldsymbol{\rho}}$  obtained by APM will depend on the selected parameters  $\epsilon$  and  $tol$  [119]: for  $tol = 10^{-10}$ , the effect of eigenvalue  $\epsilon$  to Frobenius distance  $FD = \|\boldsymbol{\rho} - \hat{\boldsymbol{\rho}}\|_F$  is illustrated in Tab. 5.4. The results show that FD decreases when a smaller value of  $\epsilon$  is used to substitute originally

negative eigenvalues. However, the selection of small  $\epsilon$  will proportionally increase the eigenvalues and coefficients of the inverse correlation matrix,  $\hat{\rho}^{-1}$ . This will consequently increase the dissimilarity with all other scenarios. As compromise, the new **WINNER** correlation coefficients corresponding to positive definite matrix are recomputed for  $\epsilon = 10^{-2}$  and  $tol = 10^{-10}$  and given in Tab. 5.3. The maximal absolute modification of original correlation coefficients per scenario,  $max\{|\Delta\rho_{i,j}|\}$ , where  $\Delta\rho_{i,j} = \rho_{i,j} - \hat{\rho}_{i,j}$ , is given in Tab. 5.4. The highest absolute correction  $\Delta\rho = 0.13$  is applied to C2-NLoS scenario.

The minimum number of decimal places required to keep  $\hat{\rho}$  positive definite is determined for different values of  $\epsilon$  and listed in Tab. 5.4. The results show that smaller Frobenius distance requires higher precision for saving coefficients. For  $\epsilon = 10^{-2}$  two decimal places are sufficient to express correlation coefficients for all scenarios (Tab. 5.3).

### 5.2.3 Distances in WIM Scenarios

Although **WIM** describes the propagation environment implicitly within **LSP** parametric space, it is still using distance to govern transmission loss and spatial variations of **LSP** realizations.

Local Stationarity Region represents a larger area where multipath structure of physical propagation channel does not change significantly (“local region of stationarity” [120], “drop” [34], “channel segment” [5]) and it is therefore characterized by a single realization from multidimensional **LSP** distribution. In **WINNER** model it is conveniently assumed that the extent of a Local Stationarity Region can be represented by a scenario-dependent constant (*decorrelation distance*) that is independent of the **LSP** cross-correlations.

Both transmission loss and decorrelation distance are deterministic features in **WIM**. They do not impact **MVN** distribution of **TLSPs** and could be analyzed independently. Therefore, we investigate **MVN** process as joint model for **WINNER** **LSP** marginal distributions and cross-correlation coefficients. This representation of multidimensional channel, on the scenario scale, can be considered as a generalization of the 1-D small-scale fading channel approach, where stochastic properties of instantaneous envelope are characterized by **PDF**.

## 5.3 Quantification of Distances Between WINNER Scenarios

For objective comparison and classification of measurements into scenario classes a metric is required to quantify the distance between reference scenarios and measurements. Since a generic model uses the same set of parameters for representing different scenarios, this parameter set provides a convenient base for scenario comparison. The parameter space of the **WINNER** model is, among others, described by normal probability distributions and correlation coefficients that provide a suitable space for comparison.

As stated in Sec. 5.2, the parameter set of **WINNER** model is equivalent to the parameters of the multivariate normal distribution. Therefore, all measurement projections and reference scenarios share the same parameter set and could be treated as multivariate probability distributions. This enables the introduction

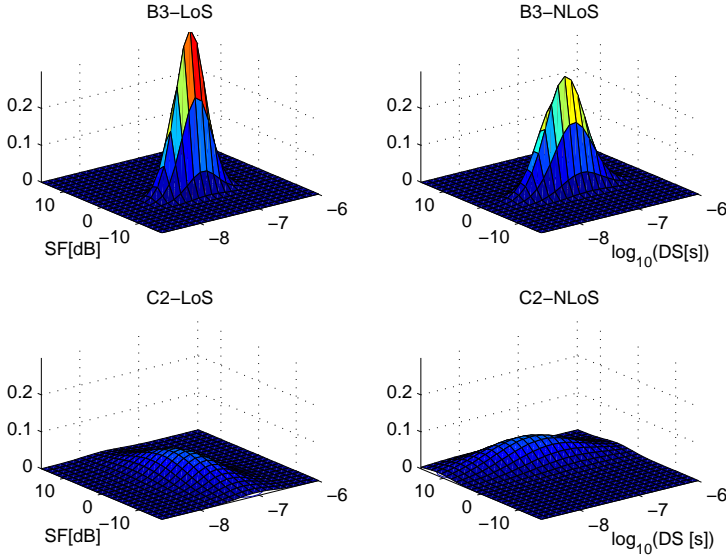


Figure 5.2: Comparison of joint  $(DS, SF)$  PDFs for B3 and C2 WINNER scenarios, for LoS and NLoS propagation [121].

of a metric to quantify the divergence (distance) between different projections of measurements on the parameter set of the model, and between representations of different reference scenarios

In order to illustrate the (dis)similarity between B3 and C2 WINNER scenarios under LoS and NLoS propagation, joint 2-D PDFs of delay spread and shadow fading are presented in Fig. 5.2. We observe that these scenarios have differences, but some kind of similarity measure will be useful. Having in mind that we want to quantify the distance between two distributions  $P$  and  $Q$ , it is possible to apply some form of relative entropy, e.g., Kullback-Leibler (KL) divergence [122]:

$$D_{\text{KL}}(P||Q) = \int_{\mathbf{x} \in \mathbb{R}^k} p(\mathbf{x}) \log_2 \frac{p(\mathbf{x})}{q(\mathbf{x})} d\mathbf{x}, \quad (5.8)$$

where  $p$  and  $q$  denote the densities of  $P$  and  $Q$ . The computation of the KL divergence according to (5.8) would require multidimensional mapping of the  $\mathbb{R}^k$  subset into two PDFs:  $p$  and  $q$ . This approach may become impractical for a large number of dimensions: in the case of WINNER it is necessary to consider up to 8 dimensions (although the XPR is not correlated with other LSPs). The marginal PDFs of K-factor are given only for scenarios with LoS propagation, which reduces the dimensionality of MVN distribution for NLoS propagation with one.

In the special case of considering divergence between two MVN distributions it is possible to construct an analytical expression that depends solely on distribution parameters. The Kullback-Leibler divergence from  $\mathcal{N}_0(\mu_0, \Sigma_0)$  to  $\mathcal{N}_1(\mu_1, \Sigma_1)$ , for



non-singular matrices  $\Sigma_0$  and  $\Sigma_1 \in \mathbb{R}^{k \times k}$ , is [123]:

$$D_{\text{KL}}(\mathcal{N}_0 \parallel \mathcal{N}_1) = \frac{1}{2 \log_e 2} \cdot \left[ \log_e \left( \frac{\det\{\Sigma_1\}}{\det\{\Sigma_0\}} \right) + \text{tr}(\Sigma_1^{-1} \Sigma_0) + (\mu_1 - \mu_0)^\top \Sigma_1^{-1} (\mu_1 - \mu_0) - k \right]. \quad (5.9)$$

This metric enables a simple comparison of reference **WINNER** scenarios. Therefore, the original form of KL metric (5.8) is more suitable for this particular problem than its symmetrized form, the Jansen-Shannon divergence [124]. Since KL divergence is not symmetric, it is necessary to define some other symmetrized extension to obtain proper distance metric. We propose to use mean KL divergence:

$$D_{\overline{\text{KL}}}(P \parallel Q) = \frac{1}{2} [D_{\text{KL}}(P \parallel Q) + D_{\text{KL}}(Q \parallel P)]. \quad (5.10)$$

### 5.3.1 Mean KL Scenario Divergence

In order to compare scenarios that do not share all parameter dimensions, (e.g., **LoS** and **NLoS** scenarios as for the latter no K-factor is defined), a reduction of dimensionality was necessary: only those dimensions existing in both scenarios are used to calculate the mean KL divergence. This means that scenarios with lower number of resolved dimensions could exhibit more similarity as a consequence of incomplete representation. A fair comparison would be possible only if all scenarios have the same number of dimensions. The respective mean KL divergences between all **WINNER** scenarios and Ilmenau (IL) and Dresden (DR) measurements, are given in Tab. 5.5<sup>‡</sup>.

In order to simplify the analysis of obtained results, for each (scenario, propagation) combination the closest match is listed in Tab. 5.6. Divergences within the same **WINNER** scenario group, or having same propagation conditions are not minimum as may have been expected. Tab. 5.6 shows that only 5 among 16 **WINNER** (scenario, propagation) pairs have the closest match within the same **WINNER** scenario group (A, B, C, D). This comes as consequence of subjective classification of similar environments, without previously introduced metric. The minimum distances from Tab. 5.6,  $D_{\overline{\text{KL}}} = 0.1$ , confirm some expectations: **B4-NLoS** (outdoor-to-indoor) is closest to **A2-NLoS** (indoor-to-outdoor) because these are reciprocal scenarios.<sup>§</sup> Also, micro-cell and macro-cell versions of outdoor-to-indoor (B4 and C4) are the closest although not belonging to the same group. Mean KL divergences from Tab. 5.6 suggest that there is a better way to group available scenarios.

<sup>‡</sup>For **WINNER** scenarios that give two sets of LoS parameters, mean KL distances are computed for **LoS** parameters before break-point distance of transmission loss.

<sup>§</sup>Results reported in [125] confirm the similarity of outdoor-to-indoor and indoor-to-outdoor scenarios also for cluster-level parameters (number, birthrate, lifetime etc.) that are not accounted by comparison of **LSP** distributions.



Table 5.6: Closest (scenario, propagation) pairs according to mean KL divergence.

Scen.1	Prop.1	Scen.2	Prop.2	$D_{KL}$
A1	LoS	A2	NLoS	11.0
A1	NLoS	B3	LoS	8.3
A2	NLoS	B4	NLoS	0.1
B1	LoS	D2a	LoS	6.1
B1	NLoS	B3	NLoS	10.1
B3	LoS	B3	NLoS	5.4
B3	NLoS	B3	LoS	5.4
B4	NLoS	A2	NLoS	0.1
C1	LoS	D1	LoS	5.9
C1	NLoS	D1	NLoS	4.8
C2	LoS	D1	NLoS	5.6
C2	NLoS	DR	NLoS	11.0
C4	NLoS	B4	NLoS	9.8
D1	LoS	C1	LoS	5.9
D1	NLoS	C1	NLoS	4.8
D2a	LoS	D1	NLoS	5.4
IL	LoS	IL	NLoS	2.8
IL	NLoS	IL	LoS	2.8
DR	LoS	DR	NLoS	2.7
DR	NLoS	DR	LoS	2.7

The average distances between all scenarios from one WINNER group to all scenarios in the other groups are given in Tab. 5.7. If all groups gather the most similar scenarios, an average distance between any two groups will be higher than the average distance within a single group. From Tab. 5.7 we can see that this applies to groups A and D, which are, according to average inter-group distance, closest to themselves. This indicates that subjective WINNER grouping can be partially supported by mean KL distance. However, the deviations are observable for groups B and C where other groups appear to be closer (at a lower average distance) than other scenarios from the same group. This situation is possibly caused by inappropriate assignment of distant scenarios, outdoor-to-indoor micro-cell scenario B4-NLoS and suburban C1-NLoS, to the corresponding groups.

A closer inspection of Tab. 5.4 reveals that the majority of scenarios with increased dimensionality (resolved elevations) comes from groups B and C. This means that larger intra-group distance may appear due to increased dimensionality. Additionally, their correlation matrices have been modified by APM method,

Table 5.7: Average distance between WINNER scenario groups: A, B, C, D.

$D_{KL}$	A	B	C	D
D	22.6	19.1	14.5	6.3
C	88.8	70.6	45.0	
B	32.1	35.0		
A	15.3			

Table 5.8: Average distance between WINNER LoS and NLoS propagation conditions.

$D_{\overline{KL}}$	LoS	NLoS
NLoS	42.1	50.9
LoS	31.8	

so that the parameter  $\epsilon$  impacts the absolute value of the mean KL distance. The joint effect of these phenomena is illustrated by mean KL distances along the antidiagonal of Tab. 5.7: they are proportional to the number of modified group members that are listed in Tab. 5.4:  $\#_D = 0, \#_A = 1, \#_B = 3, \#_C = 6$ .

For 6 out of 16 (scenario, propagation) pairs the best match has the opposite propagation condition (LoS, instead of NLoS, and vice versa), indicating that WINNER LoS and NLoS parameters do not form disjunctive sets (Tab. 5.6). Calculation of the mean distance between all LoS and NLoS scenarios in Tab. 5.8 shows that lower average distance can be expected between scenarios having LoS propagation condition (they are more similar than different scenarios with NLoS propagation).

### 5.3.2 Classification of Measurements

The same criterion, KL divergence, can be applied to classify measurements as well. For this purpose even empirical distributions of LSPs can be used since KL metric (5.8) supports that. However, the extraction of the corresponding WINNER parameters simplifies the comparison since analytical expression (5.9) can be applied. Therefore we use the latter approach to compare Ilmenau and Dresden measurements (Sec. A.2.3) with other WINNER scenarios. The parameters of marginal LSPs and corresponding correlation coefficients estimated from these measurements are given in Tab. 5.2 and 5.3 together with parameters describing WINNER reference propagation scenarios. Additional details regarding Ilmenau and Dresden measurements and analysis can be found in [126] and [127], respectively.

Since both measurements have been performed in urban environments with macro-cell setup (antennas were elevated above rooftops), it is expected that the closest scenario will be WINNER C2, which represents typical urban macro-cells. These measurements are conducted after the publication of WIM-C2 parameters and therefore provide a proper test set for the validation of reported WIM parameters. The expectations are met for Ilmenau measurements, where WINNER C2-NLoS is the closest scenario for both LoS and NLoS conditions, with minimal distances  $D_{\overline{KL}} = 16.9$  and  $D_{\overline{KL}} = 15.3$  (Tab. 5.5). In the case of Dresden measurements minimal mean KL divergences (8.6 and 11.6) indicate that the closest WIM scenario is C1-LoS, for both LoS and NLoS propagation conditions. This resemblance of Dresden measurements to suburban propagation (WINNER C1) may come from dominant height of BS positions with respect to environment.

Fig. 5.3 shows the 2-D PDFs of the reference WINNER C2-NLoS scenario together with joint LSP realizations from Ilmenau and Dresden measurements. For the NLoS propagation condition Ilmenau and Dresden measurements are quite close to C2: C2-NLoS is the best match for Ilmenau-NLoS ( $D_{\overline{KL}} = 16.3$ ) and the second

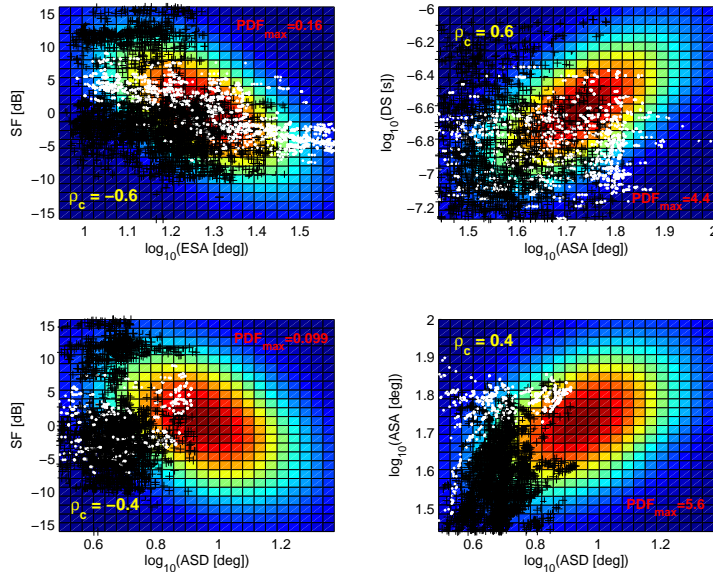


Figure 5.3: Comparison of joint WINNER C2 2-D PDFs with the LSP realizations from Ilmenau (black pluses) and Dresden (white dots), for NLoS propagation [121].

best match for Dresden NLoS data ( $D_{\overline{KL}} = 11$ ). Additionally, among all results presented in Tab. 5.5 the closest match of WIM C2-NLoS is just Dresden-NLoS (row showed in red).

For LoS conditions, distances from WINNER C2 and Ilmenau and Dresden measurements are larger (35.7 and 23.9) which classifies Ilmenau-LoS to C2-NLoS ( $D_{\overline{KL}}=16.9$ ) and Dresden-LoS into C1-LoS ( $D_{\overline{KL}}=11.6$ ). Tab. 5.6 shows the increased similarity between LoS and NLoS propagation condition in Ilmenau and Dresden measurements. This occurs also for WINNER B3, while other WINNER scenarios do not show this property. One possible interpretation comes from the data segmentation into LoS and NLoS classes: the actual propagation conditions for the LoS or NLoS-labeled data may actually correspond to, e.g., Obstructed Line-of-Sight (OLOs). The previous analysis demonstrates that mean KL divergence, additionally to the comparison of different measurements, enables the quantification of complex relations between different data segments of the same measurement, as long as they use the same LSP space representation.

The mean KL distances between Ilmenau and Dresden measurements (38.3–LoS and 22.8–NLoS) are higher than corresponding distances from these measurements to the reference WINNER-C2 scenario. This confirms that WINNER C2 parameters provide appropriate representation for a wide class of urban macro-cell environments.

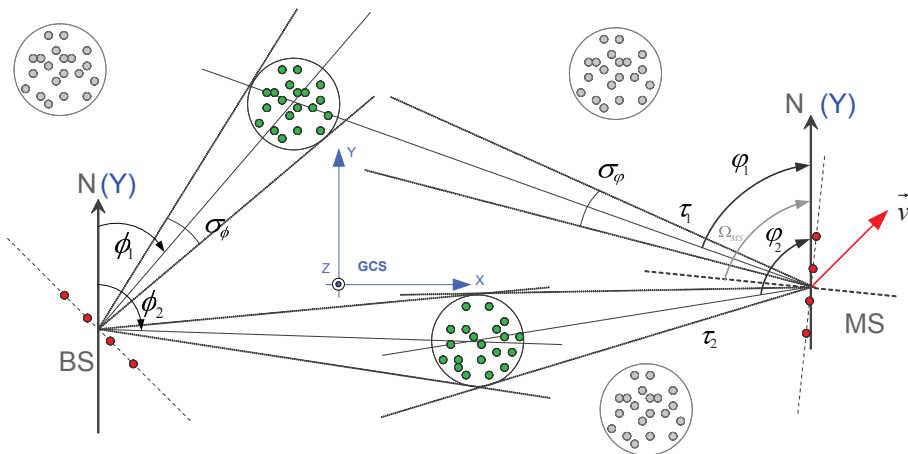


Figure 5.4: WINNER model of single radio link. [5]

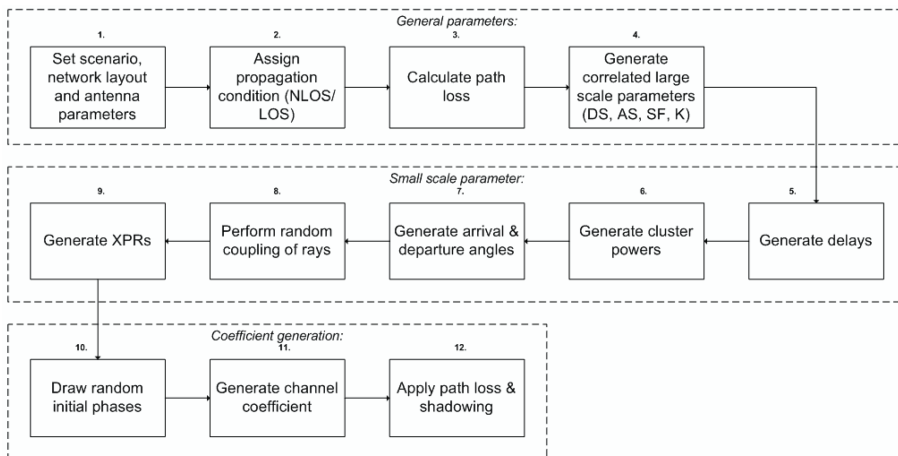


Figure 5.5: Generation procedure of WINNER channel coefficients (Kyösti [5]).

### 5.4 Generation of WINNER Channel Coefficients

A WINNER model of single BS-MS link, with used parameters, is shown in Fig. 5.4. The circles with dots represent scattering region that correspond to single cluster. The number of clusters varies from 8 to 20, depending on scenario, while the number of rays (subpaths) is fixed to 20 for all scenarios.

The procedure of impulse response generation for WINNER II channel model is depicted in the Fig. 5.5. It consists of 12 blocks that are organized into three different parts: a) determination of network layout and large scale channel parameters, b) determination of small scale propagation parameters, and c) the actual creation of the channel realizations.

### 5.4.1 General Parameters:

**Step 1:** Set the environment, network layout and antenna array parameters

- a) Choose one of the scenarios (A1, A2, B1, . . . );
- b) Give number of BS and MS;
- c) Give locations of BS and MS, or equally distances of each BS and MS and relative directions  $\phi_{LOS}$  and  $\varphi_{LOS}$  of each BS and MS;
- d) Give BS and MS antenna field patterns  $F_{rx}$  and  $F_{tx}$ , and array geometries;
- e) Give BS and MS array orientations with respect to north (reference) direction;
- f) Give speed and direction of motion of MS;
- g) Give system center frequency.

### 5.4.2 Large-scale Parameters:

**Step 2:** Assign the propagation condition (LoS/NLoS) according to the probability described in Table 4-7 of [5].

**Step 3:** Calculate the path loss with formulas of Table 4-4 from [5] for each BS-MS link to be modeled.

**Step 4:** Generate the correlated large scale parameters, i.e. delay spread, angular spreads, Ricean K-factor and shadow fading term according to instructions in Sec. 3.3.1 “Correlations between large scale parameters” of [5].

### 5.4.3 Small-scale (Cluster and Ray) Parameters:

**Step 5:** Generate the delays  $\tau$ .

Delays are drawn randomly from the delay distribution defined in Tab. 5.12. With exponential delay distribution calculate

$$\tau'_n = -r_\tau \sigma_\tau \ln(X_n), \quad (5.11)$$

where  $r_\tau$  is the delay distribution proportionality factor,  $\sigma_\tau$  is delay spread,  $X_n \sim \mathcal{U}(0, 1)$  and cluster index  $n = 1, \dots, N$ . With uniform delay distribution the delay values  $\tau'_n$  are drawn from the corresponding range. Normalize the delays by subtracting with minimum delay and sort the normalized delays to descending order.

$$\tau_n = \text{sort}\{\tau'_n - \min(\tau'_n)\}. \quad (5.12)$$

In the case of LoS condition additional scaling of delays is required to compensate the effect of LoS peak addition to the delay spread. Heuristically determined Ricean K-factor dependent scaling constant is

$$D = 0.7705 - 0.0433K + 0.0002K^2 + 0.000017K^3, \quad (5.13)$$

Table 5.9: Scaling factor applied in inverse Gaussian mapping is related to total number of clusters.

# clusters	4	5	8	10	11	12	14	15	16	20
$C$	0.779	0.860	1.018	1.090	1.123	1.146	1.190	1.211	1.226	1.289

where  $K$  [dB] is the Ricean K-factor defined in Tab. 5.12. Scaled delays are

$$\tau_n^{LOS} = \tau_n/D, \quad (5.14)$$

they are **not** to be used in cluster power generation.

**Step 6:** Generate the cluster powers  $P$ .

The cluster powers are calculated assuming a single slope exponential power delay profile. Power assignment depends on the delay distribution defined in Tab. 5.12. With exponential delay distribution the cluster powers are determined by

$$P'_n = \exp\left(-\tau_n \frac{r_\tau - 1}{r_\tau \sigma_\tau}\right) \cdot 10^{-\frac{Z_n}{10}} \quad (5.15)$$

and with uniform delay distribution they are determined by

$$P'_n = \exp\left(\frac{-\tau_n}{\sigma_\tau}\right) \cdot 10^{-\frac{Z_n}{10}}, \quad (5.16)$$

where  $Z_n \sim \mathcal{N}(0, \zeta)$  is the per cluster shadowing term in [dB]. Normalize the powers so that sum power of all clusters is equal to one

$$P_n = \frac{P'_n}{\sum_{n=1}^N P'_n} \quad (5.17)$$

Assign the power of each ray within a cluster as  $P_n/M$ , where  $M$  is the number of rays per cluster.

**Step 7:** Generate the azimuth arrival angles  $\varphi$  and azimuth departure angles  $\phi$ .

If the composite PAS of all clusters is modeled as wrapped Gaussian (see Tab. 5.12) the AoA are determined by applying inverse Gaussian function with input parameters  $P_n$  and RMS angle spread  $\sigma_\varphi$

$$\varphi'_n = \frac{2\sigma_{AoA} \sqrt{-\ln(P_n/\max(P_n))}}{C}. \quad (5.18)$$

In equation above  $\sigma_{AoA} = \sigma_\varphi/1.4$  is the standard deviation of arrival angles (factor 1.4 is the ratio of Gaussian std and corresponding ‘‘RMS spread’’). Constant  $C$  is a scaling factor related to total number of clusters and is given in Tab. 5.9.



Table 5.10: Ray offset angles within a cluster, given for 1° RMS angle spread.

Ray number $m$	Basis vector of offset angles $\alpha_m$
1,2	$\pm 0.0447$
3,4	$\pm 0.1413$
5,6	$\pm 0.2492$
7,8	$\pm 0.3715$
9,10	$\pm 0.5129$
11,12	$\pm 0.6797$
13,14	$\pm 0.8844$
15,16	$\pm 1.1481$
17,18	$\pm 1.5195$
19,20	$\pm 2.1551$

In the *LoS* case constant  $C$  is dependent also on Ricean  $K$ -factor. Constant  $C$  in eq. (5.20) is substituted by  $C^{LOS}$ . Additional scaling of angles is required to compensate the effect of *LoS* peak addition to the angle spread. Heuristically determined Ricean  $K$ -factor dependent scaling constant is

$$C^{LOS} = C \cdot (1.1035 - 0.028K - 0.002K^2 + 0.0001K^3), \quad (5.19)$$

where  $K$  [dB] is the Ricean  $K$ -factor defined in Tab. 5.12.

Assign a positive or negative sign to the angles by multiplying with a random variable  $X_n$  with uniform distribution over the discrete set of  $\{1, -1\}$ , add component  $Y_n \sim \mathcal{N}(0, \sigma_{AoA}/5)$  to introduce random variation

$$\varphi_n = X_n \varphi'_n + Y_n + \varphi_{LOS}, \quad (5.20)$$

where  $\varphi_{LOS}$  is the *LoS* direction defined in the network layout description Step 1.c.

In the *LoS* case substitute (5.22) by (5.23) to enforce the first cluster to the *LoS* direction  $\varphi_{LOS}$

$$\varphi_n = (X_n \varphi'_n + Y_n) - (X_n \varphi'_1 + Y_1 - \varphi_{LOS}). \quad (5.21)$$

Finally add the offset angles  $a_m$  from Tab. 5.10 to cluster angles

$$\varphi_{n,m} = \varphi_n + c_{AoA} \alpha_m, \quad (5.22)$$

where  $c_{AoA}$  is the cluster-wise rms azimuth spread of arrival angles (cluster *ASA*) in Tab. 5.12.

For departure angles  $\phi_n$  the procedure is analogous.

**Step 7b:** *If the elevation angles are supported:* Generate elevation arrival angles  $\psi$  and elevation departure angles  $\gamma$ .

Draw elevation angles with the same procedure as azimuth angles on Step 7. Azimuth *RMS* angle spread values and cluster-wise azimuth spread values are replaced by corresponding elevation parameters from Table 4-6 in [5].

**Step 8:** Random coupling of rays within clusters.

Couple randomly the departure ray angles  $\phi_{n,m}$  to the arrival ray angles  $\varphi_{n,m}$  within a cluster  $n$ , or within a sub-cluster in the case of two strongest clusters (see Step 11 and Tab. 5.11).

If the elevation angles are supported, they are coupled with the same procedure.

**Step 9:** Generate the cross polarization power ratios (XPR)  $\kappa$  for each ray  $m$  of each cluster  $n$ .

XPR is log-normal distributed. Draw XPR values as

$$\kappa_{m,n} = 10^{X/10}, \quad (5.23)$$

where ray index  $m = 1, \dots, M$ ,  $X \sim \mathcal{N}(\mu, \sigma)$  is Gaussian distributed with  $\mu$  and  $\sigma$  from Tab. 5.12 for XPR.

#### 5.4.4 Coefficient Generation:

**Step 10:** Draw the random initial phase  $\{\Phi_{n,m}^{VV}, \Phi_{n,m}^{VH}, \Phi_{n,m}^{HV}, \Phi_{n,m}^{HH}\}$  for each ray  $m$  of each cluster  $n$  and for four different polarization combinations (VV, VH, HV, HH). Distribution for the initial phases is uniform,  $\mathcal{U}(-\pi, \pi)$ .

In the LoS case draw also random initial phases  $\{\Phi_{LOS}^{VV}, \Phi_{LOS}^{HH}\}$  for both VV and HH polarizations.

**Step 11:** Generate the channel coefficients for each cluster  $n$  and each receiver and transmitter element pair  $(u, s)$ .

For the  $N - 2$  weakest clusters, say  $n = 3, 4, \dots, N$ , and arbitrary antenna arrays, the channel coefficients are given by:

$$\begin{aligned} h_{u,s,n}(t) = & \sqrt{P_n} \sum_{m=1}^M \left[ \begin{array}{c} F_{Tx,s}^V \left( \vec{\Omega}_{n,m}^{Tx} \right) \\ F_{Tx,s}^H \left( \vec{\Omega}_{n,m}^{Tx} \right) \end{array} \right]^T \\ & \cdot \left[ \begin{array}{cc} \exp(j\Phi_{n,m}^{VV}) & \sqrt{\kappa_{n,m}} \exp(j\Phi_{n,m}^{VH}) \\ \sqrt{\kappa_{n,m}} \exp(j\Phi_{n,m}^{HV}) & \exp(j\Phi_{n,m}^{HH}) \end{array} \right] \left[ \begin{array}{c} F_{Rx,u}^V \left( \vec{\Omega}_{n,m}^{Rx} \right) \\ F_{Rx,u}^H \left( \vec{\Omega}_{n,m}^{Rx} \right) \end{array} \right] \\ & \cdot \exp(j2\pi\lambda_0^{-1} \vec{d}_s \cdot \vec{\Omega}_{n,m}^{Tx}) \exp(j2\pi\lambda_0^{-1} \vec{d}_u \cdot \vec{\Omega}_{n,m}^{Rx}) \exp(j2\pi\nu_{n,m}t) \end{aligned} \quad (5.24)$$

where  $\lambda_0$  is the wave length on carrier frequency,  $F_{Rx,u}^V$  and  $F_{Rx,u}^H$  are radiation patterns of Rx antenna element  $u$ , for vertical and horizontal polarizations respectively,  $\vec{d}_u$  is location vector of Rx array element  $u$  and  $\vec{\Omega}_{n,m}^{Rx}$  is departure direction  $(\theta_{n,m}, \varphi_{n,m})$  of ray  $(n, m)$ . If  $x_s, y_s$  and  $z_s$  are Cartesian coordinates of  $\vec{d}_u$  the scalar product can be determined as

$$\vec{d}_u \cdot \vec{\Omega}_{n,m} = x_s \sin \theta_{n,m} \cos \varphi_{n,m} + y_s \sin \theta_{n,m} \sin \varphi_{n,m} + z_s \cos \theta_{n,m}. \quad (5.25)$$

Table 5.11: Sub-cluster information for intra cluster delay spread clusters.

sub-cluster #	mapping to rays	power	delay offset
1	1,2,3,4,5,6,7,8,19,20	10/20	0 ns
2	9,10,11,12,17,18	6/20	5 ns
3	13,14,15,16	4/20	10 ns

Correspondingly,  $\vec{d}_s \cdot \vec{\Omega}_{n,m}^{Tx}$  is a scalar product of Tx antenna element  $s$  and vector defining the departure direction of ray  $(n, m)$ .

If elevations are omitted or simpler array geometries (e.g., linear or planar) are used the (5.24) can be simplified.

If polarizations are disregarded, 2x2 polarization matrix can be replaced by scalar  $\exp(j\Phi_{n,m})$  and only vertically polarized radiation patterns applied.

For the fixed feeder link scenarios, B5, the Doppler frequency component  $\nu_{n,m}$  is tabulated for the first ray of each cluster, and for the other rays  $\nu_{n,m} = 0$ . For all other scenarios, the Doppler frequency

$$\nu_{n,m} = \frac{\vec{v} \cdot \vec{\Omega}_{n,m}^{Rx}}{\lambda_0}, \quad (5.26)$$

is calculated from direction of arrival  $\vec{\Omega}_{n,m}^{Rx}$  and MS velocity  $\vec{v}$ . If only horizontal movement of terminal is considered, than Doppler frequency is:

$$\nu_{n,m} = \frac{|\vec{v}| \cos \varphi_v \sin \theta_{n,m} \cos \varphi_{n,m} + |\vec{v}| \sin \varphi_v \sin \theta_{n,m} \sin \varphi_{n,m}}{\lambda_0}, \quad (5.27)$$

where  $\varphi_v$  designates direction of travel. When elevations are not modeled, co-elevation angles  $\theta_{n,m} \equiv \pi/2$ .

For the two strongest clusters, say  $n = 1$  and 2, rays are spread in delay to three sub-clusters (per cluster), with fixed delay offset  $\{0, 5, 10 \text{ ns}\}$  (see Tab. 5.11). Delays of sub-clusters are

$$\begin{aligned} \tau_{n,1} &= \tau_n + 0 \text{ ns} \\ \tau_{n,2} &= \tau_n + 5 \text{ ns} \\ \tau_{n,3} &= \tau_n + 10 \text{ ns} \end{aligned} \quad (5.28)$$

Twenty rays of a cluster are mapped to sub-clusters like presented in Tab. 5.11 below. Corresponding offset angles are taken from Tab. 5.10.

The channel impulse response is obtained as:

$$h_{u,s}(t, \tau) = \sum_{n=1}^N h_{u,s}(t) \delta(\tau - \tau_n), \quad (5.29)$$

where  $\delta(\cdot)$  is the Dirac's delta function.

In the *LoS* case single line-of-sight ray is added and the CIR is re-scaled (including all other channel coefficients generated by (5.24)) to fit targeted K-factor  $K_R$ .

$$\begin{aligned}
h_{u,s}^{LOS}(t,\tau) &= \sqrt{\frac{1}{K_R+1}} h_{u,s}(t,\tau) \\
&+ \sqrt{\frac{K_R}{K_R+1}} \left[ \begin{array}{c} F_{Tx,s}^V \left( \vec{\Omega}_{LOS}^{Tx} \right) \\ F_{Tx,s}^H \left( \vec{\Omega}_{LOS}^{Tx} \right) \end{array} \right]^T \\
&\cdot \left[ \begin{array}{cc} \exp(j\Phi_{LOS}^{VV}) & 0 \\ 0 & \exp(j\Phi_{LOS}^{HH}) \end{array} \right] \left[ \begin{array}{c} F_{Rx,u}^V \left( \vec{\Omega}_{LOS}^{Rx} \right) \\ F_{Rx,u}^H \left( \vec{\Omega}_{LOS}^{Rx} \right) \end{array} \right] \\
&\cdot \exp\left(j2\pi\lambda_0^{-1} \vec{d}_s \cdot \vec{\Omega}_{LOS}^{Tx}\right) \exp\left(j2\pi\lambda_0^{-1} \vec{d}_u \cdot \vec{\Omega}_{LOS}^{Rx}\right) \\
&\cdot \exp(j2\pi\nu_{LOS}t) \delta(\tau)
\end{aligned} \tag{5.30}$$

where  $K_R$  is the Ricean K-factor defined in Tab. 5.12 converted to linear scale.

**Step 12:** Apply the path loss and shadowing for the channel coefficients.

Table 5.12: Parameters of WIM generic model.

Scenarios Propagation	A1		A2/B4/C4#		B1		B3		C1		C2		D1		D2a	
	LOS	NLOS	NLOS	NLOS	LOS	NLOS	LOS	NLOS	LOS	NLOS	LOS	NLOS	LOS	NLOS	LOS	NLOS
Correlation distance [m]	<i>DS</i>	7	4	$21/10^\Delta$	9	8	3	1	6	40	40	40	64	36	64	36
	<i>ASD</i>	6	5	$15/11^\Delta$	13	10	1	0.5	15	30	15	50	25	30	30	25
	<i>ASA</i>	2	3	$35/17^\Delta$	12	9	2	0.5	20	30	15	50	40	40	40	40
	<i>SF</i>	6	4	$14/7^\Delta$	14	12	3	3	40	50	45	50	40	120	40	40
Number of clusters	<i>K</i>	6	N/A	N/A	10	N/A	1	N/A	10	N/A	12	N/A	40	N/A	40	N/A
		12	16	12	8	16	10	15	15	14	8	20	11	10	8	8
Per cluster shadowing std. $\zeta$ [dB]	6	3	4	3	3	3	3	3	3	3	3	3	3	3	3	3
Number of rays per cluster	20	20	20	20	20	20	20	20	20	20	20	20	20	20	20	20
Delay distribution	Exp	Exp	Exp	Exp	Exp	Uniform $\leq 800$ ns	Exp	Exp	Exp	Exp	Exp	Exp	Exp	Exp	Exp	Exp
Delay scaling parameter $\tau_r$	3	2.4	2.2	3.2	—	—	1.9	1.6	2.4	1.5	2.5	2.3	3.8	1.7	3.8	3.8
AoD and AoA distribution	Wrapped Gaussian															
Cluster <i>ASD</i>	5	5	8	3	10	5	6	5	5	2	6	2	2	2	2	2
Cluster <i>ASA</i>	5	5	5	18	22	5	13	5	10	10	12	15	3	3	3	3

NOTE! With arrival and departure directions we consider downlink case, i.e. departure refers to BS and arrival refers to MS.

$\Delta$  In case column A2/B4/C4 contains two parameter values, the left value corresponds to A2 Indoor-to-Outdoor and the right value to B4/C4 Outdoor-to-Indoor.



## Chapter 6

---

# System-level, Wideband, MIMO Radio Channel Models

---

System level simulations change perspective from single radio-link to the radio network context. Since a radio-network includes multiple radio links it is clear that complexity increases with the number of communicating terminals, the number of transmitting/receiving antennas and the transmission bandwidth. Additionally, wideband **MIMO** system-level model cannot be considered as a collection of independent narrowband **SISO** link realizations, since correlation between frequencies, antennas and links should be accounted for. On the other side, due to a large number of terminals covered by the simulation, a network-level analysis cannot rely on very complex radio-link description. Therefore, the radio channel models intended for system performance assessment need to find appropriate balance between accuracy (realism) and complexity. Following the inherent limitations on complexity, different channel models could be developed to suit particular purposes.

This chapter consists of five sections. The first section targets the model optimizations process. The controlled approximation of the model, i.e., reduction of its realism is considered as mean for complexity depreciation. Expressing the computation complexity of a model by an equivalent number of real operations enables straightforward comparison of different modeling approaches. The optimal strategy for usage of **3-D** antenna arrays in simulation is proposed in the second section. The third section analyzes simplified **ST** evolution of **GSCM** that is based on the “drop” concept. The necessity for **LSP** correlations to enforce **ST** consistency is discussed in the context of the **WINNER** model. Specific aspects of spatially-distributed transmission corresponding to cooperative downlink are given in Sec. 6.4.3. The last section discusses global relations between **COST 273/2100**, **3GPP SCM** and **WINNER** state-of-the-art models being intended for Beyond-3G (B3G) **MIMO** simulations.

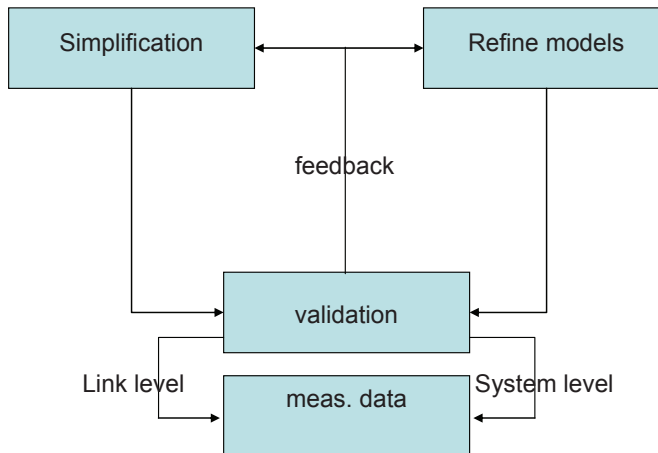


Figure 6.1: Process of model optimization: relations between validation, simplification and refinement.

## 6.1 Model Optimization

Simulation of wireless communication systems is becoming more complex and time-consuming due to the increased data rates, bandwidths, number of antennas, Quality-of-service (QoS) demands, more complex algorithms, and necessity of system-level simulations [128]. Even recent development in computer technology does not compensate the increased requirements, since the realistic multidimensional channel models are needed to obtain accurate and reliable simulation results. Thus, the modeling goal becomes to achieve as realistic channel model as possible with reasonable complexity.

Since the modeling process offers multitude of solutions with different complexities, there is a need to evaluate their suitability (optimality) for a particular problem. The targeted realism of a model is related to the system perception of the channel: only for given Key Performance Indicators (KPIs) and their maximum allowed tolerances, different models can be compared regarding their complexity. This means that reproduction of physical reality is not the goal by itself. Instead, the relevance of physical phenomena is evaluated by its impact to KPIs. Thus, an optimization of the model has to be performed in the context of a given number of KPIs that should be reproduced. If the model will be used to reproduce only certain system aspects, the non-generic, non-spatial or even non-physical modeling approaches, having lower complexity, may be preferred.

In general, the necessity for model simplification or refinement stems from the outcome of the system performance evaluation. A close match between model-based and measurement data simulations allows a simplification of the model (for particular KPIs), whereas too large deviations call for model refinement, Fig. 6.1. Another approach would be to sacrifice some of the model's realism to reduce its complexity. Since the term “simplification” does not suggest any loss in the model realism, the term “approximation” is more appropriate when new methods increase the gap from the starting model w.r.t. relevant KPIs.



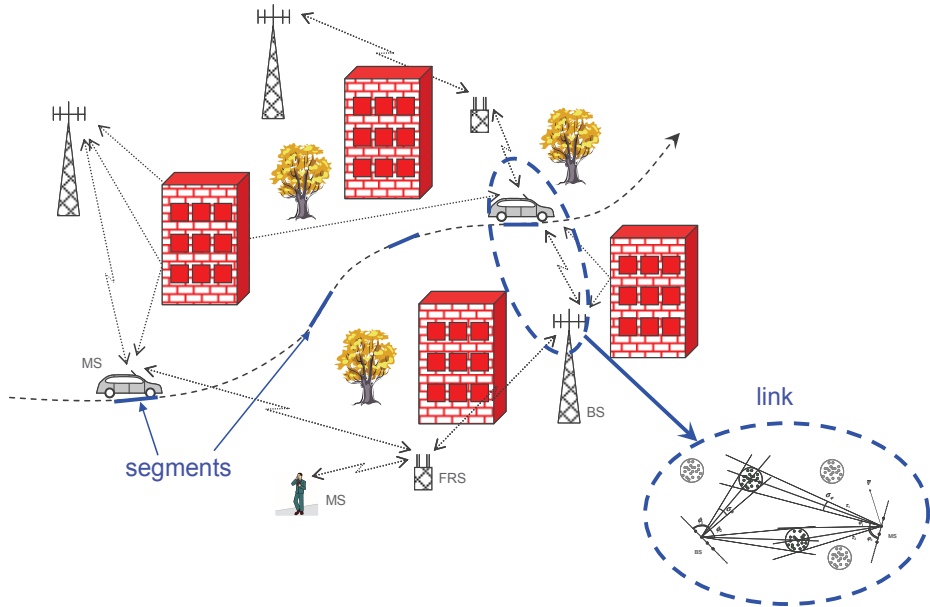


Figure 6.2: In WIM system-level approach, the spatial simulation area is divided into channel segments (drops). [5]

### 6.1.1 Simplification (Approximation) of the WINNER Model

The purpose of the channel model in the **WINNER** project is to support evaluation of both link and system features by means of simulations, emulations and demonstrations. In link and system level simulations the properly tuned model should generate a significant number of channel realizations, necessary to test different algorithms in terms of KPIs such as throughput, BER, etc. System-level simulations may include multiple base stations, multiple relay stations, and multiple mobile terminals, as shown in Fig. 6.2. All modeled links are evolved simultaneously.

The **WINNER** model, however, has a considerable complexity in terms of model parameters, scenarios and computational complexity. A further simplification of the proposed generic channel model would enable a faster evaluation of system features. In order to optimize the model complexity, a reliable reference is needed. The measurements used for the development of **WIM** could be used to simulate reference system performance, and evaluate (validate) models with a different complexity, as indicated in Fig. 6.3.

#### Trading Generality for Simplicity

Having more general models typically means higher model complexity. Generality can be related to applicability of the model to different environments, or to ability of the model to reproduce all known (observed) propagation effects.

The **WIM** uses generic model with scenario-specific parameters. This means that structure corresponding to each scenario can have different complexity (e.g.,

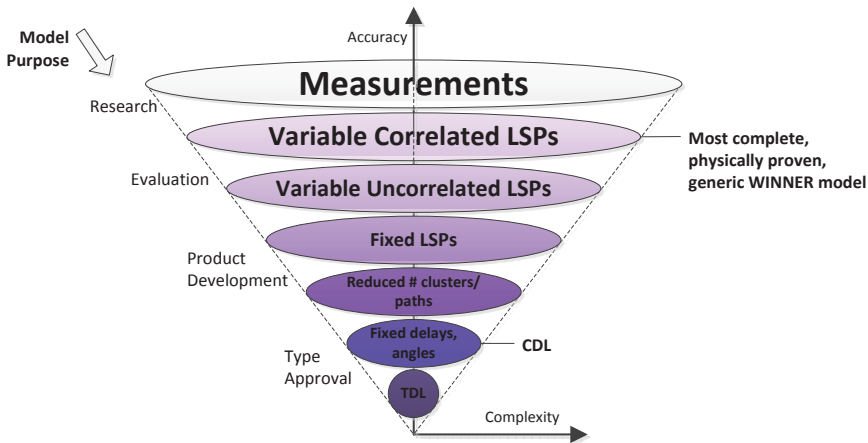


Figure 6.3: Simplification/approximation of the WINNER model. (after Jämsä [129])

different number of clusters or rays), without impact to the generic nature of the model. One possible approach to simplification can be related to different “approximation” space inside every particular scenario. This comes under the assumption that different sensitivity of the model can be exhibited for different scenarios. If after individual approximation, all scenarios are still represented with a physical propagation model, the generic nature is kept, otherwise there is no single generic core used for representation. In that case the concept of “common modeling framework” can be exploited to associate different scenario representations.

### Top-down Approximation of the Physical Model

Starting from the best attainable model of the radio-channel, it is possible to produce optimized, i.e., simplified/approximated version that still meets targeted **KPI** tolerances. The basic idea of the **WINNER** model simplification/approximation is illustrated in Fig. 6.3, [129]. The proposed approximation steps should provide the simplest model for the targeted accuracy. Approximations are based on ignoring of certain dependencies between model parameters, or intentional reduction of the number or variability of parameters over different modeling levels. The following approximation directions could be identified:

1. Ignoring (by setting to zero) auto/cross-correlations between the Large-Scale Parameters (**LSPs**).
2. Fixing certain number of **LSPs** to median values. If all **LSPs** are fixed, this corresponds to a single-drop model whose relevance is discussed in Sec. 6.3.2.
3. Reducing the total number of clusters/paths.
4. Fixing the part of, or entire multipath structure (delays or/and angles). The reduced complexity **WIM** model that assumes fully fixed delays and angles is introduced under the name *Clustered Delay Line* (**CDL**) model.

The fact that some of the approximation steps require others is reflected in structuring of the given list: fixing the multipath structure assumes that **LSPs** are already fixed.

### Approximation by Non-physical (Filtering-based) Models

There are different ways to model spatial dimension of the propagation, however, methodology offering acceptable complexity for network level simulations typically considers only filtering methods (characterized by explicit correlation matrices), and physical models that reconstruct geometry of propagation (at least to certain extent). The **WINNER Channel Model (WIM)** itself belong to the category of **Geometry-based Stochastic Channel Models (GSCMs)** that are antenna-independent and its complexity becomes weakly dependent on the number of **Tx/Rx** antennas. The conceptual and computational complexity of the **GSCM**, however, exceeds explicit correlation methods. For selected antennas, approximation with a non-physical model can reduce complexity; however, there is an issue with reproduction of **LSP** statistic that corresponds to targeted radio-environment (scenario). Due to above restriction, approximation of the **GSCM** with filtering model is applicable on per-drop bases only. Namely, in order to transfer current **WIM** representation that is related to **LSP** distributions it would be necessary to create many instances of correlation matrices, corresponding to different drops. Therefore, a reproduction of **WIM LSPs** would require multitude of correlation matrices that correspond to different drops. Although this may be performed offline, the resulting model would be away from compact and easy to handle solution, as will be shown in Sec. 6.1.2.

If a correlation model is desired, correlation matrices can be calculated from the **Clustered Delay Line (CDL)** model by fixing the antenna structure. In general, the full correlation matrices show dependencies over all propagation dimensions: time, frequency and space. However, they are rarely used in that form for the channel modeling. In this modeling approach different approximation levels of full spatial correlation matrix could be introduced:

1. spatial correlation matrices are fixed (averaged) in time but delay dependent,
2. spatial correlation matrices are averaged over both time and frequency,
3. full spatial correlation matrix is separated on **Tx** and **Rx** side correlations (Kronecker approximation, Sec. 3.2.2),
4. spatial correlations are ignored. The resulting wideband channel can be represented by **Tapped Delay Line (TDL)** that gives independent realizations for different antenna elements.

Further approximations regarding the single-antenna or narrowband transmission result in further simplifications, but they are not of interest here.

Table 6.1: Equivalent computational complexity of mathematical functions and operations.

Operation	Equivalent Complexity [ # of Real Op.]
complex multiplication	6
complex division	11
complex addition	2
$\sin x$	7
$e^x$	15
Uniform RV	5
Gaussian RV, $X$	72
Log-normal RV, $10^X = e^{X \ln 10}$	$72+1+15=88$
multiplication of a matrix $\in \mathbb{R}^{N \times N}$ and a vector $\in \mathbb{R}^{N \times 1}$	$N \cdot (2 \cdot N - 1)$

### 6.1.2 Estimation of Computational Complexity

The computational complexity per time sample of the generated channel can be compared in terms of the number of “real operations”, as suggested in [130] and [128]. The term *Real Operation* (RO) equates complexity of the real multiplication, division, addition and table lookup. All other operations could be transformed to or approximated by these four basic operations. For example, the complexity of the complex multiplication, division and addition is 6, 11 and 2 real operations, respectively. The equivalent complexity of function computation, matrix operations and random number generations from [130] is listed in Tab. 6.1.

#### Complexity of WINNER Channel Impulse Response Generation

The procedure of impulse response generation for the **WINNER** channel model is divided into 12 blocks and shown in Fig. 5.5. The presented analysis is originally published in [128] and focuses on blocks 4 to 10 that cover the determination of propagation parameters (e.g., random delays, powers and azimuth angles etc.) and pre-processing of block 11 (antenna response and calculation of channel coefficients).

**Correlated large-scale parameters** The first step of interest is the *generation of correlated large scale parameters* in the block 4 of Fig. 5.5. Depending on **LoS/NLoS** propagation conditions and availability of estimation parameters, the **WINNER** model uses  $L$  correlated **LSPs**,  $4 \leq L \leq 8$ . The number of real operations in drawing  $L$  log-normal random numbers is  $L \cdot 88$ . **LSPs** are then correlated by multiplying  $1 \times L$  random number vector by a matrix square root of the  $L \times L$  correlation matrix. As both the vector and the matrix are real, the matrix multiplication will take  $L \cdot L$  real multiplications and  $L \cdot (L - 1)$  real additions. The total number of real operations needed to generate correlated **LSPs** for a single drop is:

$$C_{ls} = L \cdot (88 + L + L - 1) = (2L + 87)L. \quad (6.1)$$

Factorization of the correlation matrix is excluded from (6.1), because the matrix will not vary from drop to drop.

Table 6.2: Complexity of WINNER coefficient generation for ULA geometries under NLoS.

Block	Generation/Determinaiton of	Label	Equivalent Complexity [ # of Real Op.]
4	Correlated LSPs	$C_{ls}$	$(2L + 87)L$
5	Cluster delays	$C_\tau$	$N^2 + 74N + 1$
6	Cluser powers	$C_P$	$92N + 3$
7	Azimuth angles	$C_{az}$	$166N + 4 + 2M(N + 1)$
8	Random coupling of rays	$C_{coup}$	$5(M - 1)N$
9	XPR	$C_{XPR}$	$89MN$
10	Random ray phases	$C_\Phi$	$5\mathcal{P}^2MN$
11a	Antenna array response	$C_{rp}$	$13(U + S)\mathcal{P}MN$
11b	Calculation of channel coefficients	$C_h$	$(134M + 6)USN$

Generation of small-scale propagation parameters such as delays, powers, angles of arrival (AoA), angles of departure (AoD) and cross polarization power ratios (XPR) is performed in blocks 5 to 9 in Fig. 5.5 and described in Sec. 5.4. The procedure distinguishes propagation conditions (LoS/NLoS, planar/3-D) and array geometries, which results in different complexities. Here we discuss only the NLoS case with propagation in horizontal plane and ULA geometries.

**Cluster delays** A single delay value is drawn according to (5.11):  $\tau'_n = -r_\tau \sigma_\tau \ln X_n$ , where all the terms are real and  $X_n$  is a Gaussian random number. Generating  $\tau'_n$  takes two real multiplications, one logarithm which is implemented as a table look-up, and 72 real operations for Gaussian  $X_n$ . Delays are then sorted in a descending order  $\vec{\tau}' = \text{sort}\{\tau'_n\}$  and normalized by the subtraction of the shortest delay  $\vec{\tau} = \vec{\tau}' - \tau'_1$ , similarly to (5.12). For normalization one real subtraction per delay value is necessary. The complexity of sorting in the worst case can be approximated by  $(N - 1)^2$  operations, where  $N$  is the number of clusters. The total number of real operations required for delay parameters (block 5) is

$$C_\tau = (2 + 1 + 72 + 1)N + (N - 1)^2 = N^2 + 74N + 1 \quad (6.2)$$

**Cluster powers** are calculated according to (5.15):  $P'_n = \exp\left(-\tau_n \frac{r_\tau - 1}{r_\tau \sigma_\tau}\right) 10^{\frac{-Z_n}{10}} = \exp(a \cdot \tau_n - b \cdot Z_n)$ , where  $Z_n$  is a Gaussian random number. The computation of constants  $a = \frac{1 - r_\tau}{r_\tau \sigma_\tau}$  and  $b = \frac{\ln(10)}{10}$  is performed only once for all clusters, and requires  $3 + 1 = 4$  Real Operations (ROs) in total. The calculation of the power requires a Gaussian random number, two multiplications, single subtraction and an exponentiation, i.e.,  $72 + 3 + 15 = 90$  real operations per cluster. The powers of clusters are normalized by the sum of all powers according to (5.17):  $P_n = \frac{P'_n}{\sum_{n=1}^N P'_n}$ . For  $N$  clusters, the power normalization requires  $N - 1$  additions and  $N$  divisions. The total number of real operations required for cluster power generation (block 6) is

$$C_P = 90 \cdot N + 4 + N + (N - 1) = 92N + 3. \quad (6.3)$$

**Azimuth angles** on departure and arrival are generated according to the offset from the LoS direction, (5.18):  $\varphi'_n = 2\sigma_{\text{AoA}} \sqrt{-\ln(P_n/\max(P_n))} / C$ . The constant  $c = 2\sigma_{\text{AoA}} / C$  requires 2 real operations and can be determined only once. The same applies for sorting the powers in  $\max(P_n)$ , which has complexity of  $N - 1$  RO. The equation is then reduced to one multiplication, one division, one logarithm and one square root per cluster. Assuming that real square root needs only one real operation, the total number of real operations is  $4N + 2$ . The azimuth angles for rays (and sub-rays) are determined according to (5.20) and (5.22):  $\varphi_{n,m} = X_n \varphi'_n + Y_n + \varphi_{\text{LOS}} c_{\text{AoA}} \alpha_m$ , where  $X_n$  is a discrete RV that takes values  $\{1, -1\}$  with equal probability,  $Y_n$  is a Gaussian random number, and  $\alpha_m$  are tabulated offset angles. The last term is independent of  $n$  and has complexity of  $M + 1$ . The realization of  $X_n \in \{1, -1\}$  determines between addition and subtraction of  $\varphi'_n$  and  $Y_n$ . Offsetting of  $M$  rays in  $N$  clusters requires  $NM$  additions. Therefore, generation of both arrival and departure angles requires in total

$$\begin{aligned} C_{az} &= 2 \cdot (4N + 2 + (N - 1) + (72 + 1 + 5)N + (M + 1) + NM) \\ &= 166N + 4 + 2M(N + 1), \end{aligned} \quad (6.4)$$

where  $N$  clusters and  $M$  rays per cluster are assumed.

**Random coupling of rays** (block 8) can be performed by assigning uniformly distributed random number to each of the  $M$  rays. This requires drawing  $M - 1$  uniformly distributed random numbers per cluster with complexity

$$C_{coup} = 5(M - 1)N \quad (6.5)$$

**XPR** values are determined according to (5.23):  $\kappa_{m,n} = 10^{X/10}$  (block 9). This requires drawing one Gaussian random number, one division and one exponentiation per ray. The total complexity of ray XPRs is:

$$C_{\text{XPR}} = (72 + 1 + 16)MN = 89MN. \quad (6.6)$$

The overall preprocessing complexity, which corresponds to generation of the propagation parameters being constant within a drop, is a sum of the terms expressed in equations (6.1), (6.2), (6.3), (6.4), (6.5) and (6.6).

*Calculation of channel impulse response coefficients* is performed on per-cluster basis in block 11 of Fig. 5.5. A channel coefficient of  $n^{\text{th}}$  cluster between  $s^{\text{th}}$  transmit and  $u^{\text{th}}$  receive antenna element is calculated according to (5.24). By assuming the uniform linear arrays on both sides of radio link, that expression simplifies to:

$$\begin{aligned} h_{u,s,n}(t) &= \sqrt{P_n} \cdot \sum_{n=1}^N \sum_{m=1}^M \left[ \begin{array}{c} F_s^V(\phi_{n,m}) \\ F_s^H(\phi_{n,m}) \end{array} \right]^T \mathbf{A}_{n,m} \left[ \begin{array}{c} F_u^V(\varphi_{n,m}) \\ F_u^H(\varphi_{n,m}) \end{array} \right] \\ &\cdot \exp(jk(d_s \sin(\phi_{n,m}) + d_u \sin(\varphi_{n,m}))) \\ &\cdot \exp(j2\pi\nu_{n,m}t) \delta(\tau - \tau_n), \end{aligned} \quad (6.7)$$

where  $F_s$  and  $F_u$  are the antenna radiation patterns of **Tx** and **Rx** antenna elements  $s$  and  $u$ , respectively. The polarization matrix  $\mathbf{A}$  corresponds to

$$\mathbf{A}_{n,m} = \begin{bmatrix} e^{j\Phi_{n,m}^{vv}} & \sqrt{\kappa_{n,m}} e^{j\Phi_{n,m}^{vh}} \\ \sqrt{\kappa_{n,m}} e^{j\Phi_{n,m}^{hv}} & e^{j\Phi_{n,m}^{hh}} \end{bmatrix}, \quad (6.8)$$

where  $\Phi_{n,m}$  and  $\kappa_{n,m}$  are the random phase and XPR of  $m^{\text{th}}$  ray in  $n^{\text{th}}$  cluster, respectively.  $\mathcal{P}$  is used to designate number of accounted polarization dimensions, and  $\mathcal{P} \times \mathcal{P}$  corresponds to dimensions of the matrix  $\mathbf{A}$ .

**Random initial phases**  $\Phi_{n,m}$  for the matrix  $\mathbf{A}$  are drawn from uniform distribution  $\mathcal{U}(-\pi, \pi)$  in block 10. For each of the  $\mathcal{P}^2$  phase values in (6.8) the complexity is 5 real operations. Therefore, the complexity of random phases generation is

$$C_{\Phi} = 5\mathcal{P}^2 MN. \quad (6.9)$$

**Antenna array response** The responses of antenna arrays for given azimuth angles on departure and arrival have to be determined before computing  $h_{u,s,n}(t)$  coefficients. The complexity of antenna embedding will depend on the chosen representation of the *radiation pattern*. If we assume that linear interpolation of complex samples meets required accuracy, its computational complexity, per polarization, will be determined with two real subtractions, one real division, two complex additions and one complex multiplication.

$$\begin{aligned} C_{rp} &= (2 + 1 + 2 \cdot 2 + 1 \cdot 6)\mathcal{P}(U + S)MN \\ &= 13(U + S)\mathcal{P}MN \end{aligned} \quad (6.10)$$

Application of **EADF** for radiation pattern representation in the **WINNER** channel model is described in [7]. The computational complexity of **EADF** radiation pattern interpolation can be approximated by  $(23W + 2) \cdot \mathcal{P}(S + U)MN$ , where  $W$  designates the number of **EADF** complex coefficients.

**Generation of channel coefficients** Preprocessing, related to computing coefficients  $h_{u,s,n}(t)$ , excludes the impact of the Doppler term in (6.7). The inclusion of the Doppler phase shift,  $2\pi\nu_{n,m}t$ , and summation over  $MN$  rays is done once per each simulated time sample.

The computation of the polarization matrix  $\mathbf{A}$  in (6.8) requires four exponentiations, one square root and two multiplications between complex and real number, for each ray and **Tx/Rx** antenna pair, in total  $4 \cdot 15 + 1 + 2 \cdot 2 = 65$  (15 if  $\mathcal{P} = 1$ ).

Matrix multiplications of real 1x2 **Tx** and 2x1 **Rx** radiation pattern vectors with complex 2x2 polarization matrix  $\mathbf{A}$  take  $16 + 8 = 24$  real multiplications and 3 complex additions per **Tx/Rx** antenna pair per ray, in total  $24 + 3 \cdot 2 = 30$  (4 if  $\mathcal{P} = 1$ ).

The relative phase differences between antenna elements are calculated on the second row of (6.7). The calculation includes two sine values, three real

Table 6.3: Computational complexity of geometry-based and correlation-based methods for 4x4 MIMO,  $N=20$  cluster, and  $M=20$  rays per clusters, expressed in  $\times 1000$  real operations (after Kyösti [128]).

Processing stage	Operation	Geom.		Corr.
		$\mathcal{P} = 2$	$\mathcal{P} = 1$	$\mathcal{P} = 1$
Drop preprocessing	Gener. of prop. param.	46.3	46.3	46.3
	Comput. of chan. coeff.	1021.1	467.9	540.2
Process. per time sample (from [130])		N/A	140.8	127.7

multiplications, one real addition and one exponential per Tx/Rx antenna pair per ray, in total  $2 \cdot 7 + 3 + 1 + 15 = 33$ .

Finally, the two aforementioned complex terms are multiplied, and additional complex multiplication with  $\sqrt{P_n}$  is performed on cluster level. Therefore, the total preprocessing complexity of cluster response coefficient  $h_{u,s,n}$  is

$$C_h = [(65 + 30 + 33 + 1 \cdot 6)M + 1 \cdot 6]USN = (134M + 6)USN \quad (6.11)$$

but it reduces to  $(58M + 6)USN$  if  $\mathcal{P} = 1$ .

**Transmission loss and shadow fading**, introduced in blocks 3 and 12, determine SNR for which simulations are performed. The most efficient way to include them is to scale the transmitted signal. Therefore, the computational complexity is equivalent to complex multiplication per transmitted symbol.

The overall preprocessing complexity of the cluster response computation is the sum of the terms given by equations (6.9), (6.10) and (6.11).

Numerical values of the computational complexity for different stages of MIMO channel coefficient generation are given in Tab. 6.3, for 4x4 MIMO, i.e.,  $U = S = 4$ ,  $N = 20$  clusters and  $M = 20$  rays per cluster. It can be observed that the preprocessing related to computation of cluster response coefficients dominates the overall complexity.

The total preprocessing complexity is relatively low compared to per time sample complexity: generation of about five or more time samples for a drop requires more computing than all the preprocessing (related to the drop). When typical channel simulation covers thousands of time samples within a drop, the per drop preprocessing has only minimal impact to the total channel generation computing time.

The proper representation of polarizations in geometrical approach (dual polarized model with  $\mathcal{P} = 2$ ) approximately doubles complexity of simulations, see Tab. 6.3 and Fig. 6.4a. Similar situation appears for geometrical models with different numbers of clusters: from Fig. 6.4b it can be observed that complexity increases approximately linearly with the number of clusters. This means that a simulation of WINNER scenarios with different number of clusters can have significantly different complexity.



### Complexity Comparison between Geometry- and Filtering-based Approach

The paper [128] analyzes complexity of the filtering-based approach under assumption that space-time evolution of the model is deduced from equivalent geometry-based approach. Therefore, for comparison of the geometric WINNER method with the derived correlation matrix based method, the large scale and propagation parameter determination (blocks 4-10) are assumed to be equivalent. The difference exists in the channel coefficient generation (blocks 10-11).

Preprocessing in the filtering-based approach is related to determination of MIMO correlation matrices and Doppler spectrum shaping filters for each cluster [130]. Both features can be estimated according to propagation parameters and antenna information. The Kronecker model is assumed in [128] and necessary correlation matrices are independently estimated between transmit and receive antennas.

Due to lack of an established method for representation of dual polarization in correlation matrices, the complexity comparison is performed for single polarization,  $\mathcal{P} = 1$ .

The comparison of preprocessing complexity between the geometric and correlation methods is given in Fig. 6.4 for different MIMO configurations, as a function of the total number of Tx/Rx antenna pairs ( $US$ ). The geometric method is more computationally effective than the correlation based method for all MIMO configurations due to significant computation effort required for estimation of MIMO correlation matrices for all clusters in each drop. For MIMO configurations larger than 4x4, the complexity of the correlation based method increases much faster with number of used antennas  $US$  than complexity of the geometry-based approach.

The correlation-based models are usually favored due to their simplicity. However, if these models are extended to reproduce proper ST evolution, the complexity of channel coefficient generation is comparable to geometry-based models [128]. We can, therefore, conclude that models like Kronecker or Weichselberger are popular due to their simple interpretation and simple parameter extraction, but they not necessarily offer lower simulation complexity in cases when large-scale statistic should be properly reproduced.

## 6.2 Usage of 3-D Antenna Arrays in Simulations

In this section two different strategies of using 3-D antenna arrays in channel model simulations are proposed and discussed. Both methods are compared in terms of the computational complexity and their suitability for the WIM channel model. The representation of arbitrary 3-D antenna structures is necessary for both modeling and validation purposes since antenna arrays define the spatial dimension of the radio-channel. General 3-D antenna array description also embeds polarization concepts that are becoming important for modeling of 3-D rotation of antenna array. In order to develop and to validate an antenna-independent MIMO channel model from/against channel sounding data, it is necessary to use a full 3-D antenna polarimetric description. In the spatial-channel modeling GCS is used to define radio-network system layout that also includes positions of the radio-equipment (antenna arrays). The introduction of ACS is necessary to describe simultaneous

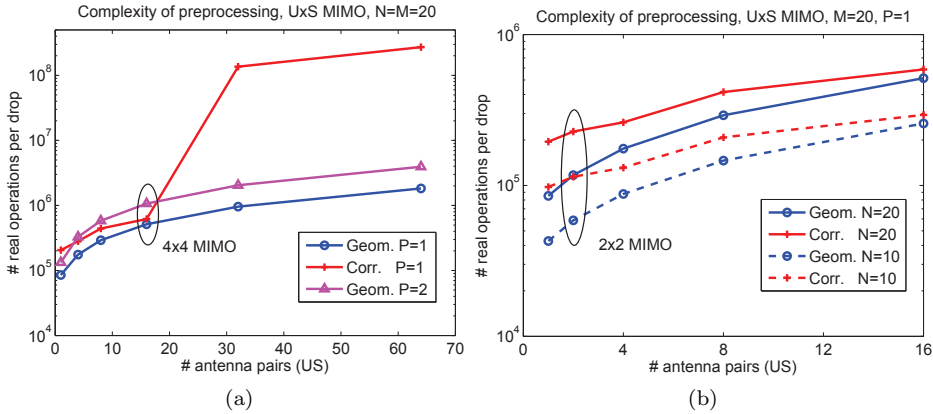


Figure 6.4: Preprocessing complexity comparison of geom. and corr. approach for different number of Tx/Rx antennas (Kyösti [128]).

movement of elements belonging to the same array. For representation of antenna-element complex radiation patterns (2.31) it is possible to use either ACS or ECS. Selection of ACS for this purpose is especially favorable for measured radiation patterns when whole antenna array is calibrated jointly. In that case measured beam patterns already include coupling effects.

The usage of an additional reference system - ECS is suitable for synthetic arrays where all elements share the same Radiation Pattern (RP). However, it will be demonstrated here that this approach increases complexity of ray-based channel simulations, and therefore radiation patterns should be expressed in ACS as well [7].

### 6.2.1 Representations of 3D Antenna Arrays in WIM

In WIM [110], the channel impulse response from transmitter antenna element  $s$  to receiver antenna element  $u$  is determined according to (3.25), and the complex, polarimetric response of antenna elements  $s$  and  $u$  is given by (2.31):

$$\vec{F}(\vec{\Omega}) = [F_{\theta}(\vec{\Omega}), F_{\varphi}(\vec{\Omega})]^T \cdot e^{-j\frac{2\pi}{\lambda}\vec{\Omega}^T \vec{d}},$$

that includes the effects of: spatial displacement, directional filtering and polarization mismatch. The radiation patterns  $[F_{\theta}(\vec{\Omega}), F_{\varphi}(\vec{\Omega})]^T$  express antenna related depolarization (XPD) in local ACS/ECS, while an environmental cross-polarization (XPR) is described in GCS by matrix  $\alpha$ , expression (3.26). The position of ACS/ECS in respect to GCS defines relation between environmental cross-polarization (XPR), being described globally, and antenna depolarization (XPD) which is described in local spherical CS. This means that propagation model has to include projections from GCS into ACS/ECS as showed in Fig. 2.3.

**Spatial Displacement** A spatial displacement can be easily described if ACS origin is taken as zero-phase reference point from which all distances in GCS (WINNER layout) are measured. In this case it is most appropriate to describe MPC phase offsets in ACS, as described in Sec. 2.4.4.

**Directional Filtering** In order to determine effect of directional filtering, a DoD/DoA for all MPCs and antenna radiation pattern has to be expressed in the same coordinate system. For that purpose it is possible to use either ECS or ACS, however the complexity of implementation would not be the same since original information about antenna element 3-D radiation patterns would be exploited in different ways in channel simulations. Thus two approaches could be distinguished:

**Approach I** If directional filtering is calculated in ECS, DoD/DoA for each MPC is transformed from GCS into ACS and from ACS into ECS.

**Approach II** The alternative approach, where directional filtering is calculated in ACS, have the potential to speed up the simulation if the array model is used very often for large number of MPCs. In this approach, the radiation patterns of all antenna elements are rotated from ECS to the ACS in a preprocessing phase. Thus, there is no need to perform DoD/DoA rotations from ACS to ECS in the subsequent simulations.

**Polarization Mismatch** Since polarization properties of a single antenna element are related to its geometry, a comparison of polarization vectors between impinging wave and the analyzed antenna element has to be performed in the coordinate system having the full antenna description. One possibility is to perform two rotations of polarization vectors (GCS→ACS and ACS→ECS) for each simulated MPC and to calculate projections in ECS (Fig. 2.3). Another possibility is to use ACS: since array geometry is not changing, the polarization vectors of antenna elements are constant in ACS. In this case, polarization vectors are rotated from both GCS and ECS into ACS, and responses of all antenna elements are calculated in ACS. This approach is equivalent to approach II described for directional filtering since rotation of complete 3-D antenna element radiation pattern (including polarization vectors) is required.

## 6.2.2 Representation of Radiation Pattern

When *Radiation Pattern* (RP) of each antenna element is measured separately, the presence of other elements in array influence the measured RP and the effect of mutual antenna coupling will be contained in acquired RPs. If RP of every element in the antenna array is sampled with  $1^\circ$  both in azimuth and elevation, the  $360 \times 180$  vectors  $\vec{F}(\theta_n, \varphi_n)$  are obtained. Therefore, the representation of polarimetric RP for a single antenna\* requires  $2 \times 360 \times 180$  coefficients. The memory storage requirements could be reduced if, instead of the radiation pattern, its 2-D Fourier transform, EADF, is used [131]. The EADF can achieve a high data compression since spatial limitation of antenna aperture causes particular spectrum concentration in the transformed domain (Fig. 6.5b).

Furthermore, the EADF provides an effective way of interpolating the radiation pattern for arbitrary angles in azimuth and elevation that is superior in computation

---

\*The single port for the dual-polarized antenna.

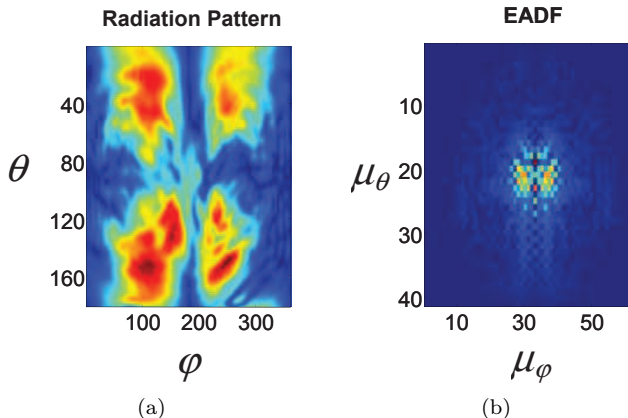


Figure 6.5: EADF compression capabilities: instead of  $180 \times 360$  beam pattern values (a), the equivalent EADF (b) needs approximately  $40 \times 60$  values (Landmann [7]).

time and interpolation error to, e.g., a spline interpolation of the radiation patterns [131]:

$$\vec{F}_k(\theta, \varphi) = a_1^T(\theta) G_k a_2(\varphi), \quad k \in \{\theta, \varphi\}, \quad (6.12)$$

where  $a_i(\alpha) = e^{j\alpha\mu_i}$ ,  $\mu_i = \left[-\frac{(L_i-1)}{2}, \dots, \frac{(L_i-1)}{2}\right]^T$ ,  $i = 1, 2$  and  $G_k$  is EADF matrix with dimensions  $L_1 \times L_2$ .

The sampling grid of the antenna RP for EADF calculation contains repetition of the pole values and because of that EADF is dependent upon referent coordinate system. As a consequence, after antenna rotation, the resampling of the radiation pattern in respect to a new pole is necessary. Since sampling grids before and after the rotation, in general, do not coincide, rotation will introduce interpolation errors. One way to resolve this issue is to represent antenna beam pattern with its *Vector Spherical Fourier Transform* (VSFT). Since Vector Spherical Fourier Transform (VSFT) uses suitable kernel functions for spherical CS (Vector Spherical Harmonics) it allows rotating the beam pattern by manipulating VSFT coefficients. Furthermore, VSFT offers better data compression than EADF [132]. Despite all this benefits, usage of VSFT for radiation pattern interpolation is considerably more complex than EADF, and because of that VSFT representation is not appropriate for system-level simulations.

### Complexity Analysis

The rotation of  $\vec{\Omega}$  vectors (defining DoD/DoA and associated  $\theta/\varphi$  polarization vectors) from the ACS to the ECS can be avoided during the simulation if radiation patterns of all antenna elements are rotated in a preprocessing phase ( $P^3$ ) and expressed in ACS. The computational complexity of this phase depends heavily on the representation of the radiation pattern and the interpolation function. The comparison given in Tab. 6.4 is based on EADF representation that requires a resampling of the radiation pattern: each pair of azimuth and elevation from the

Table 6.4: Complexity comparison for different usage of array in simulations.

Approach	I	II	
Phase	Simulation	Simulation	Preprocessing
# Rotations	$3(U + S) + 3$	3	$3(U + S)W/2$
# Interpolations	$2(U + S)$	$2(U + S)$	$(U + S)W$

ACS is transformed to the ECS and the element response is calculated using the interpolation function. Interpolation errors could be avoided if VSFT is employed for the rotation of the radiation pattern in the preprocessing phase. However, a more precise description would additionally increase the complexity of  $P^3$  and it is not considered here.

A rough estimate of the differences between the approaches I (ECS is used for radiation pattern (RP) representation, there is no  $P^3$ ) and II (ECS is not used in a simulation since 3-D antenna patterns are expressed in ACS, rotations are performed in  $P^3$ ) is given in Tab. 6.4. The table shows that number of required operations (rotations and interpolations) per single MPC depends on the total number of elements within the arrays,  $(U + S)$ , and the radiation pattern representation complexity,  $W$ . The *radiation pattern representation complexity* corresponds to number of coefficients (or samples) necessary for representation of complex polarimetric RP in (2.31). If EADF corresponds to  $L_1 \times L_2$  complex matrix, in the polarimetric case ( $P = 2$ ) the RP will have representation complexity of  $W = 2L_1L_2$ .

In both approaches it is necessary to rotate DoA/DoD from GCS into ACS, as well as  $\theta$  and  $\varphi$  polarization vectors of the impinging wave. The interpolations of radiation pattern for given DoA/DoD are handled separately for both antenna polarizations. Since antenna polarization directions are related to its geometry, in approach II (rotation of 3-D RP from ECS to ACS)  $\theta$  and  $\varphi$  polarization vectors defined in ECS will not correspond to spherical unit vectors  $i_\theta^{ACS}$  and  $i_\varphi^{ACS}$ . Instead, they will be represented as a linear combination of both (Fig. 2.3).

From Tab. 6.4 it can be seen that for given constant number of MPCs,  $NM$ , second approach can offer complexity reduction after  $D$  simulated channel segments (drops):

$$D = \frac{W}{NM} \left( \frac{1}{2} + \frac{C_I}{3C_R} \right). \quad (6.13)$$

Here,  $C_I$  and  $C_R$  are representing complexity of interpolation and rotation, respectively. In order to simplify the comparison, the basic complexity unit (BCU) will consist of complex exponent generation and complex multiplication. According to the Tab. 6.1 introduced BCU have complexity equivalent to 21 real operations. From (6.13) it can be seen that the number of antenna elements does not influence the value of  $D$ .

If EADF is used for interpolation according to (6.12), for each interpolation  $L_1+L_2$  complex exponentials are generated,  $L_1 \cdot (L_2+1)$  complex multiplications and  $L_1L_2 - 1$  complex additions are performed. In order to simplify dependence from EADF size, the complexity of EADF interpolation is approximated with  $C_I = W$  BCU, where  $W = 2L_1L_2$ . Each of 2-D rotations requires generation of one complex exponential and one complex multiplication, giving complexity of  $C_R = 3$  BCU

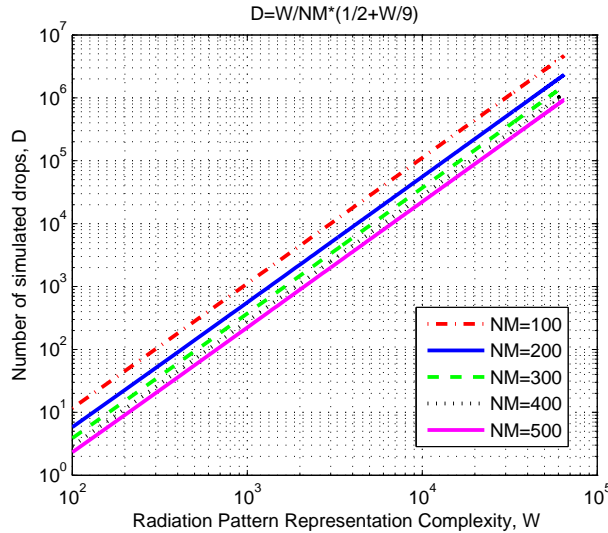


Figure 6.6: Number of simulated drops,  $D$ , that compensates complexity of 3-D antenna radiation pattern rotation in approach II, parameterized with number of MPCs ( $NM$ ) [7].

in total. Using the above assumptions, it is possible to determine the number of simulated drops  $D$ , after which the second approach offers lower total complexity, Fig. 6.6. If the total usage of the channel model (in multiple runs) for a given antenna array exceeds the value of  $D$  given in Fig. 6.6, approach II should be applied. Since departure/arrival angles of the WINNER model are updated on drop-basis, the number of simulated time-samples is not relevant for presented complexity analysis.

When a rotation of 3-D antenna RP is performed in the preprocessing phase, the complexity of simulations is reduced. However, the reduction of the total complexity (including necessary operations for the rotation of RP) is dependent on the representation complexity of the RP and the number of MPCs used in simulations. If EADF of applied antenna requires  $L_1 \times L_2 = 40 \times 60$  coefficients (Fig. 6.5b), the complexity of C2 NLoS scenario ( $N = M = 20$ ) simulation can be reduced after  $D = \frac{2*40*60}{20*20} \left( \frac{1}{2} + \frac{2*40*60}{3*3} \right) = 6406$  drops.

### 6.3 Space-Time Model Evolution

One of the most important characteristics of the channel model is its evolution over space and/or time, since variability is inherent characteristic of radio-channel. The causes for variations could be related to: i) movement of communication terminals, ii) movement of objects in environment, or iii) changes of the communication medium.

#### Motion in Radio Environment

For stationary transmitter and receiver small temporal variations in radio channel

will appear due to motion within the propagation environment. The moving scatterers could be vehicles, plants exposed to wind, living beings, machinery, doors, etc. The impact of individual moving scatterers to the power and frequency of the Doppler shift depend on their size and speed. Larger objects produce components with more power, while faster objects introduce components with higher Doppler frequencies into the Doppler spectrum. However, in general, the most moving scatterers, have small effect on Doppler spectrum. This is pointed in [28] in the form of the “big-slow rule”, where speed by which objects move is inversely proportional to their size. The consequence will be that faster/smaller object contributes small amount of power at high Doppler frequencies and power-significant contribution of slow/big object occurs only at low Doppler frequencies. Therefore, Doppler spectrum appears as monotonically decreasing.

### 6.3.1 Stationarity Assumptions

Typically, in mobile radio applications the channel becomes time-variant due to motion of communication terminals. If all scatterers contributing to the propagation channel are stationary, the channel will appear time-invariant whenever terminal stops moving. Under such assumptions, the channel characteristics are dependent on the transmitter and receiver positions and therefore time variance becomes equivalent to spatial variance [9]. All system level models being considered in this thesis (Sec. 6.5) are representing the wideband MIMO channels in static environments for non-stationary users.

#### Impact of Terminal Velocity

For static environments, the change of channel characteristics does not come from speed but from translation from one spot to the other. Done fast, the changes are fast, done slowly, the changes are slow, but essentially the total changes are identical for both cases. Although WINNER scenarios listed in Tab. 5.1 assume a certain range of terminal speed, this is mainly exploited during the synthesis of CIR where maximum Doppler frequency is to be determined. Therefore, the translation speed is important in running the model, but none of the model parameters are speed dependent (except maximal Doppler shift). Thus, a driving speed during measurements is not important, as long as the environment was nearly static during the measurements. This means that measurements for WINNER characterization are NOT performed by different speeds in order to select the closest dataset during the model usage.

#### Constraints Regarding Experimental Characterization

The MIMO channel sounding used for WINNER parameterization has a goal to resolve multipath structure for every position of measurement terminals. Therefore the maximal speed of terminal during the measurement is limited by the spatial extent of the area with the same multipath and time that a sounder needs to record single channel snapshot (CIRs between all Tx and Rx antennas for both vertical and horizontal polarization). The time required for single snapshot in RUSK system depends on applied measurement antenna arrays, and typically takes the values of several [ms]. During that interval the structure of multipath should

be unaltered. Since any movement of terminal or interacting objects is reflected in temporal domain (and corresponding Doppler spectrum), the proper sampling frequency should be ensured. According to the sampling theorem, for snapshot frequency  $f_S = \frac{1}{T_S}$  it is possible to resolve Doppler frequencies up to  $f_S/2$ . For maximal Doppler shift  $\nu_{max} = \frac{v}{\lambda} \leq \frac{1}{2T_S}$ , the maximum allowed speed between objects and measurement terminal is,

$$v \leq \frac{\lambda}{2T_S}, \quad (6.14)$$

where  $T_S$  is snapshot duration in [s]. Under these conditions channels are properly sampled in space-time.

### 6.3.2 Drop-based Simulations

One way to approach the **ST** variability is to divide the analyzed space-time domain into small regions with high similarity between channel realizations, named the Local Stationarity Regions (**LSRs**) [8]. This concept can be applied for channel characterization, but also for channel simulation with low complexity. Local stationarity regions are implemented in many current **GSCM**, but often under different names ('drops', 'channel segments', 'local-area' etc.). In **3GPP SCM** drop is designating area with fixed multipath structure, in which phases are updated to represent fast fading. The same feature is used in **WINNER** and later adopted in **IMT-Advanced channel model** [63]. According to the drop concept, radio channel is modeled as a number of stationary drops where multipath structure is assumed to be invariable. This concept enables multi-link and system level simulations with a relatively low complexity, Fig. 6.2.

#### Performance Evaluation by Drop-based Simulations

The analysis performed in [49] indicates that autocorrelation of **SoS** models is not ergodic if gains or frequencies are modeled as random variables. Since change of multipath profile from drop to drop results in random ray gains and Doppler frequencies, the drop-based geometric model is not ergodic. For ergodic models a single simulation trial represents the whole ensemble, while models with stochastic parameters require more simulation trials [133]. Therefore, drop-based geometric models are more complex than deterministic methods being discussed in Sec. 3.3.2. It is however possible to establish equivalence between them for single realization of multipath: e.g., within single drop **WINNER** model pseudo-randomly updates the ray phases according to Doppler shift. Thus, drop-based simulation correspond to running multiple deterministic **SoS** models (being ergodic within **LSRs**) in order to collect statistic relevant for complete scenario. Therefore, the proper evaluation of average performances, that characterize the whole environment, requires instantiation of large number of drops corresponding to different multipath realizations.

If only single drop is initiated during simulation this would correspond to estimation of the link performance of mobile terminal that is moving over the small spatial area, having almost constant multipath profile and experiencing only small-scale fading. Therefore, this kind of simulation will provide performance indicator



$BER = f(SNR)$  that is conditioned for single realization of multipath. This corresponds to simulation of the multiple environment realizations with the same multipath structure but randomly changed phases of MPCs<sup>†</sup>. This approach however, does not represent environment to the full extent, since variation of the multipath structure over the space-time is not considered.

In 3GPP SCM, WINNER and IMT-Advanced channel models the concepts of Large-Scale Parameter is exploited as tool to grasp the variations of the multipath profile in space-time. The observed statistic is then used during simulation to reproduce realistic space-time evolution. The single-drop model approximation have problem of the adequate environment representation: selection of the single drop exhibiting e.g. average LSP, does not necessary mean that some performance metric calculated for that selected drop represents mean of all metrics in full representation of the environment. If we assume that performance indicator  $\vec{I}_n = \mathcal{M}(\mathbf{H}(\vec{L}_n))$  depends on  $n^{th}$  realization  $\vec{L}_n$  of LSP parameters, than average performance for certain scenario is determined by averaging over different realizations of the environments:  $\vec{I}_{av} = \frac{1}{N} \sum_{n=1}^N \mathcal{M}(\mathbf{H}(\vec{L}_n))$ . Note that even for fully linear performance metric function,  $\mathcal{M}$ , averaging of channel realizations before metric calculation does not provide useful result.

The impact of propagation environment variation between drops on BER and MIMO capacity is reported in [128] and shown in Fig. 6.7. The evaluation is performed by placing a number of terminals into random network topology and simulating the short segments of the radio channel. The BER performance is evaluated for WINNER indoor A1 NLoS scenario [5]. Simulations for every drop and SNR value are performed during 50 seconds and obtained curves  $BER(\vec{L}_n) = f(SNR|\vec{L}_n)$  are represented with different colors on 6.7a. The variation of about 5 dB on  $10^{-3}$  BER level emphasize the necessity of using multiple drop realizations during performance evaluation.

The channel capacity is evaluated for 1000 drops of WINNER Urban macro C2 NLoS channel and fixed signal-to-noise ratio of 20 dB. The obtained histogram in Fig. 6.7b shows the large variations of channel capacity (about 12bps) between the drops. Observed relations imply that statistically valid results (matching continuous channel evolution) require performance averaging over multiple drop simulations.

### Complexity of Drop-based Simulations

The complexity of *drop-based* MIMO simulations is investigated in [128]. Two major aspects of GSCM are analyzed in the context of WINNER II channel model: the generation of the propagation parameters and computation of channel response coefficients. The resulting computational complexity is quantified by the number of *real operations* [130] and displayed in Tab. 6.3.

The idea behind drop-based simulations is to keep the multipath structure constant in the local stationarity region (“drop”). This has the advantage that all

---

<sup>†</sup> The same idea was used in [134] to approximate capacity CDF curves from estimated MPC (specular) parameters.

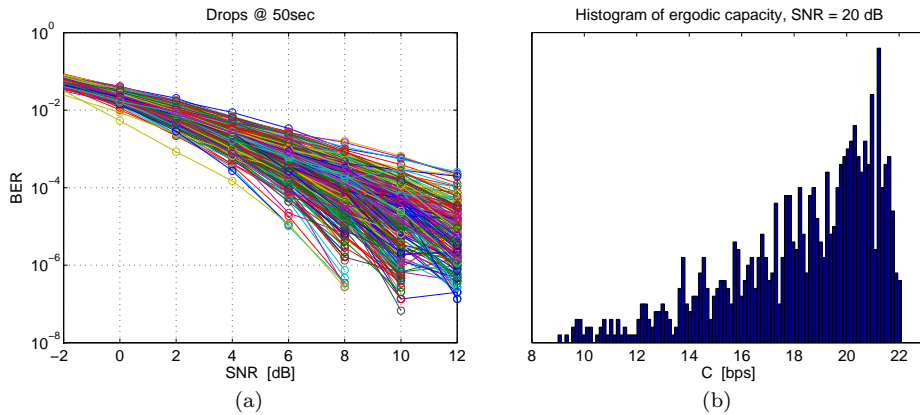


Figure 6.7: Variations of KPIs between different drops: a) BER curves simulated on 350 drops, b) histogram of ergodic capacity over 1000 drops for SNR = 10 dB (Kyösti [128]).

time-independent operations can be performed only once per drop, in a preprocessing phase. In this way, the recomputation of all MPC parameters and the complete generation of channel coefficients is avoided in consecutive simulation time instants. For GSCM using only a single polarization ( $\mathcal{P} = 1$ ), this saves 514 200 real operations and reduces complexity by 78.5% per time sample. According to Tab. 6.3, the generation of five or more time samples within a drop during a simulation requires more computation than the complete drop-related preprocessing. These results show that drop based simulation does not significantly increase the complexity of simulation if compared to the traditional synthetic fading models that does not account for channel geometry or ST evolution.

The reduction of ray-tracing complexity by a drop-like concept is also analyzed in the context of 802.11g-based ad-hoc networks [135]. The extent of the *homogeneous zone* is defined by the radius for which the autocorrelation function of the received power levels drops below 50%. In order to reduce complexity of simulations the received power level was kept constant within a homogeneous zones. According to the time that mobile spends within the same homogeneous zone and due to a dropout of unfeasible connections, a reduction of the computation time of  $\approx 50\%$  is reported.

### 6.3.3 ST Evolution of WINNER Model

Multi-link channel models can be distinguished by their consistency in representing the proper space-time evolution of multiple radio links. The proper ST evolution of all simulated links is important since it will influence system-level performance.

It is previously pointed in Sec. 3.6 that geometry-based models could use different strategies for environment representation: “real” positioning of scatters within simulation coordinate system or virtual positing in direction-delay domain. When ST evolution is related to cluster placement it inherently provides proper correlation of consecutive channel realization. Therefore, in the first case, a geometry-based approach of GSCM ensures a high consistency of the environment. The realism of

space-time evolution in COST 273 [60] and the COST 2100 models [105] is enforced by introducing the concept of visibility regions.

When a consistent description of the environment is not available, the knowledge of joint link properties is required to emulate *realistic* space-time relations. This is the case with models that place MPCs directly in the parameter space (angle/delay/Doppler). Examples for such models are the 3GPP SCM [34], the WINNER channel model [5] and the ITU model [63].

### LoS/NLoS Propagation Conditions

For most WIM scenarios, two different sets of model parameters are defined according to existence of an unobstructed line-of-sight (LoS) propagation path between the BS and the MS. Depending on the available environment model, the existence of LoS/NLoS propagation conditions can be determined in two different ways during simulations. If the terminal locations are known with respect to a street grid, the propagation condition can be determined deterministically. On the other hand, if such knowledge about an environment is not available, the WIM uses the scenario-dependent probabilities for LOS path existence.

The LoS probabilities depend on basic deployment parameters such as horizontal distance ( $d$ ) between the BS and the MS, BS and MS height, as well as parameters that characterize the radio environment. All expressions for LoS probability in WIM2 exhibit a dependence on  $d$  having the form  $\exp(-d/L)$ , in which  $L$  is a scenario-specific constant. It can be shown that this mathematical form arises from the assumption that equal length, but non-overlapping, segments of the direct propagation path have equal and independent probabilities of being obstructed. This assumption is considered to be reasonable for most actual radio environments, as long as the spatial distribution of objects that can potentially obstruct the direct path, is approximately uniform. The parameter  $L$  represents mean unobstructed path length, and tends to become smaller if the density of potentially obstructing objects increases. Results of ray-tracing simulations carried out in WINNER II framework indicate that the exponential model mentioned above is valid for dense urban areas as long as the BS and the MS are not located in the same, straight street canyon [125].

During dynamic simulations, the LoS probability determines the percentages of space and time in which the LoS and NLoS model parameters are used. In drop-based simulations, the LoS/NLoS conditions for all links are set at the beginning of each drop and kept constant until the next drop.

### ST Evolution Along the Route

WINNER models have kept the concept of drops being introduced by its 3GPP SCM precursor, under new name *channel segments*. The channel segment corresponds to a local stationarity region, in which propagation delays and DoA/DoDs, as well as LSPs: DS, AS and SF, do not change considerably. The original SCM/WIM1 framework uses quasi-stationary environment in which consecutive simulated channel segments do not necessarily follow predefined mobile route. Instead, they correspond to randomly chosen positions of MSs. However, for consistent ST evolution along the route it is necessary to determine how channel evolves

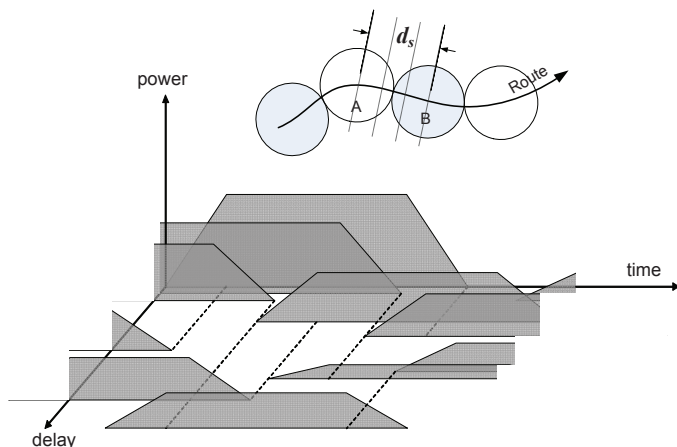


Figure 6.8: Model evolution: smooth transition between channel segments along mobile route is attained by power ramp-up and ramp-down of clusters. [125]

between two spatially neighboring drops. Attempts to introduce continuous evolution of angles and delays in extended SCM [66] have resulted in the computationally complex model, which is not suitable for system-level simulations.

Since a time-evolution of the channel model may have a considerable impact to the system performance evaluation, the new low-complexity approach is adopted for WIM2. The route to be modeled is covered by adjacent channel segments (Fig. 6.8), where the distance between segments,  $d_s$ , is equal to the extent of the local stationarity region. In order to support “smooth” model evolution in time, transitions from segment to segment are carried out by replacing clusters of the “old” segment by clusters of the “new” segment, one by one, by linearly decreasing/increasing their powers. The basic idea behind the substitution method is depicted in Fig. 6.8. The route between adjacent channel segments is divided into subintervals. Their number,  $n_{AB} = \max\{N_A, N_B\}$ , is equal to maximum number of clusters within the neighboring channel segments A and B. During each subinterval the power of one old cluster ramps down and one new cluster ramps up. Clusters from the old and new segments are coupled based on their power. If number of clusters is different in the channel segments the weakest clusters are ramped up or down without a pair from other cluster. With this concept, transitions between LoS/NLoS propagation conditions and different scenarios are supported.

### Usage of Correlations to Enforce ST Consistency

LSPs describing every particular drop are generated as uncorrelated random numbers from LSP probability distributions. However, it is necessary to account for similarities of links with close terminal positions. Since WIM does not “know” scatterer positions it has to enforce similarity using the correlations of LSPs.<sup>‡</sup>

<sup>‡</sup>The concept of LSP correlations is quite different from explicit sub-link correlations being exploited in filtering-based models. Actually, the latter models are not appropriate for system-level simulations due its limited ability to ensure consistency of ST evolution.

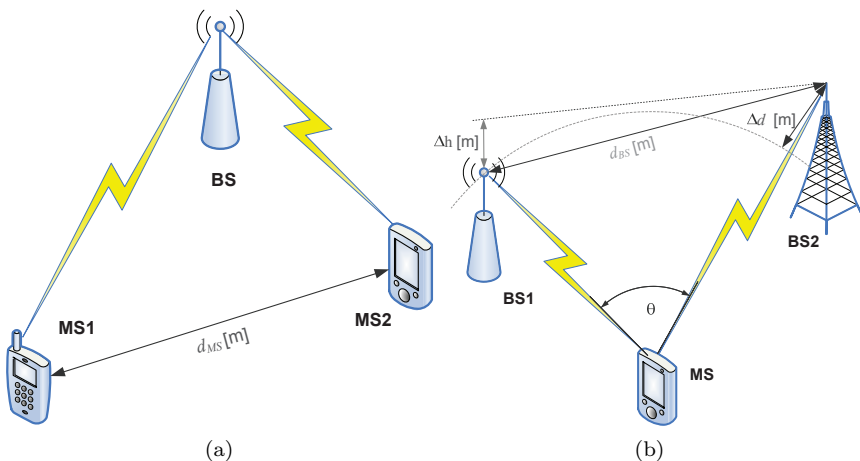


Figure 6.9: Correlation of radio links with common station: a) intra-cell, and b) inter-cell [125].

Under the assumption that the system layout information about position of all stations is available, **WIM** uses positions of **MS** to introduce the scenario-specific correlation of **LSPs** for **MSs** being connected to the same **BS**. Thus, multiple correlated links with the common **BS** can be simulated simultaneously in **WIM**.

In cellular networks two types of correlations could be identified at the system-level (Fig. 6.9): a) intra-cell correlations between **MSs** connected to the same **BS**, and b) inter-cell correlations of links from the single **MS** to multiple **BSs**. In both correlation types, an environment similarity comes from equivalent or common scatterers contributing to different links. However, due to different deployment assumptions for **BS** and **MS**, a difference between intra- and inter-cell correlations is observed in measurement data.

#### Intra-cell Correlations

In **WINNER** channel model intra-cell correlations are determined between subset of **LSPs**: **DS**, **AS** of both departure and arrival angles, and **SF**. **WIM2** assumes that intra-cell correlations are dependent only on distance between **MSs** ( $d_{MS}$ ), and uses correlation coefficient to express them:

$$\rho_{\tilde{x}\tilde{y}}(d_{MS}) = \frac{C_{\tilde{x}\tilde{y}}(d_{MS})}{\sqrt{C_{\tilde{x}\tilde{x}}(0)C_{\tilde{y}\tilde{y}}(0)}}. \quad (6.15)$$

Prior to quantifying their correlation, measured Large-Scale Parameter  $x$  and  $y$  are transformed into normally distributed processes  $\tilde{x}$  and  $\tilde{y}$ , using appropriate mapping  $g(\cdot)$ , Sec. 3.7.1. The cross-covariance function between transformed **LSPs**  $\tilde{x}$  and  $\tilde{y}$  is then determined as:

$$C_{\tilde{x}\tilde{y}}(d_{MS}) = E \{ (\tilde{x}(\vec{r}_1) - E \{ \tilde{x}(\vec{r}_1) \}) \cdot (\tilde{y}(\vec{r}_2) - E \{ \tilde{y}(\vec{r}_2) \}) \}, \quad (6.16)$$

where averaging is performed over all pairs of position vectors  $(\vec{r}_1, \vec{r}_2)$  being at distance  $d_{MS} = \|\vec{r}_1 - \vec{r}_2\|_2^2$ .

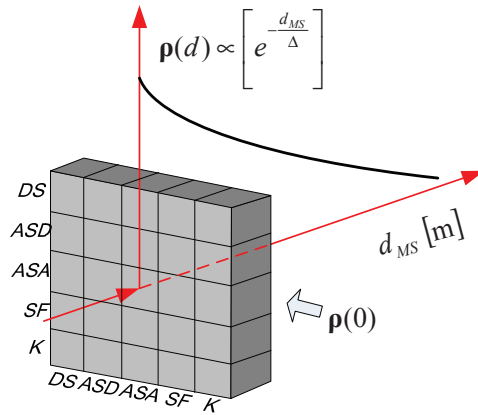


Figure 6.10: Distance dependent correlation coefficients used in WINNER channel model.

The LSP correlations observed in WINNER measurements (e.g., [99], [102]) show an exponential decay over distance, as previously reported in [136] and [137]. Similarly to [137], [138], [139], and [103] the experimentally determined dependence of correlation coefficient over distance is approximated by exponential model:

$$\hat{\rho}_{\tilde{x}\tilde{y}}(d_{MS}) = \exp\left(-\frac{d_{MS}}{d_c^{\tilde{x}\tilde{y}}}\right), \quad (6.17)$$

with single parameter  $d_c^{\tilde{x}\tilde{y}}$  that is called *de-correlation distance*. Accordingly, LSPs of two links toward the same BS would experience correlations that are proportional to their relative distance  $d_{MS}$ . The de-correlation distance is defined as the distance between MSs at which the correlation coefficient drops to  $e^{-1}$ .

Since every link (i.e., corresponding MS position) in WIM is characterized by several correlated LSPs, it would be necessary to quantify distance dependent correlations between all of them. In order to simplify correlation dependence from network layout, the correlations are characterized in two separate ways. The cross-correlations are considered only at zero distance,  $d_{MS} = 0$ , and only auto-correlations show distance dependence, as illustrated in Fig. 6.10. Correspondingly WIM reproduces LSP dependence from link-level cross-correlations and distance-based auto-correlations being introduced in Sec. 4.3.2. Distance based auto-correlations are characterized independently for every LSP, and applied for spatial filtering of independent LSP realizations, generated on drop basis. The matrix of cross-correlation coefficients define the shape of MVN distribution that represents scenario.

For modeling purposes correlations  $\hat{\rho}_{\tilde{x}\tilde{y}}(d_{MS})$  are introduced between independent Gaussian random variables with zero mean and unit variance according to (5.1). The correlated Gaussian RVs are afterward mapped to LSP values by using  $g^{-1}(\cdot)$ , Sec. 3.7.1. The given procedure enables the reproduction of distance-based intra-cell LSP correlations observed in measurement data, as demonstrated in Appx. B.2.

### Inter-cell Correlations

Inter-cell correlations are not supported in **WIM2** implementation, primarily due to lack of empirically supported results. An appropriate characterization of inter-cell correlations for different **WINNER** scenarios requires considerable amount of data being collected under specific measurement setups. **WIM2** assumes that neighboring **BSs** are sufficiently separated not to exhibit significant inter-cell correlations. On the other side, different sectors of the same **BS** are co-located and therefore their links show full correlation. In order to extend **WIM** capabilities for simulation of more complex network topologies, e.g., multihop links, ad-hoc links, peer-to-peer connections, it is necessary to extend model and incorporate the concept of inter-cell **LSP** correlations. The discussion about an extension of **LSP** correlation concepts toward representation of arbitrary inter-link dependencies is continued in Sec. 6.4.3.

## 6.4 Interlink Dependencies

Many wireless network concepts being investigated nowadays employ the multiple links: mesh topologies, relaying, distributed antennas, cooperative transmission, virtual **MIMO** etc. They tend to exploit an existence of spatially distributed terminals by their smart cooperation on the network level. A design and a performance evaluation of the systems incorporating multiple links require reliable models of coexisting radio channels.

Additionally, multi-link scenarios range from cellular multi-**BS** cooperation to peer-to-peer links, (where terminals on both link-ends can be mobile) and relay feeder links (with stationary terminals on both ends). These scenarios significantly differ from the classical cellular concept: changes in terminal deployment (height) and mobility pattern result in considerably different propagation conditions.

The dependency of different links on each other is a significant aspect in multi-user channel modeling. Therefore, for proper channel simulation, such dependencies need to be modeled accordingly.

### 6.4.1 Channel Similarity Measures

For multi-link channels it is necessary to quantify similarity between different links. Depending on the link similarity, the processing algorithms or transmission strategies could show different performance.

Typically, a correlation-like measures are used to characterize the similarity: interlink eigenvalue correlations and shadowing correlation are two examples. These correlations are equally applicable to link-dependencies with and without embedded space-time evolution. Alternatively, stochastic characterization of the ratios/differences between corresponding link properties can be applied, like in [140].

The applied approach in representation of similarities will be closely related to modeling strategy. The geometry-based models, being representatives of sum-of-rays approach are more suitable for this purpose than filtering-based models that already use explicit correlation between **MIMO** sub-links. The similarity of narrow-band **MIMO** channels, whose realizations correspond to matrix, could be expressed by appropriate projections such as *matrix collinearity* [141] or relations between

singular values (e.g. ratio of condition numbers [142]). In general, different measures as condition number ratio and matrix collinearity provide a different notion of the (dis)similarity of the spatial structure: while the condition number ratio reflects the channel directivity, the collinearity measure is sensitive to the alignment of the dominant propagation directions [105].

## 6.4.2 Impact of Common Scatterers on Interlink Correlation

For the development of multi-link channel models, it is essential to have understanding about the physical phenomena that increase correlation between different links, such as scatterers that are common for two or more links, i.e. common scatterers (or clusters of scatterers). Common scatterers are especially harmful for systems that depend on the spatial characteristics of the channel, since underestimating the significance of common scatterers in simulations would result in overestimating the system performance.

In [143] it is shown that large indoor structures as pillars can correlate shadowing realizations of two links that are established from nearby mobile terminal toward two significantly separated access points. Although different dominant propagation mechanisms are identified for links, their relevant MPCs have similar departure/arrival directions at the mobile side, causing a significant correlation of the received power.

In order to quantify the amount of energy that propagates via the same scatterers in different links, a measure called the significance of common scatterers was introduced in [144] as follows. In a dual-link case, the significance of the  $n^{\text{th}}$  common scatterer is denoted as a function of a time instant  $k$  by

$$S_{\text{common}}^n(k) = \sqrt{s_{\text{common}}^{(1),n}(k) \cdot s_{\text{common}}^{(2),n}(k)}, \quad (6.18)$$

where  $s_{\text{common}}^{(i),n}(k)$  is the proportion of the  $n^{\text{th}}$  common scatterer in total power in the  $i^{\text{th}}$  link. If the number of scatterers that are common for the different links is denoted by  $N(k)$ , the total significance of the common scatterers can be expressed by the sum of the significances of the individual common scatterers  $S_{\text{common}}^n(k)$  by

$$S_{\text{common,tot}}(k) = \sum_{n=1}^{N(k)} S_{\text{common}}^n(k). \quad (6.19)$$

The total significance of the common scatterers  $S_{\text{common,tot}}(k)$  gets values between 0 and 1, where 0 means that the different links have no common scatterers and 1 indicates that all scatterers are common for the two links. This concept is embedded into the COST 2100 model [105].

The significance of common scatterers was studied in [144]. It is found that in corridors the total significance of common scatterers is typically between 60% and 90%. The impact of common clusters to inter-link correlations is evaluated in [145] by the collinearity of generated correlation matrices. The simulated scenario considers links from two BSs to a single (fixed) mobile. These links share a single common cluster and have up to five additional clusters per link, all of which are randomly positioned. It was found that higher common cluster significance leads to increased collinearity, since it shifts collinearity CDF to the right.



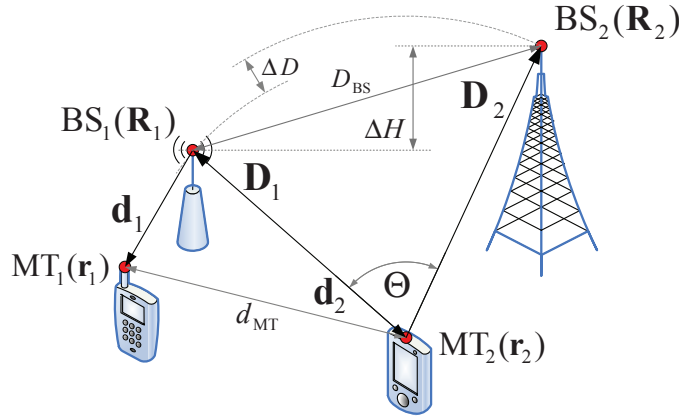


Figure 6.11: System layout defined by positions of communication terminals [64].

### 6.4.3 Correlations of LSPs Describing Different Links

#### Dependence of LSP Covariance Matrix on System Layout

The channel model of a system with  $K$  coexisting links should generate  $K \cdot M$  correlated LSPs, where  $M$  is the number of LSP per each link. The corresponding full covariance matrix  $\mathbf{C}\mathbf{C}^T$  would have, for each time instant, size  $M \cdot K \times M \cdot K$ . This matrix characterizes the correlations between all LSPs describing all coexisting links, however its proper synthesis is not trivial due to strong dependence upon the system layout. The problem can be addressed by proper decomposition of the transformation matrix,  $\mathbf{C}$ , according to *link-level*<sup>§</sup> and *layout-level* correlations. The link-level correlations correspond to cross-correlations of the LSPs characterising the same link, and according to the proposed simplification they will not change over space-time. On the other hand, the layout-level correlations explicitly depend on the relative position of the terminals at both link ends. Depending on at which link's end a terminal displacement occurs, it is possible to distinguish *intra-site* and *inter-site* correlations (Fig. 6.11). Since two different links with single common end could not simultaneously exhibit both correlation types, the intra-site ( $\mathbf{R}_i = \mathbf{R}_j$ ) and inter-site ( $\mathbf{r}_i = \mathbf{r}_j$ ) correlations could be conveniently combined for given system layout. These correlations are typically expressed in the form of layout-dependent correlation coefficient  $\rho_{XY}(\mathbf{L}) = \frac{\sigma_{XY}}{\sqrt{\sigma_{XX}\sigma_{YY}}}$ , where  $\sigma_{XY} = E[(X - E[X])(Y - E[Y])]$  denotes covariance between LSPs  $X$  and  $Y$ . The geometry parameters  $\mathbf{L}$  are determined from the vectors defining the relative position of mobile terminals  $(\mathbf{d}_i, \mathbf{d}_j) = (\mathbf{r}_i - \mathbf{R}_j, \mathbf{r}_j - \mathbf{R}_i)$  or base stations  $(\mathbf{D}_i, \mathbf{D}_j) = (\mathbf{R}_i - \mathbf{r}, \mathbf{R}_j - \mathbf{r})$  w.r.t. to single common position (Fig. 6.11). The set of relevant parameters  $\mathbf{L}$  for intra-site correlations could be reduced to Euclidian distance between mobile terminals  $d_{MT} = \|\mathbf{r}_i - \mathbf{r}_j\|$  [5]. Opposite to the intra-cell correlations, inter-cell correlations show dependence upon many layout param-

<sup>§</sup>A single link realisation, when compared to itself, could be considered as a special case in system layout, where there is neither displacement of the mobile terminal nor of the base station.

ters:<sup>¶</sup> [103], [139], [146], [147]. Therefore, the characterization of inter-site correlations requires a more complex parameter space  $\mathbf{L} = [\Theta, \Delta D, D_{\text{BS}}, \Delta H]^T$  [125] being defined at Fig. 6.11:  $\Theta = \angle(\mathbf{D}_i, \mathbf{D}_j)$  designates the angular separation of the base stations as seen from the position of the mobile terminal,  $\Delta D = \|\mathbf{D}_i\|_F - \|\mathbf{D}_j\|_F$  is the difference in distance of the mobile terminal to the respective base stations,  $D_{\text{BS}}$  is the distance between the base stations and  $\Delta H$  is their height difference.

### Inter-site correlations

*Inter-site* large-scale parameter correlations are an important property because their existence affects system performance [148]. Some general observations from literature are that the correlation is low when the BSs are in opposite directions as seen from the mobile. However, even for small angular separation between BS correlation can be low, if distances to the MS are not similar. Additionally, different height of BSs can considerably reduce correlation level. According to these results inter-site correlations show dependence on four parameters,  $\rho(\Theta, \Delta D, D_{\text{BS}}, \Delta H)$ , as illustrated in Fig. 6.11. Different correlation properties are expected in indoor and outdoor environments and under different LoS/NLoS conditions.

In [149] the inter-site correlations between links from different base-stations are analyzed. The assessment is based on simultaneous multi base-station measurements conducted by Ericsson in Stockholm. The parameter correlations between all combinations of shadow fading and delay spread of two links are investigated in both NLoS and LoS situations.

It is demonstrated that careful selection of spatial regions where correlations are calculated (manual selection of “similar” environments, small angular separation of BS, same propagation conditions, etc.) easily boosts intra-correlation levels above  $1/e$ . Generally, when the MS is between two BSs and also the main lobe of the BSs face to the routes, a high inter-site correlation exists – even if the BSs are far away from each other. If the MS is moving towards, or away from both BSs, positive inter-site correlations are obtained, otherwise negative correlations are obtained.

The (conventional) intra-site parameter correlations and their autocorrelation values were found to be similar to the established parameters in COST 2100 [105] and in the WINNER II C2 model.

### Cooperative Downlink

In configurations with spatially distributed communication sources a receiving terminal simultaneously receives multiple signals.

The power of the signals transmitted through a radio channel is spread over delay and angular dimensions, both at transmitter and receiver side. When these spreads become relevant for system design (e.g. wideband or MIMO transmission) they should be properly represented in radio-channel model.

Usage of spreads is intuitive way to represent physical channel propagation. According to its mathematical formulation spreads are independent from the absolute power level. This favourable property enables separate characterization of

---

<sup>¶</sup>These results do not match with 3GPP SCM assumption that shadowing fading exhibits constant (layout independent) correlation coefficient of 0.5.

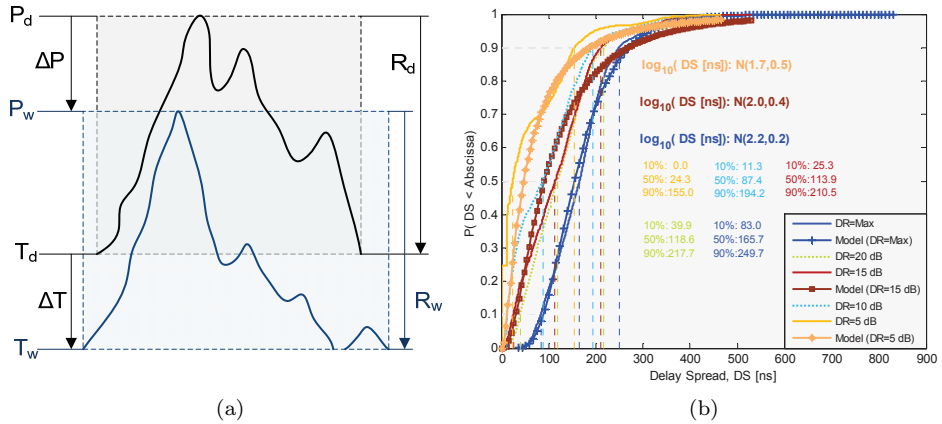


Figure 6.12: a) Impact of the power peak level differences to perceived spreads, b) DS PDF (empirical distribution and log-normal fit) as a function of effective dynamic range [150].

the power spreading and overall transmission loss. Many current models use the statistics of the measured power spreading to describe large-scale channel evolution [34], [5], [63]. They, however, do not consider downlink in a cooperative mode: a setup with common receiver and several spatially distributed transmitters, e.g. links  $(-\mathbf{D}_1, -\mathbf{D}_2)$  from Fig. 6.11.

When characterizing the cooperative downlink it is not possible to disregard the influence of the receiver's limited dynamic range on *perceived* LSPs of the cooperative links [150]. Due to the reception of signals with different power levels and the limited dynamic range of the receiver, a perception of power spreading in weaker links reduces. The presence of a dominant (stronger) link forces the weaker links out of the useful Dynamic Range (DR), as illustrated in Fig. 6.12a.

The perception of power spreading expressed by DS or AS depends on the *effective dynamic range* of the particular radio-link, as shown in Fig. 6.12b. Consequently, the characterization of inter-site correlations between cooperative links requires previous adjustment of effective dynamic ranges<sup>||</sup>. These will depend on the total power received from all cooperative links, and in general they will be lower for the weaker links.

The strategy of joint representation of distributed/cooperative wideband MIMO channels with common sink is proposed in [150], in which the modeling of cooperative links can be based on appropriate relations between *relative shadowing* and *perceived power spreading* [140]. The proposed strategy is described in the context of WINNER model and therefore relevant Large-Scale Parameters (LSPs) including Transmission Loss (TL), Delay Spread (DS), Angular Spread (AS) are determined according to the procedures from Sec. 4.3.

#### Statistics of Power Level Differences

The pointed LSP inter-dependence on link-level could be decoupled if spread-

<sup>||</sup>When measured separately each link will be characterized according to the dynamic range of the measurement equipment, what is not relevant for reception of simultaneous signals.

independent power reference is used. Therefore *peak power* is used instead of cumulative power. This parameter can be related to the power of the strongest multi path component, or (under certain conditions) to the maximum peak of Power-Delay Profile. The peak power can be characterized using the same procedures normally applied for the cumulative power analysis: a distance dependence can be expressed by regression model

$$\hat{P}(d) = A \cdot \log_{10}(d) + B. \quad (6.20)$$

Differences in peak-power levels from cooperative links are determined from multi-run measurements, by performing distance-based pair-wise snapshot matching [150]. The power peak difference,  $\Delta P$ , between cooperative links determines the effective DRs and consequently perceived power spreading. The measured *peak power level difference*,  $\Delta P = P_1 - P_2$  is related to peak power regression over the distance and shadowing realizations  $S_i$  of considered links  $i = 1, 2$ :

$$\Delta P = \hat{P}(d_1) + S_1 - (\hat{P}(d_2) + S_2). \quad (6.21)$$

Therefore, *relative shadowing* (difference between shadowing realizations on two links) can be calculated as:

$$\Delta S = S_1 - S_2 = \Delta P - (\hat{P}(d_1) - \hat{P}(d_2)). \quad (6.22)$$

The relative shadowing can be statistically characterized for particular multi-link configurations and targeted scenario, and parameters of corresponding PDFs can be included into model as an additional LSPs [150].\*\* The statistics of relative shadowing for routes '9a-9b', '10b-9a' and '41a-42' and base stations 'BS1', 'BS2' and 'BS3' at height of 25 m from Ilmenau measurement (Sec. A.2.3) is showed in Fig. 6.13a. The obtained empirical distribution can be roughly approximated as being uniform in the range from -8 dB to 17dB, or more complex multi-kernel representation can be used.

For a given realization of the peak power differences (random process) and a dynamic range of the receiver, the effective dynamic ranges for each of cooperative links can be determined.

### Perceived Power Spreading

As a consequence of the mutual interaction between links, the effective DRs will impact the distributions of perceived power spreads. The model should, therefore, quantify a general dependence between the effective DR and power spreads, whose significance is not limited to distributed links [71]. For this purpose the delay and angular spreads have been calculated for different dynamic ranges. The dynamic ranges being lower than the DR of a channel-sounder are emulated by thresholding the (marginal) power spectrum,  $S(x)$ , with respect to peak power level,  $\max\{S(x)\}$ . The analysis is performed for Delay Spread (DS), Azimuth Spread on Departure

---

\*\*Alternatively, the correlation coefficients between shadowing at cooperative links, (e.g.  $S_1$  and  $S_2$ ), can be used to represent the multiple-link channel. By using the letter approach narrowband and/or SISO links are analysed in inter-site configurations [147], [146], [103].

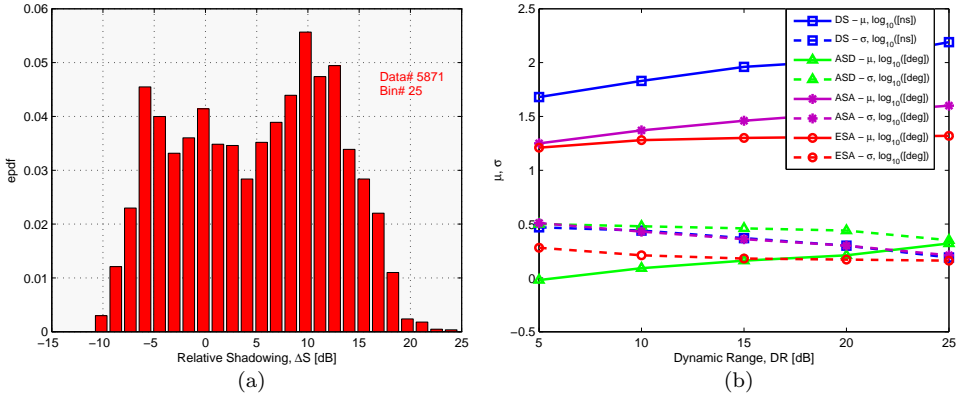


Figure 6.13: a) Empirical PDF of relative (pair-wise) shadowing, b) dependence of power spread log-normal PDF parameters from effective dynamic range [140].

Table 6.5: Dependence of power spread distributions from effective dynamic range.

Dynamic Range [dB]		5	10	15	20	Max
<b>Delay Spread</b> $\log_{10}$ ([ns])	$\mu$	1.68	1.83	1.96	2.02	2.19
	$\sigma$	0.47	0.44	0.37	0.30	0.19
<b>AzimuthSpread@Departure</b> $\log_{10}$ ([deg])	$\mu$	-0.02	0.09	0.16	0.21	0.32
	$\sigma$	0.50	0.48	0.46	0.44	0.35
<b>AzimuthSpread@Arrival</b> $\log_{10}$ ([deg])	$\mu$	1.25	1.37	1.46	1.53	1.60
	$\sigma$	0.51	0.43	0.36	0.30	0.21
<b>ElevationSpread @Arrival</b> $\log_{10}$ ([deg])	$\mu$	1.21	1.28	1.30	1.31	1.32
	$\sigma$	0.28	0.21	0.18	0.17	0.16

(ASD), Azimuth Spread on Arrival (ASA), and Elevation Spread on Arrival (ESA). The elevation angles on transmitter side have not been estimated, since geometry of the used linear array (ULA) is not suitable for this purpose.

For every computed empirical distribution an appropriate log-normal fitting is performed, as illustrated in Fig. 6.12b for DS. The observed dependence of log-normal model parameters ( $\mu, \sigma$ ) from effective dynamic range is showed in Fig. 6.13b and summarized in Tab. 6.5. From Fig. 6.13b it can be noticed that mean values ( $\mu$ ) of the spread distributions increase for higher dynamic range, while simultaneously their standard deviations ( $\sigma$ ) show slight decay. The rate of the change is the highest for DS. The ESA shows the lowest sensitivity to DR change, meaning that dominant multi path components are well distributed in the covered elevation range.

#### Extended Multi-Link Channel Model

After considering the mutual interaction of spatially distributed cooperative links, it was found that the power level differences and their interactions with perceived spreads should be properly modeled. In order to avoid correlation between spreads and reference power-level parameters on link level, it is proposed to refer to the peak instead of the cumulative power. Following the WINNER approach for other

parameters, the statistical characterization of peak power-level differences is performed at scenario level. This statistics can be used in direct form, or by accounting for peak level dependence over distance (equivalent to transmission-loss model). In the latter case relative shadowing is characterized stochastically, similarly to SF in existing models.

During model synthesis the randomly generated values of relative shadowing  $\Delta S$  will define the effective dynamic ranges, and the parameters of spread-related LSP distributions should be modified accordingly. In this manner, a representation of cooperative links is adjusted according to the receiver perception. Since the proposed approach enables simple manipulation of distributions of spreads, it is also suitable for dynamic simulations.

Above reasoning applies to models that use spreads based on relative power level, i.e. using an independent transmission-loss model. In the case of WINNER, this would mean modification of the global PDFs that characterize LSP distributions for weaker link(s). For the COST 273/2100 model, the consequence is that spreads of the clusters associated with weaker link(s) should be reduced. In both cases, the explicit assumption is that reference spread values refer to the maximum dynamic range for a single-link characterization.

One of the implications of “receiver perceived” channel representation is that reciprocity (normally assumed in channel modelling) will not be preserved. In a mesh network, the link between two communication sinks, each having other spatially distributed links too, will be experienced differently by the two sinks because of the unequal influence of the additional (distributed) links at both sides.

## 6.5 Comparison of WIM with Other State-of-Art System-level Models

The aim of WINNER (Wireless world INitiative NEw Radio) project [151] was to define a single ubiquitous radio access concept for beyond Third Generation (3G) systems, being scalable and adaptable to different short range and wide area scenarios and considering frequencies up to 5 GHz and bandwidths of 100 MHz. Since the radio interface have been seen as the key part of this concept, realistic propagation models covering many different environments were required for its design. Developed WINNER Channel Model (WIM) [5] has advanced 3GPP SCM [62] concepts toward a single generic framework that is capable to represent all targeted indoor/outdoor environments (scenarios). Different (scenario-specific) parameter sets for the generic model are based on series of wideband, polarimetric, MIMO radio channel sounding experiments.

Fig. 6.14 illustrates the relations between the COST, 3GPP, and WINNER state-of-art models that will be discussed here. By its nature, these models are representing the wideband MIMO channels in static environments for non-stationary users. WIM has been developed starting from the Spatial Channel Model framework, and therefore these models share many concepts, as will be shown here. Somehow in parallel, a generic COST 273 [60] model is developed from the COST 259 framework, having similar objectives as WIM. Since results of COST 259 action have influenced 3GPP SCM as well (SCM is in essence also double directional

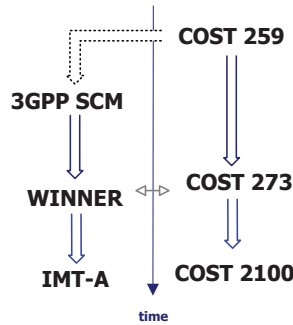


Figure 6.14: Relation between modeling activities: majority of contributions originate from academy (COST) or industry (SCM/WINNER).

channel model), it is reasonable to expect that WIM and COST 273 model share some similarities. However, SCM have been developed for system-level performance analysis and therefore introduced many simplifications to reduce complexity (computation time). COST 273 model designers have claimed that introduced simplifications could restrict the general applicability of the model and therefore decided to provide more universal concept. In similar manner, descendant action COST 2100 [152] has continued tuning and parameterization of the COST 273 model, disregarding WIM/SCM simplifications.

In the meantime WIM concept (being further developed within WINNER+ project) has impacted IMT-Advanced standardization: ITU-R M.2135 Report takes slightly modified WINNER model as reference for evaluation of IMT-Advanced radio interface technologies. [63]

### 6.5.1 Common Modeling Concepts

All compared models support representation of *wideband MIMO* radio channel between *multiple* transmitting and receiving *stations*. Therefore, they are suitable for system-level (multiple link) performance evaluation.

The basic modeling philosophy behind all compared models (SCM/SCME/WIM/COST) is the same: the sum of specular components is used to describe the changes in the CIR between each transmitting and receiving antenna element by using SoS approach. Due to the different spatial position of elements inside Tx/Rx antenna array, different channel characteristics are obtained and MIMO concept is supported.

All compared models can be classified as stochastically controlled spatial channel models what means that parameters of randomly selected MPC are related to its physical propagation in space-time. All these models use GSCM approach, where MPCs are grouped into *clusters*. Distinction between SCM/WINNER models on one side and COST models on another, comes from concept of stochastic model driving, as indicated in Sec. 3.6. This have consequences to consistency ST model evolution Sec. 6.3.3, and necessity of SCM/WIM to use correlation for characterization of inter-link dependencies Sec. 6.3.3.

To characterize different environments (*scenarios*) **SCM**/**WINNER**/**COST** models are using (temporal and spatial) parameters obtained from measured **CIRs**. For each scenario measured data is analyzed and processed to obtain scenario-specific parameters. After this point, same *generic* model is used to represent all scenarios, just by using different values of control parameters.

*Transmission-loss* models are defined explicitly (separately from other features) in both **COST** and **SCM**/**WIM**. This allows use of the existing transmission-loss models, however, **WIM**'s transmission-loss models are mainly based on measurements taken during the **WINNER** project [112].

In all models power ratio between orthogonal signal *polarizations* is expressed by log-normally distributed **CROSS-Polarization-Discrimination-Ratios** (**XPD** in **COST** 273 and **XPR** in **SCM**/**WIM**).

For *LoS* cases ratio of direct power and reflected/diffracted power is adjusted in both models. In **SCM**/**WIM** this parameter is called Ricean K-factor (following analogy with narrowband case), while **COST** models termed this quantity “LoS power factor”. In all models this is log-normal random variable.

## 6.5.2 (Extended) Spatial Channel Model

This subsection is summarizing all important differences and compares features and performances of **WINNER** channel model with Spatial Channel Model (**SCM**) and its extension (**SCME**). Compared models are offering complete channel model description in a sense of large-scale as well as small-scale effects in **MIMO** radio channel. Since **SCM** was originally proposed for 2 GHz range and 5 MHz bandwidth, certain extensions were necessary. At the beginning of the **WINNER** project, before having a full insight into the measurement results, mainly theoretical extension of **SCM** is provided under name **SCME**. It was found that the main limitations of the proposed approach come from the decision to attain backward compatibility with **SCM**. That was the motivation to start using the new **WINNER** generic channel model, where model parameters are extracted from channel-sounding measurements covering frequencies up to 5 GHz and bandwidths of 100 MHz, in different types of environments.

### Supported Scenarios

**SCM** was originally dedicated to outdoor propagation, and defines three environments: Suburban macro, Urban macro, Urban micro. In **SCME** number of scenarios is not extended. **WINNER** models are supporting considerably larger number of scenarios than **SCM**/**SCME**, as discussed in Sec. 5.1.

Usually, even for the same scenario, existence of *LoS* component substantially influences values of model parameters. Regarding to this property, each **WINNER** scenario is differentiating between *LoS* and *NLoS* conditions. Originally this was not the case with **SCM** where *LoS* condition was analyzed only in the context of Urban Micro scenario, but **SCME** provided the extensions for the other **SCM** scenarios.



### System Dependence

**Carrier Frequency:** Dependence on carrier frequency in **SCM/SCME/WIM** is found in transmission-loss models. In **SCM**, **COST 231 Urban Hata** (macro-cell) and **COST 231 Walfish-Ikegami** (micro-cell) transmission-loss models are adopted and adjusted for frequencies of 1.9 GHz. In **SCME** frequency range for **SCM** scenarios is extended based on correction of the frequency dependent free space loss:

$$\Delta TL(f_c) = 20 \log \left( \frac{f_c}{2} \right), \quad (6.23)$$

where  $f_c$  is carrier frequency in [GHz]. Additionally, in **SCME**, the **COST 231 Walfish-Ikegami** transmission-loss model was applied also for macro-cell environments in 5GHz range since usage of higher frequencies decreases coverage area. Following **SCME** approach, all scenarios defined by **WIM** support frequency dependant path-loss models valid for the ranges of 2 – 6 GHz.

From **WINNER** measurement results and literature survey it was found that model parameters Delay Spread, Angular Spread and Rician K-factor do not show significant frequency dependence [66]. From that reason these parameters show only dependence on environment (scenario).

For modeling systems with Time Division Duplex (**TDD**) all models (**SCM/SCME/ WIM**) are using same (large-scale and small-scale) parameters for both Up-Link (**UL**) and Down-Link (**DL**). If system is using different carriers for duplexing (**FDD**), than (additionally to transmission loss) random phases between **UL** and **DL** are independent.

**Bandwidth:** In **3GPP SCM** reference document [62] there is a note that usage of 6 paths (clusters) may not be suitable for bandwidths higher than 5MHz. This reflects the possible influence of system bandwidth to the complexity of model structure, e.g., number of clusters, number of **MPCs** per cluster. Following the approach described in [153] for indoor propagation modeling, **SCME** used intra-cluster delay spread as a mean to support bandwidth extension. However, since **SCM** forced backward-compatibility (to attain comparability with **SCM**, number of clusters and total number of **MPCs** are not increased. Instead, **SCM** cluster with 20 **MPCs** is subdivided into 3-4 zero-delay sub-clusters (“mid-paths”), keeping total number of **MPCs** constant. Introduced delay spread per cluster (10ns) reflects the targeted 100 MHz bandwidth, and redistribution of equal power **MPCs** between sub-clusters matches **PDP** decay, Fig. 3.9.

In **WIM** different philosophy is applied: since measurement systems were supporting 100 MHz bandwidth, during **WIM** parameterization number of clusters was traced in delay and angular domains from measured **CIR**. In this way number of clusters reflects both system bandwidth and scenario dependence. It is not expected that intra-cluster spread concept with unchanged number of **MPCs** better reflects bandwidth dependence than introduction of the new clusters. However, the latter approach also increases complexity since total number of **MPCs** would be increased. Therefore, both approaches are combined in **WIM2**.

**Antenna Arrays:** **SCM/SCME/WIM1** introduce additional support for cross-polarized antenna arrays because default representation for antenna arrays was not general enough (the reference polarizations of antennas and environments are not modeled separately). The full polarimetric antenna description was developed in **WIM2** [7] and described in Sec. 6.2.

### System Level Description

In order to calculate transmission-loss, the information about distance between transmitting and receiving station is necessary for all compared models. Accordingly, the system layout requires positions of all stations. However, the system layout in these models usually does not contain additional informations about simulated environment. Only exception is related to the positions of far scatterers in the **SCM** and **WIM2**.

**Correlation at System Layout Level:** In all models all **LSPs** are fully correlated for links between **MS** and different sectors of the same **BS**. In this way, influences of selective antenna gain pattern or different **LoS** conditions between certain sectors to the level of **LSP** correlation are not regarded.

Additionally to **SCM**, the **WIM** uses positions of **MS** to introduce scenario-specific correlation of link **LSPs** for **MSs** being connected to the same **BS**. In **SCM/SCME** correlation of **LSPs** between different **MS** is not supported.

In **SCM**, a standard deviation of shadowing fading for links from one **MS** to different **BSs** (“site-to-site”) has constant correlation coefficient equal to 0.5. Introduced correlation does not depend on distances between **BSs** or their relative angular positions as seen from **MS** and therefore it is not layout dependant. **WIM** does not support layout independent inter-cell correlations and same applies to **SCM/SCME** implementations supported by **WINNER**.

### Complexity Issues

**SCM/SCME/WIM** are intended for system level evaluation. In order to keep complexity reasonably low, these models are relying on some quasi-realistic assumptions and concepts:

**Channel Segment/Drop:** Channel segment (drop) represents period of quasi-stationarity in which probability distributions of low-level parameters are not changed. During this period all large-scale control parameters, as well as velocity and direction-of-travel for mobile station are held constant in **SCM/WIM** models. Contrary, **SCME** has allowed simultaneous drifting of arriving angles and delays for every **MPC** at each simulation step inside a drop. In respect to this property **SCME** can be classified as model with continuous evolution (in discrete steps, being smaller than drop). Consequence was substantial increase of complexity and simulation time length in comparison to **SCM/WIM1**. **WIM2** uses a reduced complexity time evolution in comparison to **SCME**, which is based on cluster replacement between neighboring drops and described in Sec. 6.3.3.

Table 6.6: Feature comparison of SCM, SCME, WIM1 and WIM2.

Feature	SCM	SCME	WINNER I	WINNER II
Bandwidth $\geq 100$ MHz	No	Yes	Yes	Yes
Indoor scenarios	No	No	Yes	Yes
Outdoor-to-indoor and indoor-to-outdoor scen.	No	No	No	Yes
AoA/AoD elevation	No	No	Yes	Yes
Intra-cluster delay spread	No	Yes	No	Yes
TDL model based on the generic model	No	Yes	Yes*	Yes
Intra-cell correlations between MSs	No	No	Yes	Yes
Time evolution of model parameters	No	Yes**	No	Yes

\* TDL model is based on the same measurements as generic model, but analyzed separately.

\*\* Continuous time evolution.

**Zero Delay Spread Cluster (ZDSC):** MPCs belonging to the same cluster (path in SCM terminology) have “close” values of both delay and angular parameters. If all MPCs belonging to the same cluster have exactly the same delay, it is possible to define extremely simple relation between SCM/WIM and Tapped Delay Line (TDL) model. Due to mentioned similarity, the spatial extension of TDL is also called CDL model in WINNER terminology. This type of reduced-complexity model is offered in SCM/SCME/WIM for link-level simulations and calibration purposes. The support of intra-cluster delay spread concept in SCME increases number of “taps” in TDL/CDL model 3 or 4 times, since cluster is represented by 3 or 4 zero-delay sub-clusters.

**Predefined Angular Offsets from the Cluster Center:** This property is used by SCM/SCME/ WIM to avoid random generation of MPC angles in each drop. Difference is that WIM scales initial offsets with standard deviation of angles per cluster, while SCM uses predefined values for intra-cluster (sub-path) departure angle spreads of  $2^\circ$  (macro) and  $5^\circ$  (micro) and  $35^\circ$  for spread of arrival angles. When separate drifting of MPCs inside cluster (continuous evolution) is used by SCME, angular offsets are not constant any more.

**Comparison Tables** Tab. 6.6 summarize the qualitative differences between SCM/SCME/ WIM1/ WIM2 features, while the Tab. 6.7 gives their numerical comparison. DS values in WIM2 scenarios are generally lower then for WIM1 due to the new estimation procedure that regards only upper 20 dB of the observed signal range in CIR. The higher DS range in Tab. 6.7 corresponds to the bad urban scenarios that are modeled with an additional far-cluster option. Additionally, other parameters of WIM1-supported scenarios are also slightly tuned for WIM2 according to the newly performed measurements.

Table 6.7: Numerical comparison of SCM, SCME, WINNER I and WINNER II.

Parameter	Unit	SCM	SCME	WINNER I	WINNER II
Max. bandwidth	MHz	5	100*	100**	100**
Frequency range	GHz	2	2 – 6	2 – 6	2 – 6
No. of scenarios		3	3	7	12
No. of clusters		6	6	4-24	4-20
No. of mid-paths per cluster		1	3 – 4	1	1 – 3
No. of sub-paths per cluster		20	20	10	20
No. of taps		6	18 – 24	4-24	4-20
BS angle spread		5 – 19	4.7 – 18.2	3.0 – 38.0	2.5 – 53.7
MS angle spread		68	62.2 – 67.8	9.5 – 53.0	11.7 – 52.5
Delay spread	ns	170 – 650	231 – 841	1.6 – 313.0	16 – 630
Shadow fading stand. deviation	dB	4 – 10	4 – 10	1.4 – 8.0	2 – 8

\* artificial extension from 5 MHz bandwidth

\*\* based on 100 MHz measurements

## Performance Figures

**Frequency Correlation** Under the joint WSS (i.e., WSSUS) assumption, the Frequency Correlation Function (FCF) is related to the average Power-Delay Profile (PDP) through a Fourier transform (Wiener-Khintchine theorem, Appx. C). Since the compared models are using only specular components, the FCF is estimated from discrete PDP by using:

$$R(\Delta f) = \frac{\sum_i S(\tau_i) \exp(-j2\pi\tau_i\Delta f)}{\sum_i S(\tau_i)}, \quad (6.24)$$

where  $\Delta f$  is the frequency difference,  $\tau_i$  is the delay and  $P_i$  is the power of the  $i^{\text{th}}$  path.

Fig. 6.15a depicts frequency correlation of SCM, SCME, and WINNER I models in 100 MHz bandwidth [154], [155]. The correlations are based on the respective TDL models of suburban NLoS scenarios.<sup>††</sup> This figure shows that the correlation of SCM model for bandwidths exceeding 10 MHz is considerably higher than correlation of SCME and WINNER models.

**Fading Distribution and Autocorrelation of Equivalent Narrowband Channels** The amplitude fading, autocorrelation, level crossing rate and Doppler spread are important measures of the channel model performance. However, statistical analysis of these parameters have shown very similar results in all compared models. Fig. 6.15b shows the temporal auto-correlation functions as example.

<sup>††</sup>The TDL of SCM was taken from SCME by removing the intra-cluster delay spread.

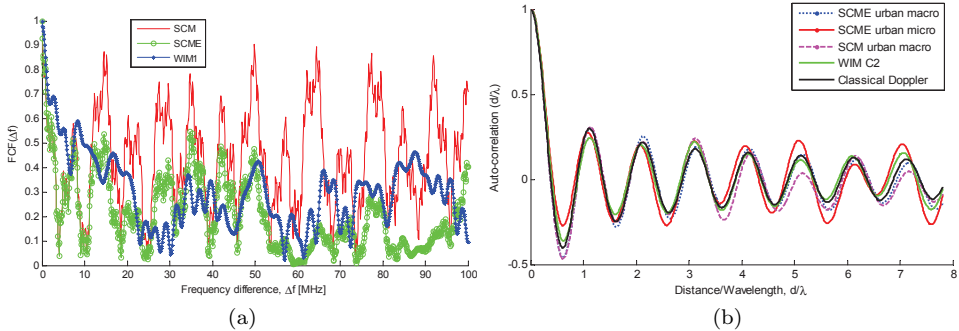


Figure 6.15: Comparison of correlation function between SCM, SCME, and WIM: a) Frequency correlation function for Suburban scenario. b) Temporal auto-correlation functions of the equivalent narrowband channels (Kyösti [70]).



Figure 6.16: MIMO antenna configuration for capacity calculation. [70]

**Outage Capacity of Equivalent Narrowband Channels** Both spatial and polarization characteristics of the models are investigated by the means of a channel capacity. Based on the assumption that the channel state information is unknown to the transmitter, the narrowband capacity is calculated by

$$C = \log_2 \det \left\{ \mathbf{I} + \frac{P}{\sigma^2} \mathbf{H} \mathbf{H}^H \right\}, \quad (6.25)$$

where  $\mathbf{I}$  is the identity matrix,  $P/\sigma^2$  is the average SNR,  $\mathbf{H}$  is the narrowband channel matrix and  $(\cdot)^H$  denotes the Hermitian transpose operation.

Capacity curves are simulated for signal to noise power ratio of 14 dB for all (three) scenarios supported by SCM/SCME and shown in Fig. 6.17. The complementary cumulative distribution function of capacity is plotted for a several independent channel snapshots and compared to Gaussian i.i.d. channel matrix. The reference antenna configuration is 4x4 MIMO with two sub-groups of  $\pm 45^\circ$  slanted single polarized elements whose spacing is 4 wavelengths on BS and half of wavelength on MS, see Fig. 6.16. For the all three scenarios the median outage capacity is about 7 bits/s/Hz lower than Gaussian i.i.d. reference curve. As expected, SCME gives equal outage capacities to SCM because its spatial and polarization characteristics are not changed in the respect to the basic SCM. The outage capacity of the WIM1 deviates slightly from SCM/SCME in Urban Micro scenario, while in Urban Macro scenario WINNER model shows higher capacity than SCM/SCME.

As could be seen from previous discussion, modeling methodology and certain SCM concepts are still part of WIM. The similarity is observed in the narrowband capacity measures that reflect the spatial and polarization properties of the models.

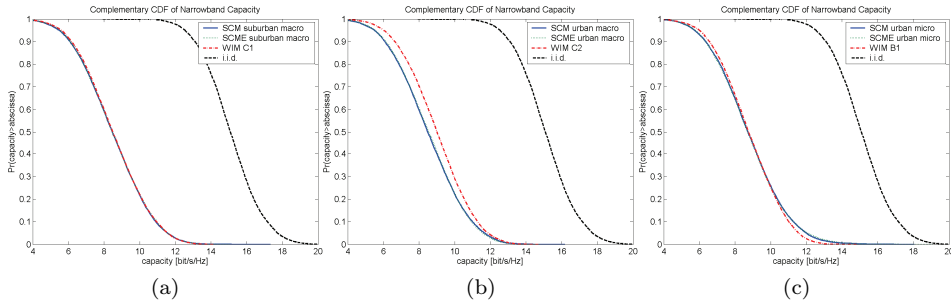


Figure 6.17: Comparison of outage capacity between SCM, SCME, and WINNER: a) Suburban Macro, b) Urban Macro, and c) Urban Micro scenario (Kyösti [70]).

However, without extensions provided in **WINNER** it would not be possible to apply **SCM**-based methodology to the frequency ranges and extended system bandwidths. The main strength of **WIM** is based in scenario-customized parameters that are making possible to apply generic spatial-channel-model to the numerous of different environments. Special **WIM** quality also comes from the fact that parameterization is based upon the real channel-sounding measurements.

### 6.5.3 COST Models

**WINNER** and **COST 273** channel models have been developed for generic (multiple-environment) representation of the wideband **MIMO** radio channel. Although both models belong to the class of Geometry-based Stochastic Channel Models and use similar concepts, there are still significant differences in model structuring and parameterization. This section compares modeling strategies adopted by **WINNER** and **COST 273** and analyzes relevant differences.

#### Global vs. Cluster-level Characterization

It is necessary to be cautious, when comparing **WIM** and **COST 273** models since similar terms are applied on different levels of the model characterization: **WIM** is introducing Large-Scale Parameters (i.e. angular and delay spreads, shadow fading, K-factor) on the global level, while **COST 273** is often using the same parameters on cluster-level.

*If we disregard the level at which characterization is performed* it is possible to recognize that the general approach is the same: the control variables are generated as correlated random numbers from predefined distributions. There is however difference in the number of the correlated control variables: **SCM** e.g. uses shadow fading, delay spread, and spread of departure angles. **COST 273** model additionally considers spread of arriving angles, referring to both azimuth and elevation angles (if applicable). In **WIM** there is one more parameter: K-factor is used under **LoS** conditions, what gives 7 correlated variables in total.

### Cluster Generation

The **COST 273** model makes a distinction between clusters involved into single and multiple interactions. This model allows two different strategies for cluster generation: “geometric” and “angular spectrum”. The geometric generation assumes cluster placement in a referent coordinating system via the concept of “visibility regions”. Different geometric strategies are proposed for both single and multiple interaction clusters. In “angular spectrum” approach a mean **DoD**, **DoA** and delay are generated as random variables from predetermined distribution (like in **WIM**). The “angular spectrum” strategy is intended only for multiple interaction clusters.

In the **SCM/WIM** models there are no distinction between clusters based on the number of interactions and the only “angular spectrum” strategy is used for their generation. This can be considered as one of the essential differences between **COST 273** and **WIM**. It follows from different viewpoints of measurement-based characterization (**WIM**, i.e., “angular spectrum”) and synthetic model generation (“geometric” strategy). After acquiring **MPC** parameters from high-resolution algorithms, antenna centric view of the channel is obtained. This analysis gives power distribution over delay, direction and polarization domains. Such a representation is suited for “angular spectrum” approach, and enables straightforward extraction of model parameters. The missing part, that makes this approach different from geometric cluster generation, is distance between **BS/MT** and the last interacting cluster. This step is, however, necessary if we would like to determine scatters positions from the measurement data. Some related work can be found in [156] and [29].

#### Impact of scatterer positioning to model parameterization/validation

The positioning of Interacting Object (**IO**) in the *geometry* domain during model synthesis makes model less suitable for the experimentally-based parameterization, since additional transformation of the measured features from *parametric* domain (Doppler, delay, angular, polarization) into **IO** positions is required. It can be recognized that this type of analysis tremendously increases data analysis requirements, which have been already very high due to high-resolution parameter estimation. (The procedure is simple only for single interaction case [157].) In contrast, the **WIM** model is synthesized in *parametric* domain, without excursion into geometry domain, what enables straightforward parameterization from measurements.

Additionally if “visibility regions” of single clusters should be determined from measurements, it would be necessary to perform rendering of the complete **2-D** plane/**3-D** volume. Typically, measurements have been performed mainly over straight routes since storage capacities and necessary analysis time are putting limit to reasonable number of snapshots that should be taken during the measurements. Having this in mind, it becomes clear that verification of geometric cluster generation cannot be easily performed from measurements!

There is another approach to this problem: a development of mechanisms for geometric cluster positioning that mimic observed signal statistics. For this purpose **COST 273** proposes different strategies for clusters with single and multiple interactions.

**Number of Clusters** In **COST 273** model cluster visibility regions (geometry approach) are placed to reflect constant number of visible clusters in average. “Angular spectrum” approach, determines the number of “visible” clusters as random variable with predefined distribution. **WINNER** model introduces further simplification and for given scenario uses constant number of clusters that is equal to the mean number of clusters observed in measurement data.

**Space-Time Channel Evolution** A placement of the visibility regions in **COST 273** model is indirectly defining space-time evolution of the propagation channel (e.g. for given trajectory of the **MT**), and correlation between different spatial positions. In the original **SCM** concept a quasi-static approach is used that does not take care about evolution – consecutive simulation “drops” correspond to random locations of the **MT**. In **WIM** concept evolutionary transitions between neighboring “drops” are supported. Since **WIM** does not use **IO** positioning (i.e. environment structure), (dis)appearance of the clusters is considered in parametric “delay-directional” domain. In order to emulate **ST** evolution in parametric domain **WIM** uses distance-based correlation of the Large-Scale Parameters.

### Cluster Structure

In **COST 273** model each cluster (opposite to **WINNER**, Sec. 5.4) is characterized with its own (correlated) angular and delay spread parameters. These spreads are controlling *intra-cluster* angular (Laplacian) and delay (exponential) power distributions.

**SCM/WIM** use predetermined cluster structure where all **MPCs** in cluster share equal powers. This is not the case in **COST 273** model where the power of **MPCs** is characterized by a Ricean distribution. It should be noted that **COST 273** approach differs from the usage of per-cluster K-factor in [158]. The latter model assumes that **MPCs** have equal power (like **WIM**), but allows existence of group with coherent **MPCs** (forming dominant scatterer).

### Correspondence between WINNER and COST 273 Scenarios

The **WIM LoS** and **NLoS** conditions are not distinguished only by the existence of the single strong **LoS** component. Instead, all scenario-dependent parameters are calculated separately for the **LoS** and **NLoS** propagation conditions. When simulations are performed without knowledge of street grid or building layout, the **WIM** model rely on a set of scenario-dependent expressions for **LoS** probability.

In the parameterized **COST 273** scenarios **LoS** occurrence is determined using the “visibility region” concept. The probability of **LoS** regions in this model decreases rapidly with the **BS-MT** distance, and becomes zero after cut-off distance.

The classification of the **COST 273** scenarios is shown in Fig. 6.18. As in the case of the **WINNER RPS**, the **COST 273** scenario definitions are model independent, but all of them are being represented by the single generic channel model.

From Fig. 6.18 it can be recognized that significant overlap exist between **COST 273** and propagation scenarios investigated in **WINNER** project. Some **COST 273** scenarios (microcell open space, tunnels and home environment) have not been



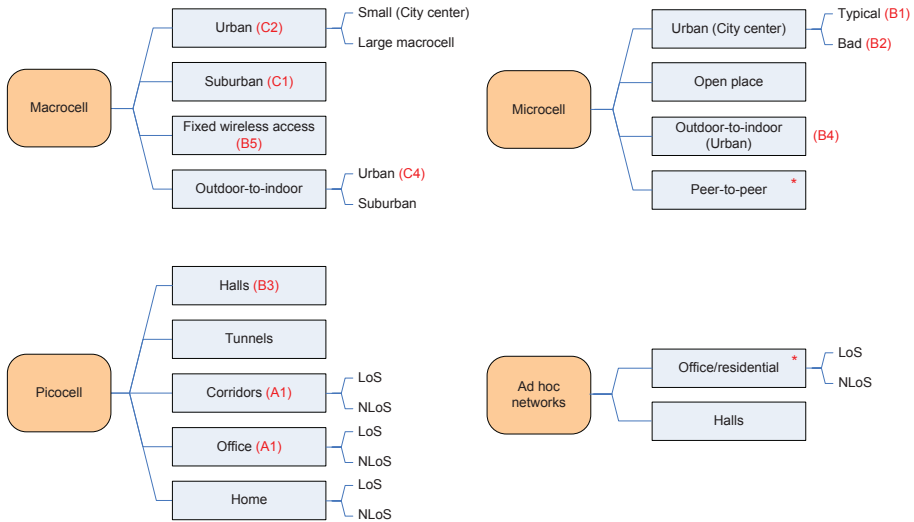


Figure 6.18: COST 273 model scenarios (WINNER matching scenarios are indicated in brackets) [72].

analyzed in **WINNER**. On the other hand, some **WINNER** scenarios: Indoor-to-outdoor, Rural and Moving Networks are not included into **COST 273** scenario classification. Additional measurement have been performed in **WINNER+** project [151], without providing explicit scenario parameters.

### Software Implementations

In the course of the **WINNER** project, **SCM**, **SCME** and **WIM** (phase I and II) models are implemented in **MATLAB/C** and made available through the official web site [151]. The latest **WIM2** implementation includes polarimetric representation for 3-D antenna arrays [7] and distribution parameters for elevation angles for many scenarios [5].

The **MATLAB** implementation of the **COST 273** model is provided by Helmut Hofstetter, from Telecommunications Research Center Vienna (FTW). Supported **CIR** calculations are valid only for the short MT movements, since the long term evolution of the model is missing. The implementation covers the core part of the model (with the placement of the clusters and **IOs**) and it is available at [30]. Recently, **COST 2100** model implementation is provided at [159] under Open Source license.

### General Remarks

It can be noticed that significant similarity exist between **WIM** and **COST 273** models. This becomes especially pronounced when **WIM** is compared to “angular-delay” approach of **COST 273** model. Opposite to **COST 273**, **WIM** has not proposed any “geometric” analogy to “angular-delay” representation. In that sense, the key driving parameter in the **COST 273** geometric model is a density of the

visibility regions (later transferred into the number and cluster positions), while **WIM** characterizes the measured Power-Delay-Directional Profile by using Large-Scale Parameters (angular and delay spreads, shadowing). The significant difference between these models is also related to the degrees of the freedom in cluster characterization: **WIM** have introduced many simplifications in order to reduce complexity.

Further extensions/completion of **COST 273** model are performed within **COST 2100** action. The most significant contribution in new **COST 2100** model is related to introduction of common clusters (Sec. 6.4.2) as the means for quantification and reproduction of inter-link correlations [105]. In general, appearing differences could be associated with different optimization criteria: complexity (**WINNER**) versus universality (**COST**). It shows (as expected) that a more universal concept is more difficult to parameterize and to validate: **WINNER** model currently has more parameterized scenarios. Additionally, introduced simplifications made **WINNER** model appealing for relevant standardization bodies - the **ITU-R** has accepted the **WINNER** approach as reference for evaluation of **IMT-Advanced** radio interface technologies.

## Chapter 7

---

# Concluding Remarks

---

The spatial dimensions of the radio transmission channel offer significant improvement of throughput, range or reliability of transmission. In order to keep the transmission strategy optimal, the new radio access technologies embed adaptivity to the current conditions in the propagation channel. This increases the importance of the channel model in the system design process, and motivates the development of the system-level models being discussed in the thesis.

Although, the channel is independent from the transmission system, its model is often limited in bandwidth, dynamic range, etc. On one hand, this reflects the limitations of the channel measurement and analysis procedures, while on the other, that enables a reduction of model complexity. The accuracy of the model will not be of any use if the model is too complex for the targeted application. Therefore, the appropriate balance with respect to the model's purpose has the ultimate importance. This thesis considers models intended for system-level design, where stochastic models, able to reproduce many different channel conditions, are preferred. Another important context is that analyzed models should represent the statistics of the complete propagation scenario. A proper reproduction of the measured statistics could be achieved more easily with geometry-based (sum-of-rays) models than with filtering-based models that use the explicit correlation between antennas.

Once the class of geometry-based stochastic models is selected as the most appropriate one, it determines the place of the antenna in the model, and requires the reconstruction of spatial propagation dimension. If geometry of multipath is known, the antenna, due to its deterministic response, can be de-embedded from the radio-channel. This enables the decomposition of the radio channel and independent analysis of the propagation channel that does not include antenna arrays. However, the parameterization of the **GSCM** requires the post-processing of measured channel tensors with specialized high-resolution parameter algorithms. These algorithms could reliably resolve only a limited number of multi-path components and therefore the reached representation the channel is only conditionally independent from measurement antenna. **RIMAX** model estimates the optimal model order

(number of **MPCs**) based on parameter variances. This leads to a hybrid model in which the remaining part of the channel after the subtraction of specular components is represented with filtering-based model. In this way the realism of estimated parameters is kept under control. Otherwise, the “ghost” multipath components stemming from the estimation process and from the propagation channel could lead to misleading interpretation.

Since the targeted systems require ubiquitous coverage, the channel model should cover a large number of different scenarios. This can be handled by **GSCM** if proper parameters are estimated for all relevant scenarios. Here we can recognize the most significant contribution of the **WINNER** model: based on the simplified model with transparent parameterization procedure, stochastic characterization is performed (by many institutions) for multiple propagation scenarios. The **3GPP SCM**, **WINNER** and even the **COST** model to some extent, are made to support straightforward parameterization from the measurement experiments. These models use the double-directional concept which coincides with antenna-centric channel perspective of a channel sounding. The complete channel analysis and model synthesis are made in “parametric” domain, meaning that actual positioning of the interacting objects in some coordinate system is never performed. This approach distinguishes these models from stochastic ray-tracers (like **COST** models), and make mapping of observed channel into actual distribution of scatterers unnecessary.

The most important gain is the simplified characterization of the space-time model evolution through the concept of large-scale parameters. Large-scale parameters control the spreading of the channel power along different dimensions and, indirectly, the position of clusters/**MPCs** in delay-directional parametric space. The **LSPs** are estimated from measurements, independently for each dimension, and the collected observations of delay spread, angular spread, shadowing and other **LSPs** are fitted with log-normal distributions. The impact of parameterization procedure to the obtained parameters is limited by fixing the influencing parameters: dynamic range to 20 dB, bandwidth to 100 MHz, etc. It has been empirically proved that spatially close **LSP** estimates are correlated. This comes as a consequence of a gradual change in the multipath profile, which can not be reconstructed from the relative position of moving terminal with respect to scatterers. Therefore **SCM/WINNER** models have to use explicit characterization of the **LSP** correlations in order to emulate realistic transitions over space and time. These correlations are characterized after mapping of individual log-normal **LSP** distributions into Gaussian distributions. Therefore, the transformed **LSPs** jointly have a multi-variate normal distribution. This enables a simple comparison of different measurements and scenarios, according to an objective similarity metric. Consequently, the number of required scenarios of the generic model can be minimized.

A consistent reproduction of inter-link dependencies is also important for overall system performance especially if the cooperation between spatially distributed terminals is supported. This should be enforced in all system-level models independently from the way they handle scatterers. Therefore, the common interacting objects, contributing to multiple links, are introduced in **COST** models. The most natural way to enforce inter-link dependencies in **WINNER** model is to use correlations of **LSPs** controlling different links. The thesis introduces the guidelines for

analysis of intra-site correlations and suggests the influential geometric parameters, but does not provide actual correlation values or elaborate model extensions. This defines the necessary future work.

The specific structure of **WINNER** model, having two levels of randomness, requires a customized verification procedure that is elaborated in the appendix.



# Appendices





## Appendix A

---

# Experimental Characterization

---

The mobile communication systems are constantly improved over last decades. The higher data throughputs, mobility and quality of service are reached with the new concepts such multiple transmit and receive antennas, large transmission bandwidths (up to 100 MHz and more) etc. Because these systems are aiming to exploit as much as possible the given capacity of the channel the new system concepts are very sensitive to the changes in the propagation channel. Therefore, channel models are needed to represent the propagation in different scenarios close to the reality. The stochastic properties of the model parameters are extracted from channel sounder measurement data.

This, possibly redundant, appendix title is used to designate those parameter extraction procedures that are based on channel-sounding data post-processing. It is possible to debate that each modeling activity must rely on measurements, since they are providing necessary observations of channel behavior that is to be modeled. This is however not the case for all reported models, since there are many cases where other models are taken a reference. Usually, they use a priory knowledge for alternative model construction, increasing realism or reducing complexity. However, that knowledge is ultimately also related to channel measurement, therefore term “experimental characterization” is applied to emphasize “immediate use of experimental data”.

In the first part of the appendix, the necessary requirements for characterization of the multidimensional radio-channel are summarized. The second part presents the empirical statistics that is extracted from measurements and exploited to parameterize the **WINNER** channel model.

### A.1 Multidimensional Channel Sounding

The multidimensional sounding with proper setup enables the investigation of the complete spatio-temporal structure of a radio channel that, additionally to the temporal delay of incoming waves, includes their angular directions at transmission and at reception as well as their polarizations.

Especially the combination of angular resolution and polarimetric state is potentially very costly and laborious to record and process at its full extent. Many antenna elements are necessary for high-resolution results, both to fully cover the angular domain and to create the required apertures. Providing coverage in a particular direction demands that antenna elements still have sufficient sensitivity in that direction. Aperture, required for resolution, means that (sensitive) elements are to be spread over space. A popular shortcut like using single-polarized antenna elements leads to biased results [82]. Additionally, for accurate parameter estimation, calibration of every antenna element in the measurement array is mandatory, providing complex radiation pattern  $\mathbf{F}_r(\Omega)$  of (2.31), required to estimate parameters of resolved MPCs in (4.1), in order to relate these to observed faded dimensions. Restricting  $\tilde{\Omega}$  to the azimuthal cut, another popular saving, also means to risk grossly distorted estimates [82].

Characterization of propagation delay requires nearly instantaneous measurements, meaning the time needed for a measurement over bandwidth or over the full delay span should be considerably shorter than the time it takes the channel to change. Pseudo-random noise sequences, multi-sine tone bursts, or fast frequency-sweeps can be used, each with its own advantages and disadvantages. If the repetition rate is high enough, also the Doppler spectrum or time variability can be determined without aliasing.

The temporal and spatial dimension have to be measured jointly, but measuring all antenna elements simultaneously and all transmit-receive combinations in parallel is deemed technically infeasible (exception: the  $16 \times 4$  parallel sounding in [160]).

Therefore, the antenna combinations are multiplexed, making use of one and the same temporal sounding unit. The multiplexing units themselves are still a technical challenge, due to requirements on switching speed, damping losses, feed-through, frequency transfer, delay, and power handling (especially on the transmit side). Seen these imperfections, the multiplexing units should be calibrated too. Synchronization of transmit and receive side, which are often too far apart for synchronization through a cable connection, requires two free-running clocks of very high stability; typically Rubidium or Caesium standards.

The channel measurements require a dedicated sounding device with calibrated multiplexing equipment both at transmit and receive side, calibrated antennas, stable (atomic) clocks, and a high-speed data logger. As an example for the latter, the COST2100 urban reference scenario “Ilmenau” had to be measured at a modest trawling speed of 3 m/s, in order not to exceed the maximum sustained data transfer rate of 1.2 Gbit/s, the product of snapshot rate, number of transmit-receive combinations, impulse response length, and number of bits per time sample [161].

### A.1.1 RUSK Channel Sounder

The RUSK TUI-FAU channel sounder used at TU Ilmenau for MIMO measurements was designed by Medav, Germany [73]. RUSK is a real-time radio channel impulse response measurement system that supports multiple transmit and receive antenna element configurations.

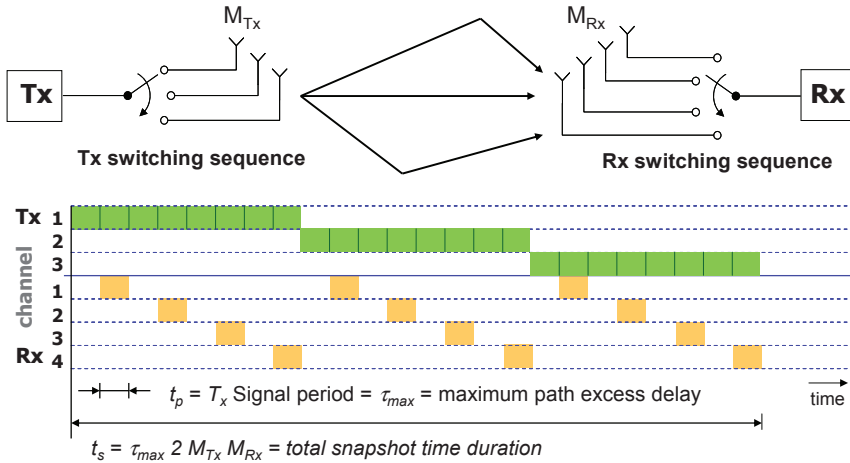


Figure A.1: MIMO sounder switching time frame.

The RUSK MIMO channel sounder measures the channel response matrix between all transmitting and receiving antenna elements sequentially by switching between different (Tx,Rx) antenna element pairs (Fig. A.1). This means that the sounder uses only one physical transmitter and receiver channel, which reduces sensitivity to channel imbalance. The switched-antenna approach offers a simple way of changing the effective number of antenna elements in the array. Additionally, since antennas are not transmitting at the same time, separation of transmitted signals at the receiver side is straightforward. To accomplish synchronous switching, rubidium reference oscillators are used at both the transmitter and the receiver. Timing and switching frame synchronization is established during an initial synchronization process prior to measurement data recording and must be maintained during the entire measurement. Synchronous switching at the Rx and Tx is required in order to clearly assign the received signal periods to any input-output combination of the channel matrix.

Fig. A.1 shows the switching time frames for the transmitting and receiving arrays with 3 and 4 antenna elements, respectively. Any rectangle block in the figure represents one period of the transmit/receive signal. For single active transmitting antenna all receive antennas are measured sequentially. The guard-time equivalent to (estimated) maximum excess delay prevents (multi-path) interference from previous transmission - it allows channel to settle completely.

New broadband systems will be deployed in higher frequency ranges what results in higher transmission-losses. For channel-sounding purposes this means that level of total received power will quickly diminish with getting away from transmitter. Since maximum transmitting power level is always limited (due to environment and beings protection) noise figure of receiver significantly reduces distance ranges in which preferable signal observation range (or dynamic range) could be obtained. Additionally, in wideband case, observation of channel dispersiveness is seriously influenced since weaker-than-noise delayed signal replicas could not be identified.

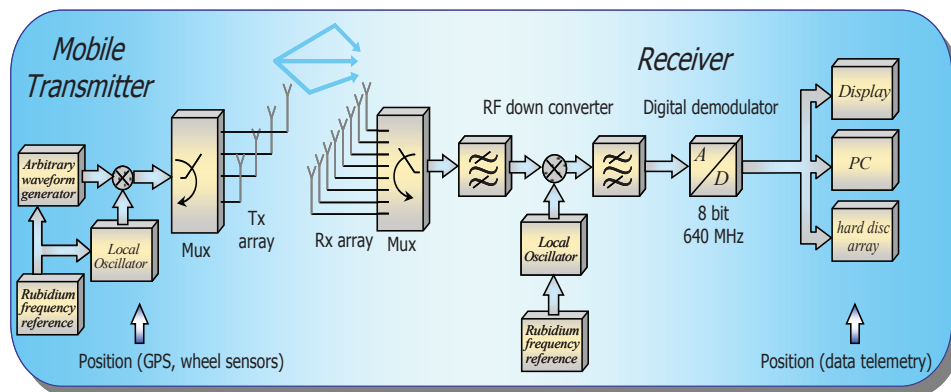


Figure A.2: Block diagram of the RUSK channel sounder from Medav.

The sequential measurements allows increase of dynamic range for certain Tx/Rx combinations (i.e., MIMO sub-channels): RUSK HyEff supports independent AGC for all Tx/Rx combinations analyzed during sounding. This functionality could not be met when simultaneous transmissions are used since sensitivity of the receiver can be adjusted at most once per Rx antenna.

Fig. A.2 shows the principal structure of the Medav RUSK Channel Sounder and Tab. A.1 summarizes the technical key features of the sounder setup, which were used during the MIMO measurements.

For channel excitation RUSK uses a multi-carrier spread spectrum signal (MCSSS) with an almost rectangular shape in the frequency domain, Fig. A.3. This approach allows precise concentration of the transmitted signal energy in the band of interest. Simultaneous sounding of multiple bands (e.g., separated up- and down-link bands in Frequency-Division Duplex (FDD)) is supported by setting some spectral magnitudes to zero. Fig. A.3 presents the MCSSS in time (top row, left) and frequency domain (top row, right). In case of multipath propagation, the received signal is impacted by frequency selective fading as illustrated in Fig. A.3 (bottom row, right). Furthermore, the impulse response (bottom row, left), which would result from inverse Fourier transform of frequency response, is shown in the same figure.

### A.1.2 Measurement Antenna Arrays

An overview of measurement-relevant technical data for the antenna arrays used in the TU-Ilmenau campaigns is given in Tab. A.2.

The monopole antenna that is mounted on the ICE roof was manufactured by Huber&Suhner, and is of type SWA 0859 – 360/4/0/DFRX30. The disc-conical antenna used for the ICE SISO measurements was designed by Kurt Blau (TU Ilmenau) for the 5.2 GHz frequency range.

Table A.1: Key features of the Medav RUSK TUI-FAU channel sounder.

RUSK TUI-FAU Sounder Property	Range of values
RF bands	5...6 GHz
Max. meas. data storage rate	(2x) *160 Mbyte/s
Test signal	Multi Carrier Spread Spectrum Signal (MCSSS)
Sequence length (defines maximum excess delay)	256 – 8192 spectral lines, depending on IR length
Number of measurement channels	up to 65536 ( $2^{16}$ )
Measurement modes	SISO, SIMO, MIMO
Sampling frequency	640 MHz at Tx and Rx
Spurious free IR dynamic range:	48 dB
Transmitter output	up to 33 dBm (2 W),
Propagation delay resolution	4.17 ns (1/Bandwidth)
Impulse response length	0.8 s – 25.6 s
RF sensitivity	-88 dBm
Control	Windows PC
Post processing	MATLAB package
Synchronisation	rubidium clock with stability of $10^{-10}$

\* Rate is doubled with additional disk storage. Second storage enables shorter time gap between Tx-Rx sub-channels.

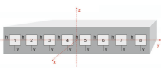

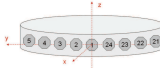

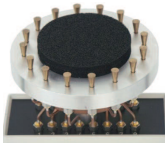


### Frequency dependence of radiation pattern

It is typically assumed that narrowband antennas could be treated as nearly frequency independent. With increased system bandwidth however this assumption becomes less applicable. Within certain limitations frequency dependence of radiation pattern can be minimized by careful design, however developing wideband system already use bandwidths exceeding range in which radiation pattern can be considered as frequency independent.

#### A.1.3 Measurement Dataset

RUSK TUI-FAU Channel Sounder uses switching between S transmitting (Tx) and U receiving (Rx) antennas, possibly having different polarization types. This means that MIMO channels are monitored sequentially (one-by-one) over time. In contrast to this, all frequencies in measurement bandwidth are excited simultaneously with multi-tone signal. Samples of received signals  $y(kT|s)$  are consecutively accumulated for all Tx/Rx ( $s, u$ ) antenna pairs (and polarization types). Extraction of channel transfer function,  $\underline{H}(t, f, s, u)$ , is performed in the post-processing phase with respect to back-to-back system calibration data.

Table A.2: Overview of TU-Ilmenau measurement antenna arrays.

Name	PULA8 (@10W)	UCA16	PUCPA24	SPUCPA 4x24
Vendor	IRK City- placeDresden	TU Ilmenau	IRK City- placeDresden	IRK City- placeDresden
Array struc- ture	uniform linear array	uniform circular array	uniform circular array	stacked uniform circular array
Polarization	dual (vertical+ horizontal)	vertical	dual (vertical+ horizontal)	dual (vertical+ horizontal)
Center frequency [GHz]	5.2	5.2	5.2	5.2
Bandwidth [MHz]	120	120	120	120
Max. Power [dBm]	27 (40)	27	25	24
Number of elements	8	16	24	96
Element type	patch	disk cone	patch	Patch
Dimension- ing	element spacing $0.4943 \lambda$	diameter 10.85 cm	diameter 19.5 cm	diameter 19.5 cm ring spacing $0.4943 \lambda$
Element ori- entation				
Picture				

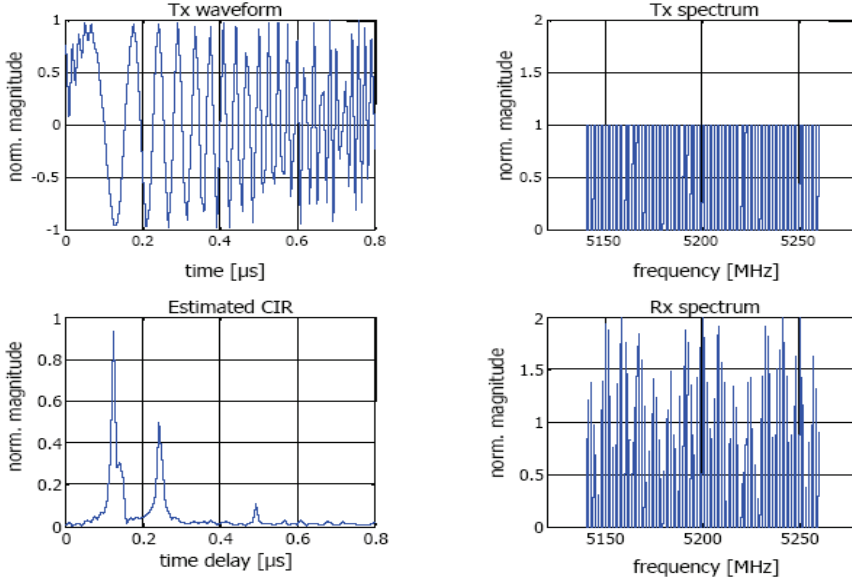


Figure A.3: Broadband multicarrier spread spectrum signal (MCSSS) magnitude in the time and frequency domain (top row) and estimated CIR and received signal spectrum (bottom row).

### Reconstruction of channel transfer function

Observations collected during sounding correspond to delay-domain samples of the received signal:

$$\underline{y}_u(\tau|t_0) = \underline{x}_s(\tau|t_0) * \frac{1}{2}\underline{h}_{u,s}(\tau|t_0) * \frac{1}{2}\underline{m}_{u,s}(\tau|t_0) + \underline{n}_{u,s}(\tau|t_0). \quad (\text{A.1})$$

The received signal in (A.1) is influenced by impulse response of the complete measurement system  $\underline{m}_{u,s}(\tau|t_0)$  and total observed noise  $\underline{n}_{u,s}(\tau|t_0)$  in snapshot  $t_0$ . The impulse response of the measurement system describes its frequency selectivity, including both limited system bandwidth and antenna frequency selectivity. Assuming that impulse responses of channel  $\frac{1}{2}\underline{h}_{u,s}(\tau|t_0)$  and measurement system  $\frac{1}{2}\underline{m}_{u,s}(\tau|t_0)$  were constant during observed snapshot, a CIR can be estimated in terms of magnitude and phase change with respect to referent measurement  $y_{ref}(\tau)$  that is obtained in back-to-back calibration. During the calibration process a channel is replaced by controlled attenuation line that enables calibration under different operating conditions of AGC, and corresponding DRs of measurement system. By switching analysis to frequency domain received spectrum becomes

$$\underline{Y}_u(f|t_k, G_{u,s}) = \underline{X}_s(f|t_k) \cdot A_{u,s}(t_k) \cdot \frac{1}{2}\underline{M}_{u,s}(f|t_k) + \underline{N}_{u,s}(f|t_k, G_{u,s}), \quad (\text{A.2})$$

where  $A_{u,s}$  designates the signal amplification introduced by attenuation line, and  $G_{u,s}$  is the resulting gain of AGC circuit. Automatic fitting of signal amplitudes

into operating range of A/D converter will change quantization noise, and therefore total level of noise is conditioned by mapping  $A_{u,s} \rightarrow G_{u,s}$ . The RUSK supports discrete number of AGC values:  $G_{u,s}[dB] \in 0, 3, 6, 10\dots$  and calibration is performed for all of them by selecting appropriate  $A_{u,s}$ . The sufficient number of time samples (snapshots)  $t_k, k \in \{1, 2, \dots, K\}$  is collected in order to average effects of the noise term  $\underline{N}_{u,s}$ . Under assumption that mean value of noise term equals to zero, the obtained calibration vector will be:

$$\underline{C}(f|s, u, G) = E_t\{\underline{Y}_u(f|t, s)/A_{u,s}(t)\} \approx E_t\{\underline{X}_s(f|t) \cdot \frac{1}{2}\underline{M}_{u,s}(f|t)\}, \quad (\text{A.3})$$

The estimate of channel transfer function is then performed by a normalization of the measured Rx signal spectra with calibration vector.

$$\frac{1}{2}\underline{H}(f|t_0, s, u, G) = \frac{\underline{Y}_u(f|t_0, s, G)}{\underline{C}(f|s, u, G)} \quad (\text{A.4})$$

### Channel Tensor

The RUSK channel sounder provides 4-dimensional channel tensor  $H(t, f, s^*, u^*)$  whose spatial channels are easily differentiated according to dominant polarizations of Tx and Rx antennas  $(s^*, u^*) \rightarrow (s, u, p), p \in \{VV, VH, HV, HH\}$ .

Therefore we can consider that output values of RUSK sounder are dependent upon 5 arguments:  $t$ -time,  $f$ -frequency,  $s$ -Tx antenna,  $u$ -Rx antenna, and  $p$ -polarization. First two arguments are related to time-dimension of (wideband) radio-channel, while others - to its spatial (MIMO) dimension.

In the case of fast-train measurement (Sec. A.2.2) one transmitting and 16 receiving antennas were used, and only vertically polarized signals are emitted and received. Transmitted test signal was composed from 769 equidistant carriers, and 30.000 time observations (snapshots) are collected during measurements. Regarding the above mentioned, dimensionality of ICE wideband SIMO measurement data is

$$\begin{pmatrix} t & f & s & u & p \\ 30000 & 769 & 1 & 16 & 1 \end{pmatrix}.$$

### Additional data describing measurements

The obtained channel representation is however still dependent upon measurement system, i.e. spatial characteristics of measurement antennas. Therefore additional information about the measurement system settings including the antenna arrays (*meta data*) has to be kept for complete measurement description.

Environment description data and positions of terminals during measurement (geographical coordinates including the height above ground and orientations of the used antenna arrays) increase the usability of measurement data, especially for analysis of spatial properties of propagation channel.

A discrimination between propagation conditions (LoS, OLoS, NLoS) facilitates the data segmentation.



**Validation of Measurement Data** Channel sounding experiments, being quite complex process, are highly susceptible to different kinds of errors: hardware defects, wrong equipment adjustment, too fast terminal movement, uncontrollable interaction of measurement environment, equipment or personnel, etc. These errors corrupt the channel tensor and easily lead to completely unusable data. The complete validation of the collected data can be performed with respect to the features of propagation channel that could be reliably deducted from environment configuration and measurement setup. Therefore an additional information, describing measurement process and environment, could become crucial in the process of measurement data validation.

## A.2 Representation of Measurements in WINNER Parametric Space

The limited number of statistical parameters is used in **WIM** to abstract the recorded realizations of propagation process. These parameters typically correspond to the modeled probability or correlation function. This section presents the empirical distributions and distance-based correlations that serve as basis for fitting of model functions and computation of final **WIM** parameters. Following this procedure every measurement dataset can have equivalent representation in **WIM** parametric space. However, since the modeling goal is to abstract the particular measurement environment, the notion of propagation scenarios is introduced. The evaluation of **WIM** scenario taxonomy and classification of the single measurement into particular scenario are discussed in Sec. 5.3.

### A.2.1 Indoor Hotspot Measurements - WINNER B3 Scenario

WINNER B3 scenario is parameterized based on two measurement campaigns: university lecture hall/foyer and industrial hall for rapid prototyping and testing. Measurements are performed in Humboldt (2004) and Newton (2006) buildings located in TU Ilmenau campus, Germany. Both buildings have steel construction and many glass walls/surfaces. The center frequency for both measurements was 5.2 GHz and the bandwidth was 120 MHz.

#### B3 – Lecture Hall Measurements

**Humboldt building** measurements are taken inside the lecture hall (conference hall) and the entrance area (foyer) next to it (Fig. A.4). The foyer is characterized by a 2 floor open environment, with dimension of 15 m × 30 m × 8 m. The conference hall is a typical lecture hall environment with gradually elevated sitting rows; the dimensions are 30 m × 35 m × 15 m.

Measurements with moving transmitter are repeated for several stationary receiver positions. Additionally, for **NLoS/OLoS** measurements in the lecture hall, **LoS** was artificially obstructed by absorbing material. These measurements were performed with the RUSK ATM **MIMO** sounder ([73], Sec. A.1.1), and PULA8 and UCA16 antenna arrays (Tab. A.2). Since disk-cones of UCA16 are single (vertically) polarized, the results given for this environment correspond to **VV** combination of

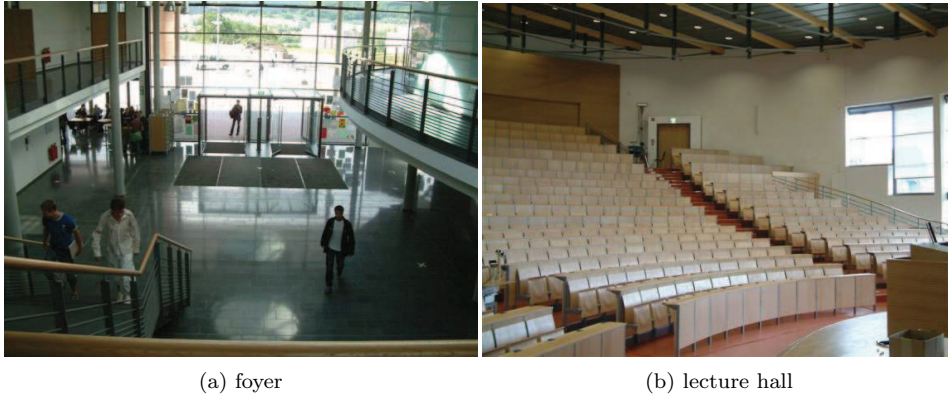


Figure A.4: Interior of Humboldt building, TU Ilmenau campus.

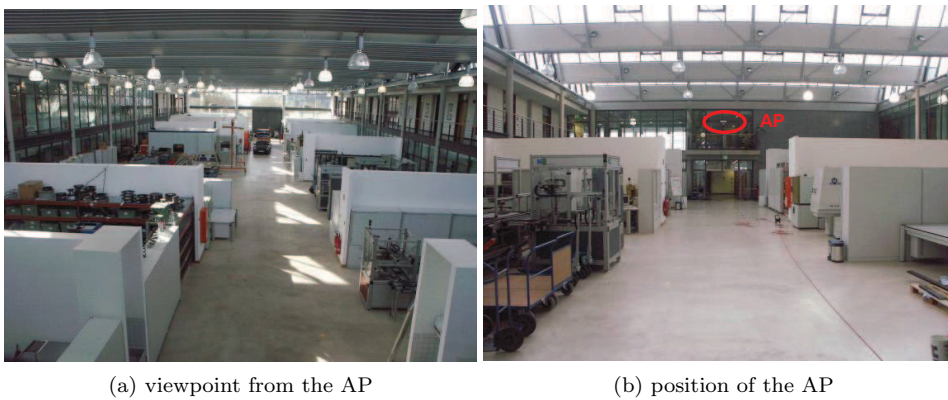


Figure A.5: Interior of the hall for rapid prototyping and testing, Newton building, TU Ilmenau campus.

Tx-Rx polarization. Model parameters are determined as mean values over data set consisting of 10 consecutive snapshots, which corresponds to modeled channel segment (stationarity region)\*.

### B3 – Industrial Hall Measurement

Inside the **Newton building** data is collected in the ground and the first floor (balcony) of the big open hall for rapid prototyping and testing (Fig. A.5) with approximate dimensions  $60\text{ m} \times 20\text{ m} \times 8\text{ m}$ .

All measurement routes (Fig. A.6) share common, highly elevated (6 m) transmitter position, marked in Fig. A.5b as AP (Access-Point). As a consequence dominant propagation condition observed in measurement data was line-of-sight (LoS)

\*The WINNER parameters corresponding to the lecture hall of Humboldt building are estimated by Aihua Hong and Christian Schneider.

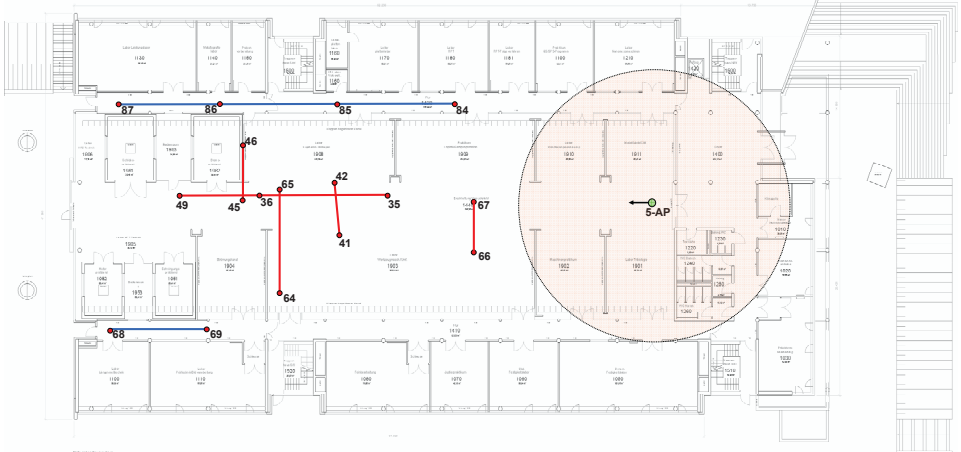


Figure A.6: Measurements routes in Newton building: red – ground floor, blue – balcony at the first floor level.

Therefore this section presents B3 LoS data used to estimate the most important large-scale parameters. The remaining parameters, as well as, B3 NLoS data, are given in the second part of [5].

Measurements were performed by RUSK TUI-FAU channel sounder (Sec. A.1.1) and PULA8 (Tx) and PUCPA24 (Rx) antenna arrays (Tab. A.2). These were full polarimetric measurement and therefore results will be presented for all combinations of Tx and Rx polarizations. However, the parameters of the WINNER model given in [5] correspond to VV case.

All model parameters are determined from the same data set. The majority of the parameters are calculated in delay domain, with exception of angular dependant parameters that are based on angles resolved with high-resolution parameter estimation (RIMAX algorithm). The data in delay domain are calculated by thresholding the average power delay profile 20 dB below the highest peak. The presented data is limited to those snapshots (space-time positions) providing all large scale parameters (LSPs) relevant for WINNER model. This was necessary to have consistent results between LSP distributions and distance dependant features as e.g., correlation coefficient or transmission loss.

### B3 LoS– Transmission Loss and Shadow Fading

The measured and modeled path loss for B3 LoS scenario is shown in Fig. A.7. The transmission loss for VV and HH combination of Tx-Rx polarizations is similar in industrial-like environment, giving:

$$L \text{ [dB]} = \begin{cases} 13.7 \log_{10}(d) + 65.3 & \text{for VV case, and} \\ 14.1 \log_{10}(d) + 63.5 & \text{for HH case.} \end{cases} \quad (\text{A.5})$$

The similar results for VV polarization are observed in lecture hall/foyer (Fig. A.7a) where linear regression of transmission loss over logarithmic distance, for LoS con-

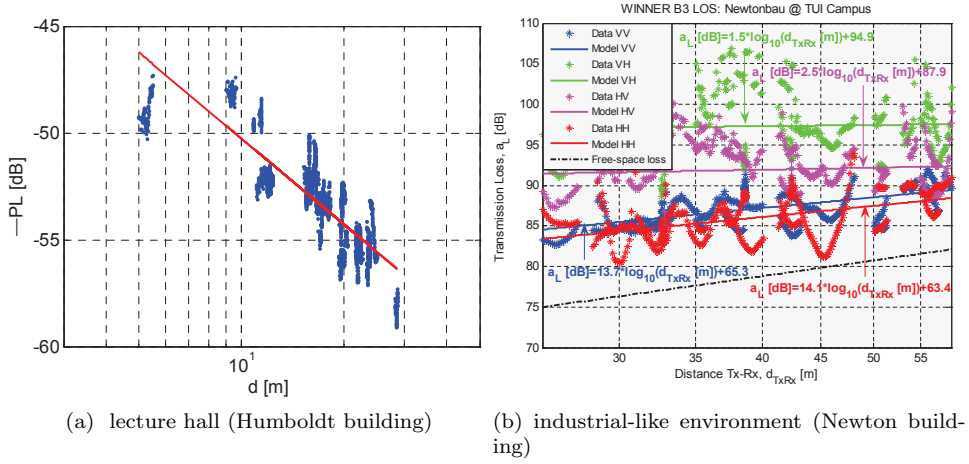


Figure A.7: Transmission loss under LoS propagation condition.

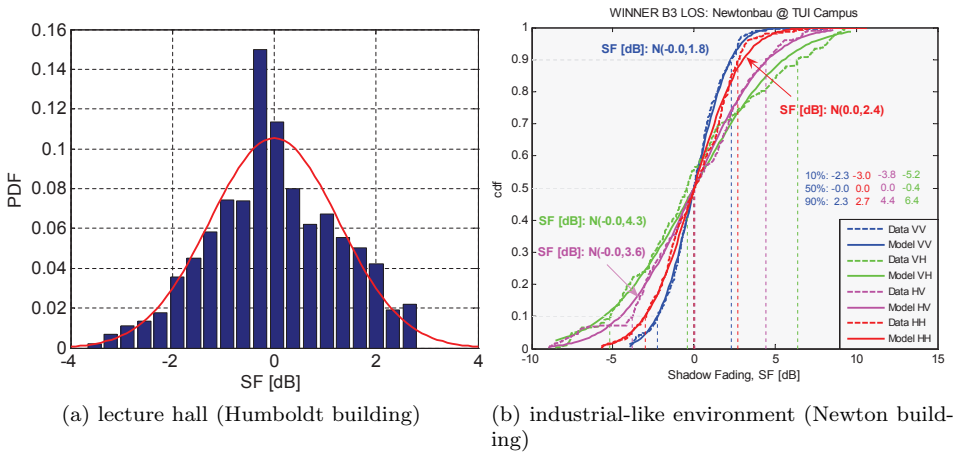


Figure A.8: Shadow Fading distribution under LoS propagation condition for B3 scenario.

dition, gives:

$$L [\text{dB}] = 13.4 \log_{10}(d) + 36.9, \quad \text{with } \sigma_{SF} = 1.4 \text{ dB.}$$

Due to reflections from the walls, floor and ceiling (wave-guiding effect), indoor propagation environments under LoS condition typically have the transmission loss distance exponent in the range from 1.3 to 1.7, [10], Pg. 86. Therefore, obtained estimates of power loss exponent are according to expectations.

Probability distributions of the shadow fading corresponding to transmission loss models from Fig. A.7 are shown in Fig. A.8. For VV polarization observed standard deviation of shadow fading were 1.8 dB in industrial hall and 1.4 dB in lecture hall.

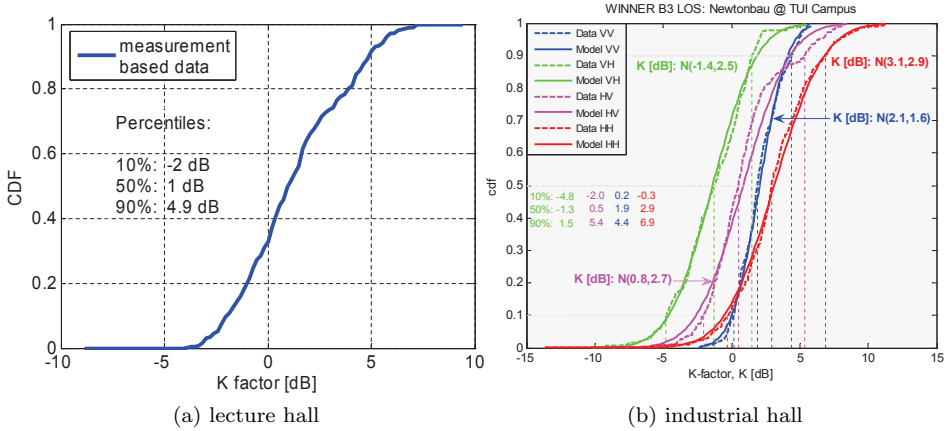


Figure A.9: CDF of Ricean K factor for B3 LoS scenario.

Table A.3: K-factor [dB] in B3 scenario for VV polarization.

K-factor [dB]		LoS		NLoS
		Lecture	Industrial	Industrial
CDF level	10 %	-2	0.2	-3.4
	50 %	1	1.9	-2.0
	90 %	4.9	4.4	-0.7

Table A.4: CDF levels of the cross-polarization ratio for B3 LoS propagation.

XPR type		V→H	H→V
CDF level	10 %	3.0	-0.3
	50 %	9.4	4.9
	90 %	15.1	10.1

### B3 LoS – Ricean K-factor

The cumulative distribution functions of Ricean K-factor for B3 LoS scenario, as well as their log-normal fit, are shown in Fig. A.9. The values of the K-factor corresponding to 10, 50 and 90 % of the CDF, are given in Tab. A.3.

The Ricean K factor for scenario B3 LoS as a function of the distance and the CDF of it are shown in Fig. A.10. By comparing the K-factor distance dependence for VV polarization in lecture hall (decreasing) and industrial hall (increasing), it is not possible to determine general behavior for B3 LoS scenario.

### B3 LoS – Cross-Polarization Ratio (XPR)

The probability density functions of V→H and H→V XPRs are shown in Fig. A.11. In analyzed measurement data V→H XPR is approx. 4 dB higher than H→V XPR. XPR under LoS condition is 3 dB (H→V) to 4 dB (V→H) bigger then for NLoS [5].

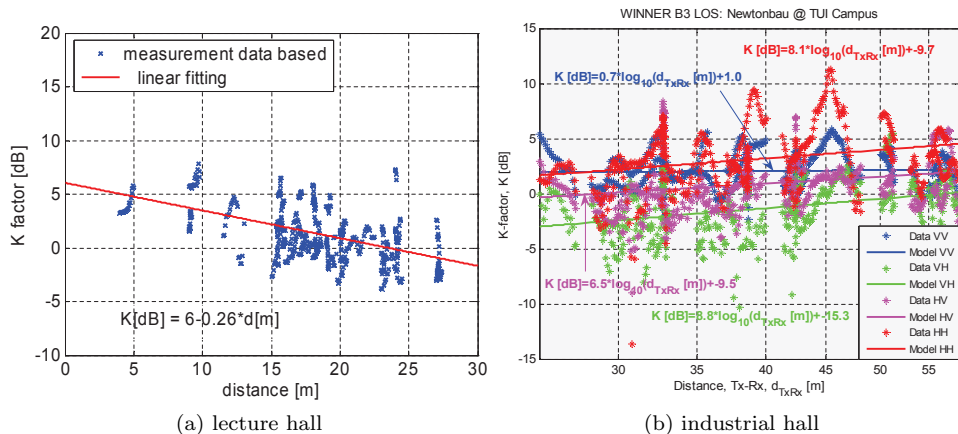


Figure A.10: Scenario B3 LoS: Ricean K factor as a function of distance.

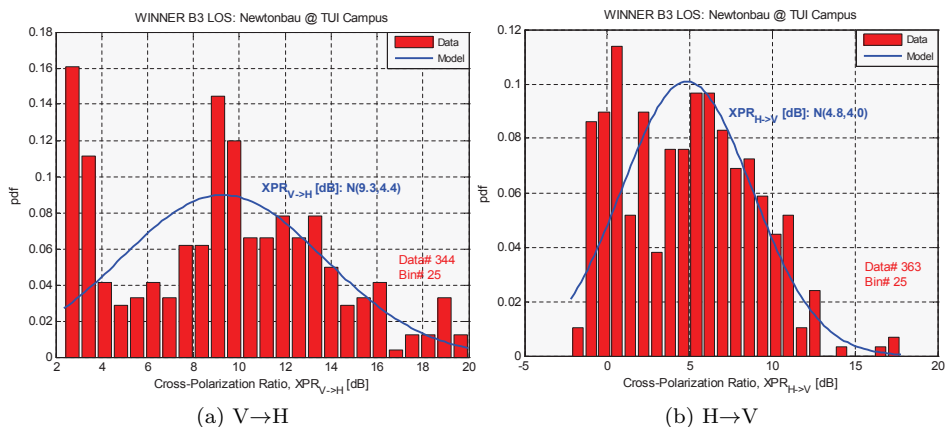


Figure A.11: Cross-Polarization Ratio (XPR) for B3 LoS scenario.

Since reference polarization for model parameterization is chosen to be VV, reference XPR will be V→H. The standard deviation for the V→H XPR under LoS was found to be 4.6 dB.

### B3 LoS – Delay Spread

Delay spread (DS) cumulative distribution functions (CDFs) are shown in Fig. A.12 for different measurement environments. DS values corresponding to 10, 50 and 90 % of the CDF, are given in Fig. A.12 and Tab. A.5. Appropriate log-normal model minimizing mean square error is also given in Fig. A.12 for each Tx–Rx polarization measured in industrial hall environment. From Fig. A.12 it can be seen that both measured environments for VV polarization show similar distribution of DS values.

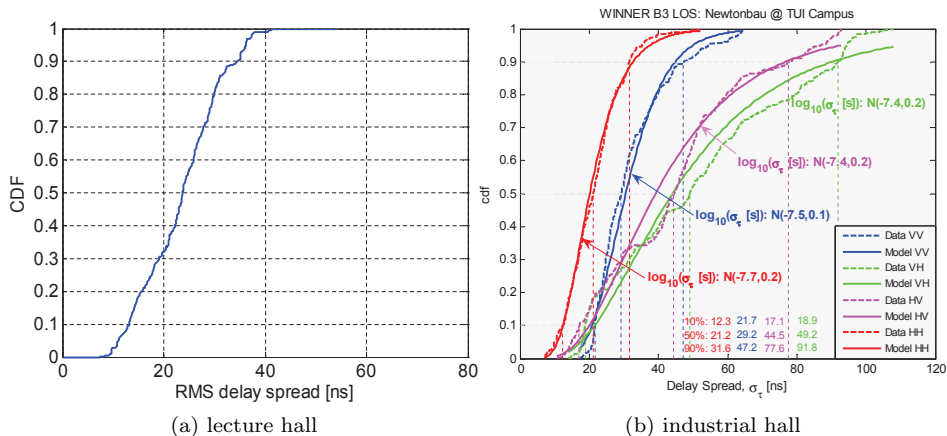


Figure A.12: B3 LoS – RMS delay spread.

Table A.5: RMS delay spread [ns] for B3 LoS scenario and VV polarization.

RMS delay spread [ns]		Lecture	Industrial
CDF level	10 %	13.2	21.7
	50 %	23.7	29.2
	90 %	34.6	47.2

### B3 LoS – Angular Spread

Departure and arrival angles that are necessary for double-directional channel characterization are estimated using high resolution parameter estimation algorithm **RIMAX**. The **RMS** angle-spread is calculated using the circular angle-spread formula [34]. Parameters of assumed log-normal model are obtained by minimizing mean square error.

#### B3 LoS – Azimuth angle spread at BS and MS

The **BS** in both measurements correspond to the measurement terminal with stationary and elevated antenna. However, **BS** is transmitter in Newtonbau measurement and receiver in Humboldttau measurement. Thus, the associated angular distribution are on departure and arrival side respectively. The values of azimuth spread (AS) corresponding to 10, 50 and 90 % of the **CDF**, are given in Tab. A.6 for both link ends, both propagation conditions and both measured environments. Going from **LoS** to **NLoS** it can be noticed that AS is slightly decreasing for highly elevated **BS** (energy that reaches receiver), while AS at **MS** is increasing.

The cumulative distribution functions of the RMS azimuth spreads of the B3 scenario for **LoS** propagation conditions is shown in Fig. A.13. Additionally, log-normal fitting of AS distribution is provided for industrial hall measurements.

#### B3 – Elevation angle spread at MS

The cumulative distribution functions of the **RMS** elevation spread (ES) of the



Table A.6: RMS azimuth spread [deg] for the B3 scenario under LoS condition for VV polarization.

Link end		BS		MS	
Environment		Lect.	Indust.	Lect.	Indust.
CDF level	10 %	9	14.6	7	18.8
	50 %	17.5	20.2	41.5	62.8
	90 %	33	23.4	55	87.3

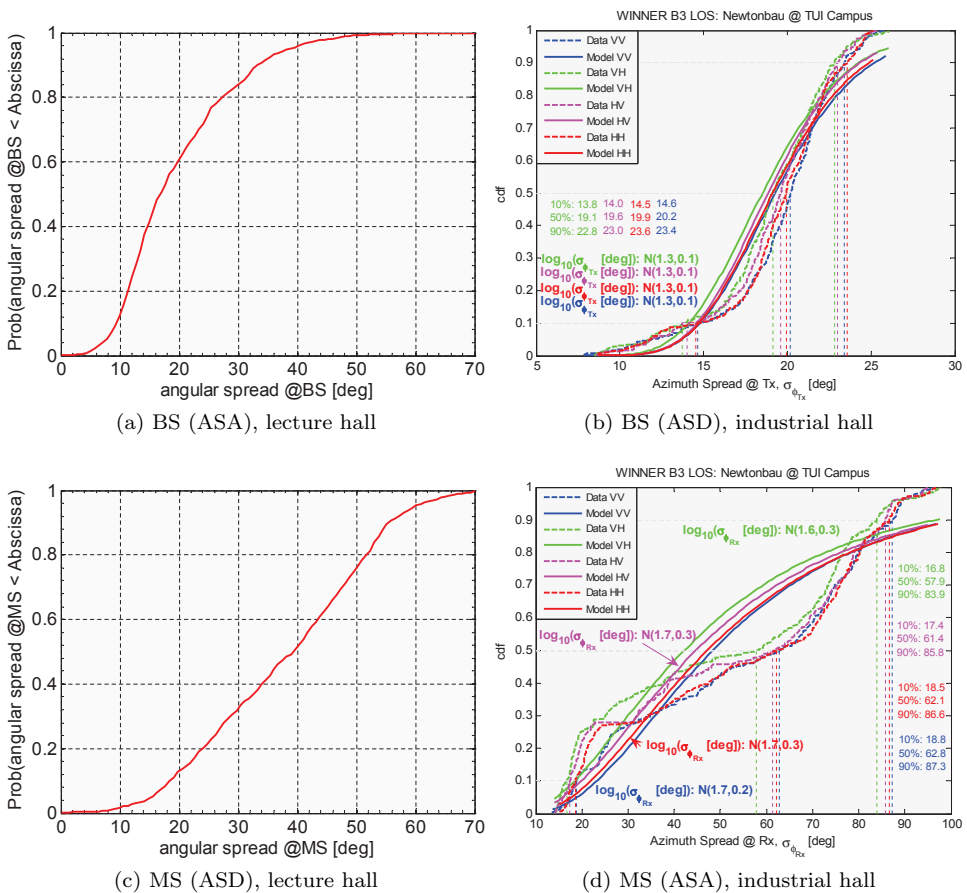


Figure A.13: RMS azimuth spreads for the B3 scenario under LoS propagation condition.



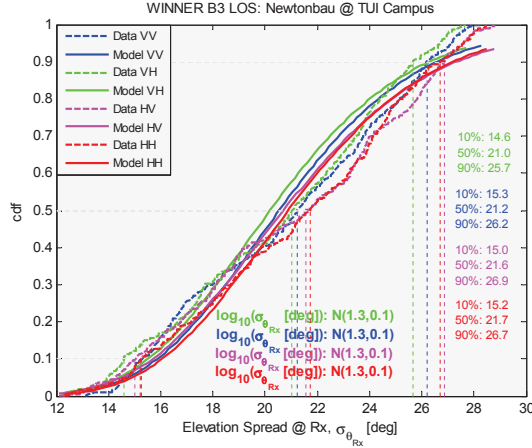


Figure A.14: RMS AoA elevation spreads (@MS) for the B3 LoS (industrial) scenario.

Table A.7: RMS AoA elevation spreads (@MS) for the B3 (industrial) scenario and VV polarization.

AoA spreads (@MS) [deg]	LoS	NLoS
10 %	15.3	17.4
50 %	21.2	22.3
90 %	26.2	24.6

B3 scenario in LoS propagation conditions is shown in Fig. A.14. Log-normal fitting of ES CDF is shown in the same figure.

The values of elevation spread (ES) corresponding to 10, 50 and 90 % of the CDF, are given in Tab. A.7 for LoS propagation condition.

### B3 LoS – LSP Correlation Coefficients

The correlated Large-Scale Parameters in WINNER channel model are Delay Spread, Angular (Azimuth, Elevation) Spreads, Shadow Fading and K-factor. The correlations are reproduced in model based on:

1. distance dependence of the auto-correlation coefficient that is determined for all LSPs,
2. cross-correlation coefficient between LSPs at zero distance.

Autocorrelation function (ACF) is modeled as exponentially decaying function with single parameter called decorrelation distance (distance at which ACF becomes lower than  $1/e$ ). In this subsection ACFs are calculated from measured data and their exponential models are given for LoS case.

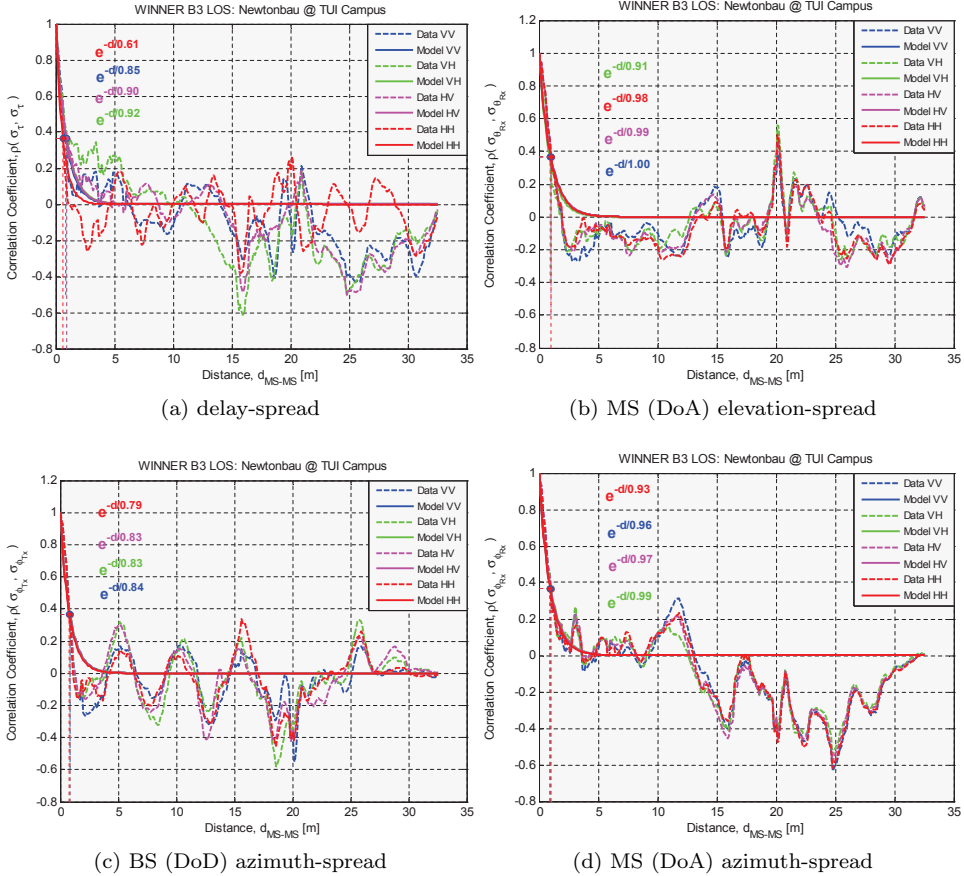


Figure A.15: Distance dependence of the LSP autocorrelation function in B3 LoS scenario.

### B3 LoS – Distance Dependent Auto-correlations

Dependence of ACF from distance is shown in Fig. A.15 for selected LSPs: DS, ES@MS, AS@BS, and AS@MS. It can be noticed that all LSPs in industrial environment have rather short decorrelation distance. Under LoS condition and for VV polarization their values are in the range from 0.7 – 1 m, and decorrelation distance is even 3–4 times lower for NLoS condition. Since higher decorrelation distances are observed in lecture hall [68], B3 model parameters are chosen as average between these two measured environments.

### B3 LoS– Cross-correlations

Cross correlations of LSPs that are calculated at zero distance under LoS condition are given in (A.6). The following labeling is used: DS denotes Delay Spread, ASD denotes Azimuth Spread on Departure, ASA is Azimuth Spread at Arrival,

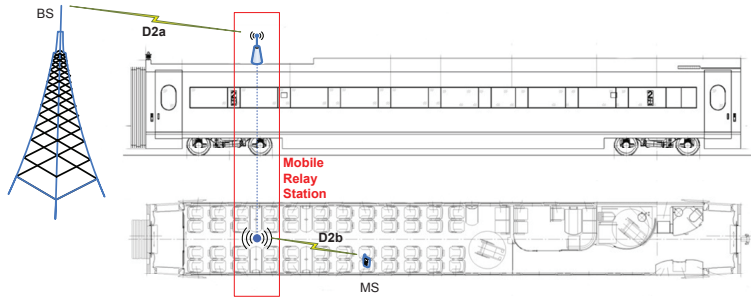


Figure A.16: Moving network (D2) reference scenario.

ESA is Elevation Spread at Arrival, SF denotes Shadow-Fading, and K is K-factor.

$$\rho_{LoS}(0) = \begin{matrix} & \begin{matrix} DS & ASD & ASA & ESA & SF & K \end{matrix} \\ \begin{matrix} DS \\ ASD \\ ASA \\ ESA \\ SF \\ K \end{matrix} & \begin{bmatrix} 1 & -0.3 & -0.4 & -0.2 & 0.1 & -0.3 \\ & 1 & 0.3 & 0.3 & -0.3 & 0.2 \\ & & 1 & 0.2 & 0.2 & -0.1 \\ & & & 1 & 0.1 & -0.1 \\ & & & & 1 & -0.6 \\ & & & & & 1 \end{bmatrix} \end{matrix} \quad (A.6)$$

For VV polarization significant negative correlation is observed between DS and ASA (-0.4) and SF and K-factor (-0.6). It is interesting to note that given cross-correlation coefficients are slightly different for HH polarization. In that case the high correlation levels are observed between DS and SF (0.6) and DS and K-factor (-0.5).

## A.2.2 Moving network measurements – WINNER D2 Scenario

“Moving network” corresponds to radio propagation in environments where both the AP (or relay station) and the UE are moving, possibly at very high speed. A typical example of this scenario are carriages of high-speed trains, shown in Fig. A.16, where wireless coverage is provided by so-called Moving Relay Station (MRS) which can be mounted, for example, to the ceiling. The MRS provides interior coverage (D2b scenario) over wireless connection to stationary AP infrastructure (D2a scenario).

The D2a model is based on the fast-train measurements with Single-Input Multiple-Output (SIMO) setup [5], “high mobility short range” (HMSR) setup [68] and measurements used for D1 (rural) scenario parameterization.

### D2a – Car-to-Bridge Measurement

The “High Mobility Short Range Hot Spot” setup is characterized by bridge-to-car measurements, Fig. A.17.

The measurements are conducted by Medav, University of Ulm and TU Ilmenau in August 2004 at a highway bridge close to City Ulm, Germany. The receiving antenna (BS) was mounted on the bridge with a height of  $\sim 5.5$  m above motorway

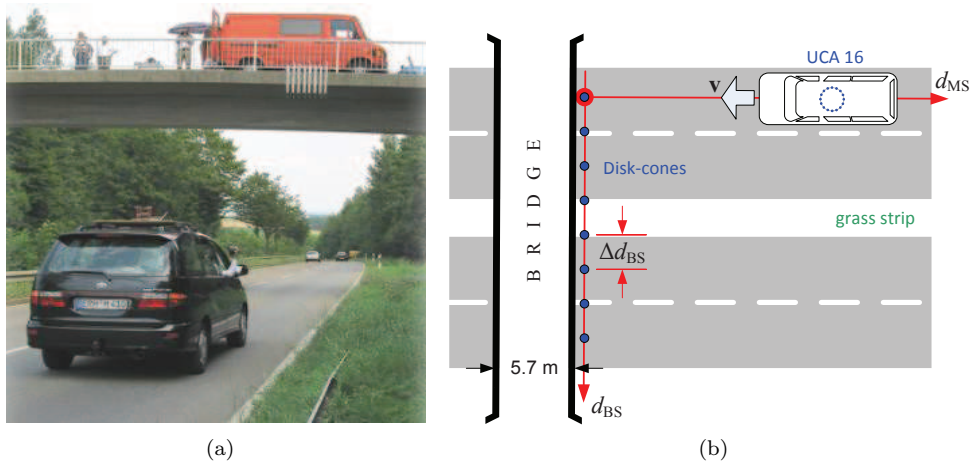


Figure A.17: Car-to-bridge measurements: a) environment, b) sketch.

and a tilt of  $-45^\circ$ , whereby the transmit antennas were placed on the roof of a car ( $\sim 2$  m height). During measurement the car was moving at a constant speed over a two lane motorway toward the receiver antenna which was mounted on a bridge. The maximum distance between Tx and Rx antenna position was 250 m, which defines the short range area for the hot spot application. In this measurement LoS was dominant propagation condition, while NLoS is exhibited after the car had been coming under the bridge. The sketch of the measurement campaign is shown in Fig. A.17b.

These measurements were performed with RUSK ATM MIMO sounder [73]. The channel measurements have covered a bandwidth of 120 MHz at a carrier frequency of 5.2 GHz (wavelength,  $\lambda=5.77$  cm). At the receiver side 8 equal spaced disc cone antennas were used. Inter-antenna spacing was  $\Delta d_{BS}=88$  cm (15  $\lambda$ ), giving the total span  $d_{BS}$  of  $7 \cdot \Delta d_{BS}$ . Each of antenna elements is treated as an individual BS. At the transmitter Uniform Circular Array (UCA) with 16 elements was used, Tab. A.2.

## D2a – Fast train (Inter-City-Express) measurement

The measurement was conducted in August 2006 by Medav, TU Karlsruhe and TU Ilmenau on the railway line between Siegburg and Frankfurt (Germany) by using different train-speeds: 20, 100 and 240 km/h. The characteristics of the radio-link between moving fast-train and fixed base station, being located next to the railroad track, were measured (Fig. A.18).

Measurements were performed by Medav RUSK TUI-FAU channel sounder [73], in 5.2 GHz frequency range, with 120 MHz bandwidth. The observed duration of channel impulse response (CIR) was  $6.4 \mu\text{s}$ . In this campaign existing monopole antenna mounted at ICE roof-top was used at transmitter side and because of that limitation only SIMO setup is supported. Additionally, it was not feasible to measure 3-D radiation pattern of the train roof-top antenna, nor to properly estimate

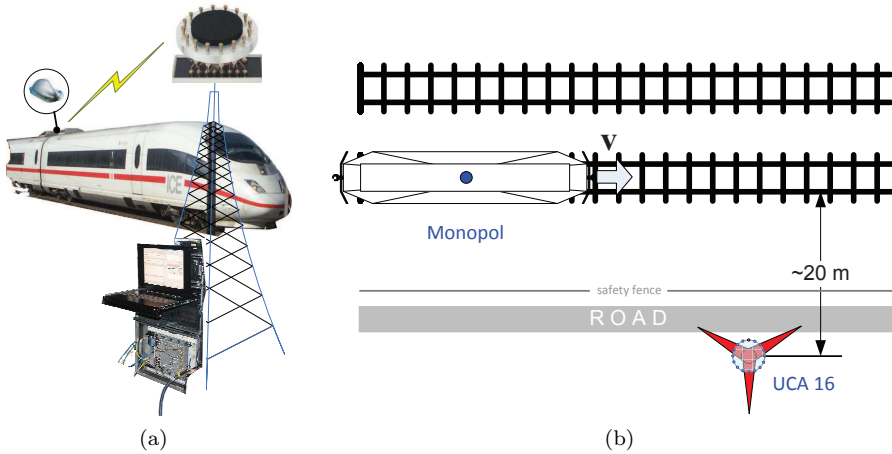


Figure A.18: Sketch of the fast train measurements.

influence of the metallic rooftop to the effective radiation pattern. Receive uniform circular array with 16 disc cone elements (UCA 16, Tab. A.2) was mounted approximately 7 m above railroad tracks level. Both antennas are supporting only vertical polarization. The data post-processing is performed according to procedures defined in Sec. 4.3.2.

It should be also noted that measurement setup does not fully match D2a reference setup since the BS height was similar to the MRS antenna height (approx. 5 m).

### D2a - Transmission Loss and Shadow Fading

Transmission loss result obtained from fast-train measurements, Fig. A.19, deviates from the expected free-space propagation: the transmission-loss exponent of the curve was too high. It was concluded that the extraordinary behavior of the propagation curve depends on the special circumstances in the measurement. The antenna used in the carriage roof of the train was a monopole that was mounted very near the roof that now acts as a ground plane. Thus the roof affects the antenna radiation pattern and possibly causes a null of the radiation pattern in the plane containing the roof. At the same time the BS antenna of the measurement equipment was quite low, which emphasizes the effect.

The model matching measured data would most probably over-estimate the path-loss for D2a reference setup, and therefore the D1 (rural area) transmission loss model is modified with additional term  $L_{env}$ .

$$L = L_{D1} + L_{env}, \text{ where } L_{env} = \begin{cases} 0, & d \leq d'_{BP} \\ 18.5 \log_{10}\left(\frac{d}{d'_{BP}}\right), & d > d'_{BP} \end{cases} \quad (\text{A.7})$$

The parameter  $d'_{BP} = 120 \text{ m}$  is the environmental break-point length, and  $L_{env}$  designates the extra attenuation caused by the train environment. It is assumed that the extra loss is caused by the placement of the MRS antenna very near the

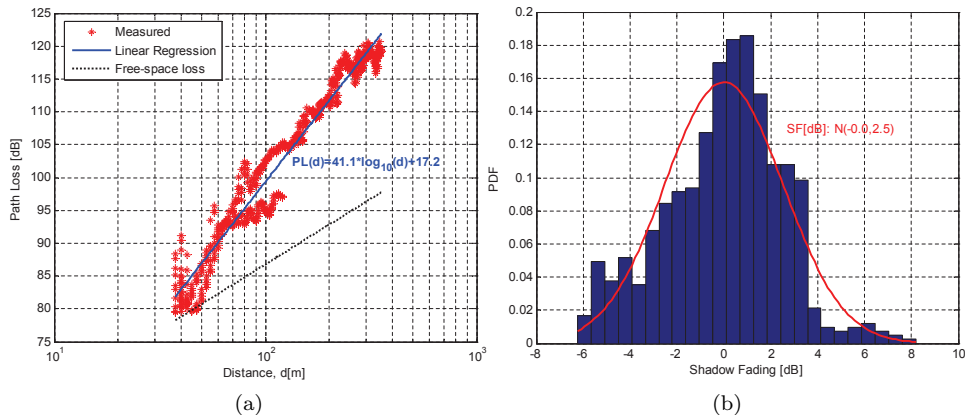


Figure A.19: Fast train measurement @ 5.2 GHz: (a) transmission loss, and (b) shadow fading.

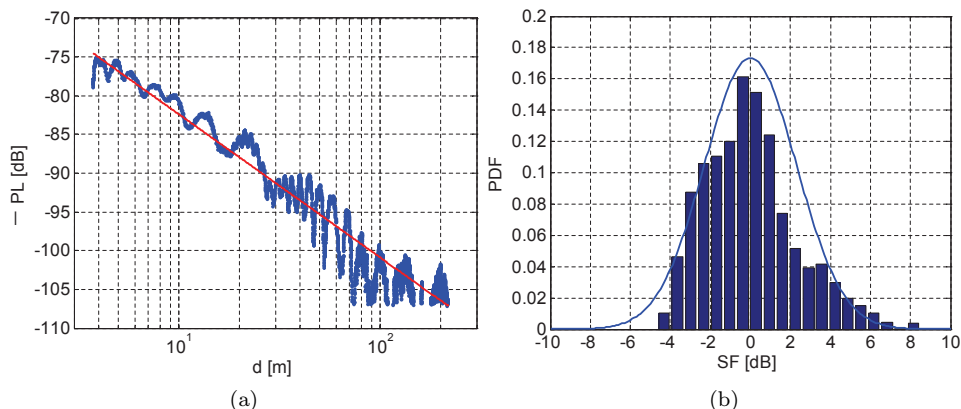


Figure A.20: Car-to-bridge measurement: (a) transmission loss, and (b) shadow fading.

carriage roof, and presented model  $L_{env}$  is probably over-pessimistic in general case. A pragmatic way around this could be to use half of this extra loss in simulations. The proposed path-loss model shows good matching to transmission-loss exponent in bridge-to-car scenario (Fig. A.20):

$$L \text{ [dB]} = 60.6 + 19.3 \log_{10}(d), \quad \text{with } \sigma = 3.1 \text{ dB},$$

however covered distances are not long enough to validate all proposed transmission loss terms.

### D2a – Ricean K-factor

The Ricean K-factor for D2a is taken from the car-to-bridge measurement: its CDF is shown in Fig. A.21. The median value of Ricean K-factor was approx. 6 dB, and

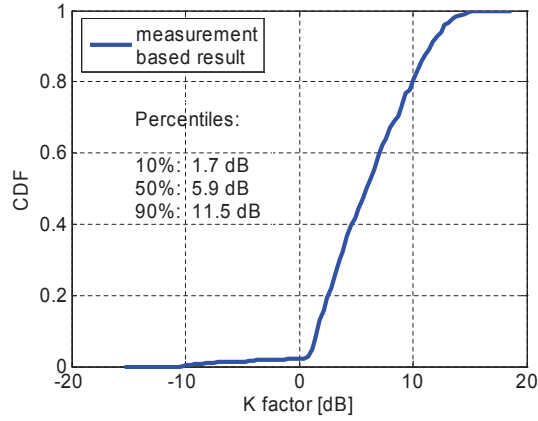


Figure A.21: CDF of Ricean K-factor for car-to-bridge measurement.

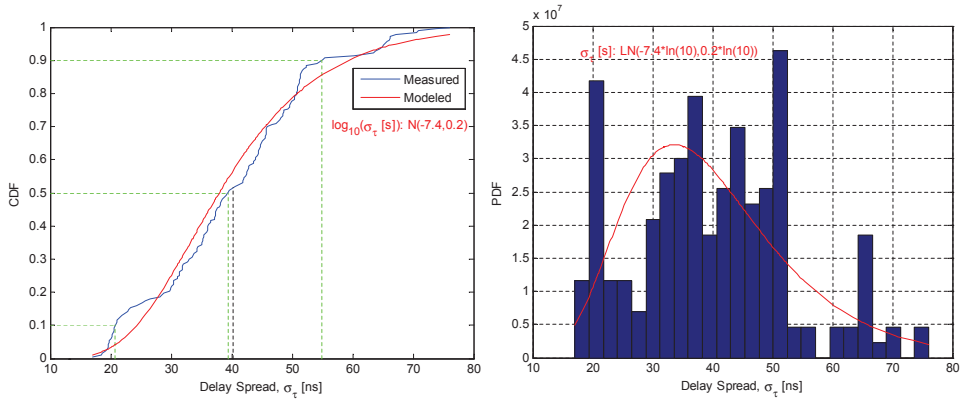


Figure A.22: Probability functions of RMS delay spread for D2a LoS scenario.

it was nearly constant over the measured distance.

### D2a – Cross-Polarization Ratio (XPR)

Since both measurements have used single polarized arrays, it was not possible to estimate XPR values. Thus, cross-polarization ratios for D2a scenario have been taken from the D1 [5].

### D2a – RMS Delay Spread

The RMS delay distributions for LoS case are determined from fast-train measurements (Fig. A.22).

Table A.8: CDF levels of RMS delay spread under LoS propagation for D2a scenario.

RMS delay spread [ns]		LoS
CDF Level	10 %	21
	50 %	39
	90 %	55
	mean	40

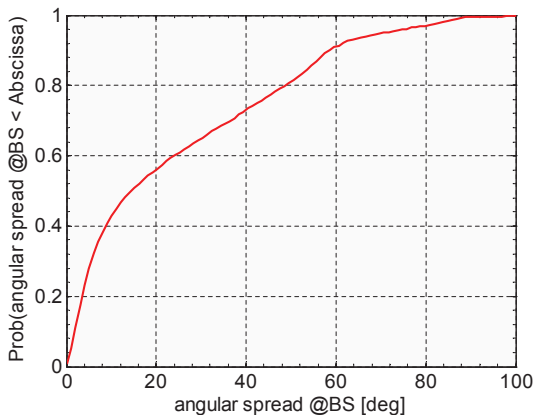


Figure A.23: RMS angular spreads at BS for the car-2-bridge measurement, under LoS propagation condition.

Table A.9: Percentiles of the RMS azimuth spread for D2a scenario.



Link end		BS, $\sigma_\phi$		MS, $\sigma_\varphi$	
D2 moving network		LoS	NLoS	LoS	NLoS
CDF Level	10 %	1	5.6	21.3	6.0
	50 %	5	18.0	30.4	22.3
	90 %	50	34.3	45.9	36.4
	mean	21.7	19.5	32.5	21.9

## D2a – Azimuth Angular Spread at BS and MS

Azimuth Angular Spread (AS) for D2a LoS is determined from the HMSR (@BS) and fast-train (@MS) measurements. The placement of the Rx in the bridge-to-car measurement corresponds to D2a reference setup with dominant BS. The CDF of circular azimuth angle spread obtained from this measurement is shown in Fig. A.23. In the fast-train measurement, height of the base station receiver antenna array is not dominant if compared to train-mounted antenna. From that reason it can be assumed that similar angular distribution will be measured at moving station. Probability distributions for azimuth angular spread at receiver side in fast-train measurements are shown in Fig. 3.5. The values of the RMS azimuth spread corresponding to 10, 50 and 90 % of the CDF are given in Tab. A.9.



Table A.10: Channel sounder settings.

Measurement		Ilmenau 2008	Dresden 2009
Picture			
Type		RUSK TUI-FAU Medav, GmbH	
Transmit power @ PA	[dBm]	46	
Centre frequency	[GHz]	2.53	
Bandwidth	[MHz]	2x40	100(20)
CIR length	[ $\mu$ s]	6.4	12.8
Snapshot rate	[Hz]	>75	
MIMO sub-channels	[#]	928 (16x58 eff.)	
AGC switching		in MIMO sub-channels	
Positioning		Odometer and GPS	

### A.2.3 Urban Macro-cell Measurements – WINNER C2 Scenario



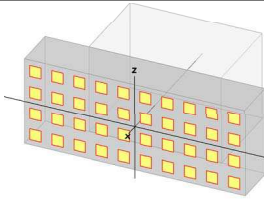
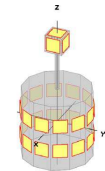
In this section data from two measurement experiments is presented: the first one is performed in Ilmenau, Germany in 2008 and the second in Dresden, Germany in 2009. In the thesis they are conveniently referred to as I08 and D09, respectively. Both measurements are performed with Medav RUSK channel sounder [73] at 2.53 GHz using frequency bandwidth up to 100 MHz.

The time necessary to record the responses of all wideband MIMO sub-channels,  $T_S$ , was 12.1 ms for Ilmenau and 24.2 ms for Dresden measurement. This limits the maximally allowed speed between the measurement vehicle and other interacting objects,  $v \leq \frac{\lambda}{2T_S}$ , to 17.6 km/h and 8.8 km/h, respectively, where  $\lambda \approx 12$  cm denotes the wavelength of the carrier.

To allow a high-resolution parameter estimations of multipath structure, dedicated antenna arrays at transmit and receive sides are used, providing a total of 928 MIMO subchannels (Tab. A.10). The linear uniform array with 8 dual polarized elements (PULA8) is used at base station positions. The mobile terminal uses the stacked uniform circular array (SUCA 2x12) that is constructed from two rings, both having 12 dual polarized patches. Additionally, a MIMO cube is placed on top of this array as shown in Tab. A.11. During measurements this antenna array was mounted on the rooftop of the car, at approximately 1.9 m above ground level.

The measurement campaign focused on gathering realistic channel data in an urban macro cell environment in the 3GPP Long Term Evolution band (LTE [162]). The measurement setup targets multi-link configurations between base station and

Table A.11: Antenna arrays.

		Tx Array		Rx Array
Picture				
Name (type)		PULA8		SPUCA 2×12 + MIMO-Cube
Drawing				
HPBW:				
azimuth	[°]	100		Omni
elevation	[°]	24		80
Measurement		I08	D09	I08 + D09
Height	[m]	25, 15 and 3.5		1.9
Tilt (down)	[deg.]	5		0
Mobility	[m/s]	0		3-5

users as well as relaying. Furthermore, the presented data offer huge potential for scientific research, because of the considered system setup, high quality of the acquired data and applicability for high resolution multipath parameter estimations [83] [88].

In both campaigns, three well separated base station locations within city centers are used (Fig. A.24b, Fig. A.25), and mobile terminal is positioned on the rooftop of the car. The same macro-cell measurement setup, including the configuration of the measurement equipment, provides the proper base for comparison of Ilmenau and Dresden propagation environments. Ilmenau is a small city compared to Dresden: whereas Ilmenau is characterized by 3-4 floor buildings, Dresden has buildings with 6-8 floors. Subsequently the base station height at Dresden ( $\sim 50$  m) was almost doubled compared to Ilmenau ( $\sim 25$  m).

## C2 – Ilmenau Inner City Measurement, 2008

The wide band channel measurements are performed in Ilmenau inner city in July 2008. The selected city area is considered as a proper representative of urban macro-cell environment, Fig. A.24a. The extensive channel sounding campaign covered the MIMO radio links from 22 mobile tracks to 3 different base stations and 1 relay station. In Fig. A.24b a map of the city center of Ilmenau is shown including the

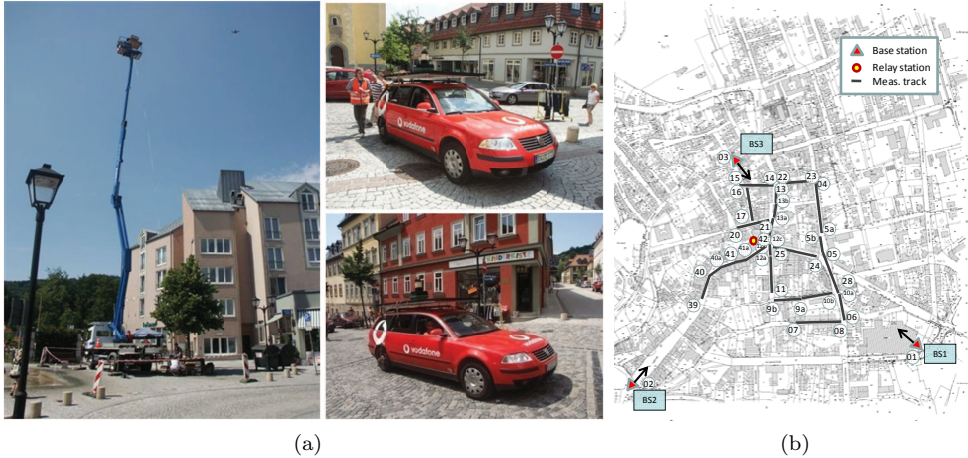


Figure A.24: Ilmenau macro-cell measurement setup: a) Measurement environment, BS and MT, b) Positions of the base stations and relevant mobile routes.

position of the base stations, the relay station, and the routes. During the channel measurements the mobile terminal that acts as Rx was moving over different tracks. A typical length of a track is 50–70 m. The inter-site distance between the base stations is found to be  $BS1-BS2 = 680$  m,  $BS2-BS3 = 580$  m and  $BS3-BS1 = 640$  m.

The sounding is performed at 2.53 GHz central frequency, and  $2 \times 40$  MHz bandwidth is used in the subsequent analysis. The more detailed information about channel sounder settings are given in Tab. A.10, and Tab. A.11 describes the used antenna arrays.

For each of the tracks and for each measured snapshot, geo-data information based on Global Positioning System (GPS), odometer and separated distance measurements via laser are available. The accuracy around the start and end points for each track is approximately 0.1 m and along the route 1m.

The parts of the measurement data (9 files describing the links from 3 base stations at the same height of 25m to 3 tracks) is shared via the web site [163] and can be considered as the COST 2100 [152] reference scenario for channel modeling and system evaluation [161].

## C2 – Dresden City Measurements, 2009

The measurements have been performed in the city centre of Dresden, Germany, within the EASY-C project [164]. Links from 3 different base stations (BSs) are sequentially monitored towards 7 mobile tracks, Fig. A.25. The BS (Tx) arrays have been placed 3–4 m above the building roof tops. Since the chosen buildings have dominant heights, this measurement setup corresponds to the urban macro-cell scenario. The antenna array acting as Mobile Terminal (MT) has been mounted on top of a car at approximately 2 m above ground. During the measurements the

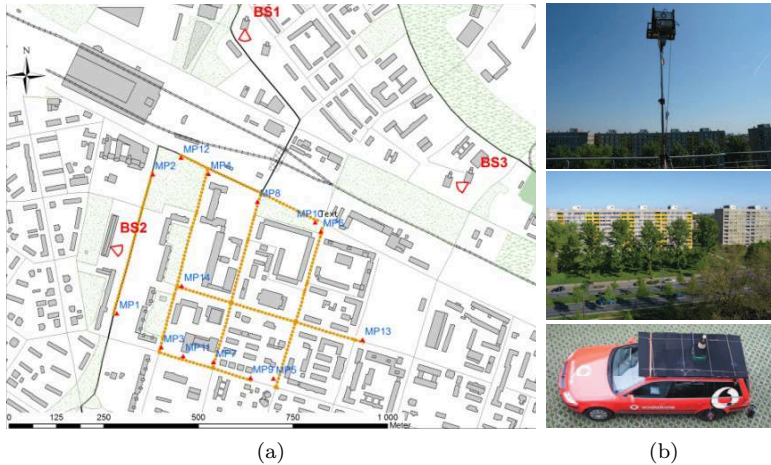


Figure A.25: Sketch of the Dresden scenario: a) Mobile tracks and base station positions, b) Placement of antennas in measurement environment.

MT has been moving by moderate speed of 3–5 m/s. The investigated environment with given antenna deployment can be classified as urban macro cell.

The measurements have been performed using a MEDAV RUSK channel sounder [73] operating at 2.53 GHz, with a bandwidth of 100 MHz. Tab. A.10 gives the basic setup parameters for the Dresden measurements. Chosen antenna arrays with 8 and 29 dual polarized patches (Tab. A.11) enable the estimation of MPC parameters with high resolution.

### Validation of WINNER C2 large-scale parameters

In this section the characterization of Large-Scale Parameter (LSP) for Ilmenau and Dresden measurements is performed. Although, the majority of the LSP could be determined without high-resolution parameter estimation (HRPE), this procedure is required for the characterization of angular spreads at departure and arrival. The joint estimation of MPC parameters is here performed by the RIMAX algorithm that combines the SAGE and gradient-based search procedures [81]. Therefore LSPs are calculated from two different domains: a) time-delay domain (DS, SF, K, XPR) and b) domain with structurally (and spatially) resolved multipath (ASD, ASA, ESA). An estimation of the elevation angles was possible only on the receiver side (MT), since geometry of the used transmitter array (Uniform Linear Arrays (ULA)) does not support it. The analysis follows the established procedures for the WINNER II channel model parametrization [5], Sec. 4.3.2. Estimation of all LSP realizations is related to spatial areas, named local-stationarity regions, where LSPs show negligible variation. In the case of Dresden measurement these regions are a priori defined as having 2.4 m extent ( $\sim 20$  wavelengths), with 50 % overlapping between neighbors. This methodology allows the accumulation of LSP realizations along measurement tracks, and consequent parameterization of their empirical probability density functions (PDFs) and correlation properties.



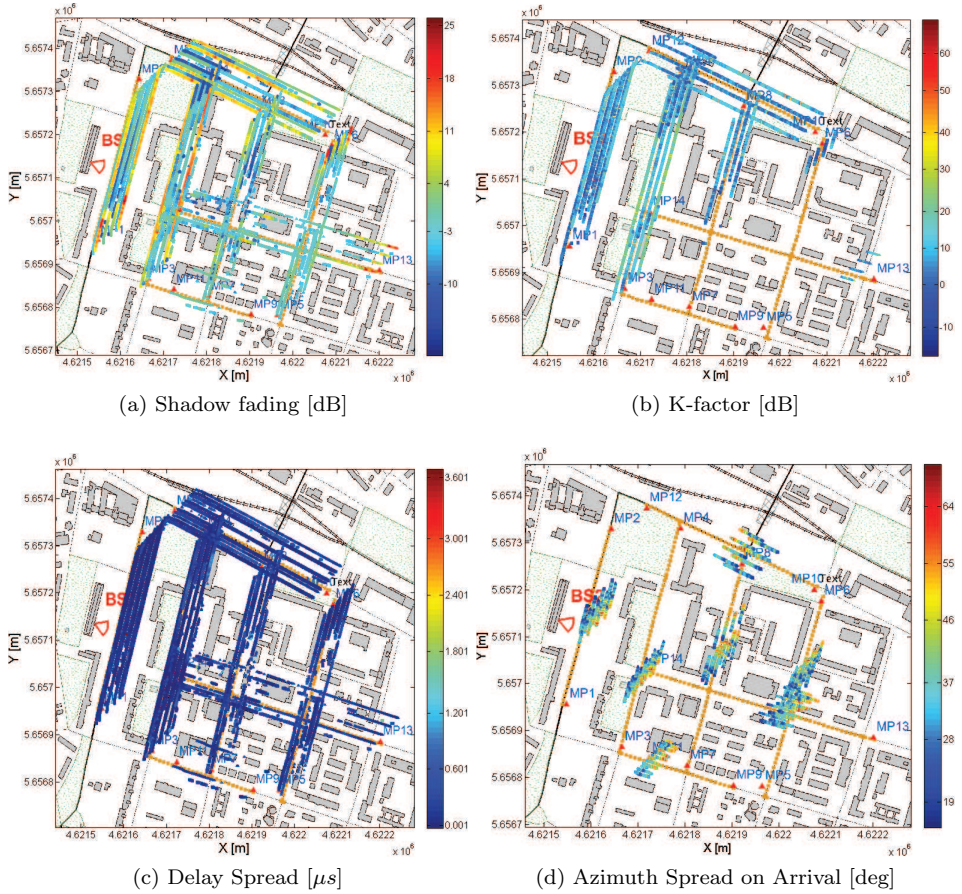


Figure A.26: Spatial (2-D) positions of calculated LSPs in the Dresden scenario.

Fig. A.26 illustrates the spatial distribution of selected LSPs, where single value is calculated and showed per local-stationarity region (single marker on figure). The LSPs corresponding to 3 different BSs and 4 different polarization groups are plotted next to each other by introduction of a small offset. In this way it is possible to observe which measurement snapshots would contribute to reported statistics: those MIMO sub-channels (combinations of Tx and Rx antenna positions and polarizations) having inadequate SNR are omitted.

The parameters computed from delay domain: delay spread (DS), the transmission loss (TL), shadow fading (SF) and the narrowband K-factor are determined using the complete measurement data set. Due to excessive time consumption, only a subset of the collected data is processed by RIMAX, reducing the number of observations for estimating the angular spreads (Fig. A.26d) and related correlation dependencies. Therefore the Large-Scale Parameters calculated from a power/delay domain use larger data sets from parameters in angular domain, which is noticeable in Fig. A.26 – regions where HRPE is conducted represent the

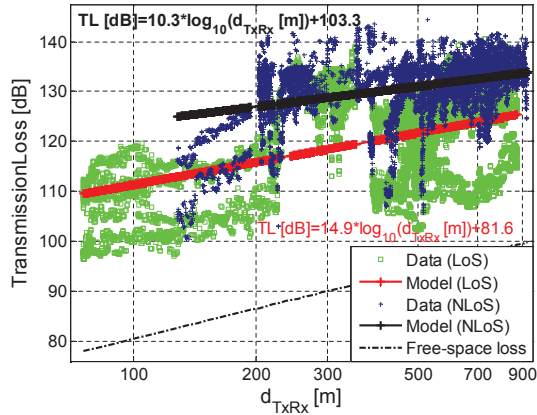


Figure A.27: Transmission loss for LoS and NLoS classes of Dresden measurement.

subset of available data. In order to further reduce computation time, the HRPE for Dresden measurement is performed in reduced 20 MHz bandwidth.

For the analyzed measurements LSPs are classified according to existence of the LoS component. The separation between LoS/NLoS is based on ray tracing and a full 3-D model of the environment. For each class all relevant parameters defining the WINNER channel model are computed: distributions of LSP values, corresponding correlation distances, and cross-correlation coefficients.

The obtained parameters are compared with the corresponding WINNER II/+ parameters. In this way we validate the WINNER model, but also empirically verify how much variation within the same scenario can be expected when measurements are performed in different cities.

The comparison of the large scale parameters, e.g. delay spread, transmission loss and shadow fading, with the corresponding scenario C2 showed a good match [126], [90], [127]. The resulting characterization in the angular domain showed partial agreement with the WINNER II tables and the same holds for the cross-correlations. Furthermore, based on presented results, the WINNER C2 model was extended with Elevation Spread on Arrival (ESA) distribution parameters.

### Transmission Loss

The transmission loss parameters are obtained using linear regression separately for LoS and NLoS. The resulting transmission loss exponents in Fig. A.27 for both classes of Dresden measurement are lower than in free space ( $< 2$ ), what supports hypothesis that strong guiding of radiated energy is experienced along the streets<sup>†</sup>. These parameters are quite different from WINNER regression parameters, as shown in Tab. A.12.

A brake-point for WINNER C2 double slope transmission loss model [5] under LoS occurs at  $d_{BP} \approx \frac{4h'_{Tx}h'_{Rx}}{\lambda} = \frac{4 \cdot 29 \cdot 1}{0.119} \approx 1$  km, since estimates of effective BS and MT heights are 29 m and 1 m, respectively. Therefore, all available data samples from Dresden measurement belong to this range.

<sup>†</sup>Data filtering according to min. required dynamic range is not applied here.

Table A.12: Transmission loss parameters for urban macro-cell.

Transmission Loss	Ilmenau, 2008		Dresden, 2009		WINNER II C2	
	LoS	NLoS	LoS	NLoS	LoS	NLoS
A	28.17	36.02	14.9	10.3	26	35.70
$B+C \cdot \log_{10} \frac{f_c[\text{GHz}]}{5}$	56.34	41.91	81.6	103.3	50.68	36.70

### LSP Distributions

The parameters of normal/log-normal distribution models have been summarized in Tab. 5.2, together with corresponding C2 WINNER II references. The WINNER model investigates LSP distributions and their correlations in transformed domain [5] where normal distributions for all transformed LSPs are assumed. For log-normally distributed LSPs (delay and angular spreads) mapping  $\tilde{s} = \log_{10}(s)$  is applied.

### Delay Domain Parameters

Parameters of their distributions acquired for Ilmenau measurement show good agreement with the WINNER II C2 model parameters [90]. Some differences can be found for the mean DS under NLoS and standard deviation of the K-factor, which is LoS parameter.

The SF standard deviation in Dresden measurement shows positive offset from WINNER C2 in LoS and negative in NLoS for approx. same absolute value of 3 dB. By looking into regression of transmission loss on Fig. A.27 it is possible to observe that LoS and NLoS classes are not significantly separated w.r.t. to the total received power on distances close to 300 m. Low-power observations being associated with LoS class (according to ray-tracing analysis) are causing increase of SF standard deviation (std.) under LoS. Additionally, their existence partially explains increased std. of K-factor. These values however do not contribute to the mean value of K-factor, which is increased with respect to WINNER C2.

Match between histograms and (log) normal model is shown on Fig. A.28 for XPR parameters of Ilmenau and Dresden measurements. Fig. A.28b indicates that, in the Dresden measurement, the mean XPR under LoS is approx. 2.5 dB higher than for NLoS case. In WINNER C2 this difference is smaller and equals 1 dB. In general, obtained parameters show good agreement with reported WINNER II C2 values.

Fitting of empirical delay spread CDF for Dresden measurement with log-normal model is shown in Fig. A.29a.

**Angular domain parameters** Inspection of Dresden LSP distribution parameters from angular domain in Tab. 5.2 reveals that they are pretty much aligned with WINNER C2 reference. The meaning of observed differences in LSPs distribution parameters is illustrated for angular spread on arrival (MT side) on Fig. A.29b. By comparing the distributions of ASA, it can be noticed that spreads observed in Dresden are slightly lower than WINNER C2 references for both LoS and NLoS. Difference of 0.15 in distribution mean,  $\mu$ , corresponds to approx. 20°, and difference of in std.  $\sigma$  is 0.07. Difference in mean translates CDF curve while difference

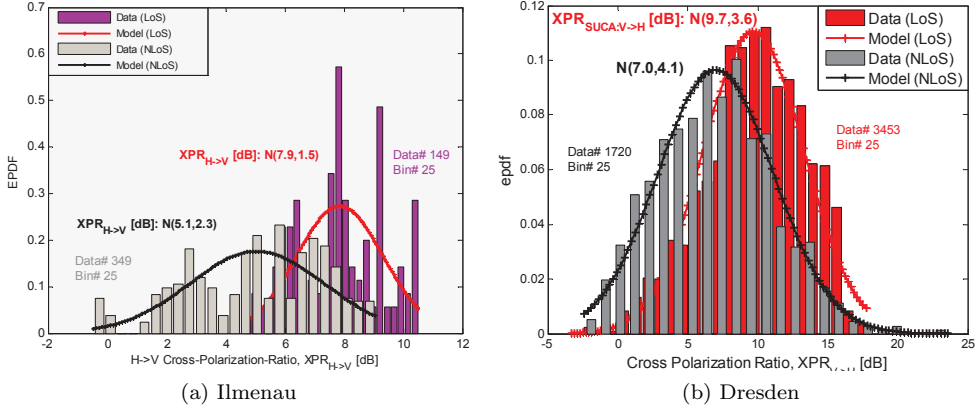


Figure A.28: Histograms and normal fit of  $V \rightarrow H$  cross-polarization ratios (XPRs).

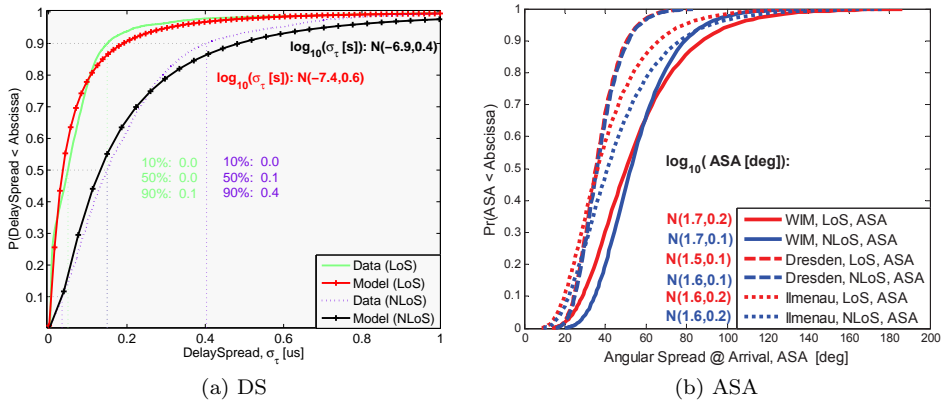


Figure A.29: Fitting of empirical CDFs: a) delay spread for Dresden measurement, b) azimuth spread on arrival.

in *std.* changes its steepness. The lower arrival and departure angles indicate that canyon effects are more pronounced on Dresden measurement site. With respect to the measurements in Ilmenau [90], [126] that are performed with the same equipment, the lower spreads are also observed: the PDFs are shifted to the left in Fig. A.29b.

The directional parameters are, for Ilmenau measurement, determined for the data subset consisting of 9 different links, established between the routes: ‘9a-9b’, ‘10b-9a’ and ‘41a-42’ (shown in red at Fig. A.24b) and base stations ‘BS1’, ‘BS2’ and ‘BS3’. Fig. A.30a shows very small values of azimuth spread on the side of base-station that are significantly smaller from the reference C2 WINNER II parameters.

The slightly larger values of elevation spreads are observed under LoS conditions. These values have not been obtained during the WINNER phase II, and therefore



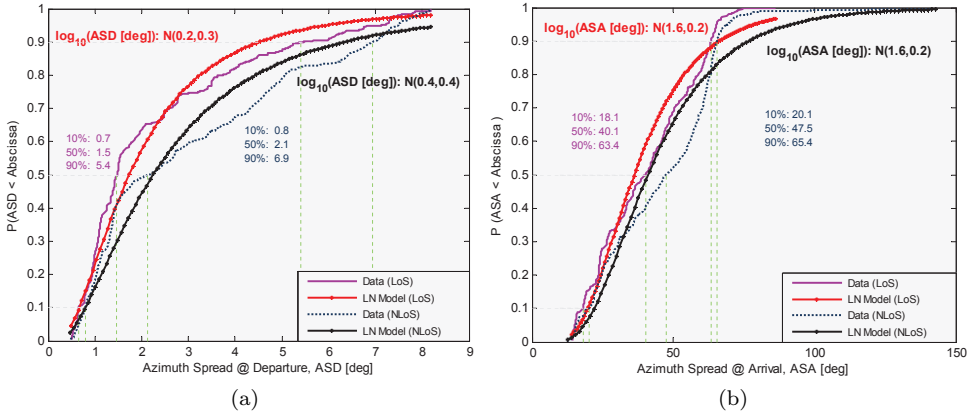


Figure A.30: Empirical CDFs for angular spreads in Ilmenau measurement: a) azimuth spread measured on the base station side, b) elevation spread measured on the side of mobile terminal.

comparison cannot be made. The opposite (larger values for NLoS) applies to azimuth spreads observed on the side of mobile terminal, as shown in Fig. A.30b. These parameters are pretty much the same as corresponding WINNER II parameters.

### Normality of Estimated LSPs in Transformed Domain

Fig. A.29a shows maximum likelihood fit of the empirical delay spread CDF from Dresden measurement with WINNER-like log-normal distribution. Although this approximation seems reasonable, the null hypothesis that transformed DS samples come from normal distribution, are rejected by both Lilliefors [165] and Jarque-Bera [166] normality tests. In contrast to the one-sample Kolmogorov-Smirnov test, these tests are suitable when parameters of null distribution are unknown and must be estimated. The normality hypothesis is also rejected for other Large-Scale Parameters estimated from Ilmenau and Dresden data, for both LoS and NLoS conditions. Therefore, the representation of measurements in WINNER parametric space can be considered as maximum-likelihood approximation of empirical multivariate distribution with MVN process.

### Cross-correlation of the Large Scale Parameters on Link-Level

In order to express dependence of separately characterized LSPs their correlations (at same MT position) are analyzed in transformed domain. Only those MT positions for which all LSPs are available contribute to the correlation matrix. Note that intersection of LSP realizations coming from different domains (time-delay and structural) further reduces number of samples used to calculate this type of correlation.

Tab. 5.3 summarizes link-level correlations from Dresden and Ilmenau measurements: the results for the cross-correlations among the LSPs are shown and compared to the results of the WINNER model. It is interesting to note that

only for few combinations similar correlations between Ilmenau measurement and **WINNER** C2 could be found, e.g. K vs. **DS**, K vs. **ASD** and K vs. **ASA**, where others show large divergence, e.g. **SF** vs. **ASD**, **DS** vs. **ASD**. Furthermore, the model is extended with new cross-correlation parameters related to the Elevation Spread on Arrival (**ESA**). The **ESA** showed similar and partly stronger correlations with other **LSPs** than the **ASA**. It is also interesting to note, that the correlation between **ASD** and **ASA** is high, around 0.6, but the **ASD** and **ESA** are negatively correlated with lower absolute level of  $\sim |-0.35|$ .

From Tab. 5.3 it is found that correlation levels of **LSPs** from Dresden measurements show better match to reference C2 scenario when both **LSPs** are calculated from the same domain. All reported angular spreads come from the structurally resolved domain, where certain amount of received energy cannot be spatially resolved by specular components [81]. Instead, the remaining energy (referred as dense multipath components) is represented in time-delay domain. This may result in correlation mismatch between angular spreads and other **LSPs** being calculated from time-delay domain. In another words the correlation may appear to be dependent on selected domains: if both delay spread and azimuth spread on arrival are estimated from structural domain (specular components) their correlation  $\rho(DS, ASA) = 0.65$  will match C2 reference. Note however that used estimate of **DS** is biased since contribution of dense multipath components is omitted. This points to the subtle uncertainty left within parameterization procedure of the **WINNER** model.

### Decorrelation Distance

The dependence of **LSP** correlation coefficient (CC) over distance is shown in Fig. A.31a for track ‘9a-9b’. This illustrates the general behavior for all tracks, where exponential decay shows strong dependence on selected base station (i.e., **Tx** location). A decorrelation distance for Large-Scale Parameters is determined as distance at which correlation coefficient drops to  $1/e$ . The corresponding decorrelation distances for Ilmenau measurement are: 8–9 m for the delay spread, 2.1–7.5 m for the shadow fading and 1.5–3 m for the K-factor [90]. These distances are significantly lower than parameters reported in **WINNER** phase II.

Fitting of empirical distance-dependent autocorrelation coefficients with exponential model for Dresden measurement is illustrated in Fig. A.31b for K-factor and azimuth spread on arrival. A decorrelation distance at which CC becomes lower than  $1/e$  is indicated on each model: 30.9 m and 5.1/5.7 m in the particular case. The complete list of **LSP** de-correlation distances is given in Tab. A.13 .

Decorrelation distances for Dresden measurement are quite different from **WINNER** C2 reference: **LSPs** calculated from time-delay domain have more than doubled decorrelation distance under **LoS** condition. This can be explained with larger **LoS** contiguous regions on Dresden measurement site. Opposite, decorrelation distances for all angular spreads (structural domain) are much smaller than **WINNER** reference. During processing of Dresden measurements HRPE is independently performed on blocks of snapshots that are spatially separated for approx. 10 m. However, this procedure does not impact reported results since calculated angular decorrelation distances are lower than length of a single estimation block.

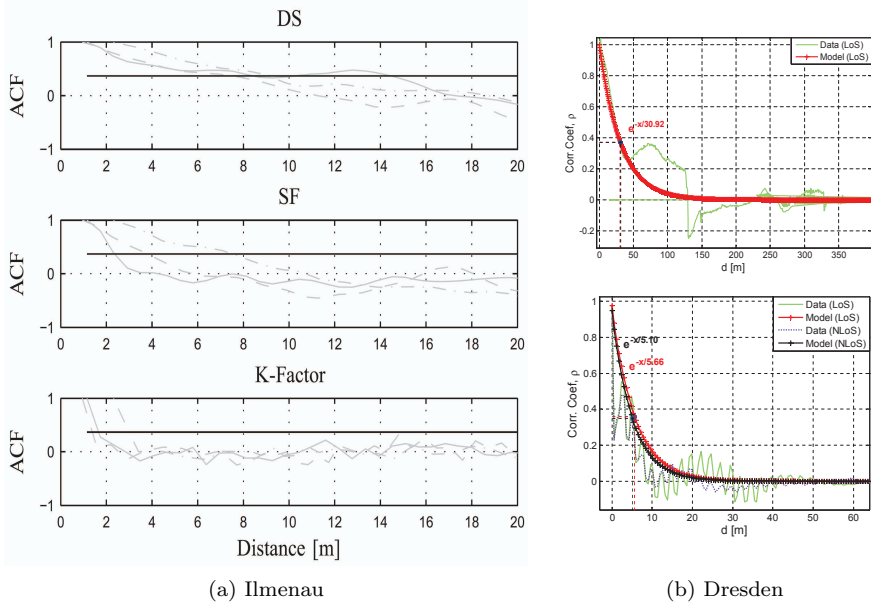


Figure A.31: Distance dependence of correlation coefficients.

Table A.13: LSP decorrelation distances for urban macro-cell.

	Ilmenau, 2008		Dresden, 2009		WINNER II C2	
	LoS	NLoS	LoS	NLoS	LoS	NLoS
SF	2.1	7.5	129	3	45	50
K	1.5	3	31	N/A	12	N/A
DS	8	9	131	38	40	40
ASD	-	-	2	2	15	50
ASA	-	-	6	5	15	50
ESA	-	-	2	2	N/A	N/A

### Similarity Between Measurements and WINNER Reference Scenario

In many aspects agreement is found between Ilmenau, Dresden LSPs and WINNER C2, however there are some features being considerably distinctive. If we allow possibility that collected number of realization is not adequate, certain findings could be specific for measurement site. It is also possible that certain features (like marginal LSP distributions) are less sensitive to limited data sample than others (transmission loss exponent, decorrelation distances). However, it is not trivial to establish required number of observations that will insure adequate scenario representation since WINNER reference parameters itself come from interpolation of many measurement campaigns.

Therefore the observed deviations can be attributed to variations of a specific environment within the abstract scenario definition. This conclusion is additionally supported by comparison to previous results based on measurement in Ilmenau

that use similar measurement setup. Namely, the difference between parameters of Dresden and Ilmenau measurements is typically lower than their distance from the **WINNER** reference.

The measure that enables the quantification of similarity between different measurements in **WIM** parametric space was introduced and discussed in Sec. 5.3.

## Appendix B

---

# Implementation and Verification of WINNER Channel Model

---

WINNER project [69] has begun in 2004, and Spatial Channel Model (SCM) was adopted for its initial channel model. SCM was developed in 3GPP/ 3GPP2 ad hoc group for spatial channel models and released in September 2003 [62]. In the beginning of 2005 the first extension of the original model was proposed by WINNER under the name SCM Extension - SCME [66]. SCME was later modified for 3GPP LTE purposes in [154], [167], [168], [169]. Development time-line of WINNER model is shown in Fig. B.1. In the end of 2005 further improvements and extensions are resulted in the model with the new name: WINNER Channel Model Phase I (WIM1). WIM1 model is described in the deliverable D5.4 [68] and published in [67]. SCM, SCME, and WIM1 models were briefly compared in [170]. The interim WINNER Channel Model Phase II (WIM2) was published in the deliverable D1.1.1 [110] and the final WIM2 model was given in project deliverable D1.1.2 [5]. In this thesis, WIM refers to WINNER model in general, WIM1 specifically to Phase I, and WIM2 specifically to Phase II.

In the course of the WINNER project all models are implemented in MATLAB/C and made available through the official web site [69]. The first part of appendix gives the short overview of implementation. A verification that WIM implementation properly reproduces targeted statistical distributions is provided in the second part of appendix.

### B.1 MATLAB Implementation of WINNER Channel Model

The implementation of the WINNER channel model is based on earlier WINNER models, Spatial Channel Model (SCM) and Spatial Channel Model Extended (SCME). The model's purpose is the generation of realistic radio propagation in different environments, under certain antenna setups, and for given transmission parameters. This section gives overview of the WIM2 implementation, while more detailed description can be found in [171].

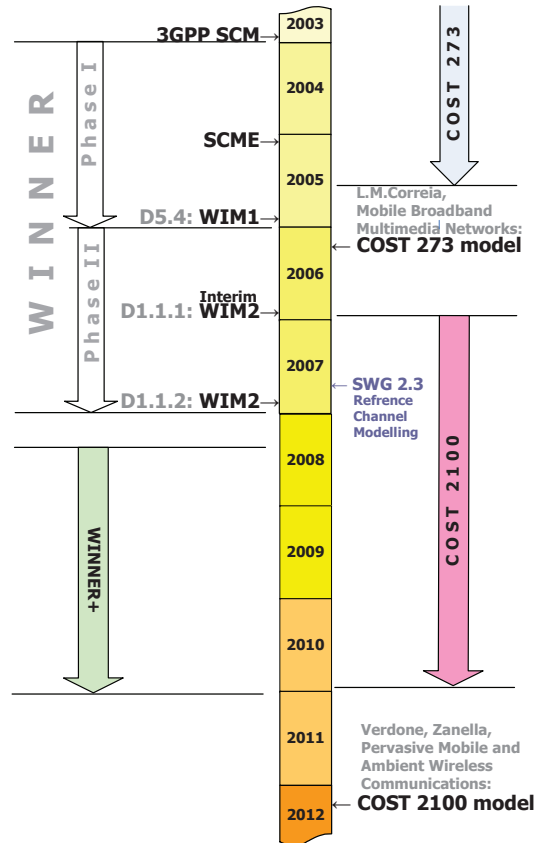


Figure B.1: Development time-line of WINNER model.

The high-level **WIM** implementation structure is shown in the block diagram given in Fig. B.2. The implementation of the **WIM** model uses large number of **MATLAB** functions. The key function for model usage is `wim.m`. This function is depicted in the middle of Fig. B.2 and will be discussed more closely in Sec. B.1.4. Other functions listed within “**WIM** implementation” block are usually referred as helper functions. Their usage makes the implementation modular and simplifies a development, modification and usage of the code. In that sense, the transmission loss model is implemented as a separate user-supplied function named `pathloss.m`. Additionally, functions used to generate the **LoS** probability for each scenario or calculate antenna response belong to this category. The functions that are not being called during evaluation of the `wim.m` are referred as external functions. E.g., it is assumed that the user mobility model is external to the channel matrix generation routine.

### B.1.1 Model Input Parameters

The model simulates radio propagation according to given input parameters that are conveniently grouped into:

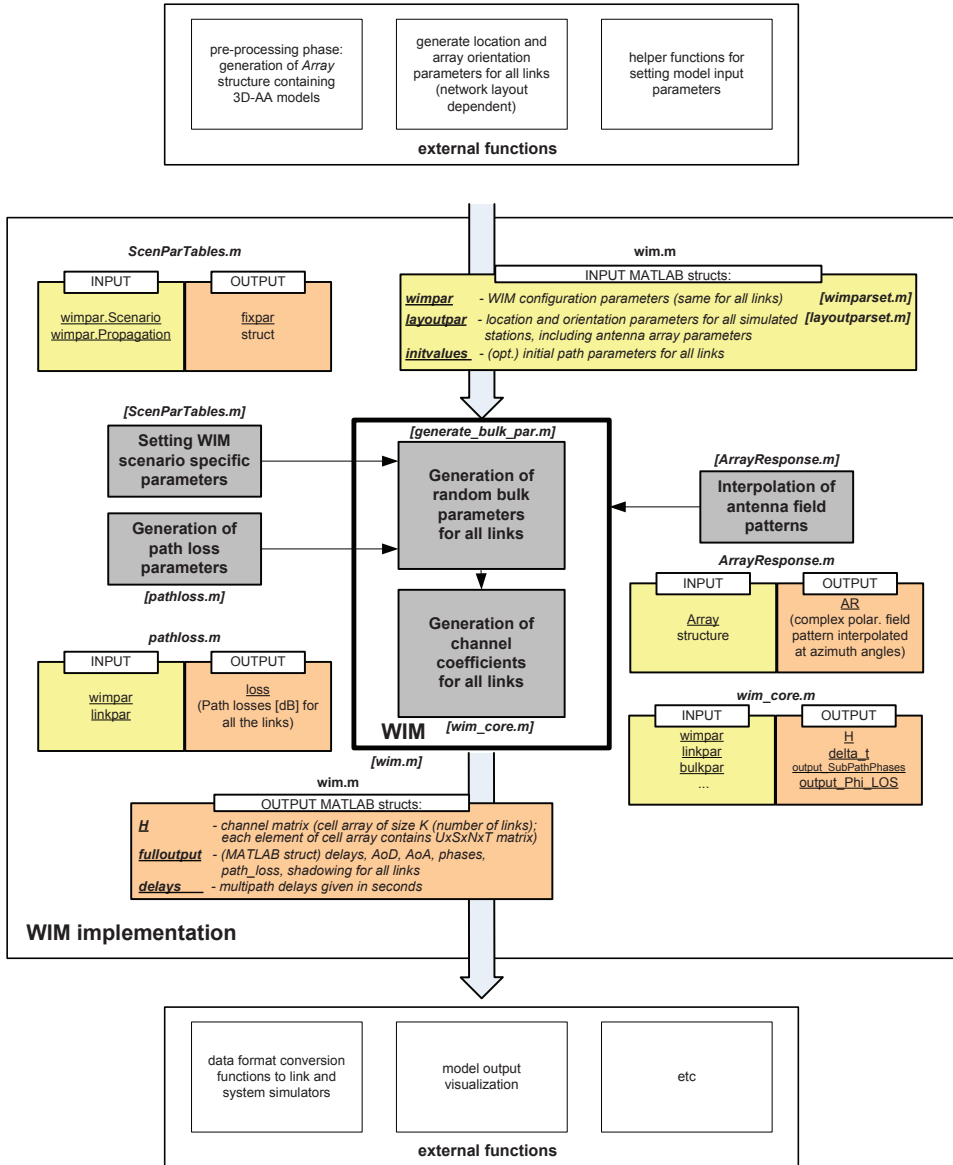


Figure B.2: High-level description of the WIM computation. The actual WIM model is shown in the central box labeled 'WIM'.

- system and model parameters (`wimpar`),
- layout parameters (`layoutpar`), and
- MIMO radio link parameters (`initvalues`).

Global simulation parameters (`wimpar`) could be classified into two major groups:

1. MDL – parameters defining model structure and system dependant parameters like `CenterFrequency`. Change of parameters from this group causes different model behavior.
2. SIM –simulation control parameters. These parameters control sampling in time and delay, parameter initialization mode (random vs. manual), and format of output parameters (e.g. inclusion/exclusion of path-loss in channel matrix  $H$ ).

Some of the free model parameters could be set in random manner. For that purpose functions as `wimparset.m` and `layoutparset.m` are used.

Scenario specific statistical parameters of the large-scale and low-level distributions are stored and retrieved by function `ScenParTables.m`. For each scenario and propagation condition they define the cross-polarization ratios, the LSP correlation coefficients and distances, the mean and standard deviation of the LSP distributions, proportionality ratios of power to probability distributions, the number of clusters and intra-cluster angle spreads. These parameters are given in Tables 5.2, 5.3, and 5.12.

### B.1.2 Construction of Antenna Array Model in Pre-processing Phase

Although WINNER channel model is constructed as antenna independent model, antenna array model is necessary to obtain signals at the output of the radio-channel. This model is deterministic and can be created independently from channel model simulations – in pre-processing phase. It is not good strategy to construct arrays each time when WIM is used, instead defined antenna arrays should be stored and retrieved when needed. This becomes particularly important when large number of operations is performed in this phase, i.e. when 3-D field patterns are rotated from ECS to ACS (Sec. 6.2).

WINNER phase II channel model uses structure `Array` for representation of 3-D Antenna Array (3DAA) model. For construction of `Array` structure MATLAB function `AntennaArray.m` is provided, Fig. B.3.

In order to make `Array` it is necessary to define its geometry (number, positions and rotation of elements), and to provide element field patterns. The arguments provided to `AntennaArray.m` are always processed in predefined way: first array geometry is created and after that field patterns are assigned.

In WIM2 interpolation of antenna radiation patterns is based on EADF representation and handled by function `AntennaResponse.m`. The verification of created 3DAA model can also be performed by the same function.



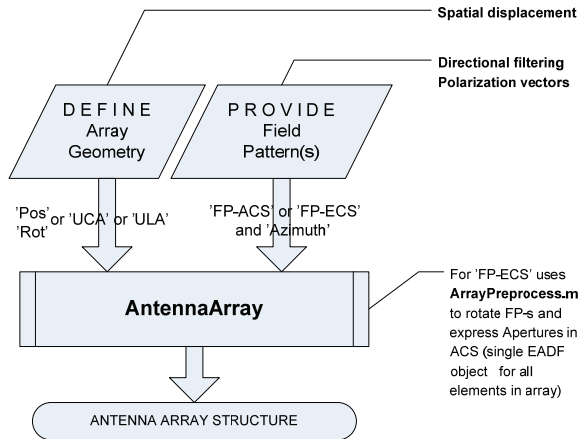


Figure B.3: Construction of antenna array [171].

### B.1.3 Description of Network Layout

WIM implementation supports a multi-base station and multi-mobile station network layout. The network layout includes information about: the number and locations of MSs and BSs in the GCS; the number of sectors in a BS (in case of a multi-cell network); the array broad side orientations at both MS and BS; the coupling of an active radio link from a MS to a certain sector of a BS (or vice-versa); and the directions of the MSs movement. More detailed guidelines for system-level simulations, including multi-cell, multi-user, multi-hop and relaying setups, could be found in [5].

Structure LAYOUTPAR defines position of terminal stations, type and orientation of antenna arrays and lists links of interest for simulation. The given parameters are related to a certain geometrical setup: the position and orientation of all antennas is expressed with respect to a global simulation coordinate system in which Y axis shows north, as shown in Fig. 5.4. Starting from the given network layout, the function layout2link creates the necessary link-level parameters.

#### Visualization of Network Layout

A rudimentary visualization of the network layout is implemented as helper utility in order to visualize the layout of the generated channel. The network layouts with 5 BSs and MS, and 7 active links are illustrated in Fig. B.4. In this figure red arrows denote the orientation of BS sector array, black arrows indicate the MS direction of motion, and blue arrows/lines show the active (modeled) links.

### B.1.4 Channel Matrix Generation

Channel matrices can be generated for multiple BS-MS links with one call of function wim.m. To calculate channel matrices from the model input, three main sub-functions of wim.m are implemented: LScorrelation.m, which generates the correlated Large Scale Parameters, generate\_bulk\_par.m where the low-level parameters are produced, and wim\_core.m which calculates the channel transfer matrix

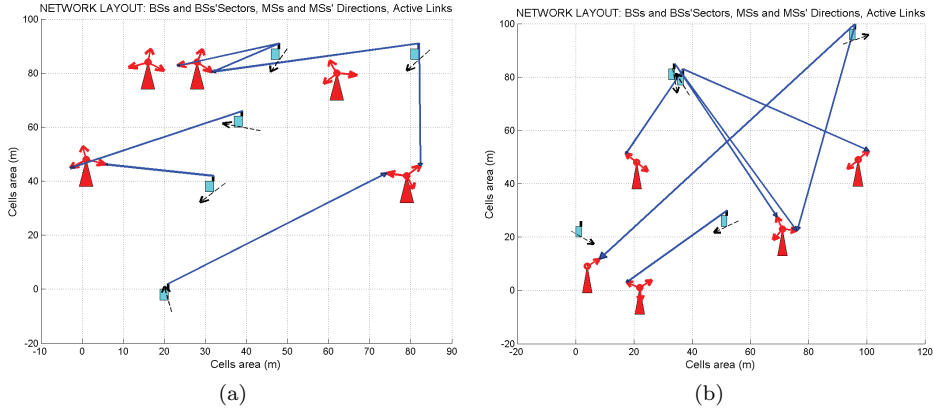


Figure B.4: Examples of the network layout visualization: a) 5 BSs (three sectors in any BS), 5 MSs and 7 active links; b) 5 BSs (number of sectors varies from 1-3 in different BSs), 5 MSs and 7 active links [171].

– **H**, afterward. More generally, the **WIM** computation is performed in two main parts:

1. the (random) generation of system/layout/model parameters (LS`correlation.m`, generate\_bulk\_par.m, and ScenParTables.m) and
2. the actual channel matrix computation (`wim_core.m`).

The computation flow, with the most important sub-functions, is shown in Fig. B.5. The full calling syntax for the `wim.m` function is:

$$[H, [DELAYS], [FULLOUTPUT]] = \text{wim}(\text{WIMPAR}, \text{LAYOUTPAR}, [\text{INITVALUES}]),$$

where  $[\cdot]$  designates optional argument(s). All input and output arguments of `wim.m` function are MATLAB structures/cells. Short description of output parameters is given in Tab. B.1

## Output Parameters

The most important output is five-dimensional array  $\mathbf{H}(U, S, N, T, K)$  which contains the coefficients of the channel transfer matrix  $\mathbf{H}$  for  $U$  Rx antenna array elements,  $S$  Tx elements,  $N$  clusters (paths),  $T$  simulated time instants, and  $K$  links.

In addition, the randomly drawn physical channel parameters for each link can be passed as an optional output argument `FULLOUTPUT`, as listed in Tab. B.1 [172]. If the option `wimpar.polarisedArrays` is used, the struct `FULLOUTPUT` contains additional array of the cross-polarization coupling power ratios V-to-H and H-to-V with the dimensions  $K \times 2 \times N$ . Also, the array with the sub-path phases is extended by additional dimension according to the four polarization combinations,  $\mathcal{P} \in \{VV, VH, HV, HH\}$ .

Table B.1: MATLAB output parameters.

Parameter name	Definition	Unit	Note
H	cell array of size $K$ (number of links). Each element of this cell array contains a $U \times S \times N \times T$ matrix.		
DELAYS	$K \times N$ vector of path delay values. Note that delays are, for compatibility with the INITVALUES, also included in FULLOUTPUT.	sec	
FULLOUTPUT	<b>MATLAB</b> structure with the following elements:		
delays	$K \times N$ matrix of path delays. This is identical to the second output argument.	sec	
path_powers	$K \times N$ array of path (cluster) powers.	linear	
aods	$K \times N \times M$ array of sub-path angles of departure	degrees	
aoas	$K \times N \times M$ array of subpath angles of arrival	degrees	
path_losses	$K \times 1$ vector	linear scale	
MsBsDistance	$1 \times K$ vector of MS-BS distances	m	
shadow_fading	$K \times 1$ vector	linear scale	
sigmas	$K \times 4$ vector of per link large scale parameters (ASD, ASA, DS, SF)	-	
propag_condition	$K \times 1$ vector indicating LoS/NLoS condition (0=NLoS, 1=LoS)	-	
Kcluster	$K \times 1$ vector defining narrowband K-factors of links.	linear scale	Only with LoS.
Phi_LOS	Final phases for LoS paths, $K \times 1$ array.	deg	Only with LoS.
scatterer_freq	$K \times N \times M$ array of subpath Doppler frequencies	Hz	Only with B5 CDL.
subpath_phases	complex-valued $K \times N \times M$ array giving the final phases of all subpaths. When polarization option is used, a $K \times P \times N \times M$ array, where $P = 4$ . In this case the second dimension includes the phases for $[VV, VH, HV, HH]$ polarized components.	degrees	
delta_t	$K \times 1$ vector defining time sampling interval for all links.	sec	
IndexOf-DividedClust	$K \times 2$ matrix. Index to two strongest clusters. These clusters are spread to three delay positions if parameter IntraClusterDsUsed = 'yes'	-	
xpr	$K \times N \times M$ array of cross-polarization coupling power ratios.	linear scale	Only with polarized-Arrays case.

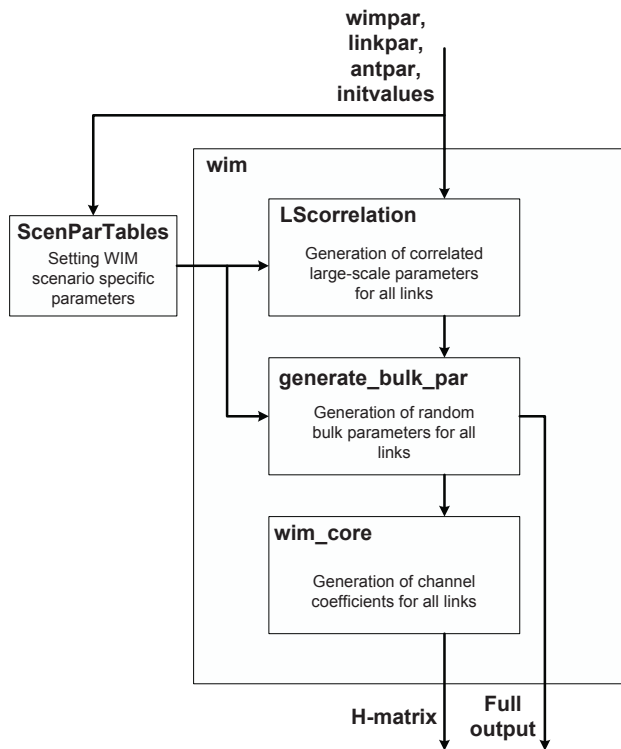


Figure B.5: Simplified structure of the WIM [171].

### B.1.5 Comparison of Phase I and Phase II Implementations

The most obvious differences between Phase I and Phase II models are related to the additionally parameterized scenarios (A2, B2, C3, B4, B5f, D2a, and D2b). Furthermore, an intra cluster delay spread and support for the far clusters are introduced. Time evolution of the **LSPs** is implemented by gradual cluster replacement between channel segments, between **NLoS** and **LoS**, and between scenarios. The propagation conditions can be determined before simulations or randomly adjusted according to the **LoS** probability, for each run and each link, of given the scenario. Also, various parameters in `ScenParTables.m` have been tuned. However, the most relevant impact on reproduced statistic is related to the modification of the angle generation. In Phase I the angles were drawn from wrapped Gaussian distributions with adaptive spreads, independently from the cluster powers. In the Phase II model, the angles are related to cluster powers, which are related to cluster delays.

## B.2 Reproduction of Targeted Statistics

To certify that a channel model offers a realistic representation of the mobile channel, the model has to be verified and validated. Distinction between these procedures is illustrated in Fig. B.6. Verification assumes testing if the channel output

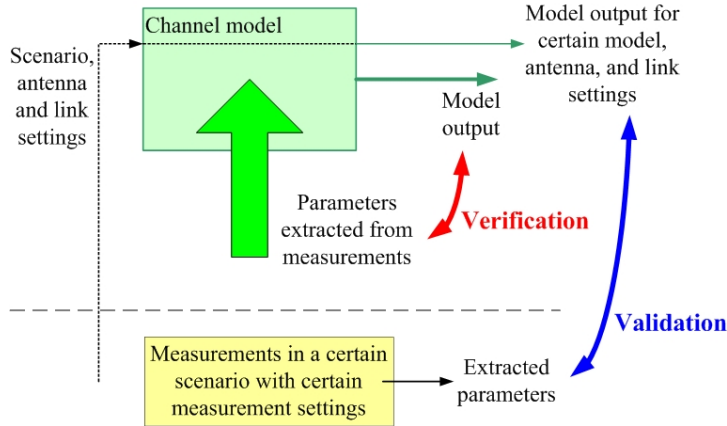


Figure B.6: Validation and verification procedures.

is being generated according to expectations for given input parameters, while validation checks whether the parameters and structure of the model are chosen so that model output correlates with realistic, measured values. Thus, verification of a model includes testing the model's implementation and comparing the model's generated output to certain input. Validation is the comparison of the generated model output with realistic values gained from measurements (Fig. B.6).

The model should not be validated with the same measurement data from which the model parameters were being extracted. This might not prove that the model is correct but would just verify that the parameters were extracted and reproduced properly [173].

As discussed in previous chapters, due to different limitations it is not possible to introduce fully system independent validation metric. This means that validation of channel model based solely on propagation channel can be performed only partially, by using synthetic data. Validation of radio channel is considered to be system-dependent since antenna embedding, and system-related filtering have to be included. Therefore, validation of WINNER Urban C2 scenario in Sec. A.2.3 is based on measurements that are performed with same equipment performed in two different cities. The observed similarity between them and WINNER C2 reference scenario parameters (Sec. 5.3) can be considered as validation of the scenario-based modeling concept and proper choice of WINNER C2 parameters.

### B.2.1 Verification Strategy

Verification of a channel model is based on the comparison of the model output to its expected outcome. As the WIM is a stochastic model, verification is related to observation and comparison of certain stochastic properties. For that purpose, the set of parameters influencing the output has to be predefined. However, the existence of two levels of randomness in the WIM model complicates comparison. Namely, the shapes of the low-level parameter (LLP) distributions are controlled by the randomly generated LSPs. Therefore verification procedure includes the following steps [174]:

1. The model is controlled by values of **LSPs** that are drawn from lognormal distributions (first level of randomness). The first step would therefore be to examine how samples drawn from those distributions are fitting to the expected analytical distributions. Furthermore it is checked if those parameters are correlated in the defined way by calculating a matrix of correlations coefficients.
2. As the **LSP** define the distribution of the **LLP** (second level of randomness), the next step is to generate low-level parameters and verify their distributions. This is done for distinct fixed values of the spread parameters, which simplifies comparison since the resulting distributions correspond only to the second level of randomness.
3. In the last step both levels of randomness are taken into consideration: the spread distributions are recalculated from the model's **LLP** output and compared to the targeted analytical **LSP** curves from the first step.

Following this verification strategy the simulations are split into three parts, Fig. B.7. In the first part the distributions of the **LSP**, the cross-correlation coefficients (**XCC**), and Cross-Polarization Ratio (**XPR**) are verified. In the second part the distributions of the **LLPs** for a fixed spread value are tested and subsequently used to recalculate the spread values. In the third part the **LSP** distributions are regenerated from the model's **LLP** output.

All results presented in this section are originally given in [174], which also contains description of related **MATLAB** implementations. The obtained histograms are presented graphically and fitted with analytical **PDF** curves. Necessary distribution parameters (mean, std.) are estimated using maximum likelihood distribution fitting, that provides the closest match from the given distribution family. The verification is performed by qualitative comparison of histograms and fitted **PDFs** shapes with analytical curves representing the expected distribution, or by comparing mean and standard deviation of the fitted distributions to expected values. The proper quantification of similarity should be based upon Kullback-Leibler (KL) divergence (5.8), however that results are currently not available.

## B.2.2 Statistics of Generated Large-Scale Parameters

Verifying of the **LSP** distributions generated by the **WIM** function `LScorrelation.m` is equivalent to testing the correctness of the function implementation. The presented verification results include the generation of 4 correlated **LSPs**: Delay Spread (**DS**), Azimuth Spread on Departure (**ASD**), Azimuth Spread on Arrival (**ASA**), and Shadow Fading (**SF**).

### Marginal Distributions of Correlated Large-Scale Parameters

In **WIM** the **LSPs** are generated as correlated random variables from log-normal distributions. Primarily, the four i.i.d. Gaussian variables  $\vec{\xi}$  are generated, and

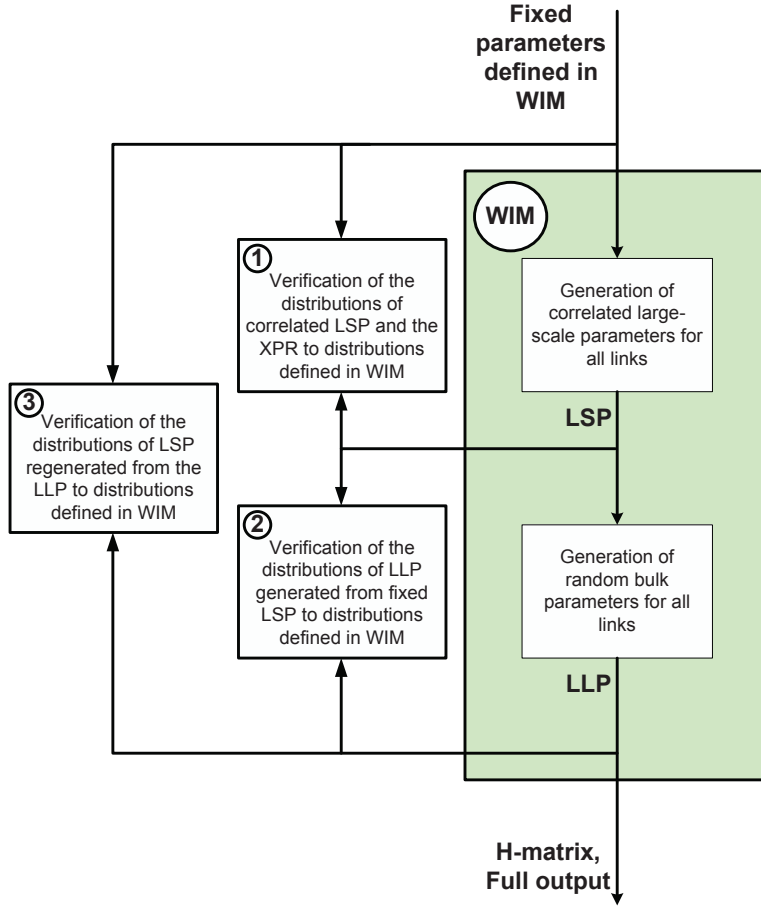


Figure B.7: Flow chart of the functions for verification and their targeting points in WIM.

subsequently correlated through multiplication with the square-root of the cross-correlation matrix:

$$\xi_c = \sqrt{\begin{bmatrix} 1 & \rho_{DS,ASD} & \rho_{DS,ASA} & \rho_{DS,SF} \\ \rho_{DS,ASD} & 1 & \rho_{ASD,ASA} & \rho_{ASD,SF} \\ \rho_{DS,ASA} & \rho_{ASD,ASA} & 1 & \rho_{ASA,SF} \\ \rho_{DS,SF} & \rho_{ASD,SF} & \rho_{ASA,SF} & 1 \end{bmatrix}} \cdot \vec{\xi}. \quad (\text{B.1})$$

The correlation coefficients  $\rho_{TLSP1,TLSP2}$  in the correlation matrix are defined in `ScenParTables.m` for each scenario and propagation condition. In the next step,  $\vec{\xi}_c \sim N(0, 1)$  is transformed to obtain the targeted variances  $\sigma_{TLSP}$  and means  $\mu_{TLSP}$ .

$$\vec{\xi}_c(\mu_{TLSP}, \sigma_{TLSP}) = \sigma_{TLSP} \cdot \vec{\xi}_c(0, 1) + \mu_{TLSP} \quad (\text{B.2})$$

The normal distributions are then transformed into log-normal ones by appropriate mapping. For **DS**, **ASA** and **DS** the mapping is:

$$LSP = 10^{\vec{\xi}_c(\mu_{TLSP}, \sigma_{TLSP})} \quad (\text{B.3})$$

All scenarios have been simulated 50000 times, and collected **LSPs**. are shown in form of histograms. Additionally, a fitted **PDF** and a analytical shape of the expected distribution are plotted in the figure for comparison. The histograms are calculated with the **MATLAB** `hist.m` function and the area of the histogram is normalized to unity. The mean and std. of the fitted **PDF** are calculated with the **MATLAB** function `lognfit.m`. The tabulated **WINNER** mean and std. parameters from `ScenParTables.m` are related to the parameters of log-normal distribution as

$$\mu_{LN} = \ln(10)\mu_{TLSP} \quad (\text{B.4})$$

$$\sigma_{LN} = \ln(10)\sigma_{TLSP}. \quad (\text{B.5})$$

From these parameters log-normal **PDF**

$$y = f(x|\mu_{LN}, \sigma_{LN}) = \frac{1}{x\sigma_{LN}\sqrt{2\pi}} e^{-\frac{(\ln x - \mu_{LN})^2}{2\sigma_{LN}^2}} \quad (\text{B.6})$$

is created analytically with `lognpdf.m`.

A very good agreement between targeted and obtained **LSP** distributions (including **XPRs**) is obtained for all scenarios. Fig. B.8 illustrates this for the A1 LoS scenario. From obtained results the conclusion can be drawn that, for all scenarios, the **LSPs** are generated as defined in WIM.

### Matrix of Cross-Correlation Coefficients

The cross-correlation coefficients of the **WINNER TLSPs** could be represented in the form of matrix (B.1). For validation purposes the cross-correlation matrix is recalculated from the intermediate model output (B.2) and compared to the initial input matrix. For every scenario and propagation condition 50000 **LSP** realizations are collected and used to calculate cross-correlation coefficients. Diverse agreement between intended and recalculated cross-correlation coefficients are observed for different scenarios. Usually, the absolute deviation is within 0.05, but in some cases it can be higher, as shown in Fig. B.9 for the A1 LoS scenario.

Observed deviation does not get significantly smaller when increasing the number of simulation runs, thus it can be affected by the way correlations are implemented in the model. It can be concluded that the targeted correlation level between the **LSPs** is not reproduced ideally during the model generation process.

### B.2.3 Distributions of Generated Low-Level Parameters

Since the low-level parameters are strongly dependent on a randomly drawn spreads (i.e., **LSP** realizations) that change during simulation, their distributions can not be simply checked from the regular output parameters of the model. For that reason it is most reasonable to check the distribution of **LLPs** for fixed distinct values of **LSPs**. This eliminates one level of randomness: by fixing the spread values the shape of **LLP** distributions is also fixed. This enables comparison of the expected outputs with reproduced **LLP** distributions. The following values of the log-normal distribution curves are chosen for verification:



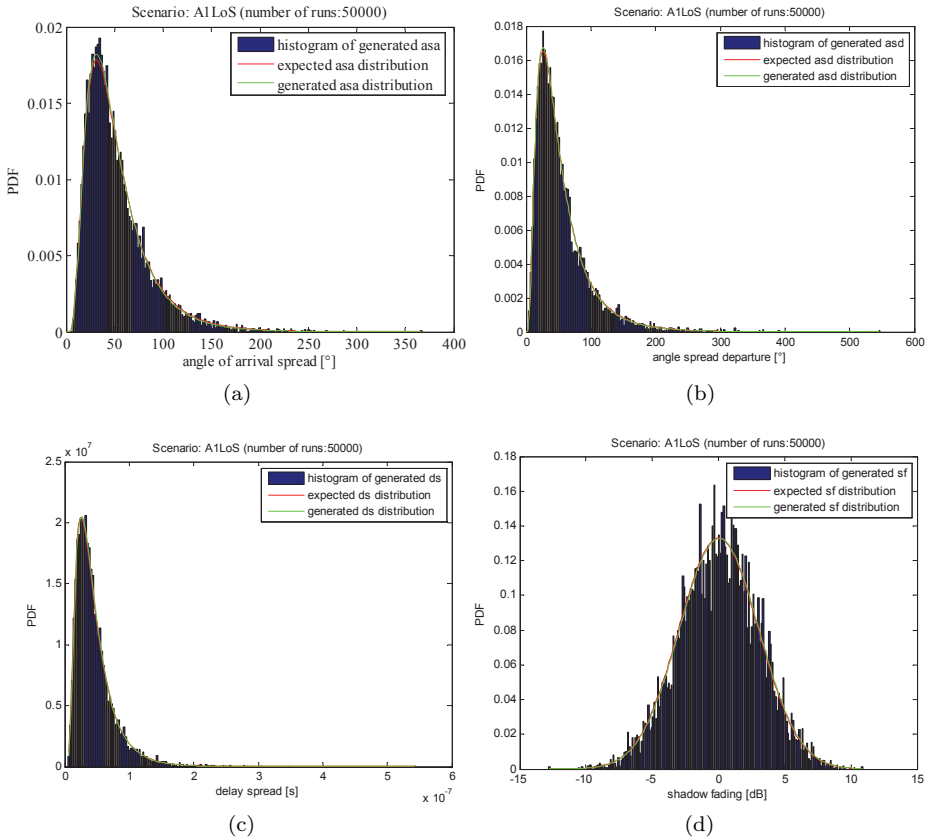


Figure B.8: Verification of LSP marginal distributions for A1 LoS scenario: a) angle spread arrival, b) angle spread departure, c) delay spread, and d) shadow fading (Fratzcher [174]).

	$\sigma_{DS}$	$\sigma_{ASD}$	$\sigma_{ASA}$	$\sigma_{SF}$
$\sigma_{DS}$	1	0.53	0.74	-0.77
$\sigma_{ASD}$	0.53	1	0.39	-0.09
$\sigma_{ASA}$	0.74	0.39	1	-0.39
$\sigma_{SF}$	-0.77	-0.09	-0.39	1

(a)

	$\sigma_{DS}$	$\sigma_{ASD}$	$\sigma_{ASA}$	$\sigma_{SF}$
$\sigma_{DS}$	1	0.5	0.7	-0.7
$\sigma_{ASD}$	0.5	1	0.4	-0.1
$\sigma_{ASA}$	0.7	0.4	1	-0.4
$\sigma_{SF}$	-0.7	-0.1	-0.4	1

(b)

Figure B.9: Comparison of the implemented (a) and the recalculated (b) cross-correlation coefficients (Fratzcher [174]).

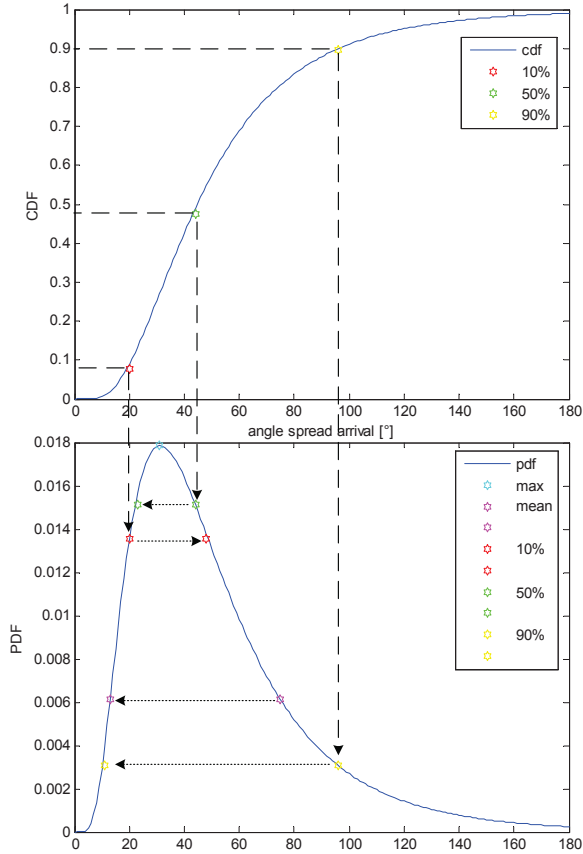


Figure B.10: Graphical representation of the LSP values selected for LLP verification (Fratzcher [174]).

1. The maximum of the PDF curve ( $\sigma^{max}$ ). It represents the spread value that occurs with the highest probability.
2. The mean (average) of the log-normal distribution curve ( $\sigma^{av}$ ) is analytically calculated as

$$\sigma^{av} = e^{\mu_{LN} + \sigma_{LN}^2/2}. \quad (\text{B.7})$$

3. The median (50 % CDF level) -  $\sigma^{50}$ .
4. The 10 %-level,  $\sigma^{10}$ .
5. The 90 %-level,  $\sigma^{90}$ .

The selected spread values  $\sigma^{10}$ ,  $\sigma^{50}$ ,  $\sigma^{90}$  define 10 %, 50 %, and 90 % CDF levels, respectively, as shown in Fig. B.10. Additional four values, having the same probability (i.e. ordinate of PDF) as already listed values, are selected from log-normal PDF curve. Therefore, all characteristic values from PDF/CDF curves  $\sigma^X$  (except

the PDF maximum) map to additional value  $\sigma^{\tilde{X}}$ . This gives nine distinct values on the distribution curves of DS, ASD, and ASA. For those fixed values the LLP were generated and verified. The complete procedure of LSPs selection for verification of LLP distributions is illustrated in Fig. B.10. The nine obtained LSP values form the verification vector:

$$\vec{\sigma} = \left[ \sigma^{max}, \sigma^{\tilde{a}v}, \sigma^{av}, \sigma^{10}, \sigma_{\tilde{10}}, \sigma^{\tilde{50}}, \sigma^{50}, \sigma^{\tilde{90}}, \sigma^{90} \right] \quad (\text{B.8})$$

For each of selected LSPs 5000 simulation runs is performed to generate LLP realizations. For that purpose the fixed spread values  $\left[ \sigma_{\tau}^X, \sigma_{\phi}^X, \sigma_{\varphi}^X \right], X \in \{max, \tilde{a}v, \dots\}$  are passed to generate\_bulk\_par.m.

The LLP realizations cannot be considered separately because delays, powers, and angles are calculated in sequence, depending on previously determined parameters. Consequently, if the delay distribution of model output deviates from expected, this will have an effect on the distributions of the generated powers and angles. Still the generation process can be followed stepwise exposing the changes of the distributions after each generation step.

The proposed verification strategy will show whether the deviations between the model output and expected distributions vary for different spread values.

### Distribution of Generated Delays

The delays are generated according to (5.11), in order to obtain exponential distribution:

$$p(\tau) = \exp\left(-\frac{\tau}{r_{\tau} \cdot \sigma_{\tau}}\right). \quad (\text{B.9})$$

The decay of distribution is inversely proportional to the delay spread value  $\sigma_{\tau}$  used for generation of delays. Their histograms in Fig. B.11 show that the exponential distribution is decaying imperceptibly faster than expected.

In the case of a LoS propagation condition the histogram of the generated delays deviates more from the expected curve. Although delays are modified for LoS condition to account for power redistribution between LoS and remaining components according to (5.14), this does not resolve the issue completely.

### Distribution of Generated Powers

WIM does not use analytical functions to describe distribution of cluster powers. Instead, Power-Delay Profiles (PDPs) is used to map cluster delays into corresponding powers, according to (5.15). Fig. B.12 shows obtained PDP and histogram for A1 LoS scenario.

The powers are exploited to establish relation between delays and angles, and cluster departure and arriving angles are based upon the Power Angular Spectrum (PAS). Therefore the accurate generation of powers from delays PDP is condition for the proper angle generation.

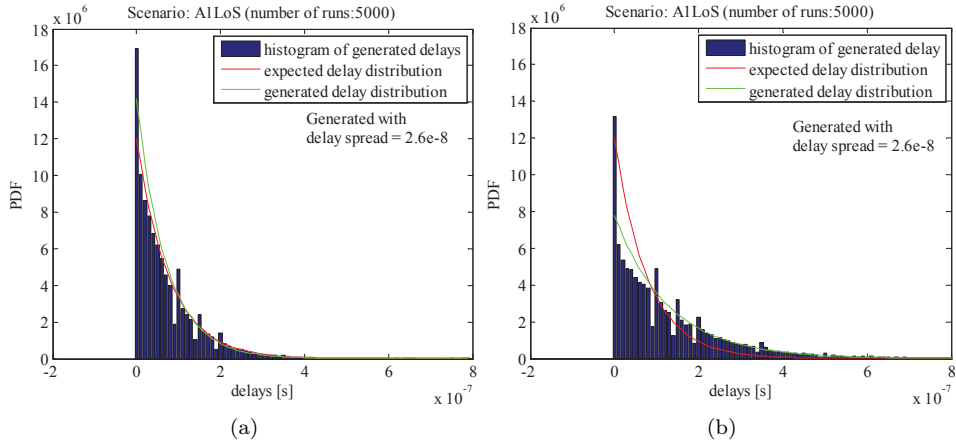


Figure B.11: A1 LoS delay distribution: a) without LoS peak, and b) with LoS peak (Fratzcher [174]).

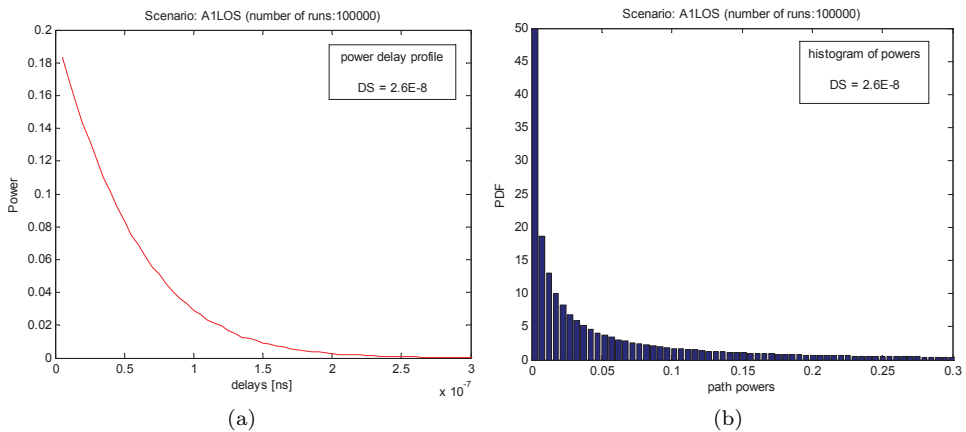


Figure B.12: Power related distributions in A1 LoS scenario: a) power-delay profile and b) histogram of cluster powers (Fratzcher [174]).

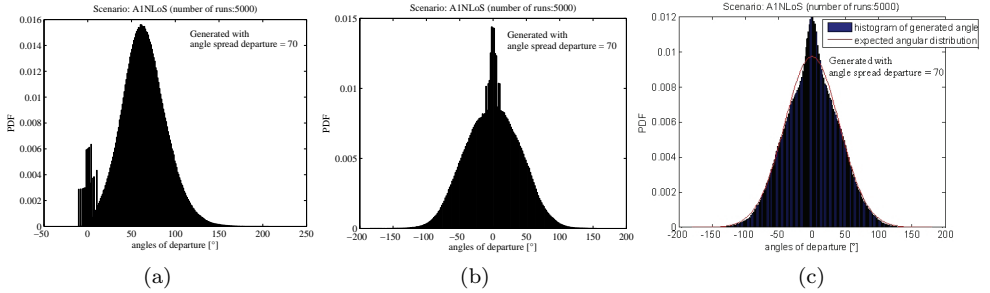


Figure B.13: PDFs related to generation of departure angles: a) max. angular offset of uniform distr., b) part of angular offset with uniform distribution, c) total angular offset with uniformly and normally distributed parts (Fratzcher [174]).

### Distribution of Generated Angles

Since the generation of the angles was changed from the WIM Phase I to the Phase II, both cases are compared here. In the Phase I model the angles are generated independently from the power distribution and therefore of the power generation does not influence the angular distribution. Both versions use the same wrapping of the Gaussian distribution to a range of  $[-180, 180]$ , as described in Sec. C.4.1.

#### WIM Phase II Implementation

In WIM Phase II implementation the angles are generated from the cluster powers. The maximum angular offset from LoS,  $\varphi_n$ , is gained from inverse PAS mapping (5.18). The actual offset is estimated as sum of uniformly and normally distributed random variables (5.20). From Fig. B.13c it can be observed that the histogram of generated angles is inconsistent with the analytical curve representing expected distribution. Unexpected deviations around zero offsets are caused by large number of  $\varphi_n$  realizations being close to zero, Fig. B.13a. This correspond to cluster with maximum powers, for which  $\ln\left(\frac{P_{max}}{P_{max}}\right) = 0$ , and additional sub-cluster spreading used for two strongest clusters Sec. 3.7.1. It may be necessary to modify described generation process to avoid disturbance of angular statistics.

After the angular wrapping, the shape of the angular distributions deviates even more from targeted reference. Further effect of angle wrapping will be analyzed in the context of WIM Phase I implementation, and LSP reconstruction in Sec. B.2.4.

**WIM Phase I implementation** For comparison the angles were also generated with a previous version (Phase I) of the WIM implementation where the angles are taken from normal distributions without any dependence on the distribution of powers. The offset angles and the LoS direction angle are added in the same way as in Phase II. The resulting histogram that includes the angular wrapping is shown in Fig. B.14.

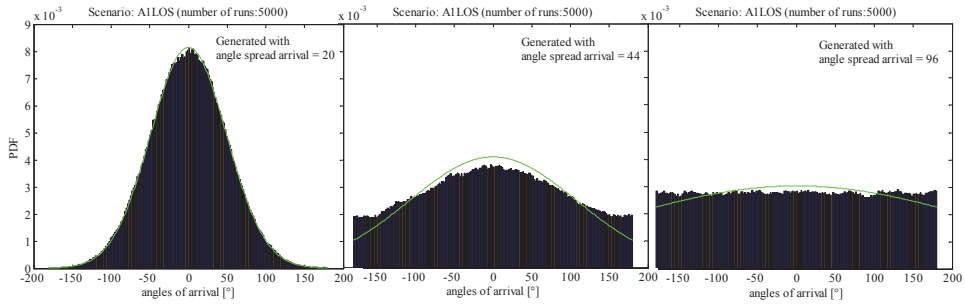


Figure B.14: The effect of the wrapping of normally distributed angles to interval  $[-180^\circ, 180^\circ]$ , (Fratzcher [174]).

## B.2.4 Reconstructing LSP Distributions from Model Output

In the last step of the verification process the **LSPs** are recalculated from the generated **LLPs**, and compared with intended values. This reveals not only the correct generation of the parameter distributions but particularly the correct generation of the model parameters themselves. Hence, if small discrepancies between the **LLP** distribution and the expected curve occur, their influence on the large scale will be examined. Two approaches have been taken to check distribution of regenerated **LSPs** [174].

**Fixed control parameters:** In the first approach, the **LSPs** are selected in same manner as for **LLP** distribution testing. The aim of verification is to check whether **LSP** values recalculated from the **LLP** output correspond to **LSP** values used to generate that **LLP** output.

**Random control parameters:** In the second approach the **LSP** distributions are being regenerated from the **LLP** output controlled by random **LSP**.

The recalculation process is the same in both approaches and equivalent to estimation of **LSPs** from measurement data, which is discussed in Sec. 4.3.

### Fixed control parameters

For each generated set of **LLPs** the corresponding **LSP** is calculated and then plotted as a histogram. Fig. B.15 shows distribution of arriving azimuth angles for A1 NLoS scenario. The expected outcome is the same spread value used to generate the **LLP**, i.e.  $31^\circ$  in this particular example. This value is marked on histograms with red star, and mean of recalculated distribution are showed with green star. Instead of having the single value of recalculated angular spread that is equal to  $31^\circ$ , lognormal distribution is observed with mean value of  $35^\circ$ . This illustrates the weak enforcement in generated **LSPs** in **SCM/WIM** models. The issue is related to selection of limited number of realizations from continuous density curves, that jointly does not reflect the spread in original distribution.

To get an impression of how the results change with higher spreads Fig. B.16 displays the histograms of regenerated **LSP** according to increasing values of the

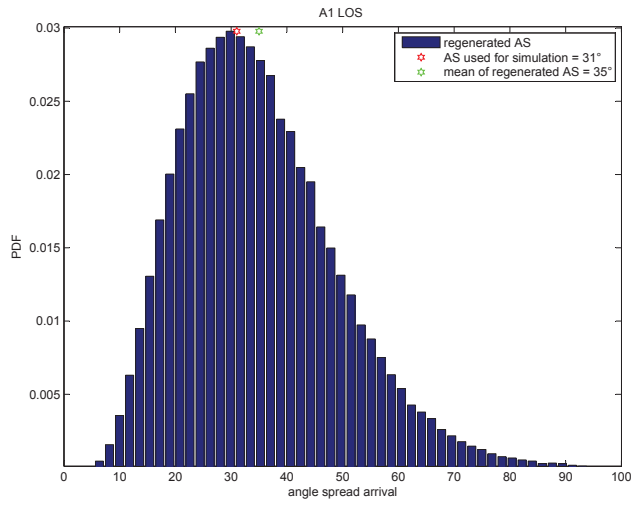


Figure B.15: Distribution of regenerated azimuth spreads at arrival (ASA) from model output (Fratzcher [174]).

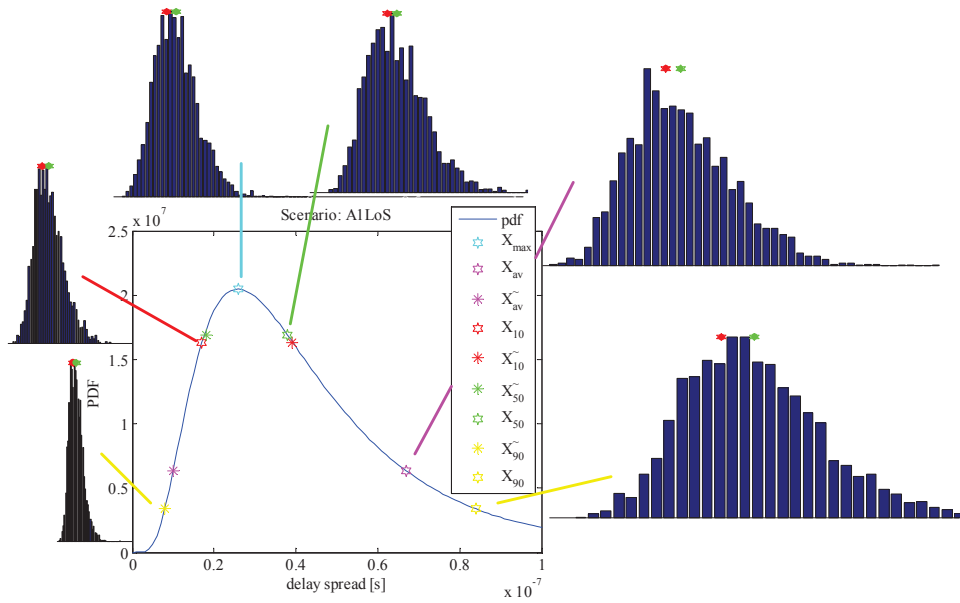


Figure B.16: Regenerated delay spread values from LLP: red dot - expected DS, green dot - mean of regenerated DS. All histograms have the same scale (Fratzcher [174]).

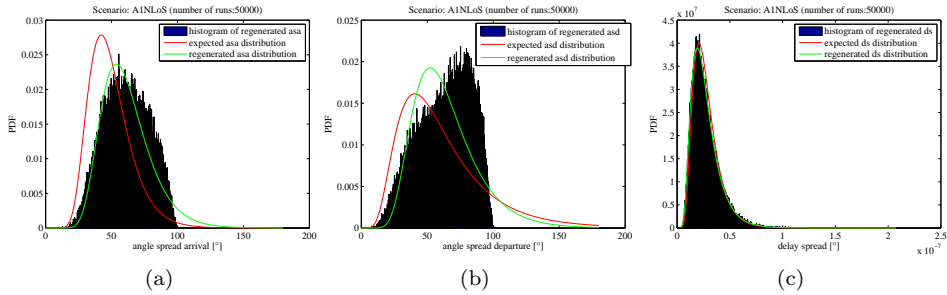


Figure B.17: LSP distributions regenerated from LLPs with Phase II implementation: a) angle of arrival spread, b) angle of departure spread, c) delay spread (Fratzcher [174]).

LSP distribution curve. The embedded graphs clearly show that the deviation of the regenerated LSP value from the expected one increases as the targeted LSP value increases: the higher the spread value the larger becomes the deviation of the recalculated mean. Also, the recalculated values are not normally distributed around the mean but have a log-normal distribution, which implies that selection of limited number of samples causes log-normal deviation of spread from the spread of initial continuous distribution.

### Random control parameters

For the second approach the model is run 50000 times. The LLP parameters are collected as the optional model output and used to recalculate LSPs. From obtained values histograms are produced, as illustrated in Fig. B.17. The shape of histogram should correspond to tabulated WINNER log-normal distribution for the corresponding LSP. For comparison, the targeted analytical curve of expected LSP distribution is also plotted in the histogram along with log-normally fitted curve of the recalculated LSP data. The reconstructed delay spread distribution matches the expected distribution quite well whereas the angle spread distributions are not even shaped lognormally in Fig. B.17.

To determine the influence of the circular angle wrapping on the shape of the distribution, the simulations were repeated without restricting the angles to the range of  $[-180,180]$ . Figure B.18 shows that the distribution of unwrapped angles have lognormal shape as expected, but with a larger spread.

The reconstruction of LSPs from Phase I model output is also performed for random control parameters and results are shown in Fig. B.19. As the angle distributions generated with the Phase I model matched the expected fairly accurate, the angular spread distribution reconstructed from those angles fits the expected distribution much better if compared with Phase II model in Fig. B.17.

Detected implementation inconsistencies of Phase II model should be fixed in the future. The method of generating the angles from the powers should be improved.



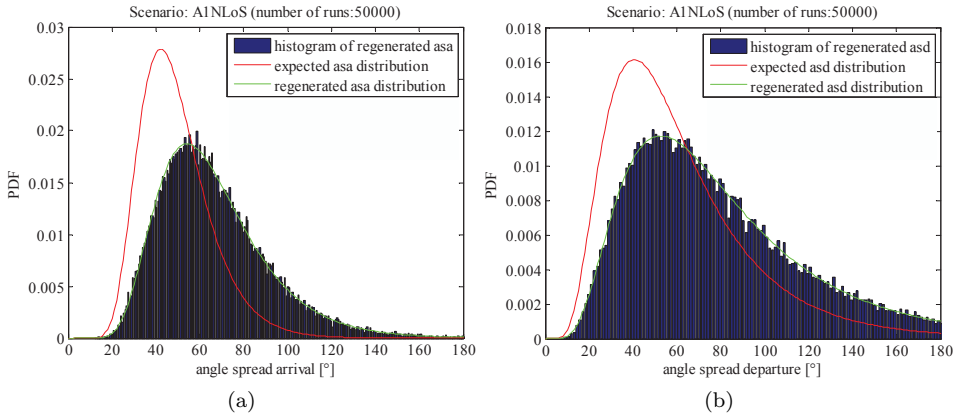


Figure B.18: Angular spreads regenerated with Phase II implementation, without angle wrapping. (Fratzcher [174])

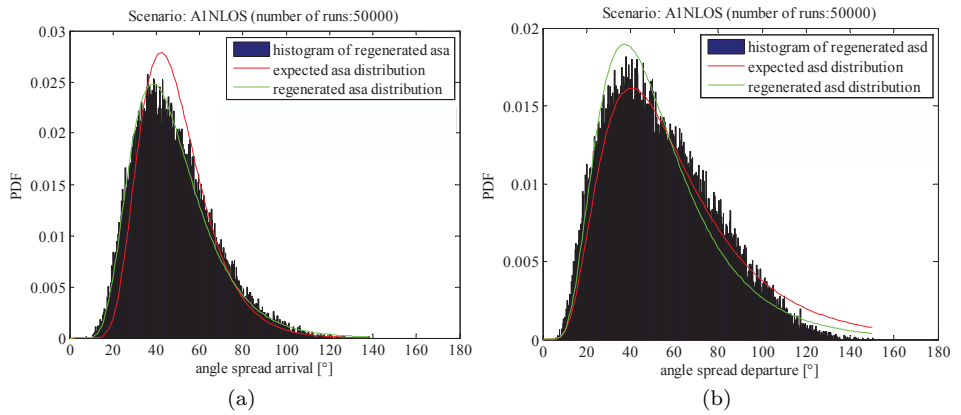


Figure B.19: Regenerated angle spreads with WIM Phase I implementation (Fratzcher [174]).



## Appendix C

---

# Random Variables and Stochastic Processes

---

### C.1 Statistical Moments

Joint *non-central* moment of RVs  $x$  and  $y$  of order  $k + r = n$  :

$$m_{xy}^{kr} = E \{x^k y^{*r}\} \quad (\text{C.1})$$

Joint *central* moment of RVs  $x$  and  $y$  of order  $k + r = n$  :

$$\mu_{xy}^{kr} = E \left\{ (x - E \{x\})^k (y - E \{y\})^{*r} \right\} \quad (\text{C.2})$$

#### C.1.1 Correlation and Covariance Functions

“In probability theory, correlation is a measure of conditional predictability (dependency) between random variables. Two random variables are *uncorrelated* if realizations of one variable does not provide any predictive information about the other random variable. This concept appears to be useful for characterization of the evolution of the random process, since closer observations (with lower separation) tend to be more correlated.” [28]

**Correlation** is non-central moment of order  $1+1=2$ :

$$R_{xy} = m_{xy}^{11} = E \{xy^*\} \quad (\text{C.3})$$

Orthogonality: Two RVs are *orthogonal* if their correlation is 0.

**Covariance** is central moment of order  $1+1=2$ :

$$C_{xy} = \mu_{xy}^{11} = E \left\{ (x - E \{x\}) (y - E \{y\})^* \right\} \quad (\text{C.4})$$

Uncorrelatedness: Two RVs are *uncorrelated* if their covariance is 0.

Correlation coefficient

$$\rho_{xy} = \frac{C_{xy}}{\sqrt{C_{xx}C_{yy}}}. \quad (\text{C.5})$$

Due to normalization  $|\rho_{xy}| \leq 1$ .

## C.2 Wide Sense Stationarity

The random process is considered to be wide sense stationary if its first two statistical moments do not change with time. In the case of second non-central moment (autocorrelation) this means that  $R_{xx}(t_1, t_2) = E\{x(t_1)x^*(t_2)\}$  depends only on time difference  $\Delta t = t_2 - t_1$ .

**Theorem 1.** *A random process  $x(t)$  is WSS if and only if spectral components of its Fourier transform  $X(\nu) = \mathcal{F}\{x(t)\}$  are uncorrelated.*

The temporal autocorrelation of random process  $x(t)$ ,

$$\begin{aligned} R_x(t_1, t_2) &= E\{x(t_1) \cdot x^*(t_2)\} \\ &= \int_{-\infty}^{\infty} \int_{-\infty}^{\infty} \underbrace{E\{X(\nu_1) \cdot X^*(\nu_2)\}}_{R_X(\nu_1, \nu_2)} e^{j2\pi(\nu_1 t_1 - \nu_2 t_2)} d\nu_1 d\nu_2, \end{aligned} \quad (\text{C.6})$$

is time independent, i.e.,  $R_x(\Delta t)$ , if and only if Doppler shifts are uncorrelated:

$$R_X(\nu_1, \nu_2) = S_X(\nu_2)\delta(\nu_1 - \nu_2). \quad (\text{C.7})$$

**Theorem 2** (Wiener-Khintchine). *The PSD and autocorrelation of a WSS random process form Fourier transform pair.*

By substituting (C.7) into (C.6):

$$R_x(\Delta t) = \int_{-\infty}^{\infty} S_X(\nu) e^{j2\pi\nu t} d\nu, \quad (\text{C.8})$$

$$S_X(\nu) = \int_{-\infty}^{\infty} R_x(\Delta t) e^{-j2\pi\nu t} d(\Delta t). \quad (\text{C.9})$$

## C.3 Ergodicity

A statistic of random process is *ergodic* when its value calculated by averaging realization of a stochastic ensemble, it is equal to the ensemble average.

Averaging of channel realizations can be performed in fading domains: time, frequency and space:

$$\langle \cdot \rangle_x = \lim_{X \rightarrow \infty} \int_{-X/2}^{X/2} (\cdot) dx, \quad x \in t, f, \vec{r}. \quad (\text{C.10})$$

Table C.1: The relevant probability density functions.

Distribution name	Analytic expression	Distribution parameters	PDF shape	Equivalence	Approximation
Nakagami-m	$f(x m, \Omega) = \frac{2}{\Gamma(m)} \left(\frac{m}{\Omega}\right)^m x^{2m-1} e^{-\frac{m}{\Omega}x^2}$	spread: $\Omega = E[X^2]$ , shape: $m = \frac{\Omega^2}{\text{Var}[X^2]}$ .		For $m=1$ equivalent to Rayleigh distribution.	For $m>1$ can be approximated with Rice distribution
Rice	$f(x \nu, \sigma) = \frac{x}{\sigma^2} \exp\left(-\frac{x^2+\nu^2}{2\sigma^2}\right) I_0\left(\frac{x\nu}{\sigma^2}\right)$	offset: $\nu \geq 0$ , scale: $\sigma \geq 0$ , K-factor: $K = \frac{\nu^2}{2\sigma^2}$ .		Equivalent to Rayleigh distribution for $\nu = 0$ .	Gaussian approximation for a large Rician K-factor, $K \gg 1$ .
Rayleigh	$f(x \sigma) = \frac{x}{\sigma^2} e^{-x^2/2\sigma^2}, \quad x \geq 0$	$2\sigma^2$ is the mean power of the multipath signal			

Continued on next page

Table C.1 Continued from previous page.

Distribution name	Analytic expression	Distribution parameters	PDF shape	Equivalence	Approximation
Normal (Gaussian)	$f(x   \mu, \sigma) = \frac{1}{\sigma\sqrt{2\pi}} e^{-\frac{(x-\mu)^2}{2\sigma^2}}$	mean: $\mu \in \mathbb{R}$ variance: $\sigma^2 > 0$	<p>The plot shows four bell-shaped curves. The legend indicates: <math>\mu=1, \sigma=0.5</math> (blue), <math>\mu=1, \sigma=0.75</math> (green), <math>\mu=2, \sigma=0.75</math> (red), and <math>\mu=2, \sigma=0.5</math> (black). The x-axis ranges from 0 to 3, and the y-axis from 0 to 1.</p>		
Log-normal	$f(x   \mu, \sigma) = \frac{1}{x\sigma\sqrt{2\pi}} e^{-\frac{(\ln x - \mu)^2}{2\sigma^2}}, \quad x > 0$	location: $\mu \in \mathbb{R}$ log-scale: $\sigma^2 > 0$	<p>The plot shows four curves that are skewed to the right. The legend indicates: <math>\mu=0, \sigma=0.5</math> (blue), <math>\mu=0, \sigma=0.75</math> (green), <math>\mu=1, \sigma=0.5</math> (red), and <math>\mu=1, \sigma=0.75</math> (black). The x-axis ranges from 0 to 3, and the y-axis from 0 to 1.</p>		
Exponential	$f(x   \lambda) = \begin{cases} \lambda e^{-\lambda x}, & x \geq 0, \\ 0, & x < 0. \end{cases}$	rate: $\lambda > 0$	<p>The plot shows four curves that decay exponentially from the y-axis. The legend indicates: <math>\lambda=1</math> (blue), <math>\lambda=2</math> (green), <math>\lambda=3</math> (red), and <math>\lambda=4</math> (black). The x-axis ranges from 0 to 3, and the y-axis from 0 to 1.</p>		

$r$  is the envelope amplitude of the received signal, and  $I_0$  is the modified Bessel function of zero order.

## C.4 Probability Density Functions – Overview

The overview of the PDFs being relevant for the thesis is given in Tab. C.1. “In communications theory, Nakagami distributions, Rician distributions, and Rayleigh distributions are used to model scattered signals that reach a receiver by multiple paths. Depending on the density of the scatter, the signal will display different fading characteristics. Rayleigh and Nakagami distributions are used to model dense scatters, while Rician distributions model fading with a stronger line-of-sight. Nakagami distributions can be reduced to Rayleigh distributions, but give more control over the extent of the fading.” [175].

### C.4.1 The Circularly Wrapped Gaussian Distribution

The azimuth angles of geometrical model span in the range of  $360^\circ$ . If angles are drawn from continuous Gaussian distribution, which theoretically have infinite domain, they have to be wrapped to the range  $[-180^\circ, 180^\circ)$ . The WINNER channel model uses circular wrapping in which  $360^\circ$  is subtracted from the angles above the range and  $360^\circ$  is added to the angles below the range. The effect of circular wrapping on the angular distribution is illustrated in Fig. C.1.

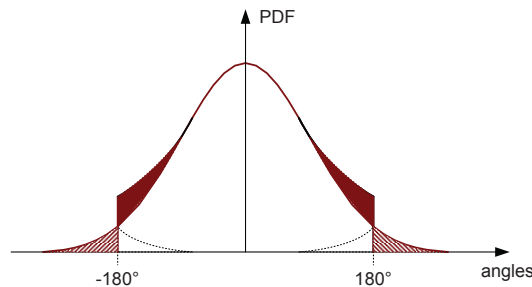


Figure C.1: Wrapping of the Gaussian distribution as implemented in WIM.

This effect is more visible for Gaussian with larger standard deviation, as the indicated in Fig. B.14. For very large standard deviation of initial Gaussian distribution the resulting distribution after wrapping can be approximated with a uniform distribution. The effect of the circular wrapping of the normal distribution on the resulting angular distribution can be approximated with *von Mises* distributions that is sometimes also referred to as circular normal distribution. The von Mises probability density function is

$$f(x | \mu, \kappa) = \frac{e^{\kappa \cos(x-\mu)}}{2\pi I_0(\kappa)}, \quad (\text{C.11})$$

where  $I_0(x)$  is the modified Bessel function of order 0. The parameter  $\mu$  defines the location, while  $\kappa$  measures the concentration. For very large values of  $\kappa$  von Mises distribution approaches a normal distribution with mean  $\mu$  and variance  $\frac{1}{\kappa}$  [176]. This is equivalent to hardly noticeable wrapping effect for Gaussian distribution with small standard deviation  $\sigma$ .

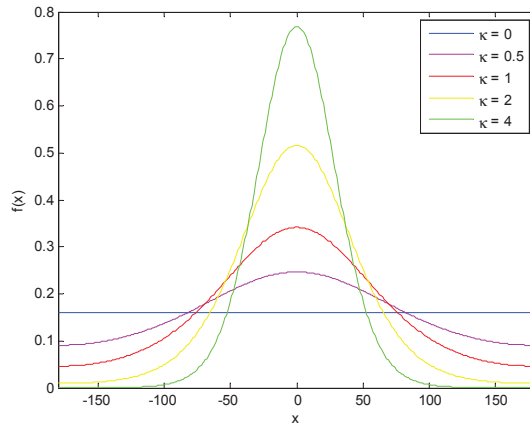


Figure C.2: Von-Mises distributions for  $\mu = 0$  and varying  $\kappa$ .



---

# Bibliography

---

- [1] S. A. Fechtel, "A novel approach to modeling and efficient simulation of frequency-selective fading radio channels," *IEEE J. Sel. Areas Commun.*, vol. 11, no. 3, pp. 422–431, 1993. [cited at p. 1, 47, 48]
- [2] G. L. Stüber, *Principles of Mobile Communications*. Kluwer Academic Publishers, 2002. [cited at p. 1, 67]
- [3] G. J. Forschini and M. J. Gans, "On limits of wireless communications in a fading environment when using multiple antennas," *Wireless Personal Communications*, vol. 6, no. 3, pp. 311–335, 1998. [cited at p. 2]
- [4] C. Schneider, G. Sommerkorn, M. Narandžić, T. Rautiainen, R. Bultitude, V.-M. Holappa, J. Meinilä, P. Kyösti, and T. Jämsä, "IST-4-027756 WINNER II internal report 1.2, measurement results and analysis items," tech. rep., IST-WINNERII, September 2007. [cited at p. 4, 72, 77]
- [5] P. Kyösti, J. Meinilä, L. Hentilä, X. Zhao, T. Jämsä, C. Schneider, M. Narandžić, M. Milojević, A. Hong, J. Ylitalo, V.-M. Holappa, M. Alatossava, R. Bultitude, Y. de Jong, and T. Rautiainen, "IST-4-027756 WINNER II deliverable 1.1.2. v.1.2, WINNER II channel models," tech. rep., IST-WINNERII, September 2007. [cited at p. 4, 52, 55, 56, 57, 58, 60, 72, 73, 77, 93, 94, 96, 97, 103, 110, 111, 113, 121, 137, 139, 145, 147, 150, 161, 179, 181, 187, 191, 196, 198, 199, 205, 209]
- [6] C. A. Balanis, *Antenna theory, Analysis and Design*. John Wiley & Sons, Inc., 2005. [cited at p. 7]
- [7] M. Narandžić, M. Käske, C. Schneider, M. Milojevic, M. Landmann, G. Sommerkorn, and R. S. Thomä, "3D-antenna array model for IST-WINNER channel simulations," in *Proc. VTC2007-Spring Vehicular Technology Conf. IEEE 65th*, pp. 319–323, 2007. [cited at p. 13, 22, 58, 127, 130, 132, 134, 154, 161]
- [8] M. Steinbauer, *The Radio Propagation Channel, A Non-Directional, Directional, and Double-Directional Point-of-View*. PhD thesis, Technische Universität Wien, Nov. 2001. [cited at p. 13, 14, 52, 67, 93, 136]
- [9] B. Sklar, "Rayleigh fading channels in mobile digital communication systems part i: Characterization," *IEEE Commun. Mag.*, vol. 35, no. 7, pp. 90–100, 1997. [cited at p. 15, 36, 39, 47, 135]
- [10] L. Correia, ed., *Wireless Flexible Personalized Communications - COST259: European Commission in Mobile Radio Research*. New York: Wiley, 2001. [cited at p. 15, 68, 93, 180]

- [11] J. C. Maxwell, "On physical lines of force," *Philosophical Magazine*, pp. –, 1861. [cited at p. 15]
- [12] S. M. Rao and N. Balakrishnan, "Computational electromagnetics a review." [cited at p. 17]
- [13] C. Christopoulos, *The Transmission-Line Modeling (TLM) Method in Electromagnetics*. Synthesis Lectures on Computational Electromagnetics, Morgan & Claypool Publishers, 2006. [cited at p. 17]
- [14] T. Kürner, D. Cichon, and W. Wiesbeck, "Concepts and results for 3D digital terrain-based wave propagation models: An overview," *IEEE J. Sel. Areas Commun.*, vol. 11, pp. 1002–1012, Sept. 1993. [cited at p. 17, 19]
- [15] H. L. Bertoni, L. R. Honcharenko, L. R. Maciel, and H. H. Xia, "UHF propagation prediction for wireless personal communications," *Proc. IEEE*, vol. 82, pp. 1333–1359, Sept. 1994. [cited at p. 17]
- [16] T. Fügen, J. Maurer, T. Kayser, and W. Wiesbeck, "Capability of 3D ray tracing for defining parameter sets for the specification of future mobile communications systems," *IEEE Transactions on Antennas and Propagation, Special Issue on Wireless Communications*, vol. 54, pp. 3125–3137, Nov. 2006. [cited at p. 17]
- [17] D. McNamara, C. Pistorius, and J. Malherbe, *Introduction to the Uniform Geometrical Theory of Diffraction*. Boston: Artech House, 1990. [cited at p. 17, 18]
- [18] J. Maurer, T. Fügen, and W. Wiesbeck, "Physical layer simulations of IEEE802.11a for vehicle-to-vehicle communications," vol. 3, (Dallas, TX), pp. 1849–1853, Sept. 2005. [cited at p. 18]
- [19] M. Narandžić, A. Hong, W. Kotterman, R. S. Thomä, L. Reichardt, T. Fügen, and T. Zwick, *OFDM Concepts for Future Communication Systems*, ch. Channel Modeling, pp. 15–31. Springer, 2011. [cited at p. 18]
- [20] S.-C. Kim, B. J. Guarino, T. I. Willis, V. Erceg, S. Fortune, R. Valenzuela, L. Thomas, J. Ling, and J. Moore, "Radio propagation measurements and prediction using three-dimensional ray tracing in urban environments at 908 MHz and 1.9 GHz," *IEEE Trans. Veh. Technol.*, vol. 48, pp. 931–946, May 1999. [cited at p. 19]
- [21] H.-J. Li, C. Chen, T.-Y. Liu, and H.-C. Lin, "Applicability of ray-tracing technique for the prediction of outdoor channel characteristics," *IEEE Trans. Veh. Technol.*, vol. 49, pp. 2336–2349, Nov. 2000. [cited at p. 19]
- [22] T. Rautiainen, G. Wölffe, and R. Hoppe, "Verifying path loss and delay spread predictions of a 3D ray tracing propagation model in urban environment," (Vancouver, BC, Canada), pp. 1264–1268, Sept. 2002. [cited at p. 19]
- [23] T. Fügen, J. Maurer, T. Kayser, and W. Wiesbeck, "Verification of 3D ray-tracing with non-directional and directional measurements in urban macrocellular environments," (Melbourne, Australia), May 2006. [cited at p. 19]
- [24] T. Fügen, J. Maurer, C. Kuhnert, and W. Wiesbeck, "A modelling approach for multiuser MIMO systems including spatially-colored interference," vol. 2, (Dallas, TX), pp. 938–942, Dec. 2004. [cited at p. 19]
- [25] E. Biglieri and G. Taricco, "Transmission and reception with multiple antennas: Theoretical foundations," *Foundations and Trends in Communications and Information Theory*, vol. 1, no. 2, 2004. [cited at p. 19, 38]

- [26] M. Steinbauer, A. Molisch, and E. Bonek, "The double-directional radio channel," *IEEE Trans. Antennas Propag.*, vol. 43, pp. 51–63, Aug. 2001. [cited at p. 22, 57]
- [27] P. Bello, "Characterization of randomly time-variant linear channels," *IEEE Transactions on Communication Systems*, vol. 11, no. 4, pp. 360–393, 1963. [cited at p. 24, 30, 66]
- [28] G. D. Durgin, *Space-Time Wireless Channels*. Prentice Hall, 2003. [cited at p. 24, 31, 33, 35, 36, 39, 50, 51, 52, 53, 135, 227]
- [29] G. D. Galdo, *Geometry-Based Channel Modeling for Multi-User MIMO Systems and Applications*. PhD thesis, Technische Universität Ilmenau, Germany, Feb. 2007. [cited at p. 27, 159]
- [30] "COST 273 channel model implementation." Available at <http://www.ftw.at/cost273>. [cited at p. 28, 161]
- [31] R. Kattenbach, "Statistical modeling of small-scale fading in directional radio channels," *IEEE J. Select. Areas Communications*, vol. 20, pp. 584–592, Apr. 2002. [cited at p. 30, 66]
- [32] W. R. Braun and U. Dersch, "A physical mobile radio channel model," *IEEE Trans. Veh. Technol.*, vol. 40, no. 2, pp. 472–482, 1991. [cited at p. 30, 31, 47, 48, 53]
- [33] M. J. Gans, "A power-spectral theory of propagation in the mobile-radio environment," *IEEE Trans. Veh. Technol.*, vol. 21, no. 1, pp. 27–38, 1972. [cited at p. 35]
- [34] "3GPP TR25.996 V9.0.0 – Spatial channel model for MIMO simulations," tech. rep., Third Generation Partnership Project (3GPP), December 2009. [cited at p. 35, 57, 93, 103, 139, 147, 183]
- [35] "Bessel function zeros." Available at <http://mathworld.wolfram.com/BesselFunctionZeros>. [cited at p. 35]
- [36] B. H. Fleury, "An uncertainty relation for WSS processes and its application to WS-SUS systems," *Communications, IEEE Transactions on*, vol. 44, no. 12, pp. 1632–1634, 1996. [cited at p. 36]
- [37] B. Sklar, "Rayleigh fading channels in mobile digital communication systems part ii: Mitigation," *IEEE Commun. Mag.*, vol. 35, no. 9, pp. 148–155, 1997. [cited at p. 39, 40]
- [38] A. F. Molisch, J. R. Foerster, and M. Pendergrass, "Channel models for ultrawideband personal area networks," *Wireless Communications, IEEE*, vol. 10, no. 6, pp. 14–21, 2003. [cited at p. 42]
- [39] M. Weis, G. Del Galdo, and M. Haardt, "A correlation tensor-based model for time variant frequency selective MIMO channels," in *Proceedings of International ITG/IEEE Workshop on Smart Antennas (WSA07)*, 2007. [cited at p. 43]
- [40] N. Costa and S. Haykin, "A novel wideband MIMO channel model and experimental validation," *Antennas and Propagation, IEEE Transactions on*, vol. 56, no. 2, pp. 550–562, 2008. [cited at p. 43]
- [41] W. Weichselberger, *Spatial Structure of Multiple Antenna Radio Channels, A Signal Processing Viewpoint*. PhD thesis, Technische Universität Wien, March 2003. [cited at p. 44]

- [42] J. Kermaol, L. Schumacher, K. Pedersen, P. Mogensen, and F. Frederiksen, “A stochastic MIMO radio channel model with experimental validation,” *IEEE J. Sel. Areas Commun.*, vol. 20, no. 6, pp. 1211–1226, 2002. [cited at p. 45]
- [43] C. Oestges, “Validity of the Kronecker model for MIMO correlated channels,” in *Vehicular Technology Conference, 2006. VTC 2006-Spring. IEEE 63rd*, vol. 6, pp. 2818–2822, 2006. [cited at p. 45]
- [44] V. Raghavan, J. Kotecha, and A. Sayeed, “Why does the Kronecker model result in misleading capacity estimates?,” *IEEE Trans. Inf. Theory*, vol. 56, no. 10, pp. 4843–4864, 2010. [cited at p. 45]
- [45] D. Porrat, A. Hayar, E. Kaminsky, and M. Uziel, “Spatial dynamics in indoor channels,” Tech. Rep. TD(09)827, Valencia, Spain, May 2009. [cited at p. 47]
- [46] R. Vaughan, *Channels, propagation and antennas for mobile communications*, vol. 50. Iet, 2003. [cited at p. 47]
- [47] G. D. Forney, “Maximum-likelihood sequence estimation of digital sequences in the presence of intersymbol interference,” *Information Theory, IEEE Transactions on*, vol. 18, no. 3, pp. 363–378, 1972. [cited at p. 47]
- [48] M. Pätzold, *Mobile fading channels*. John Wiley England, 2002. [cited at p. 49]
- [49] M. Pätzold, “Tutorial on selected topics in mobile fading channel modelling,” in *Proc. 16th IST Mobile and Wireless Communications Summit*, 2007. [cited at p. 49, 136]
- [50] M. Patzold, U. Killat, F. Laue, and Y. Li, “On the statistical properties of deterministic simulation models for mobile fading channels,” *Vehicular Technology, IEEE Transactions on*, vol. 47, no. 1, pp. 254–269, 1998. [cited at p. 49]
- [51] W. C. Jakes, *Microwave Mobile Communications*. John Wiley & Sons Inc, 1974. [cited at p. 49]
- [52] M. F. Pop and N. C. Beaulieu, “Limitations of sum-of-sinusoids fading channel simulators,” *Communications, IEEE Transactions on*, vol. 49, no. 4, pp. 699–708, 2001. [cited at p. 49]
- [53] M. Landmann, K. Sivasondhivat, J. Takada, I. Ida, and R. Thomä, “Polarization behavior of discrete multipath and diffuse scattering in urban environments at 4.5 GHz,” *EURASIP Journal on Wireless Communications and Networking*, vol. 2007, no. 1, pp. 60–60, 2007. [cited at p. 54]
- [54] L. Vuokko, V.-M. Kolmonen, J. Salo, and P. Vainikainen, “Measurement of large-scale cluster power characteristics for geometric channel models,” *IEEE Trans. Antennas Propag.*, vol. 55, pp. 3361–3365, Nov. 2007. [cited at p. 54]
- [55] A. F. Molisch, H. Asplund, R. Heddergott, M. Steinbauer, and T. Zwick, “The COST259 directional channel model part I: Overview and methodology,” *IEEE Transactions on Wireless Communications*, vol. 5, pp. 3421–3433, December 2006. [cited at p. 54, 67, 93]
- [56] N. Czink, *The Random-Cluster Model*. PhD thesis, Technische Universität Wien, 2007. [cited at p. 54]
- [57] T. Fügen, J. Maurer, W. Sörgel, and W. Wiesbeck, “Characterization of multipath clusters with ray-tracing in urban MIMO propagation environments at 2 GHz,” in *IEEE International Symposium on Antennas and Propagation*, vol. 3B, (Washington DC, USA), pp. 410–413, July 2005. [cited at p. 54]

- [58] C. Oestges, B. Clerckx, D. Vanhoenacker-Janvier, and A. J. Paulraj, "Impact of fading correlations on MIMO communication systems in geometry-based statistical channel models," *IEEE Trans. Wireless Commun.*, vol. 4, no. 3, pp. 1112–1120, 2005. [cited at p. 54]
- [59] A. G. Zajic, G. L. Stuber, T. G. Pratt, and S. T. Nguyen, "Wideband MIMO mobile-to-mobile channels: Geometry-based statistical modeling with experimental verification," *IEEE Trans. Veh. Technol.*, vol. 58, no. 2, pp. 517–534, 2009. [cited at p. 54]
- [60] L. Correia, ed., *Mobile Broadband Multimedia Networks - Techniques, Models and Tools for 4G, COST 273 Final Report*. Oxford: Elsevier, 2006. [cited at p. 55, 68, 93, 139, 150]
- [61] H. Asplund, A. A. Glazunov, A. F. Molisch, K. I. Pedersen, and M. Steinbauer, "The COST 259 directional channel model part II: Macrocells," *IEEE Transactions on Wireless Communications*, vol. 5, pp. 3434–3450, December 2006. [cited at p. 55]
- [62] "3GPP TR 25.996 V6.1.0 – Spatial channel model for MIMO simulations," tech. rep., Third Generation Partnership Project (3GPP), Sept. 2003. [cited at p. 55, 60, 66, 73, 85, 97, 150, 153, 205]
- [63] "Guidelines for evaluation of radio interface technologies for IMT-Advanced, report ITU-R M.2135-1," 12 2009. [cited at p. 55, 93, 136, 139, 147, 151]
- [64] M. Narandžić, L. Reichardt, A. Hong, T. Fügen, W. Kotterman, T. Zwick, and R. S. Thomä, *TakeOFDM Techniques, Algorithms, and Concepts for Future OFDM Systems*, ch. Chapter 2: Channel Modelling. Springer, 2011. [cited at p. 56, 145]
- [65] U. Trautwein, C. Schneider, and R. Thomä, "Measurement-based performance evaluation of advanced MIMO transceiver designs," *EURASIP Journal on Applied Signal Processing*, vol. 2005, pp. 1712–1724, 2005. [cited at p. 56, 65]
- [66] D. S. Baum, J. Salo, G. Del Galdo, M. Milojević, P. Kyösti, and J. Hansen, "An interim channel model for beyond-3G systems: extending the 3GPP spatial channel model (SCM)," in *Proc. VTC 2005-Spring Vehicular Technology Conf. 2005 IEEE 61st*, vol. 5, pp. 3132–3136, 2005. [cited at p. 56, 57, 62, 66, 140, 153, 205]
- [67] H. El-Sallabi, D. S. Baum, P. Zetterberg, P. Kyösti, T. Rautiainen, and C. Schneider, "Wideband spatial channel model for MIMO systems at 5 GHz in indoor and outdoor environments," in *Proc. VTC 2006-Spring Vehicular Technology Conf. IEEE 63rd*, vol. 6, pp. 2916–2921, 2006. [cited at p. 56, 205]
- [68] "IST-2003-507581 WINNER I Deliverable D5.4, Final report on link level and system level channel models," Tech. Rep. v1.4, 2005. 18.11.2005. [cited at p. 56, 58, 186, 187, 205]
- [69] "WINNER (Wireless world INitiative NEw Radio)." <http://www.ist-winner.org/>. [cited at p. 56, 66, 205]
- [70] M. Narandžić, C. Schneider, R. Thomä, T. Jämsä, P. Kyösti, and X. Zhao, "Comparison of SCM, SCME, and WINNER channel models," in *Proc. VTC2007-Spring Vehicular Technology Conf. IEEE 65th*, pp. 413–417, 2007. [cited at p. 57, 62, 66, 157, 158]
- [71] M. Narandžić, M. Landmann, C. Schneider, and R. S. Thomä, "Influence of extraction procedures on estimated wideband MIMO channel parameters," in *Proc. 16th IST Mobile and Wireless Communications Summit*, pp. 1–5, 2007. [cited at p. 58, 73, 86, 88, 89, 96, 148]

- [72] M. Narandžić, C. Schneider, and R. S. Thomä, “WINNER wideband MIMO system-level channel model - comparison with other reference models,” in *Internationales Wissenschaftliches Kolloquium, 54. IWK*, (Ilmenau, Germany), 2009. [cited at p. 60, 93, 97, 161]
- [73] “Rusk channel sounder.” <http://www.channelsounder.de>. [cited at p. 68, 96, 170, 177, 188, 193, 196]
- [74] L. Schumacher, L. Berger, and J. Ramiro-Moreno, “Propagation characterization and MIMO channel modeling for 3G,” in *Adaptive Antenna Arrays; Trends and Applications* (S. Chandran, ed.), pp. 377–393, Springer, 2004. [cited at p. 68]
- [75] M. Jensen and J. Wallace, “MIMO wireless channel modeling and experimental characterization,” in *Space-Time Signal Processing for MIMO Communications* (A. Gershman and N. Sidiropoulos, eds.), pp. 1–39, John Wiley & Sons, 2005. [cited at p. 68]
- [76] M. Ziskind, I. Wax, “Maximum likelihood localization of multiple sources by alternating projection,” *IEEE Trans. Acoust., Speech, Signal Process.*, vol. 36, Oct. 1988. [cited at p. 68]
- [77] A. Paulraj, R. Roy, and T. Kailath, “Estimation of signal parameters via rotational invariance techniques - ESPRIT,” in *Proceedings of the 19th Asilomar Conference on Circuits, Systems and Computers*, pp. 83–89, Nov. 1985. [cited at p. 68]
- [78] R. S. Thomä, D. Hampicke, A. Richter, G. Sommerkorn, C. Schneider, U. Trautwein, and W. Wirtzner, “Identification of time-variant directional mobile radio channels,” *IEEE Trans. Instrum. Meas.*, vol. 49, pp. 357–364, Apr. 2000. [cited at p. 68]
- [79] B. H. Fleury, M. Tschudin, R. Heddergott, D. Dahlhaus, and K. Ingeman Pedersen, “Channel parameter estimation in mobile radio environments using the SAGE algorithm,” *IEEE J. Sel. Areas Commun.*, vol. 17, pp. 434–450, Mar. 1999. [cited at p. 68]
- [80] R. S. Thomä, M. Landmann, and A. Richter, “RIMAX - a maximum likelihood framework for parameter estimation in multidimensional channel sounding,” in *2004 International Symposium on Antennas and Propagation*, (Sendai, Japan), Aug. 2004. [cited at p. 68]
- [81] A. Richter, *Estimation of Radio Channel Parameters: Models and Algorithms*. PhD thesis, Technische Universität Ilmenau, Ilmenau, Germany, 2005. [cited at p. 68, 69, 70, 71, 196, 202]
- [82] M. Landmann, *Limitations of experimental channel characterisation*. PhD thesis, Technische Universität Ilmenau, Ilmenau, Germany, March 2008. [cited at p. 68, 69, 70, 71, 72, 170]
- [83] R. S. Thomä, M. Landmann, A. Richter, and U. Trautwein, *Smart Antennas in Europe - State-of-the-Art (Eurasip Book Series on Signal Processing & Communications)*, vol. 3 of *EURASIP Book Series on SP&C*, ch. Multidimensional High-Resolution Channel Sounding. Hindawi Publishing Corporation, 2005. ISBN 977-5945-09-7. [cited at p. 68, 73, 194]
- [84] M. Landmann, A. Richter, and R. S. Thomä, “DoA resolution limits in MIMO channel sounding,” in *Antennas and Propagation Society International Symposium, 2004. IEEE*, vol. 2, pp. 1708–1711, IEEE, 2004. [cited at p. 70]
- [85] N. Czink, A. Richter, E. Bonek, J.-P. Nuutinen, and J. Ylitalo, “Including diffuse multipath parameters in MIMO channel models,” in *Vehicular Technology Conference, 2007. VTC-2007 Fall. 2007 IEEE 66th*, pp. 874–878, IEEE, 2007. [cited at p. 71]

- [86] “Pyramiden-Absorber DATENBLATT 390-1, Noppen-Absorber DATENBLATT 390-7,” tech. rep., Emc-Technik & Consulting, 2007. [cited at p. 72]
- [87] M. Landman, M. Narandžić, and R. S. Thomä, “Limits of experimental channel characterization related to antenna calibration,” in *Proc. of the XXIX General Assembly of the International Union of Radio Science (URSI)*, (Chicago, IL, USA), Aug. 2008. [cited at p. 72]
- [88] M. Landmann, W. Kotterman, and R. S. Thomä, “On the influence of incomplete data models on estimated angular distributions in channel characterisation,” 2007. [cited at p. 72, 73, 194]
- [89] M. Landmann, M. Käske, and R. S. Thomä, “Impact of incomplete and inaccurate data models on high resolution parameter estimation in multidimensional channel sounding,” *IEEE Transactions on Antennas and Propagation*, vol. 60, pp. 557–573, February 2012. [cited at p. 72]
- [90] A. Böttcher, C. Schneider, M. Narandžić, P. Vary, and R. S. Thomä, “Power and delay domain parameters of channel measurements at 2.53 GHz in an urban macro cell scenario,” in *Proc. Fourth European Conf. Antennas and Propagation (EuCAP)*, pp. 1–5, 2010. [cited at p. 73, 198, 199, 200, 202]
- [91] J. D. Parsons and A. S. Bajwa, “Wideband characterisation of fading mobile radio channels,” *Communications, Radar and Signal Processing, IEE Proceedings F*, vol. 129, no. 2, pp. 95–101, 1982. [cited at p. 76]
- [92] W. C. Y. Lee, “Estimate of local average power of a mobile radio signal,” *IEEE Trans. Veh. Technol.*, vol. 34, pp. 22–27, Feb. 1985. [cited at p. 76]
- [93] D. de la Vega, S. Lopez, J. M. Matías, U. Gil, I. Peña, M. M. Vélez, J. L. Ordiales, and P. Angueira, “Generalization of the Lee method for the analysis of the signal variability,” *Vehicular Technology, IEEE Transactions on*, vol. 58, no. 2, pp. 506–516, 2009. [cited at p. 76]
- [94] V.-M. Kolmonen, K. Haneda, T. Hult, J. Poutanen, F. Tufvesson, and P. Vainikainen, “Measurement-based evaluation of interlink correlation for indoor multi-user MIMO channels,” Tech. Rep. TD(10)10070, Athens, Greece, February 2010. [cited at p. 76]
- [95] J. Poutanen, K. Haneda, J. Salmi, V.-M. Kolmonen, F. Tufvesson, and P. Vainikainen, “Analysis of radio wave scattering processes for indoor MIMO channel models,” Tech. Rep. TD(09)839, Valencia, Spain, May 2009. [cited at p. 76]
- [96] G. Eriksson, F. Tufvesson, and A. F. Molisch, “Characteristics of MIMO peer-to-peer propagation channels at 300 MHz,” Tech. Rep. TD(07)376, Duisburg, Germany, September 2007. [cited at p. 76]
- [97] L. Hentilä, M. Narandžić, J. Meinilä, and P. Kyösti, “Measurement based parameter extraction for WINNER radio channel model,” in *Proc. of the XXIX General Assembly of the International Union of Radio Science (URSI)*, (Chicago, IL, USA), Aug. 2008. [cited at p. 81, 83, 92]
- [98] L. J. Greenstein, D. G. Michelson, and V. Erceg, “Moment-method estimation of the Ricean K-factor,” *Communications Letters, IEEE*, vol. 3, no. 6, pp. 175–176, 1999. [cited at p. 83]

- [99] A. Hong, M. Narandžić, C. Schneider, and R. S. Thomä, “Estimation of the correlation properties of large scale parameters from measurement data,” in *IEEE International Symposium on Personal, Indoor and Mobile Radio Communications (PIMRC)*, (Athens, Greece), pp. 1–5, Sep. 2007. [cited at p. 86, 88, 92, 142]
- [100] T. S. Rappaport, *Wireless Communications: Principles and Practice*. Prentice Hall PTR New Jersey, 2 ed., 2002. [cited at p. 86]
- [101] A. Böttcher, P. Vary, C. Schneider, M. Narandžić, and R. S. Thomä, “Estimation of the radio channel parameters from a circular array with directional antennas,” in *Vehicular Technology Conference (VTC Spring), 2011 IEEE 73rd*, pp. 1–5, IEEE, 2011. [cited at p. 89]
- [102] A. Hong, C. Schneider, G. Sommerkorn, M. Milojevic, R. Thomä, and W. Zirwas, “Experimental evaluation of correlation properties of large scale parameters in an indoor LOS environment,” in *Proc. 3rd Int. Symp. Wireless Communication Systems ISWCS '06*, pp. 55–59, 2006. [cited at p. 92, 142]
- [103] N. Jalden, P. Zetterberg, B. Ottersten, A. Hong, and R. Thomä, “Correlation properties of large scale fading based on indoor measurements,” in *Proc. IEEE Wireless Communications and Networking Conf. WCNC 2007*, pp. 1894–1899, 2007. [cited at p. 92, 142, 146, 148]
- [104] M. Failli, “Digital land mobile radio communications,” tech. rep., COST207, 1989. [cited at p. 93]
- [105] R. Verdone and A. Zanella, *Pervasive Mobile and Ambient Wireless Communications*. Signals and Communication Technology, Springer London Ltd., 2012. [cited at p. 93, 139, 144, 146, 162]
- [106] “Elektrobit’s Propsound.” <http://www.propsound.com>. [cited at p. 96]
- [107] M. Alatossava, V.-M. Holappa, and J. Ylitalo, “Outdoor to indoor MIMO radio channel measurements at 5.25 GHz characterization of propagation parameters,” in *The European Conference on Antennas and Propagation: EuCAP 2006*, vol. 626, p. 266, 2006. [cited at p. 96]
- [108] R. J. C. Bultitude, T. C. W. Schenk, N. A. A. O. den Kamp, and N. Adnani, “A propagation-measurement-based evaluation of channel characteristics and models pertinent to the expansion of mobile radio systems to frequencies beyond 2 GHz,” *Vehicular Technology, IEEE Transactions on*, vol. 56, no. 2, pp. 382–388, 2007. [cited at p. 96]
- [109] T. Rautiainen, J. Juntunen, and K. Kalliola, “Propagation analysis at 5.3 GHz in typical and bad urban macrocellular environments,” in *Vehicular Technology Conference, 2007. VTC2007-Spring. IEEE 65th*, pp. 501–505, IEEE, 2007. [cited at p. 96]
- [110] “IST-4-027756 WINNER II deliverable 1.1.1, WINNER II interim channel models,” tech. rep., IST-WINNERII, September 2005. [cited at p. 96, 130, 205]
- [111] WINNER WP7, *System assessment criteria specification, v1.0*, Deliverable D7.2. v1.0, 30.07.2004. [cited at p. 96]
- [112] M. Narandžić, R. S. Thomä, P. Kyösti, and J. Meinilä, “WINNER reference propagation scenarios,” in *COST 2100, TD(08)459*, (Wroclaw, Poland), February 2008. [cited at p. 96, 152]



- [113] C. Cario and B. Nelson, "Auto-regressive to anything: time series input processes for simulation," *Operations Research Letters*, vol. 19, pp. 51–58, 1996. [cited at p. 97]
- [114] S. Fitzgerald, J. Placeb, and A. van de Liefvoort, "Generating correlated matrix exponential random variables," *Advances in Engineering Software*, vol. 37, pp. 75–84, 2006. [cited at p. 97]
- [115] A. Papoulis, *Probability, Random Variables, and Stochastic Processes*. pub-mcgraw-hill: Mc-Graw Hill, 3rd ed., 1991. [cited at p. 97]
- [116] "Multivariate normal distribution." Available at [http://en.wikipedia.org/wiki/Multivariate\\_normal\\_distribution](http://en.wikipedia.org/wiki/Multivariate_normal_distribution). [cited at p. 98]
- [117] J. P. Boyle and R. L. Dykstra, "A method for finding projections onto the intersection of convex sets in Hilbert spaces," *Advances in order restricted inference*, vol. 37, pp. 28–47, 1986. [cited at p. 102]
- [118] N. J. Higham, "Computing the nearest correlation matrix - a problem from finance," *IMA Journal of Numerical Analysis*, vol. 22, 2002. [cited at p. 102]
- [119] A. P. G. Ariza and J. F. M. L. Rubio, "Alternating projection method applied to indefinite correlation matrices for generation of synthetic MIMO channels," *International Journal of Electronics and Communications*, vol. 64, 2010. [cited at p. 102]
- [120] A. Gehring, M. Steinbauer, I. Gaspard, and M. Grigat, "Empirical channel stationarity in urban environments," in *European Personal Mobile Communications Conference, EPMCC*, (Vienna, Austria), February 2001. [cited at p. 103]
- [121] M. Narandžić, C. Schneider, W. Kotterman, and R. S. Thomä, "Quantification of scenario distance within generic WINNER channel model," *International Journal of Antennas and Propagation*, vol. 2013, pp. 1–17. [cited at p. 104, 109]
- [122] S. Kullback and R. A. Leibler, "On information and sufficiency," *The Annals of Mathematical Statistics*, vol. 22, pp. 79–86, Mar 1951. [cited at p. 104]
- [123] W. D. Penny and S. J. Roberts, "Variational bayes for generalised autoregressive models," tech. rep., Department of Engineering Science, Oxford University, 2000. PARG-00-12. [cited at p. 105]
- [124] B. Fuglede and F. Topsøe, "Jensen-Shannon divergence and Hilbert space embedding." [cited at p. 105]
- [125] M. Narandžić, P. Kyösti, J. Meinilä, L. Hentilä, M. Alatosava, T. Rautiainen, Y. de Jong, C. Schneider, and R. S. Thomä, "Advances in WINNER wideband MIMO system-level channel modelling," in *Proc. of the 2nd European Conference on Antennas and Propagation (EUCAP)*, (Edinburgh, UK), pp. 1–7, Nov. 2007. [cited at p. 105, 139, 140, 141, 146]
- [126] C. Schneider, M. Narandžić, M. Käske, G. Sommerkorn, and R. S. Thomä, "Large scale parameters for the WINNER II channel model at 2.53 GHz in urban macro cell," in *IEEE 71st Vehicular Technology Conference VTC2010-Spring*, (Taipei, Taiwan), May 2010. [cited at p. 108, 198, 200]
- [127] M. Narandžić, C. Schneider, M. Käske, G. Sommerkorn, and R. S. Thomä, "Large-scale parameters of wideband MIMO channel in urban multi-cell scenario," in *5th European Conference on Antennas and Propagation EuCAP2011*, (Rome, Italy), April 2011. [cited at p. 108, 198]

- [128] P. Kyösti, T. Jämsä, A. Byman, and M. Narandžić, “Computational complexity of drop based radio channel simulation,” in *Proc. IEEE 10th International Symposium on Spread Spectrum Techniques and Applications (ISSSTA08)*, pp. 287–291, 2008. [cited at p. 120, 124, 128, 129, 130, 137, 138]
- [129] T. Jämsä and J. Iinatti, “Approximation of geometry based stochastic channel models,” in *Wireless Communication, Vehicular Technology, Information Theory and Aerospace & Electronic Systems Technology, 2009. Wireless VITAE 2009. 1st International Conference on*, (Aalborg, Denmark), pp. 693–697, May 2009. [cited at p. 122]
- [130] P. Kyösti and T. Jämsä, “Complexity comparison of MIMO channel modelling methods,” in *Proc. 4th Int. Symp. Wireless Communication Systems ISWCS 2007*, pp. 219–223, 2007. [cited at p. 124, 128, 129, 137]
- [131] M. Landmann and G. Del Galdo, “Efficient antenna description for MIMO channel modelling and estimation,” in *European microwave week*, 2004. [cited at p. 131, 132]
- [132] G. Del Galdo, J. Lotze, M. Landmann, and M. Haardt, “Modelling and manipulation of polarimetric antenna beam patterns via spherical harmonics,” in *14th Eur. Signal Processing Conf.(EUSIPCO), Florence, Italy*, 2006. [cited at p. 132]
- [133] C. S. Patel, G. L. Stuber, and T. G. Pratt, “Comparative analysis of statistical models for the simulation of Rayleigh faded cellular channels,” *IEEE Trans. Commun.*, vol. 53, no. 6, pp. 1017–1026, 2005. [cited at p. 136]
- [134] A. F. Molisch, M. Steinbauer, M. Toeltsch, E. Bonek, and R. S. Thoma, “Capacity of MIMO systems based on measured wireless channels,” *IEEE J. Sel. Areas Commun.*, vol. 20, no. 3, pp. 561–569, 2002. [cited at p. 137]
- [135] R. Delahaye, Y. Pousset, A.-M. Poussard, P. Combeau, and R. Vauzelle, “From a deterministic transmission channel modelling to an efficiency simulation of radio links quality of ad hoc networks,” Tech. Rep. TD(07)357, Duisburg, Germany, September 2007. [cited at p. 138]
- [136] A. Algans, K. I. Pedersen, and P. E. Mogensen, “Experimental analysis of the joint statistical properties of azimuth spread, delay spread, and shadow fading,” *IEEE J. Sel. Areas Commun.*, vol. 20, no. 3, pp. 523–531, 2002. [cited at p. 142]
- [137] M. Gudmundson, “Correlation model for shadow fading in mobile radio systems,” *Electronics Letters*, vol. 27, no. 23, pp. 2145–2146, 1991. [cited at p. 142]
- [138] E. Perahia, D. C. Cox, and S. Ho, “Shadow fading cross correlation between base stations,” in *Vehicular Technology Conference, 2001. VTC 2001 Spring. IEEE VTS 53rd*, vol. 1, pp. 313–317, IEEE, 2001. [cited at p. 142]
- [139] N. Jaldén, P. Zetterberg, M. Bengtsson, and B. Ottersten, “Analysis of multi-cell MIMO measurements in an urban macro cell environment,” *General Assembly of International Union of Radio Science (URSI’05)*, October 2005. [cited at p. 142, 146]
- [140] M. Narandžić, M. Käske, C. Schneider, G. Sommerkorn, A. Hong, W. Kotterman, and R. S. Thomä, “On a characterisation of large-scale channel parameters for distributed (multi-link) mimo – the impact of power level differences,” Tech. Rep. TD(09)981, Wien, Austria, September 2009. [cited at p. 143, 147, 149]
- [141] G. Golub and C. van Loan, *Matrix computations*. London: The Johns Hopkins University Press, 3 ed., 1996. [cited at p. 143]

- [142] N. Czink, B. Bandemer, G. Vazquez-Vilar, L. Jalloul, C. Oestges, and A. Paulraj, "Spatial separation of multi-user MIMO channels," Tech. Rep. TD(08)622, Lille, France, October 2008. [cited at p. 144]
- [143] J. Poutanen, K. Haneda, V.-M. Kolmonen, J. Salmi, and P. Vainikainen, "Analysis of correlated shadow fading in dual-link indoor radio wave propagation," Tech. Rep. TD(09)910, Wien, Austria, September 2009. [cited at p. 144]
- [144] J. Poutanen, K. Haneda, J. Salmi, V.-M. Kolmonen, F. Tufvesson, T. Hult, and P. Vainikainen, "Significance of common scatterers in multi-link indoor radio wave propagation," in *Antennas and Propagation (EuCAP), 2010 Proceedings of the Fourth European Conference on*, pp. 1–5, IEEE, 2010. [cited at p. 144]
- [145] J. Poutanen, F. Tufvesson, K. Haneda, V.-M. Kolmonen, and P. Vainikainen, "Effect of common clusters on inter-link correlation and sum rate capacity," Tech. Rep. TD(10)11034, Aalborg, Denmark, June 2010. [cited at p. 144]
- [146] J. Weitzen and T. J. Lowe, "Measurement of angular and distance correlation properties of log-normal shadowing at 1900 MHz and its application to design of PCS systems," *Vehicular Technology, IEEE Transactions on*, vol. 51, no. 2, pp. 265–273, 2002. [cited at p. 146, 148]
- [147] K. Zayana and B. Guisnet, "Measurements and modelisation of shadowing cross-correlations between two base-stations," in *Universal Personal Communications, 1998. ICUPC'98. IEEE 1998 International Conference on*, vol. 1, pp. 101–105, IEEE, 1998. [cited at p. 146, 148]
- [148] N. Jaldén, *Analysis and Modelling of Joint Channel Properties from Multi-site, Multi-Antenna Radio Measurements*. PhD thesis, KTH, 2010. [cited at p. 146]
- [149] M. Zhu, F. Tufvesson, and J. Medbo, "Correlation properties of large scale parameters from 2.66 GHz multi-site macro cell measurements," in *Vehicular Technology Conference (VTC Spring), 2011 IEEE 73rd*, pp. 1–5, IEEE, 2011. [cited at p. 146]
- [150] M. Narandžić, W. Kotterman, M. Käske, C. Schneider, G. Sommerkorn, A. Hong, and R. S. Thomä, "On a characterization of large-scale parameters for distributed (multi-link) MIMO - the impact of power level differences," in *European Conference on Antennas and Propagation (EuCAP)*, (Barcelona, Spain), Apr. 2010. [cited at p. 147, 148]
- [151] "WINNER+." <http://projects.celtic-initiative.org/winner+>. [cited at p. 150, 161]
- [152] "COST action 2100 - pervasive mobile & ambient wireless communications." <http://www.cost2100.org>. [cited at p. 151, 195]
- [153] A. A. M. Saleh and R. Valenzuela, "A statistical model for indoor multipath propagation," *Selected Areas in Communications, IEEE Journal on*, vol. 5, no. 2, pp. 128–137, 1987. [cited at p. 153]
- [154] "Spatial radio channel models for systems beyond 3G, contribution to 3GPP RAN4, R4-050854," tech. rep., Elektrobit, Nokia, Siemens, Philips, Alcatel, Telefonica, Lucent, Ericsson, London, September 2005. [cited at p. 156, 205]
- [155] "Spatial radio channel models for systems beyond 3G, contribution to 3GPP RAN4," Tech. Rep. 38, Elektrobit, Siemens, Ericsson, Lucent, Telefonica, Alcatel, France Telecom, Denver, USA, Feb. 2006. [cited at p. 156]

- [156] G. Del Galdo, V. Algeier, N. Czink, and M. Haardt, "Spatial localization of scattering objects from high-resolution parameter estimates," in *NEWCOM-ACORN Workshop*, 2006. [cited at p. 159]
- [157] J. Laurila, A. F. Molisch, and E. Bonek, "Influence of the scatterer distribution on power delay profiles and azimuthal power spectra of mobile radio channels," in *Spread Spectrum Techniques and Applications, 1998. Proceedings., 1998 IEEE 5th International Symposium on*, vol. 1, pp. 267–271, IEEE, 1998. [cited at p. 159]
- [158] C. Oestges and B. Clerckx, "Modeling outdoor macrocellular clusters based on 1.9 GHz experimental data," *Vehicular Technology, IEEE Transactions on*, vol. 56, no. 5, pp. 2821–2830, 2007. [cited at p. 160]
- [159] "COST 2100 channel model implementation." Available at <http://cost2100channel.sourceforge.net>. [cited at p. 161]
- [160] J. O. Nielsen, J. B. Andersen, P. C. F. Eggers, G. F. Pedersen, K. Olesen, E. H. S. rensen, and H. Suda, "Measurements of indoor 16×32 wideband MIMO channels at 5.8 GHz," in *ISSSTA2004*, pp. 864–868, 2004. [cited at p. 170]
- [161] C. Schneider, G. Sommerkorn, M. Narandžić, M. Käske, A. Hong, V. Algeier, W. Kotterman, R. Thomä, and C. Jandura, "Multi-user MIMO channel reference data for channel modelling and system evaluation from measurements," in *International IEEE Workshop on Smart Antennas (WSA 2009)*, (Berlin, Germany), February 2009. [cited at p. 170, 195]
- [162] "3GPP." <http://www.3gpp.org>. [cited at p. 193]
- [163] "Ilmenau reference scenario." Available at <http://www-emt.tu-ilmenau.de/ReferenceScenario/>. [cited at p. 195]
- [164] "EASY-C project (Enablers of Ambient Services and Systems, Part C - Wide Area Coverage)." [http://www.easy-c.de/index\\_en](http://www.easy-c.de/index_en). [cited at p. 195]
- [165] H. W. Lilliefors, "On the Kolmogorov-Smirnov test for normality with mean and variance unknown," *Journal of the American Statistical Association*, vol. 62, 1967. [cited at p. 201]
- [166] C. M. Jarque and A. K. Bera, "A test for normality of observations and regression residuals," *International Statistical Review*, vol. 55, no. 2, pp. 163–172, 1987. [cited at p. 201]
- [167] "3GPP, E-UTRA MIMO channel model text proposal, R1-061002," tech. rep. (agreed). [cited at p. 205]
- [168] "3GPP, System level channel models for E-UTRA evaluations, R1-061594," tech. rep. (agreed). [cited at p. 205]
- [169] "3GPP, Update of polarization description in link level channel model, r1-061371," tech. rep. (noted). [cited at p. 205]
- [170] "Comparison of SCM, SCME, and WINNER models, contribution to 3GPP RAN4, R4-060521," tech. rep., Elektrobit, Telefonica, Siemens, Shanghai, China, May 2006. [cited at p. 205]
- [171] M. Narandžić, P. Kyösti, L. Hentilä, and M. Käske, "MATLAB SW documentation of WIM2 model," tech. rep., 2008. [cited at p. 205, 209, 210, 212]

- [172] P. Kyösti, D. Laselva, J. Salo, and G. Del Galdo, “MATLAB SW documentation of the WIM model,” tech. rep., 30.12.2005. unpublished. [cited at p. 210]
- [173] E. Bonek, “Model validation and related metrics,” in *Mobile Broadband Multimedia Networks* (L. Correia, ed.), Amsterdam, NL: Elsevier Academic Press, 2006. COST273 report Sect.6.7. [cited at p. 213]
- [174] C. Fratzscher, “Verification of WINNER II channel model,” studienarbeit, Technische Universität Ilmenau, 2007. [cited at p. 213, 214, 217, 218, 220, 221, 222, 223, 224, 225]
- [175] “MATLAB help, statistics toolbox.” Available at <http://www.mathworks.com/help/stats/nakagami-distribution>. [cited at p. 231]
- [176] “Von Mises distribution.” Available at [http://en.wikipedia.org/wiki/Von\\_Mises\\_distribution](http://en.wikipedia.org/wiki/Von_Mises_distribution), 2007. [cited at p. 231]

